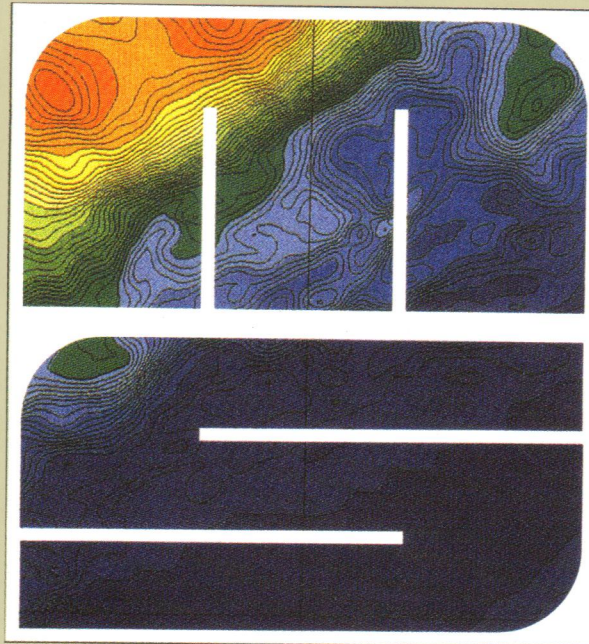


Volume 48, issues 1-4
This completes Volume 48

July 2004

ISSN 0924-7963



Special Issue
Tracer Methods in Geophysical Fluid Dynamics

edited by
Éric J.M. Delhez, Éric Deleersnijder and Michel Rixen

JOURNAL OF
MARINE
SYSTEMS

Table of Contents

- Delhez E.J.M., E. Deleersnijder and M. Rixen, 2004, Preface, *Journal of Marine Systems*, 48, 1-2
- Leffanue H. and M. Tomczak, 2004, Using OMP analysis to observe temporal variability in water mass distribution, *Journal of Marine Systems*, 48, 3-14
- Dutay J.-C., P. Jean-Baptiste, J.-M. Campin, A. Ishida, E. Maier-Reimer, R.J. Matear, A. Mouchet, I.J. Totterdell, Y. Yamanaka, K. Rodgers, G. Madec and J.C. Orr, 2004, Evaluation of OCEMIP-2 ocean models' deep circulation with mantle helium-3, *Journal of Marine Systems*, 48, 15-36
- Jean-Baptiste P., E. Fourré, N. Metz, J.F. TERNON and A. Poisson, 2004, Red Sea deep water circulation and ventilation rate deduced from ^3He and ^{14}C tracer fields, *Journal of Marine Systems*, 48, 37-50
- Hall T.M. and T.W.N. Haine, 2004, Tracer age symmetry in advective-diffusive flows, *Journal of Marine Systems*, 48, 51-59
- Deleersnijder E. and E.J.M. Delhez, 2004, Symmetry and asymmetry of water ages in a one-dimensional flow, *Journal of Marine Systems*, 48, 61-66
- Steinfeldt R., 2004, Ages and age spectra of Eastern Mediterranean Deep Water, *Journal of Marine Systems*, 48, 67-81
- Manca B., M. Burca, A. Giorgetti, C. Coatanoan, M.-J. Garcia and A. Iona, 2004, Physical and biochemical averaged vertical profiles in the Mediterranean regions: an important tool to trace the climatology of water masses and to validate incoming data from operational oceanography, *Journal of Marine Systems*, 48, 83-116
- Ivanov L.M., T.M. Margolina and A.I. Danilov, 2004, Application of inverse technique to study radioactive pollution and mixing processes in the Arctic Seas, *Journal of Marine Systems*, 48, 117-131
- Pavlov V., O. Pavlova and R. Korsnes, 2004, Sea ice fluxes and drift trajectories from potential pollution sources, computed with a statistical sea ice model of the Arctic Ocean, *Journal of Marine Systems*, 48, 133-157
- Korotenko K.A., R.M. Mamedov, A.E. Kontar and L.A. Korotenko, 2004, Particle tracking methods in the approach for prediction of oil slick transport in the sea: modelling oil pollution resulting from river input, *Journal of Marine Systems*, 48, 159-170
- Van den Eynde D., 2004, Interpretation of tracer experiments with fine-grained dredging material at the Belgian Continental Shelf by the use of numerical methods, *Journal of Marine Systems*, 48, 171-189



Preface

34th International Liège Colloquium on Ocean Dynamics

Liège, Belgium, May 6–10, 2002

Tracer methods in geophysical fluid dynamics

Available online 6 March 2004

The International Liège Colloquium on Ocean Dynamics is organized annually. The topic differs from year to year in an attempt to address, as much as possible, recent problems and incentive new subjects in oceanography.

Assembling a group of active scientists from various countries and often different disciplines, the Liège Colloquia provide a forum for discussion and foster a mutually beneficial exchange of information opening on a survey of recent discoveries, essential mechanisms, impelling questions and valuable recommendations for future research.

The 2002 issue of the Liège Colloquium focused on the use of tracers and tracer methods in geophysical fluid dynamics and environmental studies.

Natural processes and man's activities introduce into the ocean and the atmosphere constituents—or tracers—that are transported subsequently at various time and space scales. Decades of measurements of the concentrations of these tracers have generated huge data sets made available to the scientific community through—more and more open—data bases. Dealing with these figures is far from trivial, one of the reasons thereof being that there are so many of them. This is why specific methods have been designed for handling these data.

Tracers are of course important for themselves in large scale and regional pollution studies. The careful analysis of in situ measurements and the modeling and forecast of concentration fields of pollutants form indeed a prerequisite for the rational management of marine resources. Appropriate techniques for the anal-

ysis of data sets and for modeling the advection/dispersion of pollutants, especially in the context of operational oceanography, are therefore developed.

Tracers allow the definition of water masses and of their characteristics. They provide therefore an indirect appraisal of the flow and fluxes of material through the marine system. Their study delivers valuable information about the hydrodynamics of a region, the general movement of water masses and the exchange rates between adjacent basins. Many results and facts about deep water circulation, for instance, can only be inferred indirectly from the analysis of appropriate tracers (Carbon-14, Helium-3 and others).

Tracer fields are also often the main source of information available for calibrating and validating hydrodynamic models; comparing measured and computed concentration fields for various tracers provides an indirect validation of the simulated flow. This procedure of indirect validation is therefore widely used in both regional and large scale studies.

This indirect validation is particularly suited to environmental studies aiming themselves at the simulation of the advection and diffusion of pollutants. It does not however provide quantitative information about the flow itself.

To go further with the analysis of tracer fields, inverse techniques can be used to reconstruct the velocity field (or only part of it, e.g. the vertical component of the velocity vector) or some aspects of the turbulence field from tracer and density data. While the benefits of using a particular tracer are often

hampered by uncertainties about the sources and dynamics of the tracer, the use of different tracers in combinations can help to constrain the flow field and reduce the error bounds.

Other tracer methods have been developed to diagnose particular aspects of the circulation in the ocean or the stratosphere by using in situ measurements of tracer concentration or numerically simulating the fate of natural or artificial tracers. The age of a water mass or of a constituent is among those techniques. By combining advection and diffusion into a single statistics, the concept of age constitutes a very valuable tool to summarize the complex hydrodynamics of a system into a single scalar field—regardless of the particular tracer used for its computation. With the related concepts of transit time and residence time, the age provides a quantitative appraisal of the global transport rates, leading to an improved understanding of the dynamics of the system.

The different presentations made during the 2002 Liège Colloquium addressed critical issues related to tracer techniques :

- How can we maximize the information gathered from existing data bases?
- Which kind of information can be inferred from tracer concentration measurements or simulation?
- What are the errors associated with tracer methods?
- What is the impact of subgrid-scale phenomena and temporal and spatial variability?
- Can we advance tracer methods by improving our theoretical understanding of advection and diffusion phenomena?

Most of these issues are underlying or treated explicitly in the collection of papers forming this special issue of the *Journal of Marine Systems*. The variety of subjects and geographical locations dealt with in these papers reflects the wide range of applicability of tracer techniques in marine science.

The opportunity to assemble contributions from a wide panel of scientists was given by the convergent support of the *Ministère de l'Enseignement Supérieur et de la Recherche Scientifique de la Communauté Française de Belgique*, the *Fonds National de la Recherche Scientifique* (F.N.R.S., Belgium), the *Ministère de l'Emploi et de la Formation du Gouvernement Wallon*, the University of Liège, the Commission of European Union, the Scientific Committee on Oceanographic Research (SCOR), The International Oceanographic Commission of the UNESCO, the US Office of Naval Research, the National Science Foundation (NSF, USA). The Scientific Committee of the 34th Liège Colloquium expresses their gratitude to all of them.

Éric J.M. Delhez*

Éric Deleersnijder

Michel Rixen

Modélisation et Méthodes Mathématiques,

Université de Liège, Sart Tilman B37,

B-4000 Liège, Belgium

E-mail address: E.Delhez@ulg.ac.be

* Corresponding author. Tel.: +32-4-3669419; fax: +32-4-3669489.



Using OMP analysis to observe temporal variability in water mass distribution

Heidi Leffanue*, Matthias Tomczak

School of Chemistry, Physics and Earth Sciences, Flinders University of South Australia, GPO Box 2100, Adelaide SA 5001, Australia

Received 6 September 2002; received in revised form 21 February 2003; accepted 31 July 2003

Available online 19 March 2004

Abstract

Previous optimum multiparameter analyses have investigated spatial distribution of water masses and reported successful results. This study tests the method further with application to a time series to examine temporal variability in water mass distribution. Observations collected from the Sargasso Sea are utilised, mainly to detect well-documented property changes that have occurred in Labrador Sea Water, but also possible fluctuations in water mass contributions as a whole.

The results show much structure and variability in the contributions of Central Water and upper deep waters in the depth range 900–2000 m. It is proposed that the passage of warm and cold core eddies is indicated by these changes in relative contributions of water masses, although quantitative comparison of satellite altimetry data with the model results is not conclusive.

Significant irregularities in the distribution of Labrador Sea Water are also revealed by the model. Through-flow of modified (since the early 1990s) Labrador Sea Water is denoted in the results by an apparent absence from mid-1995 to early 1998. This suggests a transit time of 5–6 years between the Labrador Sea and Bermuda, which is consistent with observational findings described in the literature.

© 2004 Elsevier B.V. All rights reserved.

Keywords: Physical oceanography; Water masses; Modelling; Time series

Regional terms: North Atlantic ocean; Sargasso sea

1. Introduction

The world's oceans play a major role in climate variability and climate change as the exchange of heat and momentum with the atmosphere results in a closely coupled relationship of global influence. Water masses receive their signatures from atmospheric processes and are therefore good indicators for changes in cli-

matic conditions. To give just one example, the 'Great Salinity Anomaly' of 1968–1982, the gradual advection of a cold, fresh water mass around the northern North Atlantic Ocean, could be traced back to changes in the atmospheric circulation over the Arctic Ocean (Walsh and Chapman, 1990).

Some of the most important water masses of the global ocean are formed in polar regions during wintertime, when observations of atmospheric conditions and resulting water mass formation are difficult if not impossible. This paper explores the

* Corresponding author.

E-mail address: heidi.leffanue@flinders.edu.au (H. Leffanue).

possibility of inferring changes of water mass properties in polar and subpolar regions from data collected in the subtropics, using an optimum multiparameter (OMP) modelling technique.

OMP analysis has previously been applied to identifying spatial distribution and mixing of water masses (Tomczak and Large, 1989; Hinrichsen and Tomczak, 1993; Maamaatuaiahutapu et al., 1994; van Aken, 2000), whereas this study tests the concept to analyse temporal variability using time series data. Monthly observations made at the BATS station (Bermuda Atlantic Time-series Study) are ideal for this purpose as they comprise a high quality time series of hydrographic parameters required for OMP analysis (i.e., temperature, salinity, oxygen, nitrate, phosphate and silicate).

The BATS station is situated south east of Bermuda in the Sargasso Sea (nominal location 31°40' N, 64°10' W) and is therefore well positioned to monitor changes occurring over time in Labrador Sea Water, which flows southward through this region as the uppermost layer of North Atlantic Deep Water. This introduces an opportunity for testing OMP modelling as a tool for identifying water mass changes as variations in Labrador Sea Water properties have been well documented over the decades (e.g., Dickson and Namias, 1976; Lazier, 1980; Dickson et al., 1996).

BATS is a collaborative project between the U.S. component of the Joint Global Ocean Flux Study (JGOFS) and the Bermuda Biological Station for Research (BSSR). Nutrient observations have been obtained at the BATS station since November 1988, therefore the present study is restricted to the period 1989–1999.

TOPEX/Poseidon satellite data of sea level anomalies from observations taken in the vicinity of the BATS station (31°7.5' N, 64°7.5' W) were used for confirmation of some of the features seen in the BATS hydrographic data. The satellite data were processed by the CLS (Collecte, Localisation, Satellites) Space Oceanography Division as part of the Environment and Climate EC AGORA (ENV4-CT9560113) and DUACS (ENV4-CT96-0357) projects, using methods as described in LeTraon et al. (1998). The final altimeter product, distributed by AVISO (Archiving, Validation and Interpretation of Satellites Oceanographic data), is an interpolated data set with a resolution of 0.25° × 0.25°.

2. Background and method

Optimum multiparameter (OMP) analysis is an inverse modelling technique which determines the relative contributions of various water masses to a water sample. The method has been described in various papers, for example in Tomczak and Large (1989) and in Poole and Tomczak (1999). Classical OMP analysis assumes that all hydrographic parameters are conserved and therefore not influenced by biogeochemical processes. This is acceptable if the analysis is confined to a limited ocean region and the source water types are defined from data obtained at close proximity. The most recent development of the method (Karstensen and Tomczak, 1998) accounts for the non-conservative behaviour of oxygen and nutrients by applying Redfield ratios, thereby allowing extended OMP analysis to be applied at basin-wide scales, using source water types that originate in areas remote from the study region.

Redfield ratios were initially formulated by Redfield et al. (1963) to describe the relatively constant proportions maintained between dissolved organic carbon, nitrogen, and phosphorus (C, N, P) based on planktonic decomposition, and the related change in dissolved oxygen (O). These elements are taken up by marine organisms during synthesis of organic matter and are subsequently remineralized during oxidation when the organisms die. Silicate (Si) is present only in creatures with silica shells, therefore the regeneration rate is not as constant as for N and P and subject to regional variation. Recent studies have re-evaluated the original ratios (Takahashi et al., 1985) by accounting for mixing along isopycnal surfaces, while Poole and Tomczak (1999) determined a Redfield ratio for silicate for their specific study region by comparing preformed silicate values with observed measurements.

For this study, Redfield ratios for O:N:P of 171:17:1 were taken from Takahashi et al. (1985) and the ratio for Si:P (15:1) adopted from the study by Redfield et al. (1963) for the western Atlantic Ocean.

The OMP technique is an inversion method applied to an over-determined system of linear equations, which is solved for every individual data point. In abbreviated form it can be written as

$$Gx - d = r \quad (1)$$

where G is the matrix of source water types, d is the vector of observations, x is the solution vector and r is the vector of residuals. The equations are normalised (so that parameters measured in different units are comparable) and weighted (to account for differences in measurement accuracy or environmental variability between parameters—see below). This study utilised six hydrographic parameters (salinity, temperature, dissolved oxygen, phosphate, nitrate and silicate), therefore a maximum of six water types could be included in any one model run.

Weights for the OMP matrix were calculated for each depth range using the equation described by Tomczak and Large (1989), that is:

$$W_j = \frac{\sigma_j^2}{\delta_{j\max}} \quad (2)$$

where σ_j is a measure of the ability of parameter j to resolve differences in water mass content and $\delta_{j\max}$ is the largest of water mass variances for parameter j . σ_j was calculated from the source water matrix while $\delta_{j\max}$ was determined from available data in the *World Ocean Atlas* (1998). Annual standard deviations were extracted from the source regions of each water mass for each parameter and the variance calculated from the means. The largest variance for each parameter was then used to determine W_j . Weights for mass cannot be calculated in this manner and were therefore arbitrarily set equal to the highest parameter weight value. The consequences of this are discussed in Results.

In normal applications of OMP analysis the source water type matrix G is uniquely defined through the source water types, which have to be known before the OMP analysis can proceed. The analysis then seeks a solution to Eq. (1) for given G and d that minimises r and finds it by varying x . A strict approach to this problem would require minimisation of Eq. (1) for given d through variation of both x and G . This is a non-linear, generally ill-behaved problem, and this study did not attempt to solve it. Its approach follows the normal OMP procedure, i.e., determines source water type properties from existing historical data and defines G as a time-independent matrix. Variability in the water mass properties is then reflected in the time-behaviour of the residuals: periods of “unusual” water mass properties (which do not match the predetermined source water types) will be seen as periods of abnormally large residuals. While this does not allow the

quantitative determination of changes in water mass properties, it is a good indicator of periods of unusual air–sea interaction in the water mass formation regions.

3. Water masses

A water mass is a body of water defined by a common formation history and originating in a particular region of the ocean (Tomczak, 1999). Various water masses interact throughout the ocean at all depths and therefore any given volume of water can be composed of several water masses.

A number of water masses are usually present in and below the main thermocline in the Sargasso Sea. Preliminary model runs showed the following water masses were found to be the most appropriate choices for the study region.

3.1. Western North Atlantic Central Water (WNACW)

Central Waters are formed by subduction in subtropical regions and are the main component of the permanent thermocline throughout the world’s oceans. Emery and Meincke (1986) subdivided the Central Waters of the North Atlantic into Western and Eastern North Atlantic Central Water, based on variations in temperature and salinity. They considered the differentiation between east and west varieties expressed the physically different properties of the eastern and western portions of the northern subtropical gyre. Researchers often group these Central Waters as one water mass (Tomczak and Godfrey, 1994; Poole and Tomczak, 1999); however, a study by Hinrichsen and Tomczak (1993) conducted in a region bounded by the Sargasso Sea produced sound results using WNACW for thermocline water, showing that the influence of Eastern North Atlantic Central Water is negligible in the region. This study therefore uses WNACW as its thermocline water mass.

WNACW extends to 1000 m at mid latitudes (Hinrichsen and Tomczak, 1993) with a temperature range of 7–20 °C and salinities between 35 and 36.7 (Emery and Meincke, 1986). As Central Water masses display linear temperature–salinity relationships, it is possible to define WNACW by the two water types representing the end points of straight lines in parameter relation-

ships, with all data in between being linear combinations of these two end points.

3.2. North Atlantic Deep Water (NADW)

North Atlantic Deep Water is the generic term for several water masses which flow from their formation region in the North Atlantic to the Southern Ocean, fulfilling an important contribution to the global thermohaline circulation, and the subsequent redistribution of heat and salt (Gordon, 1986). Dickson and Brown (1994) adapted extensive previous research and used their own data sets collected from current meter arrays to show that NADW consisted of four main contributory components:

3.2.1. Labrador Sea Water (LSW)

Labrador Sea Water forms convectively during winter in the central Labrador Sea from waters supplied by the West Greenland Current and the North Atlantic Current, and is traceable by its low salinity and low potential vorticity (Pickart, 1991). It is the warmest and shallowest component of North Atlantic Deep Water, spreading out in four broad tongues from the source area at depths around 1000–2000 m (Dickson and Brown, 1994).

The formation of LSW occurs on a sporadic basis, highlighted by Talley and McCartney's study (1982) which showed that deep convection (and therefore renewal of LSW) was diminished during a 10 year period from 1962 to 1971. Similarly, Clarke and Gascard (1983) found large volumes of LSW formed in the winter of 1976, but that the strength of convection was much reduced in 1978.

More recent studies (Dickson et al., 1996; Sy et al., 1997) have also confirmed the continuing variability of LSW, with a series of intensifying deep wintertime convection events occurring after 1988 in the central Labrador Sea.

3.2.2. Iceland Scotland Overflow Water (ISOW)

Iceland Scotland Overflow Water is derived from cold Norwegian Sea water which overflows the ridges between Scotland and Iceland, initially entraining warm and saline Subpolar Mode Water. At later stages, fresher Labrador Sea Water entering the northern Iceland basin from the west is entrained from above with upper parts of Antarctic Bottom

Water mixing from below (Talley and McCartney, 1982; van Aken, 2000). Dickson and Brown (1994) noted that although ISOW overflows as a relatively fresh source, it mixes so intensely with the warm saline water from the local thermocline (i.e., Subpolar Mode Water) that it carries a high salinity tag thereafter (around 35.0).

Formed by this process of warm and cold entrainment, ISOW flows from the source region following a general westward path under the influence of the Coriolis force and enters the western North Atlantic via the Gibbs fracture zone in the mid-Atlantic ridge. South of Denmark Strait it lies below the fresh core of Labrador Sea Water but above the more dense Denmark Strait Overflow Water (Dickson and Brown, 1994).

3.2.3. Denmark Strait Overflow Water (DSOW)

Denmark Strait Overflow Water originates from a water mass found at intermediate depths in summer in the Norwegian Sea north of the sills, with salinities of 34.8–34.9. This intermediate source water mass outcrops in winter in the Iceland and Greenland Seas and overflows the Denmark Strait sill, which is at a depth of just over 600 m (Swift, 1984). DSOW is the coldest and densest of the NADW source waters and retains its salinity minimum as it overflows and blankets the lower levels of the western North Atlantic (Dickson and Brown, 1994).

3.2.4. Antarctic Bottom Water (AABW)

The formation of Antarctic Bottom Water is initially due to deep convection driven by the freezing of sea ice, but its final properties are shaped during intense subsurface mixing with Circumpolar Water (Tomczak and Godfrey, 1994). Locations of convection are difficult to verify, but evidence implies the main formation area is the Weddell Sea where 50–90% of AABW obtains its characteristics (Fahrbach et al., 1995). Lesser volumes are produced at the Amery Ice Shelf (Wong et al., 1998), the Ross Sea (Jacobs et al., 1985) and the Adélie Coast (Rintoul, 1998).

AABW spreads through the deepest layers of all Atlantic basins and is distinguishable by high silicate and low oxygen levels compared to other subpolar water masses (Dickson and Brown, 1994). It gradually warms as it spreads from the south, slowly mixing

Table 1
Cruise data details, (Used for defining source water types)

Source water	Data set	Ship	Date	Station	
				No.	Position
LSW	TTO/ NAS 55N	Knorr	01/09/81	194	58.1°N 54.3°W
ISOW	TTO/ NAS 55N	Knorr	10/07/81	280	57.4°N 22.4°W
DSOW	Reid/ Mantyla	Knorr	13/08/81	314	64.0°N 33.3°W
AABW	GEOSecs	Knorr	11/01/73	258	56.3°S 24.9°W

with deeper levels of NADW (and at this stage is often called Lower Deep Water).

4. Source water types

OMP analysis requires water masses to be quantified using source water types. A source water type is a point in n-dimensional parameter space which corresponds closely to the properties of a water mass at its source region (Tomczak, 1999).

Previous studies utilising OMP techniques (Hinrichsen and Tomczak, 1993; Poole and Tomczak, 1999) defined a source water type for the Atlantic thermocline using the hydrographic parameters required by OMP analysis, which was deemed appropriate for this study. For the deeper water masses, definitions were derived from cruise data downloaded from the Java OceanAtlas web site (2002). Source regions for the three northern components of NADW were taken from Dickson and Brown's (1994) study, while AABW data were selected from the deepest observations at high latitudes in the Southern Atlantic. Cruise data had to be carefully selected to be within the appropriate source region and include observations of temperature, salinity, oxygen and nutrients, as

required by the modelling program. Table 1 outlines cruise and station details.

Temperature data were converted to potential temperature using the equations of Fofonoff and Millard (1983). Oxygen data were converted to $\mu\text{mol l}^{-1}$ using the molar volume of oxygen given by Weiss (1981), i.e.

$$\text{mol/l} = \frac{x}{22,392} \frac{\text{ml/l}}{\text{ml/mol}}$$

Table 2 summarises the final matrix of source water types and their respective parameter definitions which were used for input into the OMP program.

Not all water masses were included in the analysis over the entire depth range. The analysis can take advantage of the vertical "stacking" of the water masses by splitting the analysis into a series of depth ranges and selecting only those water masses for the source water type matrix that can be reasonably expected to contribute to the observed water mass mix. Continuity of the result across depth range boundaries is used to verify the validity of each selection. This study divides the water column below 900 m depth into three depth ranges. Table 3 shows the water masses and weights used for each depth range.

5. Results

Fig. 1 shows the contribution of the various water masses to the make-up of the water at different depths. At the upper end of the analysed depth range close to 80% of the water is WNACW (Fig. 1a). By 1000 m the presence of WNACW has dropped sharply to 45–55% and gradually diminishes over the next 600 m to values of less than 10% at 1600 m depth (not shown).

Table 2
Source water matrix (source water types and parameter definitions for model input)

Source water	Pot. T (°C)	S (psu)	O ($\mu\text{mol/l}$)	Ph ($\mu\text{mol/l}$)	Ni ($\mu\text{mol/l}$)	Si ($\mu\text{mol/l}$)	Mass conserv.
U WNACW	18.90	36.60	190	0.25	6.0	2.0	1
L WNACW	9.40	35.10	135	1.70	24.0	15.0	1
LSW	3.165	34.832	305	1.09	16.4	9.1	1
ISOW	3.06	34.97	280	1.12	17.0	14.6	1
DSOW	0.28	34.88	314	0.92	14.1	8.2	1
AABW	−0.73	34.64	258	2.23	32.3	117.0	1

Table 3
Weights calculated and water mass selection for model input

Depth range and selected water masses	Weights						Mass cons.
	Pot. T (°C)	S (psu)	O (μmol/l)	Ph 2(μmol/l)	Ni (μmol/l)	Si (μmol/l)	
900–1400m U WNACW: L WNACW: LSW: ISOW	271	126	30	4	32	10	271
1400–2400m U WNACW: L WNACW: LSW: ISOW	271	126	30	4	32	10	271
2600–4200m ISOW: DSOW: AABW	270	60	23	56	–	–	270

The model was run without nitrate and silicate for the 2600–4200m depth range as only four parameters were required.

Fig. 1b shows much vertical structure and temporal variation in the distribution of LSW—in some cases values jump from zero to 30% between two consecutive observations. The greatest irregularity is the complete ‘absence’ of LSW throughout the water

column from mid-1995 to mid-1998. Previous to this, LSW has a patchy presence between 30% and 50% to 2000 m depth (Fig. 1c).

The contribution from ISOW (Fig. 1d and e) shows strong vertical striping and structure to depths of 2000

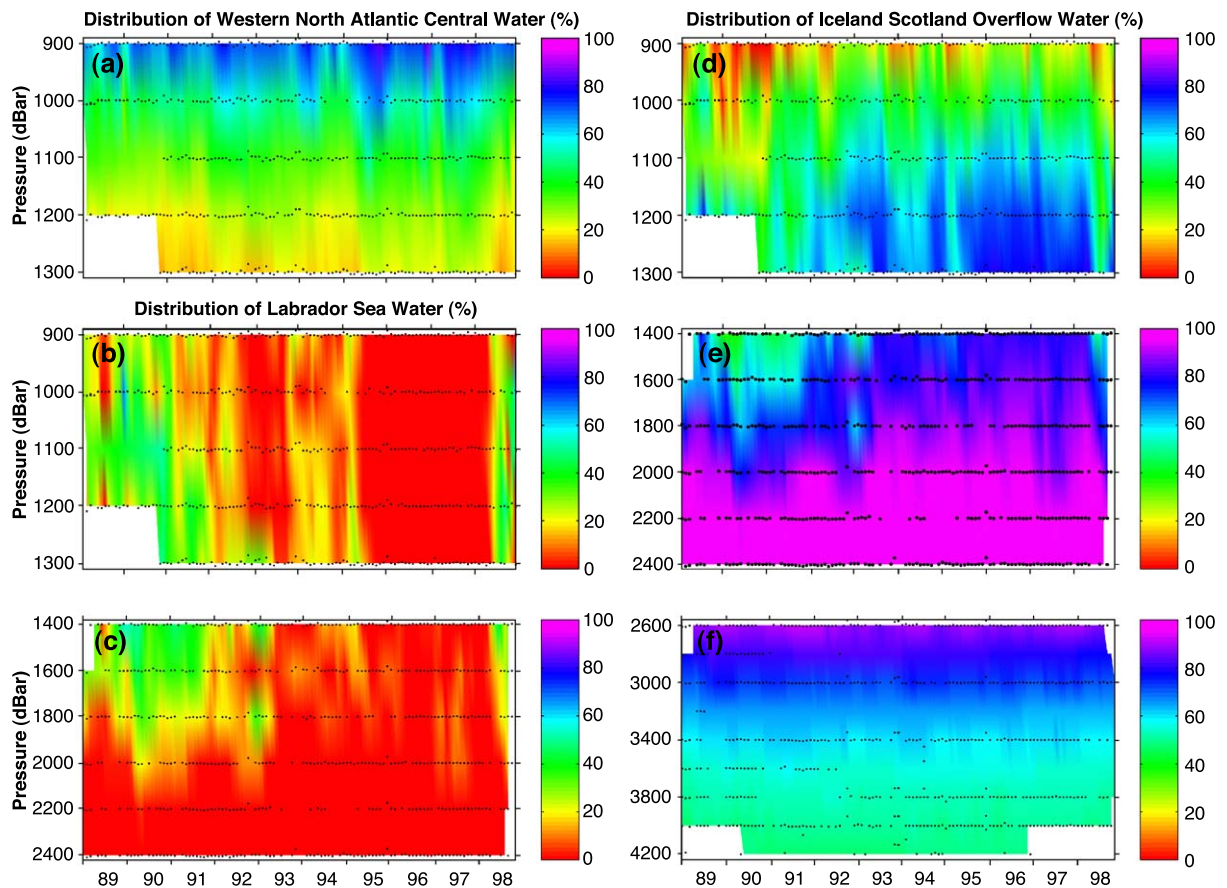


Fig. 1. Water mass contributions (%). (a) WNACW, depth range 900–1300 m; (b) LSW, depth range 900–1300 m; (c) LSW, depth range 1400–2400 m; (d) ISOW, depth range 900–1300 m; (e) ISOW, depth range 1400–2400 m; (f) ISOW, depth range 2600–4200 m.

m, reflecting the distribution pattern of LSW and the influence of WNACW. In the interval between 1995 and 1998 (when LSW is absent), ISOW intrudes as high as 1200 m with values of 75% (Fig. 1d). At depths below 2000 m, the distribution of ISOW is generally horizontal and more uniform, with values of 100% at 2200 m gradually decreasing to around 50% at the sea floor, i.e. 4200 m (Fig. 1f).

A pronounced contribution of DSOW begins around 3200 m depth (not shown); above that values are generally less than 20%. Between 3200 and 4200

m DSOW fills the profile evenly throughout the ten year period with contributions of 35–40%. AABW (not shown) is restricted mainly to the region below 3600 m and then only in negligible proportions, with contribution values of no more than 12%.

Fig. 2 shows the mass conservation residuals plotted as a percentage, to indicate the quality of the solution for each depth range. Note that the colour bar values are different for each profile; as the weights for mass conservation are arbitrary the absolute size of the mass conservation residuals is of no significance.

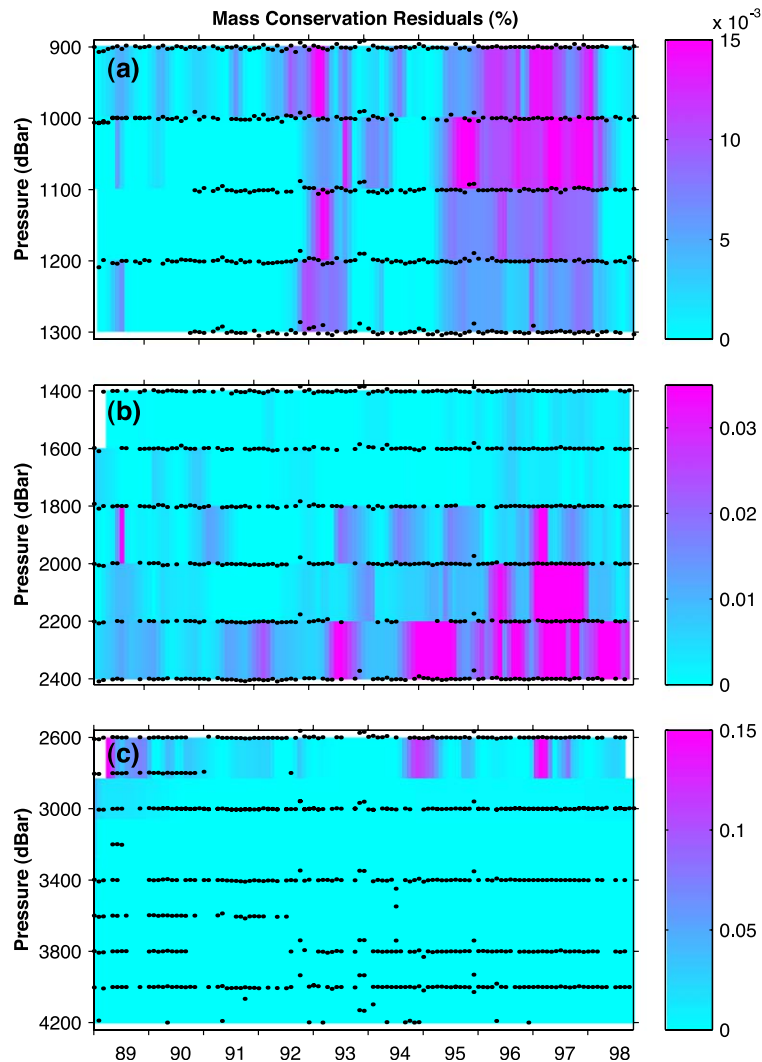


Fig. 2. Mass conservation residuals. (a) depth range 900–1300 m; (b) depth range 1400–2400 m; (c) depth range 2600–4200 m.

The residuals could be made as small as desired by increasing the weight for mass conservation, but changes of the residuals in space and time are an indicator of the quality of the solutions and can reveal significant changes or errors in source water types or water mass distribution.

The largest residuals in the 900–1300 m depth range (Fig. 2a) appear mainly in time intervals which correspond to the apparent absence of LSW in the water column (compare Fig. 1b), with the remainder of the data displaying near zero mass conservation errors.

Error results for the deep and abyssal depth ranges (Fig. 2b and c) generally indicate good matches throughout the ten year period, although inconsistencies coincident with the ‘absence’ of LSW continue down to 2000 m. A band of relatively large residuals can be seen along the 2400 and 2600 m observation levels, a region consisting almost entirely of ISOW (Fig. 1e and f). The band is the result of the water type selection for the two depth ranges (Table 2), which define ISOW as respectively the lower and upper apex of the OMP mixing regime. Even small departures of observed properties from the ISOW source water type will cause the data combination to fall outside the OMP mixing regime. OMP analysis allocates 100% ISOW to such data points and gives them a relatively large residual error.

As the water mass distributions show spatial continuity throughout all depth ranges and reflect known source waters of the region, the model is considered to be qualitatively valid. To verify the quantitative validity of the results, sensitivity to variations in the source water types was examined.

The source water definition matrix was perturbed by adding or subtracting to its elements the variances calculated from the World Ocean Atlas (1998) standard deviation data. These values correspond to environmental variability and measurement errors within a particular source water region. Variances for Western North Atlantic Central Water were taken from Hinrichsen and Tomczak’s paper (1993). Table 4 summarises the parameter variances for each source water which were used to modify the definition matrix.

Mass residuals pertaining to the perturbed results were then subtracted from the original model’s mass residuals. These differences were two orders of magnitude smaller than the conservation of mass errors, indicating that the variations have minimal influence

Table 4

Variances of parameters used for perturbed model

	U WNACW	L WNACW	LSW	ISOW	DSOW
Pot. T ($^{\circ}\text{C}$)	–	–	0.02	0.003	0.014
S (psu)	0.02	0.02	0.0005	0.0002	0.0003
O ($\mu\text{mol/l}$)	5.0	2.0	20.8	18.4	39.9
Ph ($\mu\text{mol/l}$)	0.05	0.05	0.01	0.006	0.009
Ni ($\mu\text{mol/l}$)	0.7	0.7	0.025	0.089	0.399
Si ($\mu\text{mol/l}$)	0.5	0.5	0.334	0.583	0.182

on model results and thereby confirming that the model is robust to variations in source water types.

6. Discussion

The analysis generally produced realistic models of the distribution and contribution of the various water masses present in the Sargasso Sea. Low residuals (<5%) were obtained for each depth range indicating a good match between source water types and the actual data set. The following discussion expands on some points of interest highlighted in the water mass distribution diagrams and the error plots.

7. The Eddy field

A noticeable ‘striping’ effect in the water mass distribution can be seen between 900 and 1200 m depths in the structure of WNACW, which is also reflected in LSW and ISOW distribution (Fig. 1a,b,d). It is suggested that these changes in relative contribution of upper and mid depth water masses are the result of meso-scale eddy dynamics within the Sargasso Sea.

Observations made by the MODE Group (1978) found a persistent band of eddy variability in an area southwest of Bermuda (26°N, 69°W) by undertaking an extensive program of measurements over a five month period. Frankignoul (1981) analysed 24 years of low frequency temperature fluctuations from a station 35 km south east of Bermuda and proposed that the bulk of temperature variability in this region was produced by quasi-geostrophic eddies. Investigations of the current field between Bermuda and the Azores (from approximately 65°W to 40°W) showed that the entire region was dominated by eddies produced by the Azores Current (Krauss et al., 1990).

Hinrichsen and Tomczak's study (1993) of the western North Atlantic thermocline showed the imprint of the eddy field on water mass distribution with variations in WNACW and LSW fractions. Cyclonic features (i.e. cold core rings) corresponded to smaller amounts of WNACW below depths of 600 m and higher values of LSW in the same depth range. Conversely, less LSW and higher values of WNACW were observed for anticyclonic eddies (warm core rings).

Mesoscale eddies vary in diameter from tens to hundreds of kilometres with time scales of weeks to months. Several estimates for the size of eddies and their propagation speed in the Sargasso Sea have been proposed, ranging from 70 to 100 km in diameter and travelling between 2 and 5 km/day (MODE Group, 1978) to 200–300 km at 4.5 km/day (Richardson, 1983).

Assuming a translation speed of 3–4 km per day, eddies of diameter 100 or 250 km (for example) would take approximately 1 or 2–3 months, respectively, to pass over a single observation site. It is therefore reasonable to assume that the striping effect in the time series plots denotes the passage of warm and cold core eddies through the Sargasso Sea, as each eddy event (or 'stripe') produces a 1–3 month signature in the data.

Possible warm core rings can be seen as intrusions of WNACW down to 1200 m, with contributions of 40% for periods of 1–3 months, whereas a reduced contribution of WNACW along the 900 m depth range may indicate cold core eddies with values decreasing from around 75% to 50% for intervals of 1–2 months.

Cyclonic eddies are localised regions of low pressure comprising water of cooler temperatures which is denser than the surrounding water, and can therefore be seen in satellite altimeter data by a corresponding decrease in sea level. The opposite situation applies to anticyclonic rings which are composed mainly of warmer water and show as a positive anomaly in altimeter data.

Quantitative analysis between actual sea levels (using TOPEX/Poseidon altimeter data) and model results did not provide conclusive evidence of eddy fields. Cross-correlation showed the highest correlation at 10–20 day time lags, but with a correlation coefficient of only 0.5. The time lag is most likely due to the BATS station being located approximately 60

km north of the altimeter observation point, while the poor factor of correlation could be due to comparing 900 m depth model data with surface data.

8. Changes in Labrador Sea Water

Fig. 1b and c shows many changes and a lesser contribution than expected in the occurrence of Labrador Sea Water throughout the ten year study period, with corresponding variations in Iceland Scotland Overflow Water distribution (Fig. 1d and e). It is unlikely that the irregular distribution of LSW is an indication of the physical situation in the Sargasso Sea, but rather a record of property modifications of Labrador Sea Water and the subsequent time lag between the source region and Bermuda. Such property modifications could also explain the large rise in error levels associated with the apparent variations in LSW content (Fig. 2a).

If the property definitions of one water mass change, the OMP program will allocate another water mass which is close in parameter space. The mass conservation residuals reflect this inaccuracy by showing maximum errors during times when LSW is 'absent' (i.e. 1993, and June 1995 to June 1998) and ISOW has been designated as the 'replacement' water mass.

The evolution of Labrador Sea Water properties during the last few decades has been documented by several authors. It is not the intention of this paper to add new insight to this set of observational knowledge but to use the information as validation for our model results. The following briefly summarises recent research on the various processes involved and the impact on LSW properties:

Dickson et al. (1996) have suggested that long term changes in convective activity in the North Atlantic are in response to atmospheric forcing, namely the North Atlantic Oscillation (NAO). The NAO is a large scale alternation of the atmospheric masses between the Icelandic low and the Azores high pressure cells. A 'high index' pattern indicates strong mid-latitude westerlies, which blow cold, dry air from Canada across the Labrador basin and are a significant factor in determining the depth of winter convection in the Labrador Sea. Studies on the variability of sea ice extent in the Labrador Sea, also affecting convection

rates, have associated large positive anomalies with simultaneous NAO and El Niño Southern Oscillation (ENSO) events (Wang et al., 1993; Mysak et al., 1995).

The progressive reduction and ultimate cessation of convective activity in the Labrador Sea during the 1960s, and its return in 1970/1971 has been well documented (e.g. Dickson and Namias, 1976; Lazier, 1980). From records of the ocean weather ship (OWS) *Bravo*, the restoration and increased production of deeply convected water has intensified in two main stages, the first from 1972 to 1976 and the second from 1988, producing fresher and colder Labrador Sea Water (Lazier, 1995). Dickson et al. (1996) found that continued deepening convection eventually reached into the lower layers of NADW, resulting in cooler and slightly more saline LSW from around 1990–1995. The model appears to reflect this modification of LSW if the transit time between the Labrador Sea and Bermuda is around 5–6 years.

Early studies estimated a LSW transit time from source to the subtropics of 18 years (Smethie, 1993; Doney and Jenkins, 1994), but more recent analysis of temperature, salinity and tracer data suggests a time lag of 10 years from the Labrador Sea to the Bahamas (26.5°N) (Molinari et al., 1998). These contrasting results were interpreted by the researchers as possible fluxes in the energy state of the Gulf Stream and its recirculation, with the Deep Western Boundary Current (DWBC) linking more directly with the Labrador Sea when energy levels are relatively low and therefore establishing a shorter route.

Pickart et al. (1996) argue that increased forcing due to the harsh winters of the 1980s and 1990s has led to the formation of LSW outside of the Labrador Sea, where it is easily entrained into the DWBC and carried southward quickly, evading the recirculating gyre of the Labrador Sea. Curry et al. (1998) showed that the correlation between extreme convection events in the Labrador Sea and the arrival of LSW with a cooler temperature signal near Bermuda was highest at a 5–6 year time lag. The OMP model complements these findings, and highlights LSW short term variability as source water definitions were taken from 1981 cruise data and effectively capture a small ‘plateau’ of LSW stability before the marked changes of the late 1980’s and early 1990’s (as shown in Fig. 21a of Dickson et al., 1996).

9. Conclusions

This study documents an application of OMP analysis for identifying variations in the temporal distribution of water masses in the Sargasso Sea. OMP analysis has previously been applied to mixing situations mainly in the thermocline with a minimal number of studies on water masses at deeper oceanic levels. This is possibly the first study to apply OMP analysis to a time series of data, showing changes in the contribution and properties of western North Atlantic water masses from 1989 to 1998.

Overall the analysis has produced models of water mass distributions which are reasonable and realistic, supported by low residuals in mass conservation and confirming generally accepted views of the Sargasso Sea environment. From the results, the two main areas of interest are the variations in relative contributions of water masses at intermediate depths, and the intervals of higher values for mass conservation errors which occur when Labrador Sea Water is non-existent in the model output.

The incursion of warmer Central Water down to depths of 1200 m for periods of 1–3 months and the converse situation of decreased contributions at 900 m over similar time spans, is believed to indicate the passage of warm and cold core eddies through the observation site. The literature verifies a persistent eddy field in the region, although cross correlation between satellite altimeter data and the model results is not conclusive.

Irregularities in the distribution of Labrador Sea Water, found mainly in the time interval between mid 1995 and 1998, reveal modification of LSW properties at the source region. Since 1990, severe protracted winters due to strong NAO events and/or simultaneous NAO/ENSO episodes have extended the convection process into the ISOW layer, creating LSW which is saltier and colder than the classical definition. The model indicates a transit time of around 5–6 years for this altered LSW to reach the Sargasso Sea, which is in agreement with observational findings.

In conclusion, this study has found variation in both water mass distribution and source water formation on a temporal scale. OMP analysis has proved to be an effective tool, possibly for detecting mesoscale oceanic features such as eddies, and for identifying water mass property modifications.

Future work will have to concentrate on development of OMP analysis into a nonlinear minimisation scheme that allows simultaneous variation of the water mass contribution vector x and the source water type matrix G . This would allow not only the identification of periods of unusual water mass properties (such as in this case the period mid-1995–1998 for LSW) but also a quantitative determination of the change that occurred. The result could be a time history of source water type properties for several water masses formed in different regions, derived from observations at a single location in the easily accessible subtropics. Work in that direction is proceeding.

Acknowledgements

Special thanks to Rosemary Morrow of CNES (Centre National d'Études Spatiales) for providing satellite data of sea level anomalies at very short notice, and to two anonymous reviewers whose expertise in LSW led to considerable refinement of model input and whose suggestions helped greatly to improve this paper.

References

- Clarke, R.A., Gascard, J.C., 1983. The formation of Labrador sea water Part I: large-scale processes. *Journal of Physical Oceanography* 13, 1764–1778.
- Curry, R.G., McCartney, M.S., Joyce, T.M., 1998. Oceanic transport of subpolar climate signals to mid-depth subtropical waters. *Nature* 391, 575–577.
- Dickson, R.R., Brown, J., 1994. The production of North Atlantic deep water: sources, rates and pathways. *Journal of Geophysical Research* 99 (C6), 12319–12341.
- Dickson, R.R., Namias, J., 1976. North American influences on the circulation and climate of the North Atlantic sector. *Monthly Weather Review* 104 (10), 1256–1265.
- Dickson, R.R., Lazier, J., Meincke, J., Rhines, P., Swift, J., 1996. Long term coordinated changes in convective activity of the North Atlantic. *Progress in Oceanography* 38, 241–295.
- Doney, S.C., Jenkins, W.J., 1994. Ventilation of the deep western boundary current and abyssal western North Atlantic: estimates from tritium and ^3He distributions. *Journal of Physical Oceanography* 24, 638–659.
- Emery, W.J., Meincke, J., 1986. Global water masses: summary and review. *Oceanologica Acta* 9 (4), 383–391.
- Fahrbach, E., Rohardt, G., Scheele, N., Schröder, M., Strass, V., Wisotzki, A., 1995. Formation and discharge of deep and bottom water in the northwestern Weddell Sea. *Journal of Marine Research* 53, 515–538.
- Fofonoff, P., Millard Jr., R.C. 1983. Algorithms for computation of fundamental properties of seawater. *Unesco Technical Papers in Marine Science* 44, 42–43.
- Frankignoul, C., 1981. Low-frequency temperature fluctuations off Bermuda. *Journal of Geophysical Research* 86 (C7), 6522–6528.
- Gordon, A.L., 1986. Inter-ocean exchange of thermocline water. *Journal of Geophysical Research* 91 (C4), 5037–5046.
- Hinrichsen, H.H., Tomczak, M., 1993. Optimum multiparameter analysis of the water mass structure in the Western North Atlantic ocean. *Journal of Geophysical Research* 98 (C6), 10155–10169.
- Jacobs, S.S., Fairbanks, R.G., Horibe, Y., 1985. Origin and evolution of water masses near the Antarctic continental margin: Evidence from $\text{H}_2^{18}\text{O}/\text{H}_2^{16}\text{O}$ ratios in seawater. In: Jacobs, S. (Ed.), *Oceanology of the Antarctic Continental Shelf*. Antarctic Research Series, vol. 43. AGU, Washington, DC, pp. 59–85.
- Java Ocean Atlas, S., 2002. Oceanographic Data Sets. Ocean Climate Laboratory, National Oceanographic Data Center, Silver Spring. <http://odf/ucsd/edu/joa/datasets.html>.
- Karstensen, J., Tomczak, M., 1998. Age determination of mixed water masses with CFC and oxygen data. *Journal of Geophysical Research* 24, 2777–2780.
- Krauss, W., Käse, R.H., Hinrichsen, H.H., 1990. The branching of the Gulf Stream Southeast of the Grand Banks. *Journal of Geophysical Research* 95 (C8), 13089–13103.
- Lazier, J.R.N., 1980. Oceanographic conditions at ocean weather ship *Bravo*, 1964–1974. *Atmosphere-Ocean* 18, 227–238.
- Lazier, J.R.N., 1995. The salinity decrease in the Labrador Sea over the past thirty years. In: Martinson, D.G., Bryan, K., Ghil, M., Hall, M.M., Karl, T.M., Sarachik, E.S., Sorooshian, S., Talley, L.D. (Eds.), *Natural Climate Variability on Decade-to-Century Time Scales*, pp. 295–302. National Academy Press, Washington, DC.
- LeTraon, P.Y., Nadel, F., Ducet, N., 1998. An improved mapping method of multi-satellite altimeter data. *Journal of Atmospheric and Oceanic Technology* 15, 522–533.
- Maamaatuaiahutapu, K., Garcon, G.C., Provost, C., Boulahdid, M., Bianchi, A.A., 1994. Spring and winter water mass composition in the Brazil/Malvinas confluence. *Journal of Marine Research* 52, 397–426.
- MODE Group, 1978. The mid-ocean dynamics experiment. *Deep Sea Research* 25, 859–910.
- Molinari, R.L., Fine, R.A., Wilson, W.D., Curry, R.G., Abell, J., McCartney, M.S., 1998. The arrival of recently formed Labrador Sea water in the deep Western boundary current at 26.5°N . *Geophysical Research Letters* 25 (13), 2249–2252.
- Mysak, L.A., Ingram, R.G., Wang, J., van der Baaren, A., 1995. The anomalous sea-ice extent in Hudson Bay, Baffin Bay and the Labrador Sea during three simultaneous NAO and ENSO episodes. *Atmosphere-Ocean* 34 (2), 313–343.
- Pickart, R.S., 1991. Water mass components of the North Atlantic deep western boundary current. *Deep Sea Research* 39 (II), 1553–1574.
- Pickart, R.S., Spall, M.A., Lazier, J.R.N., 1996. Mid-depth ventilation in the western boundary current system of the sub-polar gyre. *Deep Sea Research* 44, 1025–1054.

- Poole, R., Tomczak, M., 1999. Optimum multiparameter analysis of the water mass structure in the Atlantic Ocean thermocline. *Deep Sea Research* 46, 1895–1921.
- Redfield, A.C., Ketchum, B.H., Richards, F.A., 1963. The influence of organisms on the composition of sea-water. In: Hill, M.N. (Ed.), *The Sea: Ideas and Observations on Progress in the Study of the Seas*, vol. 2. Wiley, London, pp. 26–77.
- Richardson, P.L., 1983. Gulf stream rings. In: Robinson, A.R. (Ed.), *Eddies in Marine Science*. Springer Verlag, Berlin, 19–45.
- Rintoul, S.R., 1998. On the origin and influence of Adélie Land bottom water. In: Jacobs, S., Weiss, R. (Eds.), *Ocean, Ice and Atmosphere: Interactions at the Antarctic Continental Margin-Antarctic Research Series*, vol. 75. AGU, Washington, DC, pp. 151–171.
- Smethie, W.M., 1993. Tracing the thermohaline circulation in the western North Atlantic using chlorofluorocarbons. *Progress in Oceanography* 31, 51–99.
- Swift, J.H., 1984. The circulation of the Denmark strait and iceland-Scotland overflow waters in the North Atlantic. *Deep Sea Research* 31, 1339–1355.
- Sy, A., Rhein, M., Lazier, J.R.N., Koltermann, K.P., Meincke, J., Putzka, A., Bersch, M., 1997. Surprisingly rapid spreading of newly formed intermediate waters across the North Atlantic Ocean. *Nature* 386, 675–679.
- Takahashi, T., Broecker, W.S., Langer, S., 1985. Redfield ratio based on chemical data from isopycnal surfaces. *Journal of Geophysical Research* 90, 6907–6924.
- Talley, L.D., McCartney, M.S., 1982. Distribution and circulation of Labrador Sea water. *Journal of Physical Oceanography* 12, 1189–1204.
- Tomczak, M., 1999. Some historical, theoretical and applied aspects of quantitative water mass analysis. *Journal of Marine Research* 57, 275–303.
- Tomczak, M., Godfrey, J.S., 1994. *Regional Oceanography: an Introduction*. Pergamon, Oxford.
- Tomczak, M., Large, D.G.B., 1989. Optimum multiparameter analysis of mixing in the thermocline of the Eastern Indian ocean. *Journal of Geophysical Research* 94 (C11), 16141–16149.
- van Aken, H.M., 2000. The hydrography of the mid-latitude north-east Atlantic Ocean. *Deep Sea Research* 47 (I), 757–788.
- Walsh, J.E., Chapman, W.L., 1990. Arctic contribution to upper-ocean variability in the North Atlantic. *Journal of Climate* 3 (12), 1462–1473.
- Wang, J., Mysak, L.A., Ingram, R.G., 1993. Interannual variability of sea-ice cover in Hudson Bay, Baffin Bay and the Labrador Sea. *Atmosphere-Ocean* 32 (2), 421–447.
- Weiss, R., 1981. Oxygen solubility in seawater. *UNESCO Technical Papers in Marine Science* 35, 22.
- Wong, A.P.S., Bindoff, N.L., Forbes, A., 1998. Ocean-ice shelf interaction and possible bottom water formation in Prydz Bay, Antarctica. In: Jacobs, S., Weiss, R. (Eds.), *Ocean, Ice and Atmosphere: Interactions at the Antarctic Continental Margin-Antarctic Research Series*, vol. 75. AGU, Washington, DC, pp. 173–187.
- World Ocean Atlas, R., 1998. Live Access to Reference Data at PMEL, Scripps Institution of Oceanography, San Diego. <http://ferret.wrc.noaa.gov/las>.



Evaluation of OCMIP-2 ocean models' deep circulation with mantle helium-3

J.-C. Dutay^{a,*}, P. Jean-Baptiste^a, J.-M. Campin^b, A. Ishida^c, E. Maier-Reimer^d,
R.J. Matear^e, A. Mouchet^f, I.J. Totterdell^g, Y. Yamanaka^c, K. Rodgers^a,
G. Madec^h, J.C. Orr^a

^aLaboratoire des Sciences du Climat et de l'Environnement, Gif sur Yvette, France

^bInstitut d'Astronomie et de Géophysique G. Lemaître, Université Catholique de Louvain, Louvain-la-Nueve, Belgium

^cInstitute for Global Change Research, Tokyo, Japan

^dMax Planck Institut für Meteorologie, Hamburg, Germany

^eCommonwealth Science and Industrial Research Organization, Hobart, Australia

^fAstrophysics et Geophysics Institute, University of Liege, Belgium

^gSouthampton Oceanography Centre, Southampton, England, UK

^hLaboratoire d'Océanographie Dynamique et de Climatologie, Paris, France

Received 25 September 2002; received in revised form 28 April 2003; accepted 27 May 2003

Available online 20 April 2004

Abstract

We compare simulations of the injection of mantle helium-3 into the deep ocean from six global coarse resolution models which participated in the Ocean Carbon Model Intercomparison Project (OCMIP). We also discuss the results of a study carried out with one of the models, which examines the effect of the subgrid-scale mixing parameterization. These sensitivity tests provide useful information to interpret the differences among the OCMIP models and between model simulations and the data.

We find that the OCMIP models, which parameterize subgrid-scale mixing using an eddy-induced velocity, tend to underestimate the ventilation of the deep ocean, based on diagnostics with $\delta^3\text{He}$. In these models, this parameterization is implemented with a constant thickness diffusivity coefficient. In future simulations, we recommend using such a parameterization with spatially and temporally varying coefficients in order to moderate its effect on stratification.

The performance of the models with regard to the formation of AABW confirms the conclusion from a previous evaluation with CFC-11. Models coupled with a sea-ice model produce a substantial bottom water formation in the Southern Ocean that tends to overestimate AABW ventilation, while models that are not coupled with a sea-ice model systematically underestimate the formation of AABW.

We also analyze specific features of the deep ^3He distribution (^3He plumes) that are particularly well depicted in the data and which put severe constraints on the deep circulation. We show that all the models fail to reproduce a correct propagation of these plumes in the deep ocean. The resolution of the models may be too coarse to reproduce the strong and narrow currents in the deep ocean, and the models do not incorporate the geothermal heating that may also contribute to the generation of these currents. We also use the context of OCMIP-2 to explore the potential of mantle helium-3 as a tool to compare and evaluate modeled deep-ocean circulations. Although the source function of mantle helium is known with a rather large uncertainty, we

* Corresponding author. Tel.: +33-1-69-08-31-12; fax: +33-1-69-08-77-16.

E-mail address: dutay@lsce.saclay.cea.fr (J.-C. Dutay).

find that the parameterization used for the injection of mantle helium-3 is sufficient to generate realistic results, even in the Atlantic Ocean where a previous pioneering study [J. Geophys. Res. 100 (1995) 3829] claimed this parameterization generates inadequate results. These results are supported by a multi-tracer evaluation performed by considering the simulated distributions of both helium-3 and natural ^{14}C , and comparing the simulated tracer fields with available data.

© 2004 Elsevier B.V. All rights reserved.

Keywords: OCMIP-2; Helium-3; Parameterization

1. Introduction

Ocean carbon models are developed to improve our understanding of the ocean carbon cycle. There is a growing number of research groups that have implemented CO_2 cycling into their ocean models in order to study CO_2 in the oceanic reservoir and potential feedback of CO_2 on climate. The Ocean Carbon Cycle Model Intercomparison Project (OCMIP) was initiated to intercompare and evaluate existing global ocean carbon models. Thirteen modeling groups participated to the second-phase of the project (OCMIP-2), which focused in part on evaluating modeled circulation with geochemical tracers. Different geochemical tracer simulations were performed to assess the models' circulation. Surface and subsurface circulation was evaluated from the simulation of anthropogenic tracers, such as CFCs (Dutay et al., 2002) and bomb C-14, whose recent injection in the ocean is appropriate to study processes that occur over decadal timescales. Conversely, deep-ocean circulation was evaluated with tracers that have been injected over longer time scales. For this purpose, during OCMIP-2, we made simulations for both natural ^{14}C and mantle ^3He . These two tracers provide different constraints on deep-ocean circulation due to the nature of their injection: natural ^{14}C is injected at the air-sea interface, whereas mantle He-3 is injected at mid-depth along mid-ocean ridges. The injection of the hot hydrothermal fluids in the deep ocean produces large scale plumes that are highly enriched in ^3He relative to the background seawater values that are set by solubility equilibrium with atmospheric helium (Clarke et al., 1969). This ^3He signal can be used to trace patterns of the ocean circulation thousand of kilometers away from the source region (Lupton and Craig, 1981). Helium-3 measurements are available with greatly enhanced coverage thanks to the recent WOCE program. However, the global rate of mantle helium-3

injection in the ocean is still uncertain (Craig et al., 1975; Jean-Baptiste, 1992, Farley et al., 1995). Hence, using different ocean general circulation models can also help to better evaluate the limits of existing parameterization of the mantle helium injection in the ocean.

In this paper, we have two main goals. The first objective is to compare and evaluate the deep circulation of the models participating in OCMIP-2 with a standard mantle helium-3 simulation. As the physics of the OCMIP-2 models differ in many ways, we have incorporated sensitivity tests with one model to better understand the differences amongst all these models. The sensitivity tests concern the parameterization of subgrid-scale mixing in the models, which is known to have a large influence to the redistribution of tracers (England and Hirst, 1997; England and Rahmstorf, 1999).

The second objective is to explore the potential of natural helium-3 as a tool to compare and evaluate modeled deep-ocean circulations. In their work, which pioneered the use of mantle helium in a global ocean circulation model, Farley et al. (1995) proposed a parameterization for the rate of injection of this tracer based on observational studies of helium sources in mantle volcanism. This parameterization led to realistic results in their modeling study, except in the Atlantic Ocean where modeled ^3He concentrations were too high. We use the context of OCMIP-2, with several simulations from different global ocean models, to further evaluate this parameterization.

2. Description of the models

Six of the 13 modeling groups participating in OCMIP-2 made simulations of natural helium-3 (CSIRO, Australia; IGCR, Japan; IPSL, France; MPIM, Germany; SOC, UK; UL, Belgium). The

main characteristics of these models are described in Dutay et al. (2002). We briefly recall them below (Table 1) to provide the necessary information for interpreting simulations. All models but MPIM are coarse resolution primitive equation models. MPIM is a Large-scale Geostrophic Model, which neglects non-linear terms in the advection equation (Maier-Reimer et al., 1993). The dynamical forcing (surface wind stresses, heat fluxes and fresh water fluxes) is different for each of the models. The models are forced with seasonally varying fluxes, except for IGCR, which is forced at the surface with annually averaged fields and which has a prescribed cooling for the North Atlantic thermal forcing to facilitate deep water formation. The MPIM and UL models are coupled to a sea-ice model that include both thermodynamics and sea ice dynamics. The parameterization of ocean physics also differs in many aspects among the models. For instance, the lateral subgrid-scale mixing parameterization, which is known to produce a large effect on the predicted circulation and tracer redistribution (England and Hirst, 1997; England and Rahmstorf, 1999) varies among the models. It is horizontal in three models (IGCR, MPIM and UL), whereas the three others (CSIRO, IPSL and SOC) orient such mixing along isopycnal surfaces. Addi-

tionally, the latter three models also use the eddy-induced velocity parameterization proposed by Gent et al. (1995), hereafter GM.

In this paper, we have included sensitivity tests conducted with one of the models (the IPSL model) in order to better understand the influence of the different parameterization of lateral mixing on the circulation and the tracer redistribution. We show results of simulations performed with the IPSL model with the same physics and forcing as the standard version used for the OCMIP project (see Table 1), except that in one version the lateral subgrid-scale mixing parameterization is horizontal (IPSL_HOR), while in the second one, it is oriented along isopycnal surfaces (IPSL_ISOP). In all the simulations with the IPSL model, a semi-diagnostic method is applied. Temperature and salinity are restored towards the climatological observations of Levitus in the interior of the ocean, below the mixed-layer and away from the ocean-land boundaries and the Equatorial band. This method constrains the ocean interior to be close to the observed thermohaline structure. As the dynamic of the interior of the ocean is to first order geostrophic, it allows us to investigate and isolate the effects of the subgrid-scale mixing parameterization in a quasi identical and fairly realistic interior circulation fields.

Table 1
Model characteristics

	CSIRO	IGCR	IPSL	MPIM	SOC	UL
Horizontal resolution (long. × lat.)	5.6° × 3.2°	4° × 4°	From 2° × 1.5° to 0.5° Eq.	5° × 5°	2.5° × 3.75°	3° × 3°
Seasonality	yes	no	yes	yes	yes	yes
Surface boundary conditions	T,S seasonal restoring	Levitus T,S annual restoring +N. Atl cooling	flux + restoring	restoring	restoring + flux	bulk formula
Lateral subgrid-scale mixing	ISOP+GM	HOR	ISOP+GM	HOR	ISOP+GM	HOR
Sea-ice model	–	–	–	yes		yes
Reference	(Matear and Hirst, 1999)	(Yamanaka and Tajika, 1996)	(Madec et al., 1998)	(Maier-Reimer et al., 1993)	(Gordon et al., 2000)	(Goosse and Fichefet, 1999)

Levitus: Climatological Atlas of the World Ocean, NOAA, 1982.

HOR, ISOP, GM: Horizontal, Isopycnal, Gent and Mc Williams parameterization.

CSIRO (Commonwealth Science and Industrial Research Organization), Hobart, Australia.

IGCR/CCSR (Institute for Global Change Research), Tokyo, Japan.

IPSL (Institut Pierre Simon Laplace), Paris, France.

MPIM (Max Planck Institut fuer Meteorologie), Hamburg, Germany

SOC (Southampton Oceanography Centre)/SUDO/Hadley center (UK Met. Office), England.

UL (University of Liege)/UCL (Université Catholique de Louvain), Belgium.

3. Parameterization of mantle helium injection

For OCMIP-2, all models followed the same simulation protocols. The impact of geothermal heating on models circulation is ignored. The protocol for injection of mantle helium follows that proposed by Farley et al. (1995), with a few exceptions. First we simulate both ^3He and ^4He distributions as separate tracers rather than simulate solely the helium isotopic ratio. We then calculate the latter by the ^3He excess, i.e. $\delta^3\text{He}$, where $\delta^3\text{He} = 100((R_{\text{ocean}}/R_{\text{atmosphere}}) - 1)$ and $R = ^3\text{He}/^4\text{He}$ (see <http://www.ipsl.jussieu.fr/OCMIP> for details). Second, we take into account the ^3He sources from the West Pacific including Pandora-Tripartite Ridge, Tonga-Kermadec-Lau Basin, Fidji, Manus Basin, Woodlark Basin, Mariana/Izu-Bonin and Okinawa Spreading centers. Following Farley et al. (1995), the mantle helium flux is assumed to be linearly proportional to the ridge-spreading rate. The latter is tabulated for different sites from the global tectonic model of DeMets et al. (1990) (Fig. 1). We assume total ^3He and ^4He fluxes of 1000 and $90.6 \cdot 10^6 \text{ mol year}^{-1}$, respectively. Together these produce an injected mantle helium isotopic ratio $R = 8 \times R_{\text{atmosphere}}$, which is characteristic of ridge basalts and hydrothermal vents (Lupton and Craig, 1975). The total rate of injection of $1000 \text{ mol } ^3\text{He year}^{-1}$ is based on the estimation of Clarke et al. (1969), but there is at least a $\pm 25\%$ of uncertainty (Farley et al., 1995).

Maximum mantle helium fluxes (fastest spreading rates) occur in the Pacific Ocean at the East Pacific Rise (EPR); intermediate fluxes are found in the central Indian and Southern Oceans; minimum fluxes (slowest spreading rates) are found at the Mid-Atlantic Ridge (MAR) and Southwest Indian Ridge (SWIR) (Fig. 1).

Field observations in the Pacific, the Indian and Atlantic Oceans indicate that vent waters enter the ocean at several hundred degrees centigrade and typically rise a few hundred meters in the water column before achieving neutral buoyancy (Lupton et al., 1985; Jean-Baptiste et al., 1991, 1998, 1992). Thus, in the simulations, mantle-helium was injected 300 m above the ridge axis. The depth of injection of mantle helium was generally between 2000 and 3000 m (Fig. 1).

Mantle helium is a passive tracer. The only sink for oceanic helium is loss to the atmosphere. This

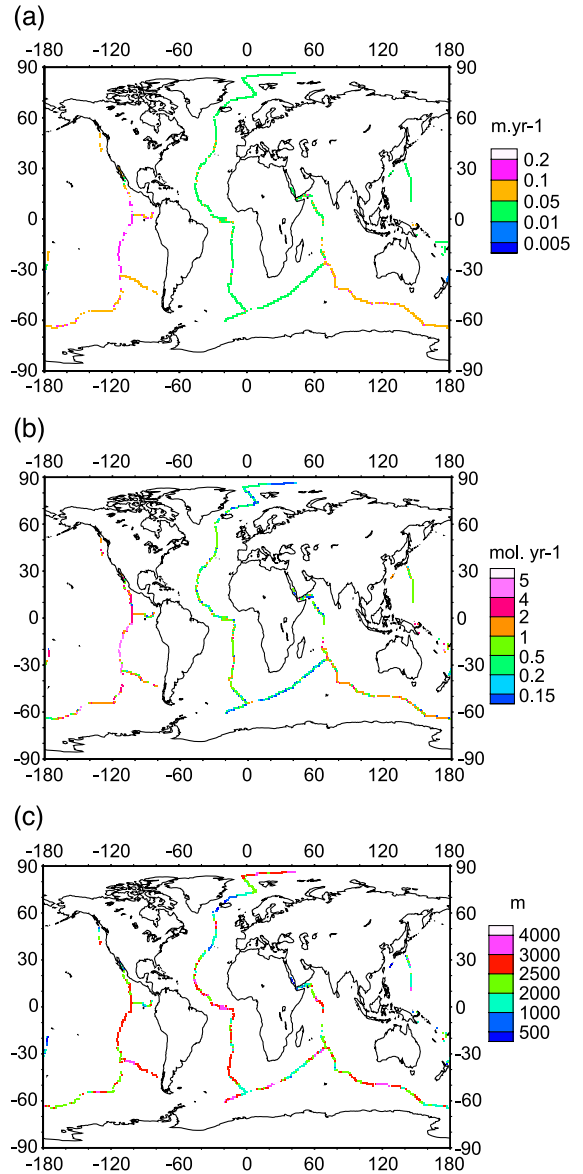


Fig. 1. (a) Ridges spreading rates in meters per year, (b) rate of injection of mantle helium-3 in moles per year and (c) depth of injection of mantle helium-3 in meters.

flux Q is parameterized by the air-sea gas exchange formula

$$Q = k(\alpha p\text{He} - C_s)$$

where k is the air-sea gas transfer velocity, whose formulation for the OCMIP-2 simulation is described

in detail in Dutay et al. (2002), α is the solubility and $p\text{He}$ is the atmospheric partial pressure of each isotope ($p^4\text{He} = 5.24 \times 10^{-6}$ and $p^3\text{He} = R_{\text{atmosphere}} \times p^4\text{He}$, where $R_{\text{atmosphere}} = 1.38 \times 10^{-6}$), and C_s is the modeled sea surface concentration. The He-4 solubility is prescribed according to the formulation of Wanninkhof (1992), using modeled sea surface temperature (SST) and salinity (SSS). The ^3He solubility is equal to the ^4He solubility times the isotope fractionation factor of 0.984 (Weiss, 1971).

The anthropogenic perturbation due to production of ^3He by the disintegration of bomb tritium is not modeled. The simulations are initialized with uniform ^3He and ^4He values of 2.35×10^{-12} and 1.73×10^{-6} mol m^{-3} , respectively. These concentrations are corresponding to those that are in solubility equilibri-

um with the partial pressures of these isotopes in the atmosphere, for seawater at $T = 10^\circ\text{C}$ and $S = 34\text{‰}$. Models simulations were integrated until they reached a quasi-steady state, i.e., until the globally integrated model drift was less than 4 mol year^{-1} for ^3He and $1 \times 10^{-6} \text{ mol year}^{-1}$ for ^4He .

4. Results

4.1. Global distributions

The $\delta^3\text{He}$ distribution at 2000 m provides a convenient description of the simulated large-scale redistribution of this tracer in the simulations (Fig. 2). The inter-basin $\delta^3\text{He}$ distribution at that depth, which is

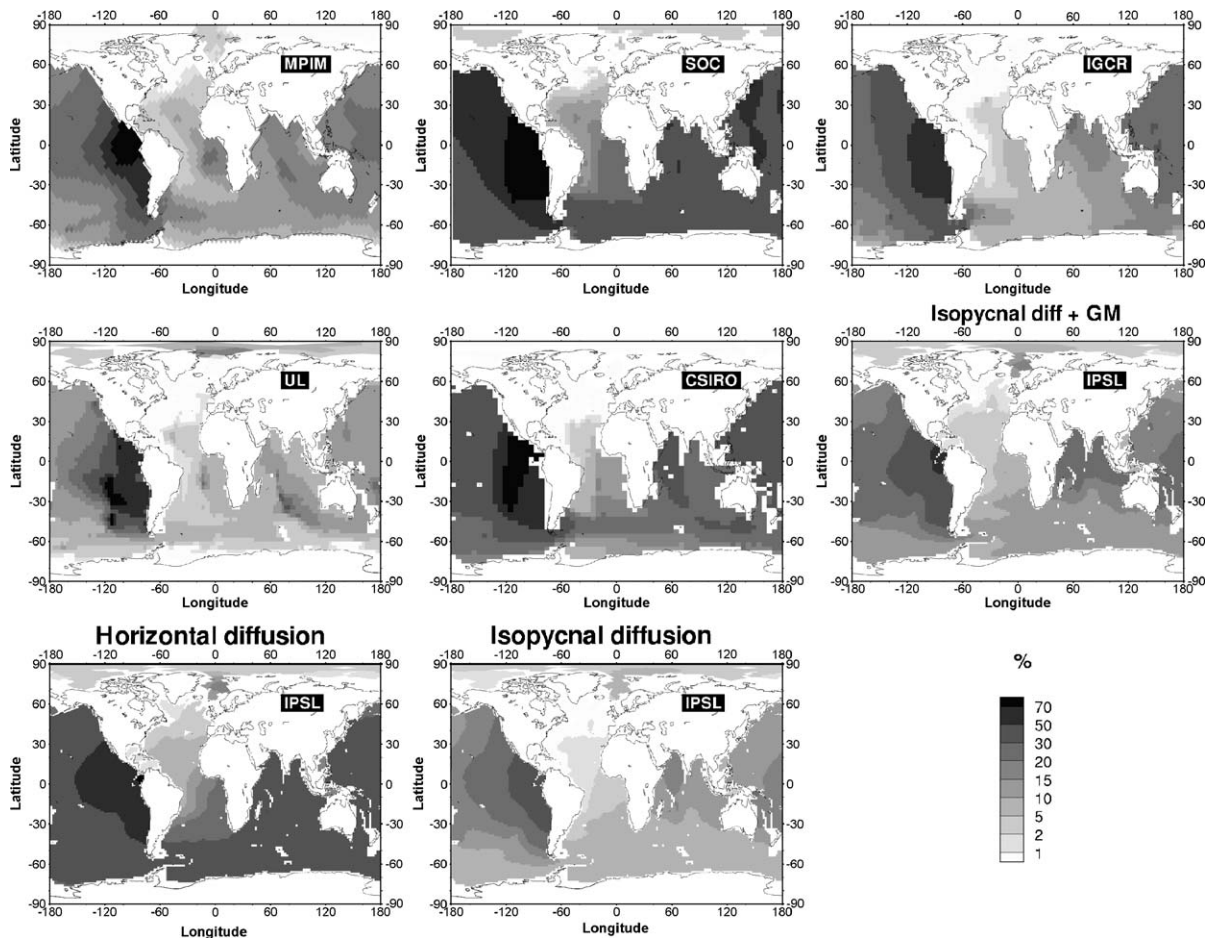


Fig. 2. Models' helium isotopic distribution at 2000 m depth, units: %.

close to the depth of the tracer injection, is qualitatively similar for all OCMIP-2 models. The highest $\delta^3\text{He}$ are observed in the Pacific Ocean, where the rate of injection is high (Fig. 1) and where no newly ventilated deep water is formed (Warren, 1983). Conversely, the lowest simulated $\delta^3\text{He}$ levels are found in the Atlantic Ocean. Here, the rate of injection is lowest and this basin is also filled by recently ventilated North Atlantic Deep Water (NADW) which has a low $\delta^3\text{He}$. All the models produce a clear signal of low $\delta^3\text{He}$ in the Deep Western Boundary Current (DWBC) (Fig. 2). This coincides with the core with high CFC concentration, which characterizes the southward flow of recently ventilated NADW (Dutay et al., 2002). This flow occurs both in the real ocean and in the models, at depths corresponding to the depth of mantle helium injection (Dutay et al., 2002). In the Indian and Southern Oceans, modeled $\delta^3\text{He}$ have intermediate values. Both basins have intermediate injection rates, with that in the Indian Ocean being slightly lower (Fig. 1). Still, $\delta^3\text{He}$ are lower in the Southern Ocean where the upwelling in the Antarctic Circumpolar Current (ACC) helps to remove the excess helium-3 by delivering it to the surface where it exchanges with the atmosphere.

Despite general similarities, the distribution of $\delta^3\text{He}$ between basins differs substantially among models. The simulated range for the average oceanic $\delta^3\text{He}$ level varies by $\pm 65\%$ around the mean (Table 2). Two models clearly stand out: SOC produces globally the highest $\delta^3\text{He}$ levels among all models, whereas the lowest levels are generated by UL.

Table 2
Averaged $\delta^3\text{He}$

	CSIRO	IGCR	IPSL	MPIM	SOC	UL
Global	20.2	15.1	14.0	14.8	33.8	9.9
Atlantic	6.1	11.3	5.8	6.4	18.6	2.1
Pacific	29.4	23.6	19.4	21.8	42.3	16.7
Indian	18.8	9.6	13.6	12.0	32.0	7.2
Austral	16.6	11.9	10.9	11.4	32.7	4.3
	IPSL_HOR		IPSL_ISOP		IPSL_GM	
Global	29.2		9.9		14.0	
Atlantic	12.8		3.5		5.8	
Pacific	36.3		14.5		19.4	
Indian	29.6		8.6		13.6	
Austral	31.0		7.4		10.9	

The sensitivity of the IPSL model's $\delta^3\text{He}$ to the parameterization of subgrid-scale mixing is large, similar to the OCMIP-2 model range. The simulation with horizontal mixing (IPSL_HOR) has the weakest deep-ocean ventilation rate and the highest $\delta^3\text{He}$. When mixing is oriented along isopycnal surfaces (IPSL_ISOP), deep-ocean ventilation rate is enhanced, and the $\delta^3\text{He}$ is reduced globally by a factor of 3. Finally, when the eddy-induced velocity parameterization is added (IPSL_GM), it acts to restratify the ocean thermohaline structure and diminish the deep-ocean ventilation rate while increasing the global $\delta^3\text{He}$ average by nearly 50%, relative to IPSL_ISOP.

4.2. Pacific Ocean

In the Pacific Ocean, all the models have their highest concentration in the eastern part of the basin, close to the main source of mantle helium-3 near the East Pacific Rise. An opportunity to evaluate the simulated helium-3 distribution in this region is provided by the WOCE P17 section at 135°W (WHPO, 2002). This meridional section is plotted in Fig. 3 along with the corresponding section in each model. Qualitatively, $\delta^3\text{He}$ distribution appears similar in both the observations and the models. Low $\delta^3\text{He}$ are observed and simulated in surface and subsurface water, high concentration prevails in the intermediate and deep ocean between 1000 and 3500 m depth, and lower $\delta^3\text{He}$ values are found at depth.

However, the details of the observed helium isotopic distribution are not well reproduced by the models. Two $\delta^3\text{He}$ maxima associated with plume jets are observed at 2500 m depth on both sides of the equator 12°S and 8°N, respectively. The spatial resolution of the OCMIP-2 models is too coarse to reproduce such detailed structure. Instead, the models produce a single maximum that spans a larger spatial extent. For the models, the contiguous $\delta^3\text{He}$ maxima lie at a depth corresponding with the observations. The maximum in the MPIM model is exceptionally shallow by nearly 1000 m. This problem in the MPIM model is due to its equatorial Pacific upwelling that is too strong (Maier-Reimer et al., 1993; Farley et al., 1995).

Quantitatively, only three models (MPIM, UL and IPSL_GM) reproduce realistic $\delta^3\text{He}$ distribution along this section. The other 3 models (SOC, IGCR and CSIRO), have excessive $\delta^3\text{He}$ when compared to the

observations. The results of the sensitivity study with the IPSL model provide us with a means to understand the differences between the OCMIP-2 models. The

simulation with horizontal mixing (IPSL_HOR) has the weakest deep-ocean ventilation rate, and its simulated $\delta^3\text{He}$ is higher than observed. When the lateral

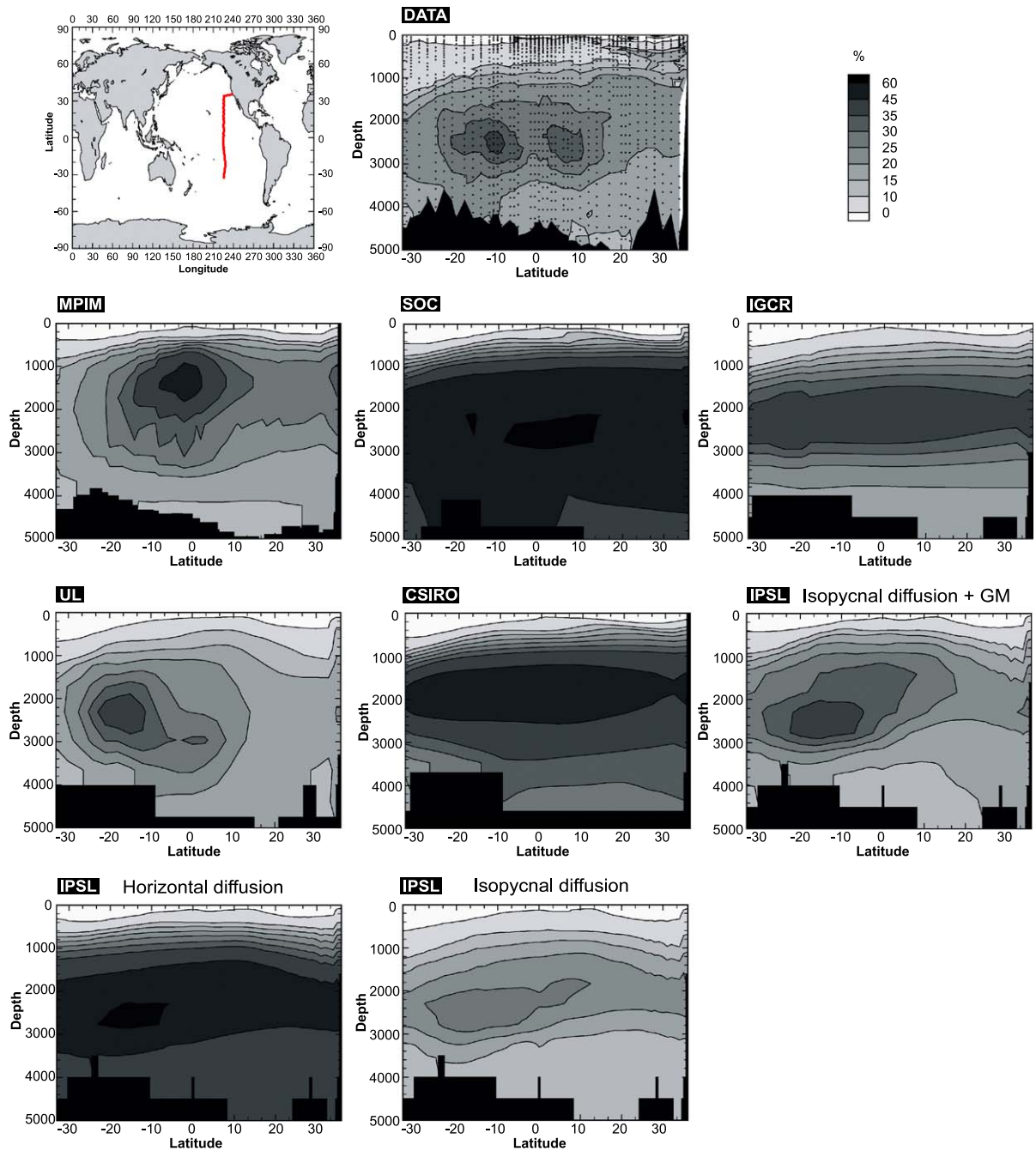


Fig. 3. Helium isotopic distribution along the WOCE P17 section (135°W), units: %.

subgrid-scale mixing is oriented along isopycnal surfaces (IPSL_ISOP), $\delta^3\text{He}$ is lower, because increased exchange between the mixed-layer and the ocean interior enhance ventilation of the deep ocean (Guiyardi et al., 2001). Eddy activity plays an important role in the subduction of water masses in the Southern Ocean (Marshall, 1997). The effect of eddy-induced velocity parameterization (GM) is an up-gradient transfer of tracers in this region (Lee et al., 1997). This acts to restratify the modeled thermohaline structure and to reduce the ventilation of the deep ocean. This effect has previously been demonstrated by England and Rahmstorf (1999) using a simulation with natural ^{14}C . In our helium-3 simulation, the GM parameterization tends to diminish the loss of tracer from the deep ocean by reducing the connection between the surface and the ocean interior. Out of the three IPSL runs, the GM simulation produces the most realistic helium-3 distribution along this section.

The SOC and CSIRO models, which also use the GM parameterization, show a very weak deep-ocean ventilation, i.e. $\delta^3\text{He}$ that is too high. It is less pronounced with the IPSL model, which produces realistic $\delta^3\text{He}$ values, because it uses the robust-diagnostic method, which tends to moderate the effects of restratification due to the GM parameterization.

The deep-ocean ventilation is weak in the IGCR model because of its annual mean forcing fields. This model then underestimates processes that are crucial for producing deep-ocean ventilation such as the formation of the deep surface mixed-layer in winter.

Having analyzed the meridional distribution of natural helium-3 in the Eastern Pacific, we now investigate the longitudinal spreading of the tracer in the basin. The WOCE P04 section at 10°N (Wijffels et al., 1996) provides a helpful longitudinal basin-scale distribution of the tracer. The observations reveal a westward propagation of the high helium-3 plume in the basin (Fig. 4). Model performances along this section resembles that along the previous section: the SOC, CSIRO and IGCR models still have $\delta^3\text{He}$ values that are too high along the whole section, but it is now less pronounced for IGCR.

The three other models (MPIM, UL and IPSL) produce a similar discrepancy relative to the observations. That is, their $\delta^3\text{He}$ that is too high in the eastern part of the section, close to the region of mantle helium injection (Fig. 1), and in the west, far from the main

source of mantle helium, the values are significantly too low. These distributions suggest that the east-to-west transport in this region is too sluggish in these coarse resolution models. Along all this and the previous section, the water enriched in helium-3 appears to flow in the same direction in both the observations and all the models. However, such is not everywhere the case. Along another section at 15°S , observations show a plume of enriched helium-3 propagating westward from the East Pacific Rise (Fig. 5) (Lupton and Craig, 1981). Conversely, all models simulate an Eastward propagation of the tracer that also appears in the idealized model of the abyssal circulation of Stommel and Arons (1960).

4.3. Indian Ocean

The observed helium-3 distribution in the Eastern Indian Ocean along the WOCE I07n section (WHPO, 2002) provides an opportunity to evaluate the simulation in this basin. Here, $\delta^3\text{He}$ levels are on average lower than those in the Pacific, for both the observations and the OCMIP-2 models (Fig. 6). Model performance in this basin is somewhat different than in the Pacific Ocean. As in the Pacific, the SOC and CSIRO models produce $\delta^3\text{He}$ levels that are generally higher than observed, and the MPIM and UL models produce more realistic values. However, IGCR results now appear more similar to those of MPIM and UL, whereas IPSL_GM is significantly overestimating $\delta^3\text{He}$ levels.

Along this section, the version of the IPSL model that looks the most similar to the MPIM and UL (the models that have been found to be most like the data in the Pacific Ocean) is the isopycnal mixing case (IPSL_ISOP). The use of the GM parameterization in the IPSL model leads to results, which differ from those of MPIM and UL in the Indian Ocean.

4.4. Southern Ocean—AABW formation

During WOCE, $\delta^3\text{He}$ was measured along several sections near sources of AABW in the Southern Ocean. The WOCE SO4p and WOCE SO4-3 (WHPO, 2002) sections provide measurements in the Ross and Weddell Seas, respectively (Figs. 7 and 8). The vertical $\delta^3\text{He}$ distribution along these two sections displays similar features: In surface and subsurface waters, $\delta^3\text{He}$ is low and close to solubility equilibrium with

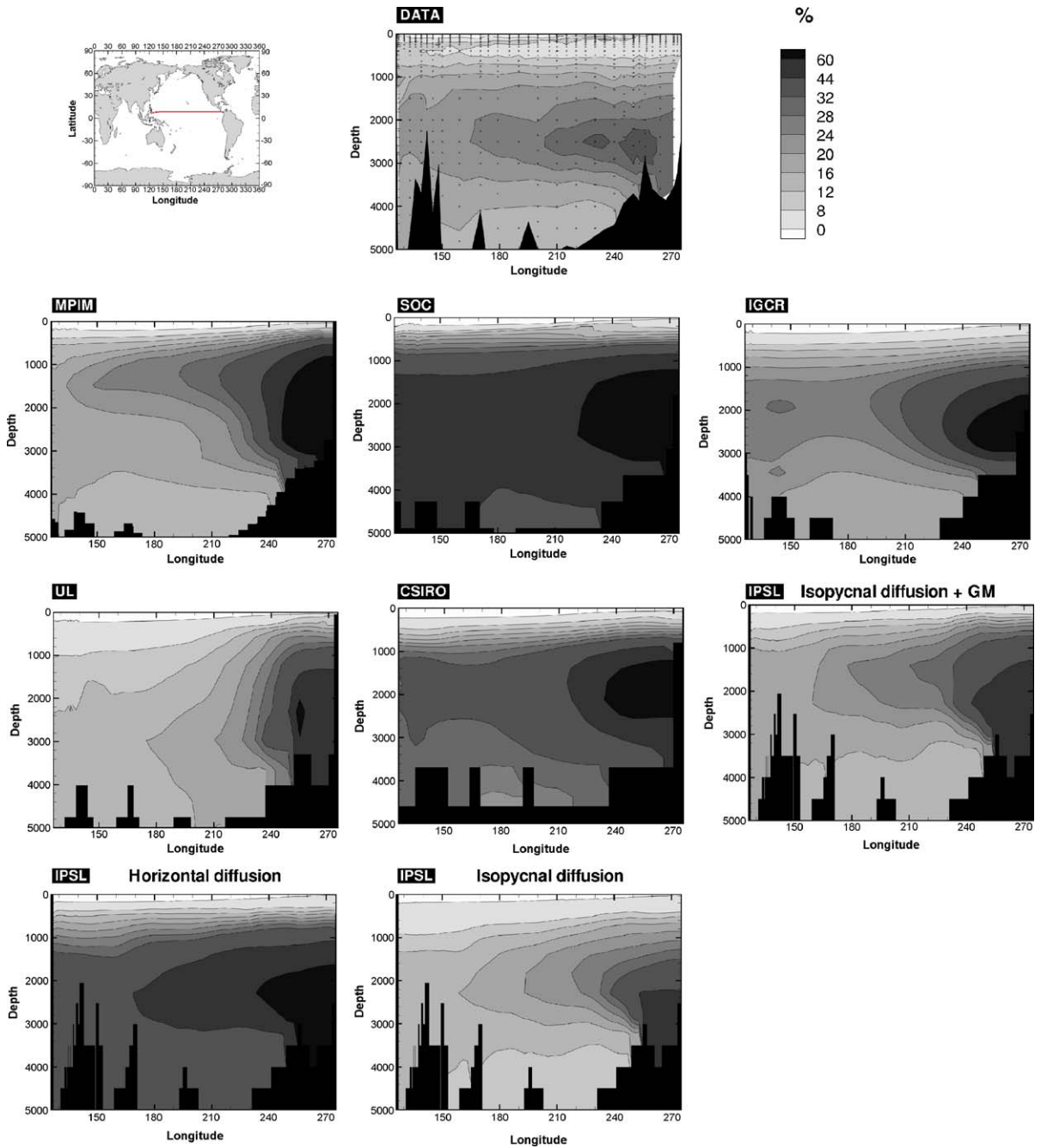


Fig. 4. Helium isotopic distribution along the WOCE P04 section (10°N), units: %.

the atmosphere. Deeper in the ocean, water masses have a large contribution of poorly ventilated Antarctic Circumpolar water, and higher $\delta^3\text{He}$, ranging between

8% and 12%. At the bottom of the ocean, lower $\delta^3\text{He}$ values are observed, with a minimum located in the western flank of the sections. This low $\delta^3\text{He}$ character-

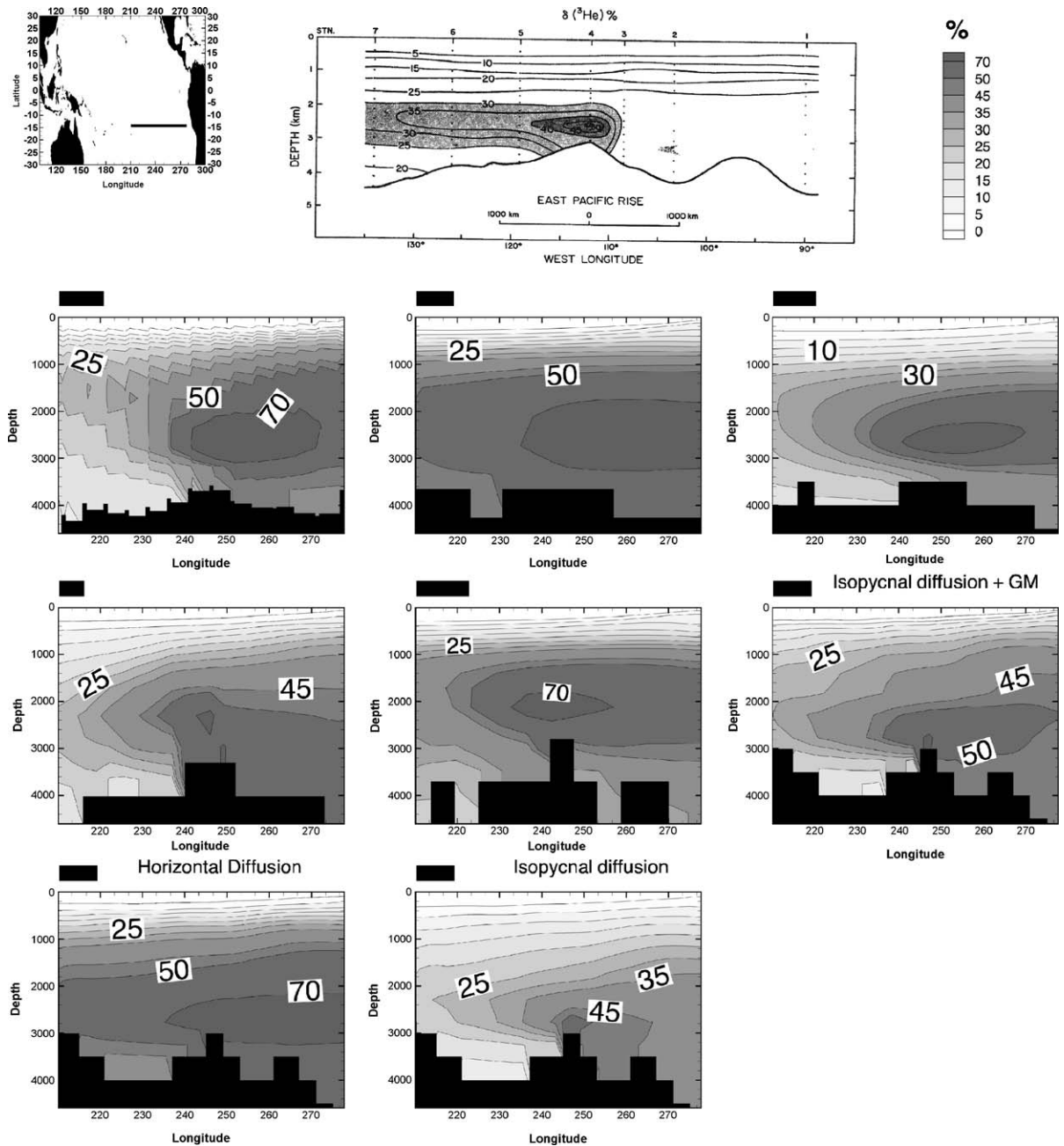


Fig. 5. Helium isotopic distribution along 15°S, units: %.

izes the presence of recently ventilated AABW that are formed in the Ross and Weddell seas, and penetrate to the bottom of the ocean by flowing along the Antarctic Coast (Wepperning et al., 1996).

There are dramatic differences in the simulation of AABW ventilation between the models. On this question, the models fall into two categories. Models that are not coupled with sea-ice models (SOC, IGCR,

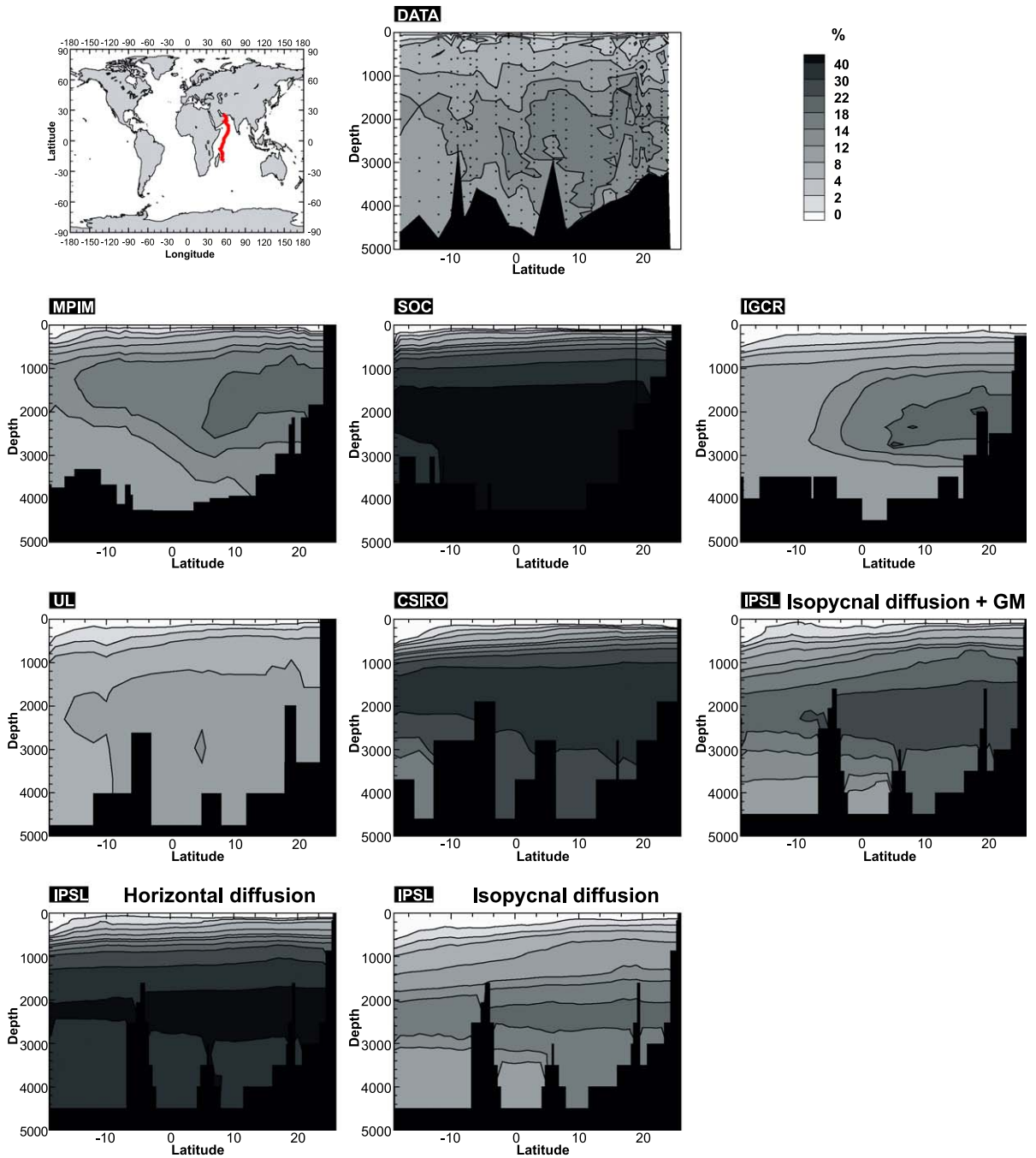


Fig. 6. Helium isotopic distribution along the WOCE I07 section, units: %.

CSIRO and IPSL) produce an AABW ventilation which is too weak, which induces bottom $\delta^3\text{He}$ values that are significantly higher than the WOCE SO4p

and SO4-3 observations. On the other hand, the two models that are coupled with sea-ice model (MPIM, UL) exhibit significantly lower $\delta^3\text{He}$ at the bottom of

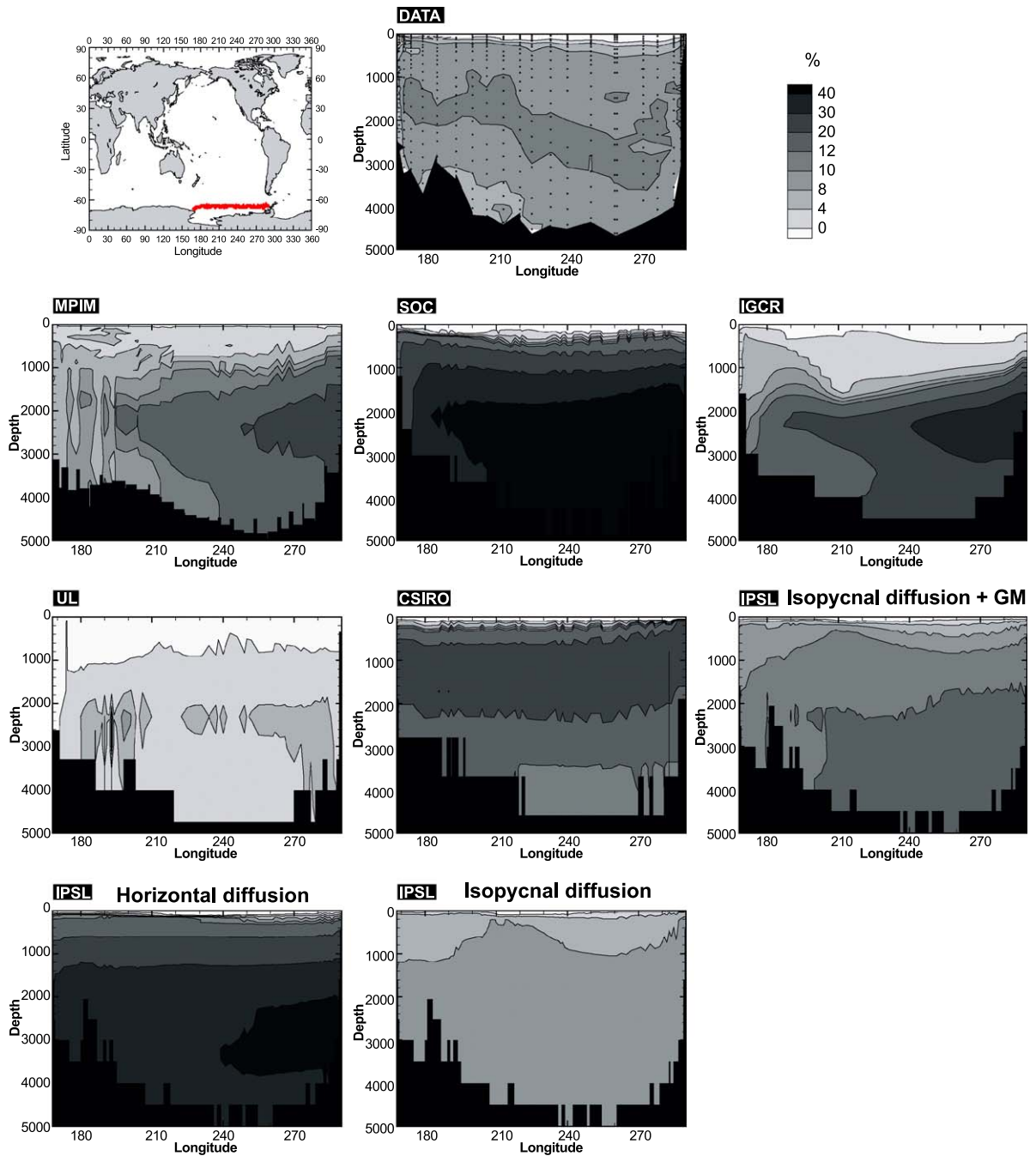


Fig. 7. Helium isotopic distribution along the WOCE SO4p section, units: %.

the ocean, which suggests substantial AABW formation along both sections. The MPIM model also produces realistic zonal gradient at the bottom of the

ocean, by producing lowest values along the western flank of the sections. However, bottom $\delta^3\text{He}$ in MPIM is slightly higher than the observations, mainly be-

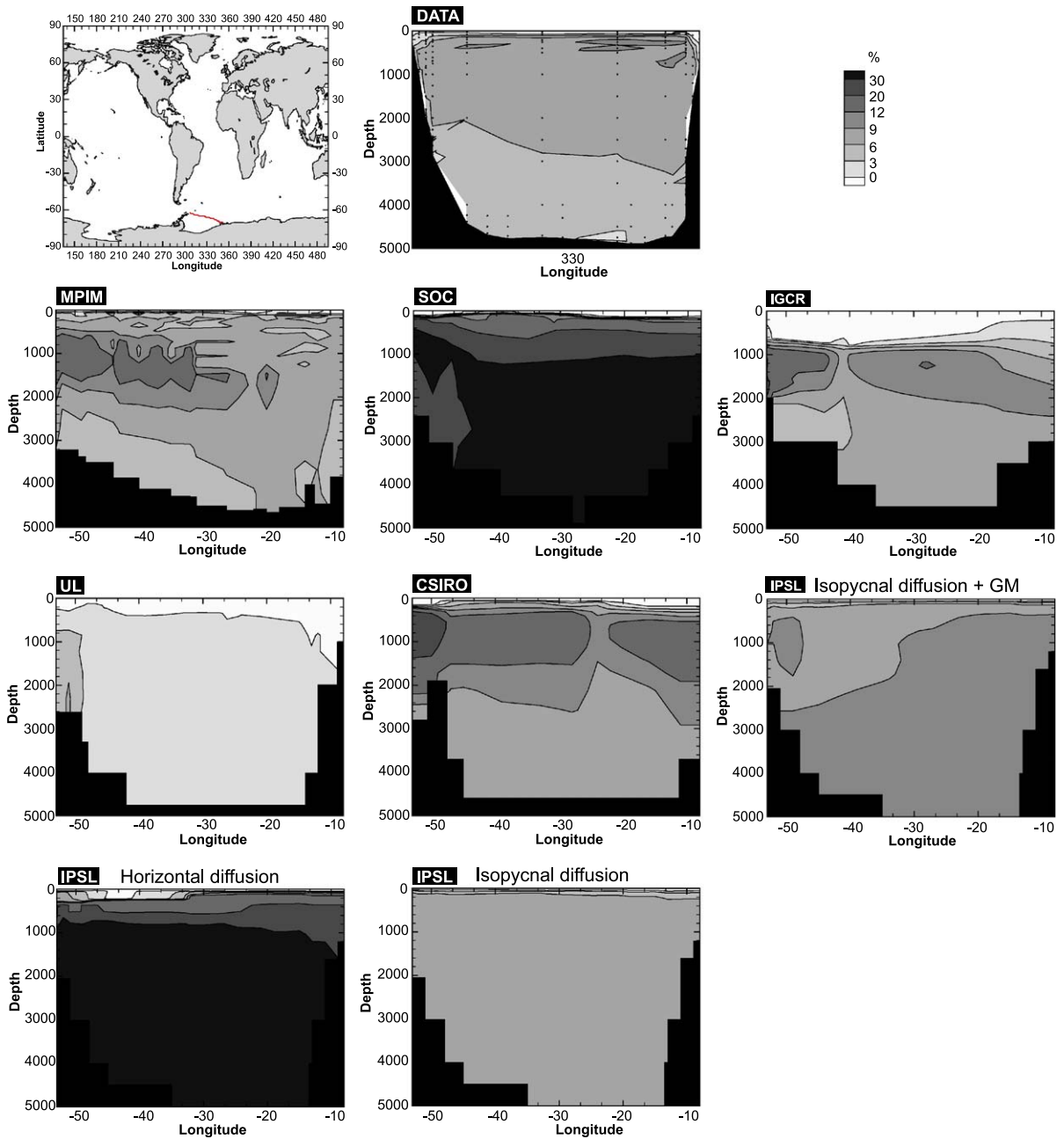


Fig. 8. Helium isotopic distribution along the WOCE SO4-3 section, units: %.

cause it overestimates $\delta^3\text{He}$ in CDW. The UL model produces a more homogeneous $\delta^3\text{He}$ distribution, but values are systematically lower than the observations. These results are consistent with those of the CFC

simulations performed during OCMIP-2 that have clearly demonstrated that the UL model largely overestimates the formation and the ventilation rate of AABW on this section.

4.5. Atlantic Ocean

The North Atlantic Ocean is a major site of deep-water formation. The $\delta^3\text{He}$ measurements in the deep waters of this basin are nowadays substantially contaminated with the bomb tritogenic ^3He component. For this reason, we choose to evaluate model results against the GEOSECS data set, which was collected in the early 1970s, at a time when the intrusion of tritogenic ^3He was much lower (Östlund and Rooth, 1990). Data measured in the Western Atlantic Ocean during the GEOSECS expedition (1972) shows low $\delta^3\text{He}$, ranging between 0% and 2%, at depth in the Atlantic Ocean. These low values are in particular contrast with the higher values observed within the CDW in the Southern Ocean (Fig. 9). The low $\delta^3\text{He}$ values observed between 1500 and 3500 m depth in the Atlantic Ocean are the signature of the southward propagation of recently ventilated NADW. On the vertical, this feature is located between the helium-rich Antarctic Bottom Water (AABW) and Antarctic Intermediate Water (AAIW) around 1000 m depth. The higher $\delta^3\text{He}$ values, ranging between 2% and 6%, outstanding in the north of the section, are attributed to the bomb tritogenic signal and must not be taken into account for our model evaluation.

Before OCMIP-2, the only existing simulation of the global oceanic natural helium-3 distribution was the study of Farley et al. (1995) with the LSG model from MPIM, although in a different configuration concerning vertical resolution and diffusion from that used in OCMIP-2. This model, in its earlier version and in its new OCMIP-2 configuration, produces $\delta^3\text{He}$ values that are too high in the Atlantic Ocean compared to the GEOSECS observations (Fig. 9). Farley et al. concluded that the hypothesis used to calculate the source function of mantle helium-3 was not appropriate for this basin. The range of models used within OCMIP-2 offers an opportunity to examine this conclusion. Fig. 9 shows that three of the OCMIP-2 models, IGCR, UL and CSIRO, succeed in producing realistic $\delta^3\text{He}$ values within their NADW outflow when using the source function proposed by Farley et al. (1995). On the other hand, two other models, SOC and IPSL_GM, overestimate $\delta^3\text{He}$ values in the Atlantic Ocean. However, we have shown previously that these models also overestimate $\delta^3\text{He}$ values in all the other basins.

Again, the results from the sensitivity test with the IPSL model help to better understand the difference amongst these models. The different versions of the IPSL model generate changes in the Atlantic similar to what we have already seen in the Pacific and Indian basins. The simulation with horizontal diffusion (IPSL_HOR) still produces the weakest deep-ocean ventilation and correspondingly $\delta^3\text{He}$ higher than observed. With mixing oriented along isopycnal surfaces, the IPSL_ISOP produces a more realistic $\delta^3\text{He}$ distribution, similar to IGCR, UL and CSIRO models and comparable to the GEOSECS measurements. When the GM parameterization is added, the IPSL model generates higher $\delta^3\text{He}$, above the values measured during GEOSECS. The GM parameterization is known to decrease ventilation rates (England and Rahmstorf, 1999), but also more specifically to reduce the transport in the DWBC, which is already too weak in coarse resolution ocean general circulation models (England and Holloway, 1998).

4.6. Natural ^{14}C vs. natural ^3He

During OCMIP-2, the modeled circulation in the deep ocean has been evaluated with two different tracers: natural $\Delta^{14}\text{C}$ and mantle ^3He . In this section, we combine the information of these two tracers. The objective is to provide a more severe constraint on the deep circulation by using two different tracers and, second, to verify, with the information gained from natural ^{14}C simulation, the potential of the ^3He simulation, to evaluate modeled deep-ocean circulation.

The constraints from these two tracers are complementary and independent because of their different modes of injection in the ocean: natural C-14 is injected at the air sea interface, while ^3He is injected at mid-depth within the ocean. The source functions of these two tracers are not known perfectly, but the parameterization for the injection of natural C-14 in the ocean is known with greater certainty than that for ^3He (England and Maier-Reimer, 2001).

The inter-basin distribution of observed $\Delta^{14}\text{C}$ and $\delta^3\text{He}$ at 2000 m during the GEOSECS expedition is shown in Fig. 10. High $\Delta^{14}\text{C}$ values indicate recent ventilation of the water mass, while lower $\Delta^{14}\text{C}$ values represent older water mass isolated from the atmosphere for a longer time. The input function of these two tracers to the ocean

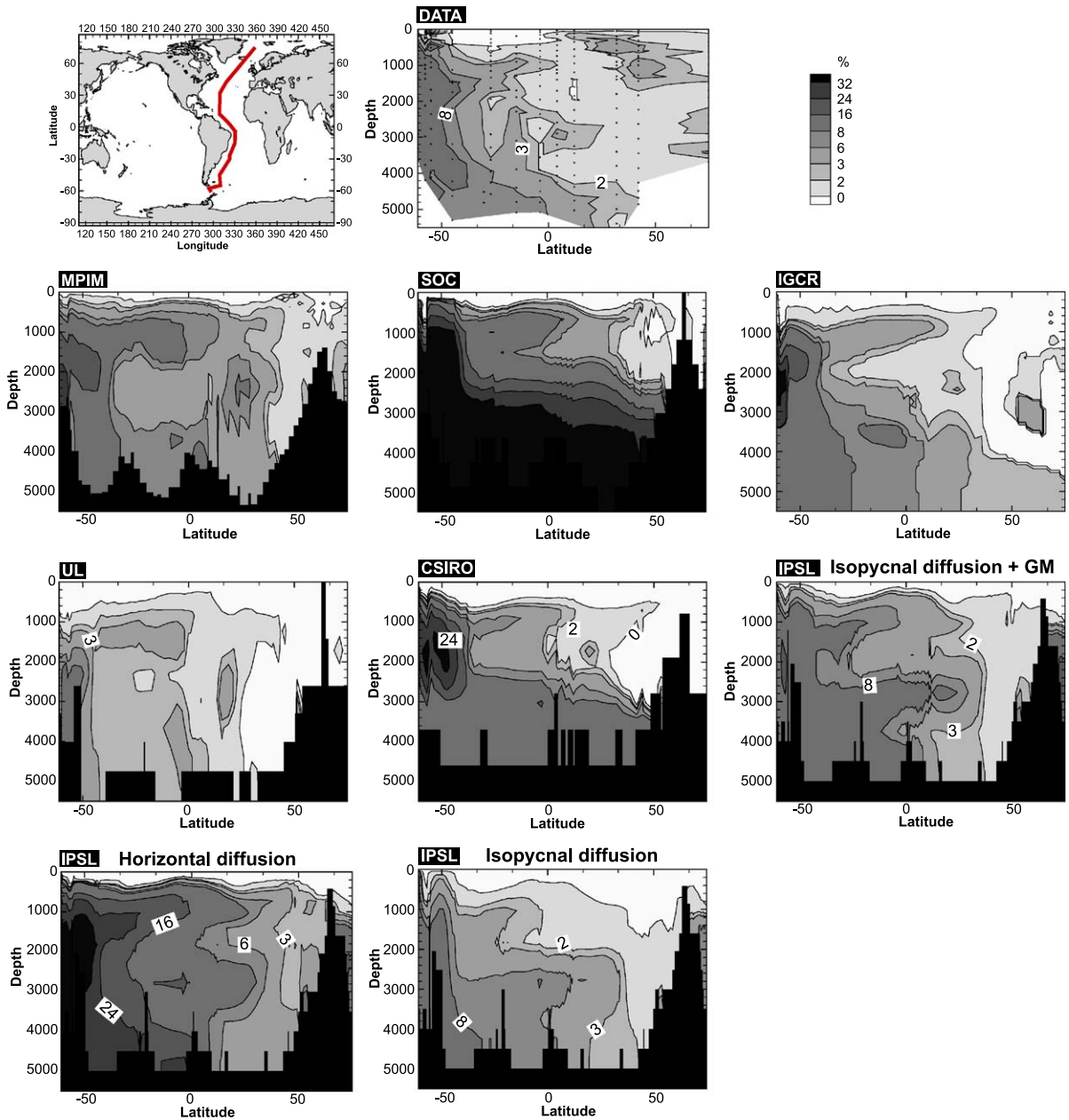


Fig. 9. helium isotopic distribution along the Atlantic GEOSECS section, units: %.

associated with the ocean circulation generate a quasi-symmetrical inter basin configuration for the GEOSECS measurements. The main characteristics of the ocean thermohaline circulation as presented by the concept of the “conveyor belt” (Broecker, 1991) are clearly recognizable on this figure. The

Atlantic Ocean with a rapid ventilation rate and weak source of helium-3 has high $\Delta^{14}\text{C}$ and low $\delta^3\text{He}$. The Antarctic Ocean, where the connection between the different oceans is achieved, has intermediate values of C-14 and He-3. Finally, the Indian and Pacific Oceans, where the oldest water

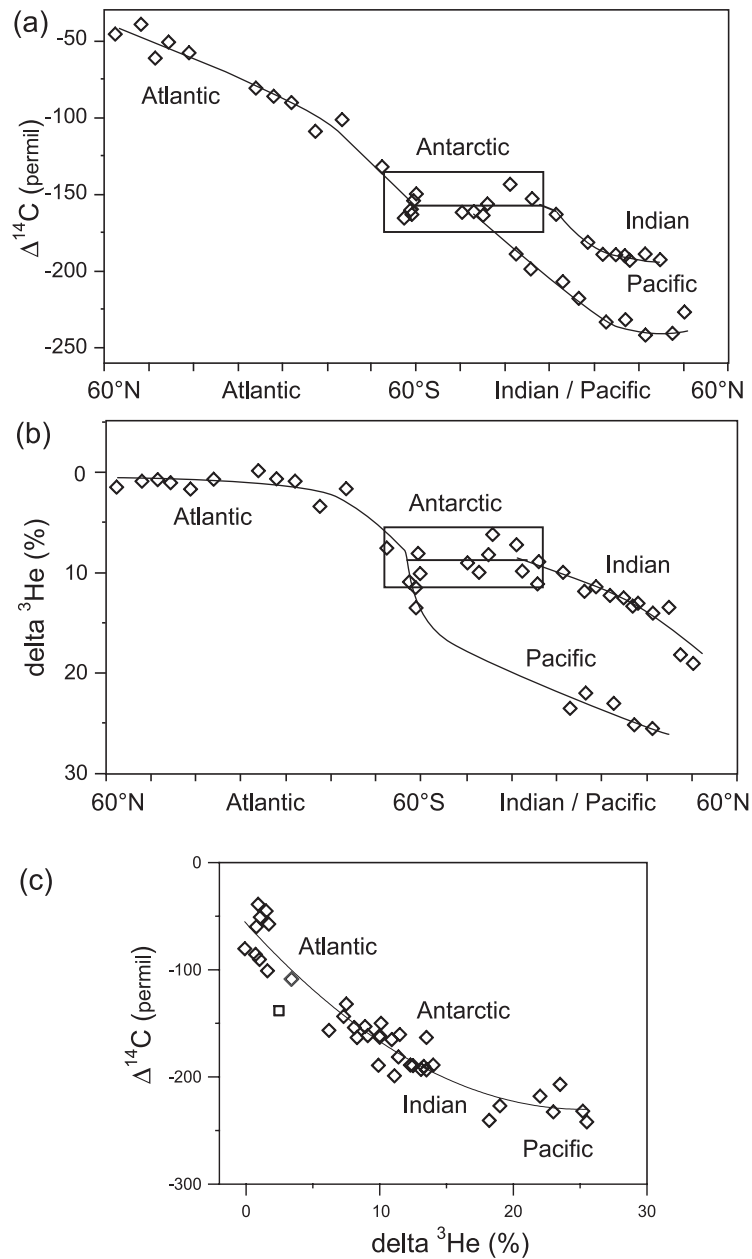


Fig. 10. (a) Inter-basin GEOSECS ^{14}C distribution at 2000 m depth (from Östlund et al. (1987)). (b) Inter-basin GEOSECS helium-3 distribution at 2000 m depth. (c) ^{14}C vs. ^3He GEOSECS observations at 2000 m depth.

masses of the ocean lies, have low $\Delta^{14}\text{C}$ and high He-3 values. A scatter plot of $\Delta^{14}\text{C}$ vs. ^3He reveals a convex structure (Fig. 10c) that provides a synthetic representation of global ocean ventilation. The basins with rapid ventilation rates are found in

the top left part of the graphic, and basins with low ventilation rates are found at the bottom-right.

Fig. 11 shows the comparable distribution for the models that performed both ^{14}C and ^3He simulations (MPIM, CSIRO, IGCR, UL, IPSL and IPSL_HOR).

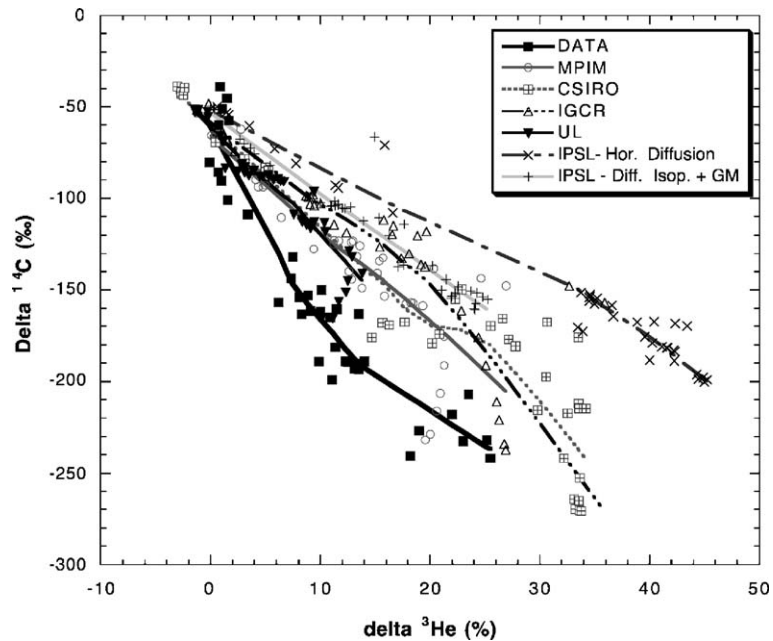


Fig. 11. Modeled and observed ^{14}C vs. ^3He at 2000 m depth at the location of the GEOSECS stations.

For most models, the two tracers deliver a similar verdict. For instance, both distributions from the CSIRO model indicate that the ventilation rate is globally too weak in these models: simulated $\Delta^{14}\text{C}$ and $\delta^3\text{He}$ values are both higher than the observations. MPIM shows results that are globally in a realistic range compared to the observations, excepted for the domain of $\delta^3\text{He}$ values ranking between 10% and 17% (corresponding to the Southern Ocean) where $\Delta^{14}\text{C}$ values are too low. The situation is more complex for simulations with the IPSL model. IPSL_GM produces realistic $\delta^3\text{He}$, but $\Delta^{14}\text{C}$ is globally too young. On the other hand, IPSL_HOR produces more realistic $\Delta^{14}\text{C}$ values, but $\delta^3\text{He}$ values are far too high, when compared to the observations and the other OCMIP models.

5. Discussion

The simulation of mantle ^3He distribution provides an independent constraint for modeled deep ocean-ocean circulation. The better global coverage of available $\delta^3\text{He}$ observations, especially since the WOCE program allows for a more careful evaluation of

model performance on both basin and regional scales. One can evaluate basin-scale ventilation rates, and diagnose detailed structure of the deep circulation (e.g., the propagation of enriched helium-3 plume jets in the deep equatorial Pacific Ocean, or recent formation of AABW water along the Antarctic coast).

Global $\delta^3\text{He}$ averages predicted by the OCMIP-2 models vary by $\pm 65\%$ around the mean. It indicates how extremely sensitive the natural helium-3 distribution is to model circulation. Thus, if one could establish global and basin observed $\delta^3\text{He}$ inventories with reasonable accuracy that would provide an important constraint for both model circulation and the rate of injection of mantle helium-3 in the ocean.

The sensitivity tests involving the parameterization of subgrid-scale mixing in the IPSL model provide information of interest for the interpretation of the results of the other OCMIP-2 models. The range in the helium-3 distribution among the three versions of the IPSL model used in this study is also very large. It clearly illustrates the large influence of the subgrid-scale mixing parameterization on models' deep-ocean. The IPSL simulation with horizontal mixing and the OCMIP-2 boundary conditions produces $\delta^3\text{He}$, which are much higher than observations as well as other

models. The differences between this version of the IPSL model and the observations are higher than the estimation of the $\pm 25\%$ uncertainties for the parameterization of mantle injection in the ocean proposed by Clarke et al. (1969). Taken alone, this suggests that the deep-ocean ventilation in IPSL_HOR is too sluggish. This tendency is also suggested by the CFC simulations (not shown). When lateral mixing is oriented along isopycnal surfaces, the connection between the surface and the deep-ocean is improved. The deep-ocean ventilation rate increases and it globally produces more realistic helium-3 values. Finally, when the effects of eddy activity are simulated by the GM parameterization, the deep-ocean ventilation rate is reduced and $\delta^3\text{He}$ increases. The comparison with the data suggests that the GM parameterization, as used in our simulation, does not improve globally the helium-3 distribution. This eddy parameterization tends to reproduce better the effects of Sub-Antarctic Mode Water (SAMW) ventilation on the renewal of the helium-3 distribution in the Southern Ocean, where inclination of the isopycnal surfaces is steep. Conversely, GM tends to degrade the model's performance in the low latitudes and the North Atlantic Ocean. The GM parameterization in the IPSL model uses a constant thickness diffusivity coefficient of $1000 \text{ m}^2/\text{s}$. These results on the natural helium-3 simulations with the IPSL model, together with its performance on the ^{14}C vs. ^3He evaluation, indicate that the concept of including thickness diffusivity coefficient that varies in both space and time might be an appropriate solution. The constant value used in the IPSL model is acceptable for regions like the Southern Ocean, where the steep incline of isopycnal surfaces generates mixing by baroclinic instabilities, but it is known to be too large for mid-latitudes where baroclinic instabilities are weak (Visbeck et al., 1997).

Our sensitivity tests suggest that much of the difference between the $\delta^3\text{He}$ in the OCMIP-2 models may be due to subgrid-scale mixing. The SOC and CSIRO models have the highest $\delta^3\text{He}$, also use the GM parameterization. The effect of the GM parameterization is even more pronounced in these models. That is the effect in IPSL_GM is damped because it uses a robust-diagnostic method which acts to moderate the restratification effect due to the GM parameterization.

In addition to providing some interesting results on the influence of the subgrid-scale mixing parameter-

ization on ocean model circulation, this $\delta^3\text{He}$ analysis has allowed us to evaluate model performance with regards to water mass formation and propagation in the ocean.

The mantle ^3He simulations provide an opportunity to evaluate model formation and ventilation of AABW. Shelf-edge processes are known to play a crucial role in the formation of deep and bottom in the Southern Ocean (Foster and Carmack, 1976). Since models lack the spatial resolution to resolve shelf-edge processes, they tend to resort to unrealistic convective processes to simulate deep and bottom ocean ventilation. These processes have already been investigated during OCMIP-2 with the analysis of the "top down" penetration of CFC-11 in the ocean (Dutay et al., 2002). The mantle helium-3 simulations, with a release of the tracer to the atmosphere from the interior of the ocean, offer a complementary "bottom-up" constraint to the surface-interior connection in the models. This approach confirms the expertise acquired from the CFC-11 evaluation. The inclusion of a sea-ice model leads to substantial AABW formation. The OCMIP-2 models, which are not coupled to a sea-ice model, have rates of AABW formation that are too low. Yet when coupled to a sea-ice model, ocean models tend to overestimate AABW production. Evaluation with CFC-11 during OCMIP-2, with a greater number of models, shows that adding a specific parameterization for brine rejection during sea-ice formation leads to more realistic AABW production. In the future, it would be of interest to use $\delta^3\text{He}$ to explore the effect of this parameterization as well as others that may contribute to improve AABW formation processes when an ocean model is associated with a sea-ice model (e.g., the GM parameterization, bottom boundary layer parameterization (Beckmann and Döscher, 1997) or parameterization of the effect of ice shelf melting around Antarctica (Beckmann and Goosse, 2003)).

The mantle helium-3 signal, with its high isotopic ratio, is a tracer that enables one to evaluate specific features of the deep circulation that are not or cannot be easily found in any other property measured during oceanic expeditions (Lupton and Craig, 1981). For instance, the mantle helium-3 distribution explicitly tags and integrates the signal of the deep jets located in the tropical Pacific Ocean. The evaluation of OCMIP models indicates that this class of models

failed in reproducing the detailed latitudinal structure of this signal and underestimates its westward propagation. A prevalent cause for these results is the coarse spatial resolution of these models, which limits their capacity to produce strong and narrow currents in the deep ocean. Our results also suggest that another factor may have a large contribution too. This model-data intercomparison reveals large discrepancies between the observations and the models, an example being when model plumes along a particular section propagate in a sense opposite to that seen in the data, which need to be explained by factors other than only model resolution. Geothermal heating, and especially the contribution from hydrothermal vents, is suspected to have a large influence on the propagation of helium-3 plumes in the deep ocean (Stommel, 1982). Adcroft et al. (2001) have shown that the geothermal heating induces substantial changes in the deep circulation of ocean numerical models. In their experiment, the geothermal heating through the sea floor is uniform, but the impact is more pronounced in the Indian and Pacific Ocean where the meridional overturning is enhanced by approximately 25%. Geothermal heating is not included in the forcing of the OCMIP-2 models, and thus may help to explain some of the discrepancies we have found with simulations of δHe . In the future, it will be of interest to continue to explore the impact of geothermal heating on the modeled deep ocean circulation, and to associate that with evaluations with mantle ^3He . This ^3He tracer source function is associated with hydrothermal activity, and thus provides an excellent test to evaluate the effects of specifying a non-uniform geothermal flux in the ocean, and to investigate the changes that such process brings about in regard to the horizontal circulation of numerical models.

A second objective of this paper is to use the context of OCMIP-2, where natural helium-3 simulations have been completed with different models, for testing the validity of the proposed parameterization of the injection of mantle helium-3 into the ocean. The assumptions proposed by Farley et al. (1995) to estimate the flux of mantle helium-3 into the ocean are a global rate of injection of $1000 \text{ mol helium-3 year}^{-1}$, with an isotopic ratio of $R = 8 \times R_{\text{atmosphere}}$, and a rate of injection proportional to ridge spreading rate. First, all the models support the inter-basin contrast of the distribution of the source

of natural helium-3 in the oceans. Using this parameterization, they all succeed to produce a qualitatively realistic inter-basin distribution of the tracer. The modeled $\delta^3\text{He}$ is highest in the Pacific and Indian Oceans, it is lowest in the Atlantic Ocean and has intermediate value in the Southern Ocean. However, quantitative considerable differences emanate from the models.

The pioneering simulation of natural helium-3 in an global ocean model performed by Farley et al. (1995) has displayed that this whole set of hypotheses leads to realistic results in the Indian and Pacific Oceans. The synthesis from all OCMIP-2 natural helium-3 simulations confirms this conclusion. Large differences are of course observed among the results of the OCMIP-2 models and, more specifically, many of these models overestimate the $\delta^3\text{He}$ in these oceans. However, some arguments tend to make a convincing case for the potential utility of the mantle helium-3 parameterization of Farley et al. (1995). First, three models succeed to produce realistic helium isotopic distributions in the Pacific and Indian Oceans. Then, for the three models that failed, a convincing argument is found to explain the unfavorable results. IGCRC has no seasonal forcing, and a previous CFC evaluation has clearly pointed out that this model underestimates deep and intermediate water formation rates in these basins (Dutay et al., 2002). For the two other models (SOC and CSIRO), the situation was cleared from the results of the sensitivity test with the IPSL model that has explained before, have depicted the negative influence of the GM parameterization on the modeled ocean ventilation. Finally, the conclusion is confirmed by the multi-tracer analysis where results from both natural $\Delta^{14}\text{C}$ and $\delta^3\text{He}$ simulations indicate that these models have a ventilation rate that is too weak.

Farley et al. (1995) in their discussion of their mantle helium-3 simulation, also expressed some doubts concerning the relevance of such parameterizations for the injection of mantle helium-3 in the Atlantic Ocean. The Large-scale Geostrophic Model from MPIM produces $\delta^3\text{He}$ that is too high in this ocean. This is also the case for two other models participating in OCMIP-2 (SOC, and the IPSL version with both isopycnal mixing and GM, IPSL-GM). However, the three other OCMIP-2 models and the IPSL model configuration with isopycnal mixing

produce acceptable results when compared with the observations. These results appear particularly remarkable because these coarse resolution models have difficulties in reproducing the detailed structure of NADW outflow (Dutay et al., 2002). They have the tendency to produce a transport in the DWBC, which is too sluggish, and this explains the tendency to simulate a $\delta^3\text{He}$ that is too high within the NADW outflow especially, in the Southern Hemisphere. Furthermore, the vertical structure of the NADW outflow is not accurate in these models. Instead of producing the two observed ventilated components of the DWBC, they simulate a single branch and particularly failed in producing realistic dense water overflow of DSOW and ISOW (Dutay et al., 2002). This generates a $\delta^3\text{He}$ that is too high below 3000 m depth in the North Atlantic Ocean. The sensitivity test with the IPSL model provides also interesting information regarding the potential of the parameterization of the rate of injection of mantle helium-3. Two version of the model produce $\delta^3\text{He}$ that are too high in NADW outflow for known reasons. The version with horizontal mixing has an inadequate representation of processes connecting the surface and interior ocean in the region of formation of NADW. The GM parameterization is known for unrealistically reducing the NADW outflow in the models (England and Holloway, 1998). On the contrary, the simulation with isopycnal mixing, which is recognized to be the most appropriate configuration for modeling the NADW outflow (England and Holloway, 1998), produces realistic $\delta^3\text{He}$ in the ventilated part of its NADW outflow. We have shown that it is possible to simulate a reasonable natural helium-3 distribution in the Atlantic Ocean with the proposed parameterization of the flux in some models participating to OCMIP-2; the results of this study disagree with the conclusion suggested by Farley et al. (1995) made with one model.

6. Conclusions

Standard mantle helium-3 simulations were made with six global coarse resolution models to evaluate deep ocean circulation. Sensitivity tests to the parameterization of subgrid-scale mixing performed with the IPSL model provide useful information for better

interpreting the differences among the models. It has been pointed out that the OCMIP models, which use the eddy-induced velocity parameterization of Gent and Mc Williams, tend to underestimate the ventilation of the deep ocean. In these models, the parameterization is implemented with a constant thickness diffusivity coefficient, and we recommend the use of such a parameterization with spatially and temporally varying coefficients in order to moderate its effect on stratification.

Regarding AABW formation, the model evaluation with helium-3 reveals model circulation patterns that are in agreement with those found with CFC-11 (Dutay et al., 2002). Models coupled with a sea-ice model induce a substantial bottom water formation in the Southern Ocean that tend to overestimate AABW ventilation, while ocean models that are not coupled with a sea-ice model systematically underestimate the formation of AABW.

The mantle helium-3 signal, with its high isotopic ratio injected in the ocean, also enables us to evaluate specific features of the deep circulation that are not easily depicted by any other tracer. We show that all the models failed to reproduce a correct propagation of plumes of enriched mantle helium-3 in the deep ocean. Models tend to produce a tracer transport, which is too sluggish in the deep ocean, and the propagation happens to be in the opposite direction than observed. The coarse resolution of these models is responsible for the inability to produce strong and narrow currents in the deep ocean, but the absence of geothermal forcing in these models also contribute to neutralize the generation of these currents in the deep ocean.

The context of OCMIP-2 with mantle helium-3 simulation from several ocean general circulation models has been used to explore the potential of natural helium-3 to help compare and evaluate modeled deep-ocean circulation. The source function of mantle helium is known with a substantial uncertainty but the synthesis of models results shows that, with the parameterization used for the injection of mantle helium-3, it is possible to generate realistic results. These results are supported by the multi-tracer evaluation performed by using natural ^{14}C alongside helium-3 for the same model runs, and comparing the results with the GEOSECS. This multi-tracer analysis shows that both tracers lead

globally to the same conclusion regarding models' ventilation performance.

Acknowledgements

We are grateful to Patrick Brockmann for the development and the maintenance of Global Analysis Package (GAP) used for the analysis performed in this paper. This work was supported by EC Environment and Climate Program's GOSAC (Contract No. ENV4-CT97-0495). We thank CEA-Grenoble for computing support.

References

- Adcroft, A., Scott, J., Marotzke, J., 2001. Impact of geothermal heating on the global ocean circulation. *Geophys. Res. Lett.* 28, 1735–1738.
- Beckmann, A., Döscher, R., 1997. A method for improved representation of dense water spreading over topography in geopotential-coordinate models. *J. Phys. Oceanogr.* 27, 581–591.
- Beckmann, A., Goosse, H., 2003. A parameterization of ice shelf-ocean interaction for climate models. *Ocean Model.* 5, 157–170.
- Broecker, W.S., 1991. The great ocean conveyor. *Oceanography* 4, 79–89.
- Clarke, W.B., Beg, M.A., Craig, H., 1969. Excess ^3He in the sea: evidence for terrestrial primordial helium. *Earth Planet. Sci. Lett.* 6, 213–220.
- Craig, H., Clarke, W.B., Beg, M.A., 1975. Excess ^3He in deep water on the east pacific rise. *Earth Planet. Sci. Lett.* 26, 125–132.
- DeMets, C., Gordon, R.G., Argus, D.F., Stein, S., 1990. Current plate motions. *Geophys. J. Int.* 101, 425–478.
- Dutay, J.-C., Bullister, J.L., Doney, S.C., Orr, J.C., Najjar, R., Caldeira, K., Campin, J.-M., Drange, H., Follows, M., Gao, Y., Gruber, N., Hecht, M.W., Ishida, A., Joos, F., Lindsay, K., Madec, G., Maier-Reimer, E., Marshall, J.C., Matear, R.J., Monfray, P., Mouchet, A., Plattner, G.-K., Sarmiento, J., Schlitzer, R., Slater, R., Totterdell, I.J., Weirig, M.-F., Yamanaka, Y., Yool, A., 2002. Evaluation of ocean model ventilation with CFC-11: comparison of 13 global ocean models. *Ocean Model.* 4, 89–120.
- England, M.H., Hirst, A.C., 1997. Chlorofluorocarbon uptake in a world ocean model: 2. Sensitivity to surface thermohaline forcing and subsurface mixing parameterizations. *J. Geophys. Res.* 102, 15,709–15,731.
- England, M., Holloway, G., 1998. Simulations of CFC content and water mass age in the deep North Atlantic. *J. Geophys. Res.* 103, 15,885–15,901.
- England, M.H., Rahmstorf, S., 1999. Sensitivity of ventilation rates and radiocarbon uptake to subgrid-scale mixing in ocean models. *J. Phys. Oceanogr.* 29, 2802–2827.
- England, M., Maier-Reimer, E., 2001. Using chemical tracers to assess ocean models. *Rev. Geophys.* 39, 29–70.
- Farley, K.A., Maier-Reimer, E., Schlosser, P., Broecker, W.S., 1995. Constraints on mantle ^3He fluxes and deep-sea circulation from an oceanic general circulation model. *J. Geophys. Res.* 100, 3829–3839.
- Foster, T.D., Carmack, E.C., 1976. Frontal zone mixing and Antarctic bottom water formation in the Southern Weddell Sea. *Deep-Sea Res.* 23, 301–317.
- Goosse, H., Fichefet, T., 1999. Importance of ice-ocean interactions for the global ocean circulation: a model study. *J. Geophys. Res.* 104, 23,337–23,355.
- Gordon, C., Cooper, C., Senior, C.A., Banks, H., Gregory, J.M., Johns, T.C., Mitchell, J.F.B., Wood, R.A., 2000. The simulation of SST, sea ice extents and ocean heat transport in a version of the Hadley Centre coupled model without flux adjustments. *Clim. Dyn.* 16, 147–168.
- Guilyardi, E., Madec, G., Terray, L., 2001. The role of lateral ocean physics in the upper ocean thermal balance of a coupled ocean-atmosphere GCM. *Clim. Dyn.* 17, 589–599.
- Gent, P.R., Willebrand, J., McDougall, T.J., McWilliams, J.C., 1995. Parameterizing eddy-induced tracer transports in ocean circulation models. *J. Phys. Oceanogr.* 25, 463–474.
- Jean-Baptiste, P., Charlou, J.L., Stievenard, M., Donval, J.P., Bougault, H., Mevel, C., 1991. Helium and methane measurements in hydrothermal fluids from the Mid Atlantic Ridge: the Snake Pit site at 23°N. *Earth Planet. Sci. Lett.* 106, 17–28.
- Jean-Baptiste, P., 1992. ^3He distribution in the deep world ocean: its relation to hydrothermal ^3He fluxes and to the terrestrial heat budget. in "isotopes of noble gases as tracers in environmental studies". Panel Proc. Ser. - Int. At. Energy Agency, 219–240 (Vienna STI/PB/859).
- Jean-Baptiste, P., Mantsi, F., Pauwels, H., Grimaud, D., Patriat, P., 1992. Hydrothermal helium-3 and manganese plumes at 19°29' South on the Central Indian Ridge. *Geophys. Res. Lett.* 19, 1787–1790.
- Jean-Baptiste, P., Bougault, H., Vangriesheim, A., Charlou, J.L., Radford-Knoery, J., Fouquet, Y., Needham, D., German, C., 1998. Mantle ^3He in hydrothermal vents and plume of the Lucky Strike site (MAR 37°17'N) and associated geothermal heat flux. *Earth Planet. Sci. Lett.* 157, 69–77.
- Lee, M.M., Marshall, D.P., Williams, R.G., 1997. On the eddy transfer of tracers: advective or diffusive? *J. Mar. Res.* 55, 483–505.
- Lupton, J.E., Craig, H., 1975. Excess He-3 in oceanic basalts: evidence for terrestrial primordial helium. *Earth Planet. Sci. Lett.* 26, 133–139.
- Lupton, J.E., Craig, H., 1981. A major helium-3 source at 15°S on the East Pacific Rise. *Science* 214, 13–18.
- Lupton, J.E., Delaney, J.R., Johnson, H.P., Tivey, M.K., 1985. Entrainment and vertical transport of deep-ocean water by buoyant hydrothermal plumes. *Nature* 316, 621–623.
- Madec, G., Delecluse, P., Imbard, M., Lévy, C., 1998. OPA8.1 ocean general circulation model reference manual. Notes Pôle Model. de l'IPSL, 11.
- Maier-Reimer, E., Mikolajewicz, U., Hasselmann, K., 1993. Mean circulation of the Hamburg LSG OGCM and its sensitivity on the thermohaline forcing. *J. Phys. Oceanogr.* 23, 731–757.

- Marshall, D., 1997. Subduction of water masses in an eddying ocean. *J. Mar. Res.* 55, 201–222.
- Matear, R.J., Hirst, A.C., 1999. Climate change feedback on the future oceanic CO₂ uptake. *Tellus* 51B, 722–733.
- Östlund, H.G., Rooth, C.G.H., 1990. The North Atlantic Tritium and Radiocarbon Transients 1972–1983. *J. Geophys. Res.* 95, 20,147–20,165.
- Östlund, H.G., Craig, H., Broecker, W.B., Spencer, D., 1987. GEOSECS Atlantic, Pacific and Indian Ocean expeditions. Shore-Based Data and Graphics, vol. 7. National Science Foundation, Washington, DC.
- Stommel, H., 1982. Is the South Pacific helium-3 plume dynamically active? *Earth Planet. Sci. Lett.* 61, 63–67.
- Stommel, H., Arons, A.B., 1960. On the abyssal circulation of the world ocean-2, an idealized model of the circulation pattern and amplitude in oceanic basins. *Deep-Sea Res.* 6, 217–233.
- Visbeck, M., Marshall, J., Haine, T., Spall, M., 1997. Specification of eddy transfer coefficients in coarse-resolution ocean circulation models. *J. Phys. Oceanogr.* 27, 381–402.
- Wanninkhof, R., 1992. Relationship between wind speed and gas exchange over the ocean. *J. Geophys. Res.* 97, 7373–7382.
- Warren, B.A., 1983. Why is no deep water formed in the North Pacific. *J. Mar. Res.* 41, 327–347.
- Weiss, R.F., 1971. Helium isotope effect in solution in water and seawater. *Science* 168, 247–248.
- Wepperning, R., Schlosser, P., Khatiwala, S., Fairbanks, R.G., 1996. Isotope data from ice station Weddell: implications for deep water formation in the Weddell Sea. *J. Geophys. Res.* 101, 25,723–25,739.
- WHPO, R.G., 2002. WOCE Global Data Version 3.0 DVD, USCD/SIO, La Jolla, CA (August).
- Wijffels, S.E., Toole, J.M., Bryden, H.L., Fine, R.A., Jenkins, W.J., Bullister, J.L., 1996. The water masses and circulation at 10N in the Pacific. *Deep-Sea Res.* 43, 501–544.
- Yamanaka, Y., Tajika, E., 1996. The role of the vertical fluxes of particulate organic matter and calcite in the oceanic carbon cycle: studies using an ocean biogeochemical model. *Glob. Biogeochem. Cycles* 10, 361–382.



ELSEVIER

Available online at www.sciencedirect.com

SCIENCE @ DIRECT®

Journal of Marine Systems 48 (2004) 37–50

JOURNAL OF
MARINE
SYSTEMS

www.elsevier.com/locate/jmarsys

Red Sea deep water circulation and ventilation rate deduced from the ^3He and ^{14}C tracer fields

P. Jean-Baptiste^{a,*}, E. Fourré^a, N. Metz^b, J.F. Ternon^c, A. Poisson^b

^aLaboratoire des Sciences du Climat et de l'Environnement, CEA-CNRS, Centre d'études de Saclay, 91191 Gif/Yvette cedex, France

^bLaboratoire de Biogéochimie et Chimie Marine, LBCM/IPSL, CNRS-UPMC, 4 place Jussieu, boîte 134, 75252 Paris Cedex 05, France

^cInstitut de Recherches pour le Développement, Cayenne, Guyane Française, France

Received 24 September 2002; received in revised form 7 April 2003; accepted 31 July 2003

Available online 27 February 2004

Abstract

^3He is injected in the deep ocean at plate boundaries in relation with hydrothermal activity. Its oceanic distribution, which is at a steady-state, shows appreciable vertical and horizontal gradients. Hence, ^3He conservation equations may be inverted to determine the flow field and mixing coefficients within the ocean.

Here, we use this technique to investigate the deep circulation of the Red Sea, whose deep thermohaline circulation is comparable to that of a miniature world ocean. ^3He data, which are a combination of the Geosecs, Meseda and Merou cruises, are inverted using a linear inverse box model.

The present study allows us to draw the details of the internal circulation. The latter is characterized by (i) a descending branch in the northernmost part of the basin, which corresponds to the sinking and subsequent north–south movement of dense surface waters and of additional water entrained by the sinking plume, (ii) by an internal counterclockwise recirculating loop with a northward return flow at intermediate depth.

In the literature, the rate and modes of renewal of the Red Sea deep waters are poorly constrained, with bulk residence time estimates ranging from a few decades to a few centuries. In our model, the deep water renewal rate is directly dependent on the magnitude of the ^3He sources. The global ^3He flux is estimated using two independent approaches. The first method is based on the calculation of the mean ^3He transfer flux at the air–sea interface. The second approach relies on recent estimates of the global terrestrial ^3He flux. Both methods agree within their respective uncertainties. The circulation scheme defined by the inversion is further constrained by simulating the bomb ^{14}C distribution. Both isotopes, one steady-state tracer (^3He) and one transient tracer (^{14}C), lead to reasonable agreement. The renewal time corresponding to the sinking of newly formed deep water in the northern part of the basin is 60 years. However, the global ventilation rate, deduced from the simulation of the decay rate of a numerical tracer, is much faster (26 years). This result shows, as already pointed out by others, that deep water formation is not the only process by which the deep Red Sea is ventilated. Although this mechanism is important in our model, the basin wide deep circulation coupled with efficient vertical exchange between the deep basin and the upper layers appear to be an even more powerful mode of ventilation.

© 2004 Elsevier B.V. All rights reserved.

Keywords: Red Sea deep water circulation; Ventilation rate; ^3He and ^{14}C tracer fields

* Corresponding author. Fax: +33-01-69-08-7-716.

E-mail address: pjb@lsce.saclay.cea.fr (P. Jean-Baptiste).

1. Introduction

Unlike most oceanic tracers, which invade the ocean from the surface, ^3He is injected in the deep ocean at plate boundaries, in relation with tectonic–magmatic activity and hydrothermal processes. This inert tracer is then dispersed by the ocean circulation and, eventually, is released to the atmosphere by the various ocean ventilation processes. ^3He oceanic distribution shows appreciable vertical and horizontal gradients within each oceanic basin and from one basin to the other so that ^3He is a potentially valuable tracer of the world deep ocean circulation. Since the timescale of the tectonic processes responsible for the ^3He injection far exceeds the ventilation time of the deep ocean, ^3He can be considered as a steady-state tracer (Dutay et al., 2004).

The same situation prevails at a reduced scale in the Red Sea, a deep narrow channel whose deep thermohaline circulation makes it look like a miniature 2-D world ocean. Red Sea deep waters equally show marked ^3He gradients due to substantial ^3He injection in the central Rift valley (Lupton et al., 1977; Andrié, 1987). Hence, Red Sea can be seen as a valuable natural laboratory for testing tracer methodology (Metzl et al., 1989). Estimates of the Red Sea deep water formation rate vary widely from 0.016 Sv (Kuntz, 1985) to 0.16 Sv (Cember, 1988), corresponding to deep water bulk residence time of a few decades to a few centuries. Similarly, little is known so far regarding the details of the Red Sea deep waters internal circulation. With respect to the deep circulation, fields of various tracers are the major source of information. Cember (1988) used a three-layer model to study the ^3He and ^{14}C distributions below 200 m depth. The issue of the ^3He distribution was revisited in more details by Eshel et al. (1994) using a box-model with 22 boxes. However, the focus of their study was clearly on the surface and intermediate circulations, with only two layers for describing the flow field below 400 m.

With respect to ^3He , we adopt an approach parallel to that of Eshel et al. (1994). However, we focus on the deep Red Sea basin (below 300 m) using a model with 36 boxes. ^3He and mass conservation equations are inverted using a linear inverse method to determine the internal circulation of the deep Red Sea.

This method allows us to infer the main patterns of the Red Sea deep circulation. However, we show that the intensity of this circulation and the subsequent ventilation rate of the deep waters cannot be determined with a good precision unless the intensity of the deep ^3He sources is known accurately, which is not the case. To overcome this limitation, the mass fluxes deduced from the ^3He inversion are used to simulate the invasion of the bomb ^{14}C transient in the deep Red Sea. By adjusting the intensity of the deep circulation in order to get the best possible agreement between the simulated ^{14}C field and the Geosecs ^{14}C data, this additional computation allows us to determine the best-estimate of the bulk residence time of the Red Sea deep waters.

One challenging aspect of the present study is that the characteristics of the two tracers that we use differ profoundly: ^3He is a steady-state tracer, ^{14}C is a transient tracer, ^3He is injected at the seafloor, ^{14}C invasion starts from the surface. This marked contrast between the two tracers puts strong constraints on solution that we seek in terms of flow field and water residence time, and therefore is a good insurance against unrealistic solutions.

2. Red Sea hydrography

The Red Sea is a rift valley separating Asia from Africa. It is almost 2000 km long for less than 300 km in width on average. The bottom topography is wedge shaped, with depths up to 2900 m in the center. This deep and narrow channel defines a nearly enclosed basin branching into the Gulf of Suez and the Gulf of Aqaba in the north, and connected to the Indian ocean (Gulf of Aden) in the south through the shallow strait of Bab el Mandeb.

2.1. Exchange through the Strait of Bab el Mandeb

A remarkable feature of the Red Sea is the intense (≈ 2 m/year) basin wide evaporation (see Sofianos et al., 2002 for review) that leads to increasing surface salinities, reaching up to 41 psu at the northern end. This surface buoyancy loss creates an inflow of Indian ocean surface waters from the gulf of Aden, compensated by a bottom outflow of salty Red Sea waters above the shallow sill of Bab el Mandeb

(≈ 140 m). This two-layer system is modulated by the seasonal reversal of the monsoon winds. During winter, northward winds enhance the surface inflow. From June to October instead, southward winds create a three-layer system in the strait, with a shallow surface outflow, intermediate inflow of water from the Gulf of Aden and bottom outflow of Red Sea water (Morcos, 1970; Patzert, 1974; Maillard and Soliman, 1986; Souvermezoglou et al., 1989; Murray and Johns, 1997).

2.2. Surface currents

The hydrography of the upper strata of the Red Sea is affected by marked seasonal variations of the wind field, which is controlled by the monsoon blowing in the Arabian Sea (Morcos, 1970; Patzert, 1974). During most of the year (October to May), the strong SSE winds present in the southern Red Sea cause a large surface inflow from the Indian ocean and the mean meridional transport at the surface is directed predominantly to the north. During the southwest monsoon (June to September), the direction of the winds over the southern Red Sea and the Gulf of Aden is reversed. The surface flow also reverses and is directed toward the Gulf of Aden. During transition periods, currents are weakest and most variable. In all seasons, hydrographic observations and velocity measurements show that surface circulation consists of a series of cyclonic and anticyclonic gyres that disappear and reappear at preferential locations (Morcos and Soliman, 1974; Quadfasel and Baudner, 1993) as a consequence of the wind field which is steered by the adjacent high topography. Thus, density forcing and the wind interact at different times and places to generate a rather complex surface circulation (Sofianos and Johns, 2003).

2.3. Intermediate and deep circulation

In response to the strong evaporation, the inflow from the Gulf of Aden gradually becomes cooler and saltier, and returns south as a denser subsurface current (Neumann and McGill, 1962; Tragou and Garrett, 1997; Quadfasel, 2001) which eventually escapes above the sill of Bab el Mandeb. Although these mean conditions are thought to be mainly driven by thermohaline forces (Phillips, 1966; Eshel and Naik, 1997; Sofianos and Johns, 2003), tracer studies show that the

subsurface circulation is largely affected by the strong seasonal modulation of the monsoon (Eshel et al., 1994). In the extreme north of the Red Sea (south of the Sinai peninsula), in the Gulf of Aqaba and particularly in the shallow Gulf of Suez where salinities are found in excess of 41 psu, denser waters are formed. Part of these waters are injected below the pycnocline and give rise to a southward flowing current at intermediate depth (Cember, 1988). A smaller portion, formed in the winter season when surface temperatures are at their lowest, is able to sink to the bottom as a slope convective current and feed the deep thermohaline circulation (Maillard, 1974; Wyrki, 1974, Cember, 1988; Woelk and Quadfasel, 1996).

3. ^3He data

The ^3He data set is combined from the Geosecs, Meseda-II and Merou expeditions. The three Geosecs stations in the Red Sea were occupied in December 1977. Helium isotopes measurements were made by J.E. Lupton and have appeared in the Geosecs Atlas (Ostlund et al., 1987). The vertical ^3He profiles are shown in Cember's paper (Cember, 1988). The Meseda cruise occurred in March–June 1979. Helium isotopes were measured at the University of Heidelberg and published in Kuntz's thesis (Kuntz, 1985). Merou data were obtained in June 1982 (Beauverger et al., 1982) and were measured by our group at Saclay (Andrié, 1987). This combined data set is identical to the ^3He data set used by Eshel et al. (1994).

The data do not allow us to resolve the seasonal and interannual variability of the deep Red Sea ventilation. However this lack of temporal resolution is of minor importance here, since we are primarily interested in the long term averaged deep circulation.

^4He concentrations are essentially constant throughout the deep basin and close to the equilibrium value with the atmosphere. Hence, the ^3He data can be expressed using the delta (δ) notation, where the ^3He excess, $\delta^3\text{He}$, is defined as the deviation in percent of the $^3\text{He}/^4\text{He}$ ratio of the sample (subscript s) from the atmospheric ratio (subscript a):

$$\delta^3\text{He}(\%) = \left[\frac{(^3\text{He}/^4\text{He})_s}{(^3\text{He}/^4\text{He})_a} - 1 \right] \times 100 \quad (1)$$

Sections of $\delta^3\text{He}$ drawn from the data of each of the three expeditions (not shown) all point to large

^3He excesses (up to 40–50%) in the deep waters of the southern half of the basin, with a clearly defined north–south gradient, consistent with the formation of well-ventilated deep waters in the north. Fig. 1 displays the $\delta^3\text{He}$ vertical section drawn from the combined data set. In the surface layer, $\delta^3\text{He}$ values are close to the equilibrium with the atmosphere. The most prominent feature is the mid-depth ^3He maximum. Having in mind the mantle ^3He injection at depth, this pattern globally support the early deep circulation scheme of Manins (1973) in which newly formed deep waters with a low $\delta^3\text{He}$ sink in the north as a convective plume and sweep excess ^3He southwards as they proceed along the slope (Fig. 2). The ^3He distribution also suggests, as hypothesized by Manins (1973), the existence of a middepth return flow, which may be due to the entrainment of intermediate waters into the sinking plume.

In the following, we assume that the tritiumgenic ^3He component is negligible. Tritium concentrations below 300 m were less than 1.5 TU at the time of the ^3He surveys (Kuntz, 1985; Ostlund et al., 1987;

Andrié and Merlivat, 1989), and were significantly lower during the preceeding years, according to the bomb ^{14}C time evolution recorded by Red Sea corals (see Section 6 for details). Hence, we calculate that the tritium contribution to the measured $\delta^3\text{He}$ since the start of the bomb tritium injection, i.e. over 20 years or so, should be less than 2%, in agreement with Kuntz model (Kuntz, 1985). Hence, owing to the large $\delta^3\text{He}$ excesses observed in the deep Red Sea, this assumption is valid.

4. Inverse model

4.1. Model geometry and formalism

As it is aimed at studying the main pattern of the deep convective circulation, the model domain is restricted to water layers below 300 m. Owing to the strong lateral confinement of the basin we adopt a two dimensional description of the Red Sea, in line with previously published works (Kuntz, 1985; Metz et al., 1989; Eshel et al., 1994).

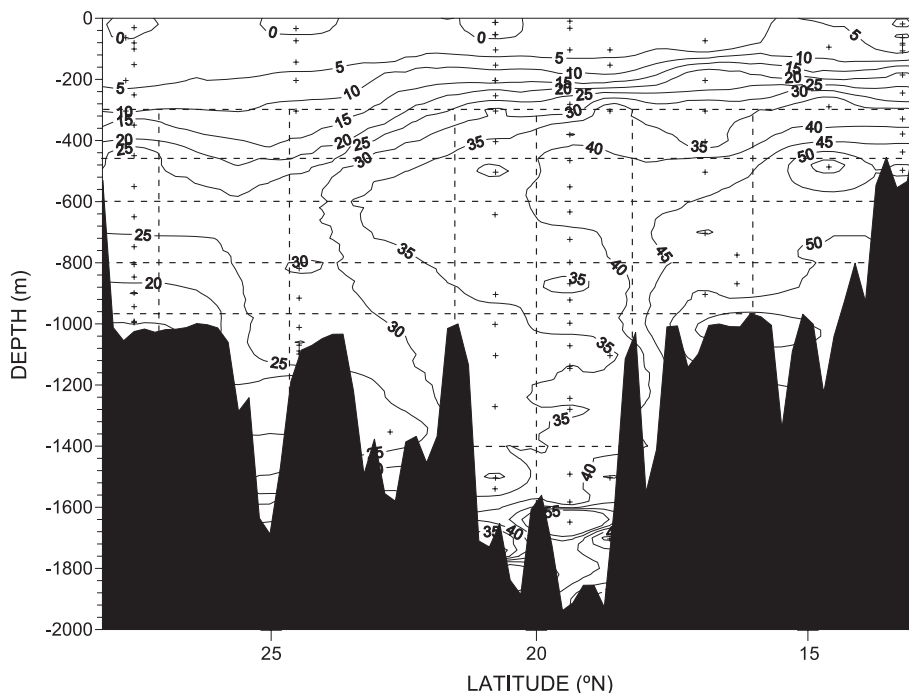


Fig. 1. Red Sea $\delta^3\text{He}$ vertical section and model geometry (dashed lines).

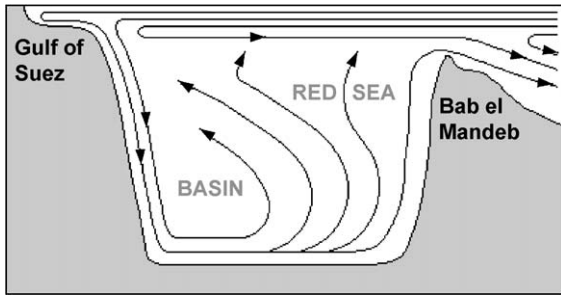


Fig. 2. Sketch of the Red Sea circulation (after Manins, 1973).

The inverse model is based on conservation of water mass and ³He in 36 boxes. The choice of the geometry of the boxes (Fig. 1) is a compromise between the need for the best possible spatial resolution and the relative sparsity of the data. The volume of the boxes and the surface area of the boxes' boundaries were computed using a bathymetry file of the US Naval Oceanographic Office. The mean ^δ³He in each box (Fig. 3) was computed from the tracer grid used to plot the ^δ³He section of Fig. 1.

Two fluxes of opposite sign are considered through each interface, to describe in the most general way the

exchange between adjacent boxes (Fig. 4), including both advection and mixing processes, thus avoiding distortion of the advection field that would result from neglecting mixing. Tracer conservation is expressed by Eq. (2) below:

$$C_{i-2,j}F_{i-1,j}^+ + C_{i,j-2}F_{i,j-1}^+ + C_{i,j+2}F_{i,j+1}^- + C_{i+2,j}F_{i+1,j}^- - C_{i,j}(F_{i-1,j}^- + F_{i,j-1}^- + F_{i,j+1}^+ + F_{i+1,j}^+) + S_{ij=0} \quad (2)$$

where $C_{i,j}$ is the concentration of the tracer (in mol/m³) in box (i,j) and where the water fluxes F^+ , F^- (in m³/s) and the tracer source in box (i,j), S_{ij} (in mol/s), are the unknowns (see Fig. 4).

For ³He, the concentrations $C_{i,j}$ in Eq. (2) can be replaced by $\delta_{i,j}$ according to Eq. (1), thus giving:

$$\delta_{i-2,j}F_{i-1,j}^+ + \delta_{i,j-2}F_{i,j-1}^+ + \delta_{i,j+2}F_{i,j+1}^- + \delta_{i+2,j}F_{i+1,j}^- - \delta_{i,j}(F_{i-1,j}^- + F_{i,j-1}^- + F_{i,j+1}^+ + F_{i+1,j}^+) + S'_{ij} = 0 \quad (2')$$

Here, S'_{ij} equals $S_{i,j} \times 100/R_a/[^4\text{He}]$, and $[^4\text{He}]$ and R_a are the helium-4 concentration in the Red Sea deep waters and the helium isotope atmospheric ratio, (³He/⁴He)_a, respectively.

	8.72%	9.93%	16.74%	27.17%	30.19%	32.10%	35.12%	300 m
13.93%	17.75% <i>2754.29</i>	14.55% <i>12013.62</i>	23.07% <i>12549.55</i>	32.83% <i>7531.82</i>	36.61% <i>7317.79</i>	34.90% <i>6074.88</i>	40.60% <i>4291.85</i>	42.37%
	26.65%	24.02%	33.36%	37.05%	41.81%	42.49%	49.63%	460 m
24.87%	2078.68	9623.42	9771.10	5952.58	5031.66	3727.51	2703.67	600 m
	25.74%	26.30%	34.38%	38.21%	40.53%	46.54%	49.23%	600 m
0%	2551.81	9962.92	9820.41	6154.47	5086.99	4117.93	2798.00	800 m
	20.64%	24.57%	31.48%	35.69%	36.73%	46.85%	51.28%	800 m
0%	1287.97	5085.97	4929.32	2986.61	2629.25	2443.04	1882.24	960 m
	15.52%	23.13%	28.42%	34.07%	35.76%	47.29%		1400 m
0%	306.32	3990.89	4389.70	3876.15	4183.66	1171.09		
				36.48% <i>1228.30</i>	43.95% <i>1583.29</i>			
				S1	S2			

Fig. 3. Mean ^δ³He in each box (box volume, in km³, is shown in italics). The left arrows represent the northern plume of dense surface water which sinks along the slope and feeds the deep layers with newly ventilated water. S1–S6 indicate the ³He sources (see Section 4.1)

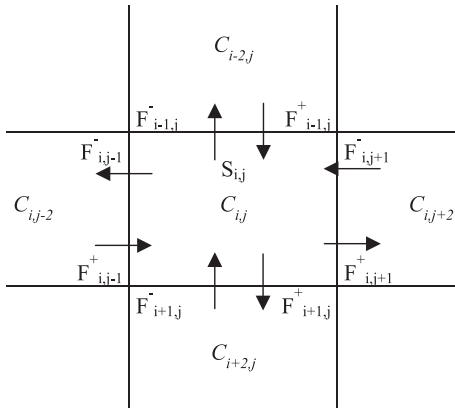


Fig. 4. Advection and mixing scheme for box (i,j) .

With respect to water mass conservation, Eq. (2) can be simply rewritten as follows:

$$(F_{i-1,j}^+ + F_{i,j-1}^+ + F_{i,j+1}^- + F_{i+1,j}^-) - (F_{i-1,j}^- + F_{i,j-1}^- + F_{i,j+1}^+ + F_{i+1,j}^+) = 0 \quad (2'')$$

Geophysical studies of the Red Sea indicate that the rift can be divided in three domains corresponding to three distinct tectonic stages of its evolution (Cochran et al., 1986; Martinez and Cochran, 1989). The southern part has been characterized by a well established seafloor spreading for the last 5 millions years whereas the northern part is still in a stage of continental rifting. In the central part, strong ^3He anomalies have been detected in deep brines (Miller et al., 1966) with a $^3\text{He}/^4\text{He}$ ratio of $8.7 \times R_a$ (Lupton et al., 1977; Andrié, 1987) typical of Mid-Ocean Ridge hydrothermal fluids (Merlivat et al., 1984; Jean-Baptiste et al., 1991, 1998). From these different informations, we assume that ^3He sources occur in the Central and Southern part of the basin only, corresponding to the six bottom boxes of the southern part of the basin (see Fig. 3).

With two tracers (^3He and water), 36 boxes, 72 interfaces and six ^3He sources, the sum of which is set to a prescribed value representing the global ^3He flux (see discussion in Section 4.2 below), we have a linear system of 73 equations with 150 unknowns, which can be written in matricial form $A \times X = B$ where A is the matrix constructed from tracer data, X is the vector of the unknowns and B is the vector representing the second term of the equations. The method also permits to impose additional constraints in the form of

inequality $G X > H$, corresponding to a priori knowledges concerning the direction and/or magnitude of the water flux at particular boundaries using field measurements such as current meters data, hydrographic measurements, etc. In our inversion, the only a priori constraints imposed upon the system are:

- the sign of the ^3He sources : $S_{ij} > 0$ in the six bottom boxes of the southern half of the basin and $S_{ij} = 0$ everywhere else.
- the sign of the flux at the northern boundary of the three northern deep boxes, corresponding to an inflow of newly formed deep water.

The model formalism follows Bolin et al. (1983), Metz et al. (1989) and others. The system is resolved by a classical least squares method with inequality constraints (LSI programming in Lawson and Hanson, 1974). All the details concerning the methodology are available in Eshel et al. (1994).

4.2. ^3He sources

In the model, the magnitude of the global ^3He injection bears directly on the strength of the deep circulation and on the time-scale of deep water renewal. The global deep Red Sea ^3He flux can be evaluated from the ^3He escape rate at the surface using the mean ^3He transfer velocity $K_{3\text{He}}$ and the mean ^3He surface concentration gradient across the air–sea interface. In his study of the bomb ^{14}C invasion of the Red Sea, Cember (1989) proposed an average value K_{CO_2} of 2.1 ± 0.5 m/day for a mean wind speed of 4.7 m/s. Scaled to the Schmidt number of ^3He (Jähne et al., 1987a,b), this leads to $K_{3\text{He}} = 4.3 \pm 1$ m/day. Recent direct measurements of $K_{3\text{He}}$ in a lake (Jean-Baptiste and Poisson, 2000; Jean-Baptiste et al., 2002) give slightly higher value of 6.3 ± 0.6 m/day for the same wind and surface temperature conditions.

Knowing the ^3He transfer coefficient, we can deduce the global ^3He flux to the atmosphere, $Q_{3\text{He}}$, using the piston velocity formula:

$$Q_{3\text{He}} = A \times K_{3\text{He}} \times (C - C_{\text{eq}}) \quad (3)$$

where $A \approx 438,000 \text{ km}^2$ is the total surface area of the Red Sea, C is the average ^3He surface concentration

and C_{eq} is the ^3He concentration in equilibrium with the atmosphere. Replacing C and C_{eq} by $\delta^3\text{He}$ and $\delta^3\text{He}_{\text{eq}}$ according to Eq. (1), we obtain:

$$Q_{^3\text{He}} = A \times R_a \times [^4\text{He}]_{\text{surf}} \times K_{^3\text{He}} \times (\delta^3\text{He} - \delta^3\text{He}_{\text{eq}}) \quad (3')$$

where $[^4\text{He}]_{\text{surf}}$ and R_a are the helium-4 concentration of surface waters and the helium isotope atmospheric ratio, respectively.

The average surface $\delta^3\text{He}$ calculated from available data in the surface layer is equal to -0.6% . This is slightly above the equilibrium value with the atmosphere, which is close to $\delta^3\text{He}_{\text{eq}} = -1.5\%$ between 25 and 30 °C (Top et al., 1987). Thus, the best estimate of the ^3He flux escaping at the surface of the Red Sea basin is 17 ± 4 mol/year. The global ^3He source released by the hydrothermal activity at the bottom of the Red Sea is equal to this surface flux corrected from the net ^3He flux exchanged through the strait of Bab el Mandeb. By combining the annual averaged data for the inflow and outflow of water through the straight given by Murray and Johns, 1997 (0.4 and 0.38 Sv, respectively), with the ^3He vertical profile at Merou station 49 located in the strait, we calculate a net annual export of 2 ± 1 mol/year of ^3He . This leads to a ^3He input into the deep Red Sea of 19 ± 5 mol/year.

An alternative way of establishing the magnitude of the deep ^3He source is to scale the Red Sea ^3He flux to the world global ^3He flux from the seafloor. The value of 2 ^3He atom/cm² of the whole earth/sec first proposed by Clarke et al. (1969) was revisited by several authors (Craig et al., 1975; Jean-Baptiste, 1992; Farley et al., 1995) and lies in the range 2–5 atom/cm²/s, or 500–1300 ^3He mol/year. As the vast majority of this flux is released along the 60,000 km of ocean ridges, we estimate the corresponding deep Red Sea ^3He flux in the range 14 ± 6 ^3He mol/year (we assume, as explained above, that the helium-3 injection occurs mainly in the active southern part of the basin, i.e. along 1000 km of rift).

These two independent approaches lead to consistent results. However, both methods show significant uncertainties and thus constrain only approximately the renewal time of the deep waters. Hence, the first merit of the ^3He inversion will be to propose a circulation pattern for the deep Red Sea. The final

step, addressed in the last section of this paper, will be to further constrain the timescale of the deep circulation scheme using the bomb ^{14}C distribution.

5. Deep circulation pattern

Below the system of currents which takes place at the surface and at intermediate depth below the pycnocline (see Section 2), lies the Red Sea deep water. This water, which forms a distinct water mass with fairly homogeneous T/S properties, fills the entire rift valley from about 300-m depth to the bottom. Whereas an appreciable number of investigators have written on the formation of the Red Sea deep water and on its bulk residence time, fewer studies have been devoted to the internal circulation of this water mass. No current velocity measurements are available, so that much of our present knowledge comes from geochemical tracers (including nutrients, O_2 , ^3He and transient tracers like ^{14}C and tritium) or from hydraulic models.

One of the first comprehensive work concerned with the description of the deep Red Sea internal circulation is the study by Manins (1973). Manins condensed the available hydrographic and dynamic knowledge of the Red Sea into an hydraulic model of the sinking plume of newly formed deep water in the north, called the “filling box model” of the Red Sea. The first component of the proposed circulation scheme (Fig. 2) consists in a dense convective plume which sinks in the extreme north of the basin. This plume entrains neighbouring waters and gives rise to a southward bottom flow which flushes the Red Sea deep basin with newly ventilated deep waters. To compensate this downward flow, the interior of the Red Sea is subject to slow ascending movements. Manins’ model indicates that part of this upwelled water feeds a mid-depth return flow which tends to replace the waters entrained in the sinking process.

Eshel’s findings (Eshel et al., 1994), based on ^3He in a multibox model with two layers (each with three boxes) below 400 m, basically support Manins’ scheme, with a sinking branch north of 27°N, a deep southward flow below 700 m which upwells throughout the deep basin, and a northward return flow between 400 and 700 m.

The advective field resulting from our own inversion, which is the difference between the two fluxes of opposite direction at each interface, is shown in Fig. 5 (the results correspond to a ^3He source of 19 mol/year). The circulation is consistent with Manins' flow field. The main features include:

- a descending branch in the northernmost part of the basin, which corresponds to the sinking of dense surface water and the entrainment of additional water by the sinking plume (note that the origin of this newly formed deep water cannot be determined from the ^3He tracer field since all surface waters have essentially the same $\delta^3\text{He}$ close to the isotopic equilibrium with the atmosphere);
- a north–south movement of this newly formed deep water below 800 m depth;
- an upwelling of the deep waters, which occurs preferentially in the southern half of the basin and which feeds a well-established return flow at intermediate depth, between 460 and 600 m.

Fig. 5 also displays a sketch of the deep Red Sea circulation based on our results. In addition to the features described above, we see that the internal circulation defines a counterclockwise recirculating loop whose spatial extension encompasses most of the deep Red Sea interior.

In the uppermost layer of the model (300–460 m), the circulation is not so well defined. This layer represents a transition between the southward intermediate circulation and the northward upper branch of the deep recirculation cell. Thus, the lack of definition of the circulation may be due to the fact that it is sandwiched between two systems of currents of opposite direction. However, some of the upwelling and downwelling model fluxes could be spurious and could also indicate the model's inability to resolve the circulation and mixing processes in this transition zone.

As already mentioned above, the intensity of the flow field deduced from the inversion is proportional to the deep ^3He flux. In the next section, in order to

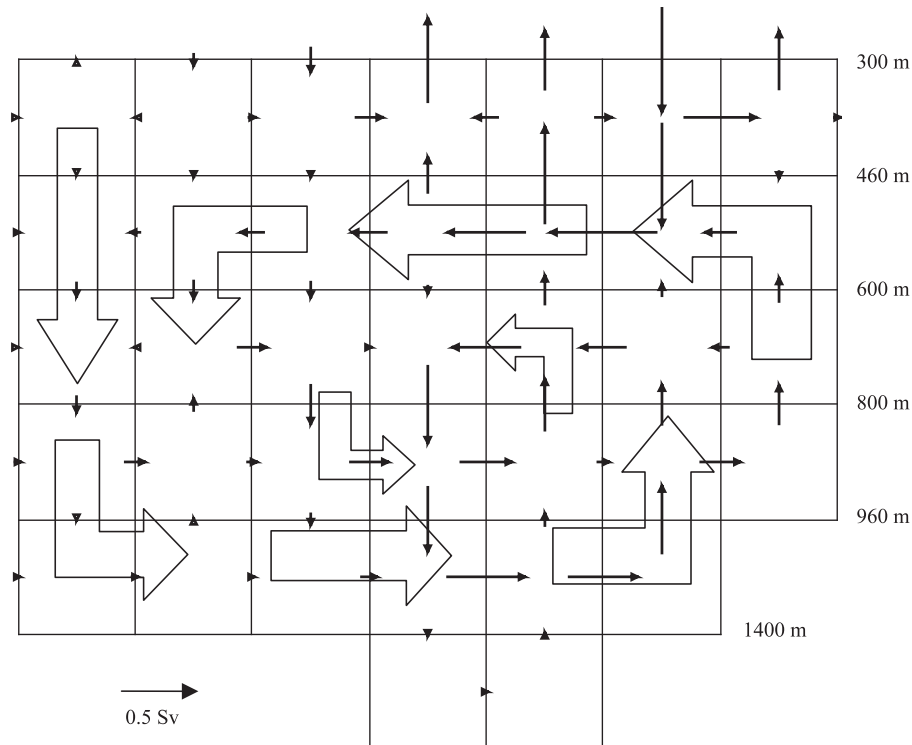


Fig. 5. Solution of the ^3He inverse problem. Arrows represent net advection fluxes.

assess more accurately the absolute value of the flow and the corresponding rate of deep water renewal, we test the present circulation scheme against the transient bomb ^{14}C distribution. The purpose of this exercise is twofold:

- (1) it will allow us to check the consistency of the circulation scheme deduced from the ^3He field inversion with the observed transient ^{14}C distribution;
- (2) it will give us an independant chronometer that will allow us to fine-tune the intensity of the circulation so as to get the best possible agreement between the simulated ^{14}C distribution and the Geosecs ^{14}C data, thus leading to a more precise determination of the bulk residence time of the Red Sea deep waters.

6. Bomb radiocarbon experiment

6.1. Radiocarbon data

Radiocarbon (^{14}C) was released in the atmosphere by the nuclear atmospheric tests of the 1950s and early 1960s. The vast majority of this ^{14}C entered the marine carbon cycle by $^{14}\text{CO}_2$ exchange at the air–sea interface, and therefore constitutes an excellent transient tracer of ocean ventilation. The penetration of bomb ^{14}C in the Red Sea at the time of Geosecs (1977), that is 12 years after the atmospheric ^{14}C peak, is displayed in Fig. 6a. It shows that the surface waters tagged with bomb ^{14}C (corresponding to well-ventilated low $\delta^3\text{He}$ waters) rapidly reached the deep layers of the northern Red Sea. Compared to pre-bomb ^{14}C estimates deduced from Red sea corals ($\Delta^{14}\text{C} \approx -75\%$), the Geosecs distribution also shows that the transient signal started to spread all across the basin interior, with no place left uncontaminated by the transient signal two decades only after the start of the tracer injection. This fact is a first clear indication of the short time scale of the residence time of the deep waters.

The surface water history of the ^{14}C transient can be reconstructed with a good accuracy by direct ^{14}C measurements on annual growth bands of Red sea corals. For this purpose, we use the same data set as Cember (1989). Fig. 7 shows the rapid rise in the

(a) $\Delta^{14}\text{C}$ (Geosecs/Dec.1977)

+6.2	+3.3	-8.0	-17.6	-20.9	-19.0	-24.2	300 m
-24.8	-25.1	-28.5	-33.2	-34.6	-35.1	-38.1	460 m
-15.7	-17.9	-24.1	-29.1	-30.8	-31.1	-33.2	600 m
+3.6	-1.2	-13.6	-22.0	-23.8	-23.0	-20.8	800 m
+22.2	+0.4	-9.5	-16.1	-17.3	-17.8		960 m
			-17.2	-17.0			1400 m

(b) Modeled $\Delta^{14}\text{C}$ (global ^3He flux = 18.7 mol $^3\text{He}/\text{year}$)

+7.9	+4.8	-24.8	-25.1	-23.2	-23.2	-24.7	300 m
-12.1	-24.4	-28.2	-26.5	-24.9	-24.2	-24.7	460 m
-12.0	-18.8	-26.3	-26.4	-25.5	-24.4	-24.3	600 m
+7.2	-4.8	-20.1	-24.3	-24.2	-22.6	-23.0	800 m
+30.0	+6.1	-9.0	-20.3	-21.2	-21.5		960 m
			-21.2	-22.4			1400 m

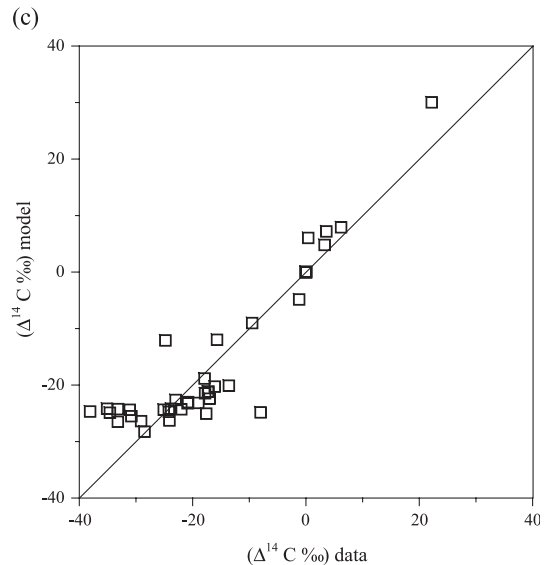


Fig. 6. (a) Mean $\Delta^{14}\text{C}$ deduced from the Geosecs vertical section (Ostlund et al., 1987). (b) Simulated $\Delta^{14}\text{C}$ distribution. (c) Comparison of the observed and simulated $\Delta^{14}\text{C}$ for the 36 boxes.

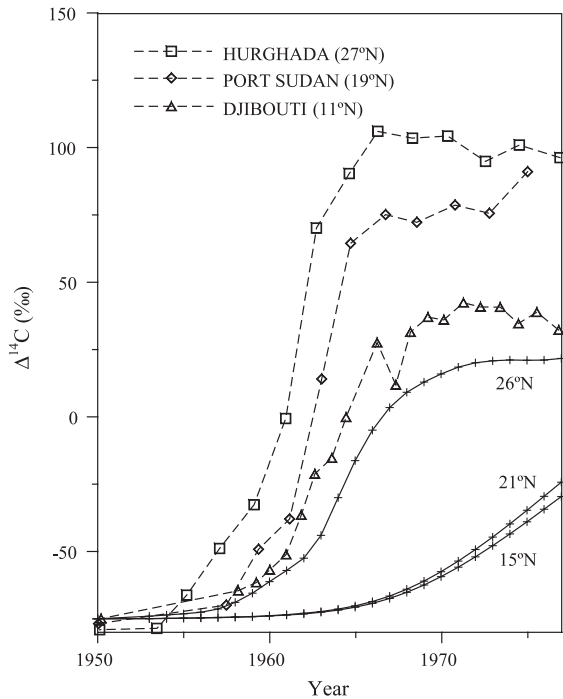


Fig. 7. Carbon-14 coral data (Cember, 1989) for the southern, central and northern part of the Red Sea (dashed lines). Solid curves show the corresponding $\Delta^{14}\text{C}$ at 300 m depth, calculated from these data using the box-model of Eshel et al. (1994).

$\Delta^{14}\text{C}$ of Red Sea surface waters recorded by corals that followed the large thermonuclear tests of the late fifties and early sixties. Also apparent in Fig. 7 is the north–south gradient in surface ^{14}C concentrations. This gradient is due to the monsoon driven seasonal upwelling in the Gulf of Aden which dilutes surface water with deeper waters depleted in ^{14}C (Cember, 1989). During their journey to the north through the strait of Bab el Mandeb, these surface waters get progressively enriched in ^{14}C by exchange with the atmosphere.

6.2. Radiocarbon simulation

This surface water $\Delta^{14}\text{C}$ history recorded in corals is translated into a $\Delta^{14}\text{C}$ record at 300 m depth, i.e., the upper boundary of our model domain, using the Eshel et al. (1994) multi-box model. This model, calibrated against several tracers including temperature, salinity and ^3He , has a good spatial resolution in

the upper and intermediate levels and thus is well adapted to our purpose.

Adopting the same formalism as before (see Fig. 4), the equation describing the evolution of the $\Delta^{14}\text{C}$ value ($\Delta^{14}\text{C}_{i,j}$) in each box (i,j) between time t and time $t + \Delta t$ is :

$$\begin{aligned} \Delta^{14}\text{C}_{i,j}(t + \Delta t) &= \Delta^{14}\text{C}_{i,j}(t) + [\Delta^{14}\text{C}_{i-2,j}F_{i-1,j}^+ + \Delta^{14}\text{C}_{i,j-2}F_{i,j-1}^+ \\ &+ \Delta^{14}\text{C}_{i,j+2}F_{i,j+1}^- + \Delta^{14}\text{C}_{i+2,j}F_{i+1,j}^- - \Delta^{14}\text{C}_{i,j} \\ &\times (F_{i-1,j}^- + F_{i,j-1}^- + F_{i,j+1}^+ + F_{i+1,j}^+)] \times \Delta t / V_{ij} \quad (4) \end{aligned}$$

where V_{ij} is the volume of box (i,j).

This time history of the bomb ^{14}C at 300 m is shown in Fig. 7 for three different latitudes.

The reconstructed record at 300 m depth, from the pre-industrial era (1950) to the time of Geosecs (1977) is stored in a computer file. It is subsequently interpolated to serve as a boundary condition to simulate the penetration of bomb ^{14}C in the deep Red Sea with our 36 box model, using the fluxes obtained from the ^3He inversion. The computation of the time evolution of the $\Delta^{14}\text{C}$ value in each of the 36 boxes of the model is carried out as above using Eq. (4).

Several runs were made with different circulation intensity, by simply multiplying all fluxes by a constant factor, to find the best agreement between the simulated ^{14}C distribution and the ^{14}C data. The best fit corresponds to a total strength of the ^3He sources of 18.7 mol/year. This figure falls within the range of ^3He fluxes estimated in Section 4.2 and is indeed extremely close to the 19 mol/year obtained from ^3He air–sea fluxes using the piston velocity equation. This excellent agreement is probably coincidental but it shows nevertheless that the timescales imposed by the ventilation of the deep ^3He sources and by the ^{14}C transient are fully consistent.

The comparison of the ^{14}C distribution simulated by the model with the observed ^{14}C field is shown in Fig. 6b and c. The agreement between both distributions is satisfactory, considering the uncertainty in the reconstruction of the ^{14}C concentration history at the model boundaries. Nevertheless, the core of low $\Delta^{14}\text{C}$ values displayed by the data in the intermediate levels of the southern Red Sea (460–600 m) appears slightly too young in the simulation (with slightly elevated

$\Delta^{14}\text{C}$), thus indicating that the recirculation loop deduced from the inversion may be somewhat over-estimated.

6.3. Deep red sea renewal rate

As a whole, our results point to the rapid renewal rate of Red Sea deep waters. We find that the newly formed deep water in the north of the basin (which is the sum of the fluxes materialized by the three arrows on the left side of Fig. 3) sinks at a rate Φ of $0.09 \times 10^6 \text{ m}^3/\text{s}$. With a volume V of the deep basin (below 300 m) of $173,889 \text{ km}^3$ (representing the sum of the 36 boxes of the model—see Fig. 3), this renewal rate corresponds to a residence time V/Φ of about 60 years. Estimates of the Red Sea deep waters' renewal rate and subsequent bulk residence time vary substantially in the literature (Table 1). Initial studies based on oxygen budget (Wyrтки, 1974) and hydrography (Manins, 1973; Maillard, 1974) favoured a rather long residence time of the deep waters. However, subsequent studies based on tritium and ^{14}C transient tracers all points to a more rapid turn-over. Various sources of deep water formation have been suggested based on hydrographic observations, including outflow of dense waters from the shallow Gulf of Suez (Maillard, 1974; Wyrтки, 1974; Cember, 1989; Woelk and Quadfasel, 1996), from the Gulf of Aqaba over the strait of Tiran (Wyrтки, 1974; Murray and Hecht, 1989), and even open sea convection off the Sinai peninsula (Wyrтки, 1974). These various contributions to the Red Sea deep waters show substantial interannual variability (Woelk and Quadfasel, 1996), a fact which may contribute to the lack of clear consensus on the source and rate of deep water

formation based on observations limited in space and time.

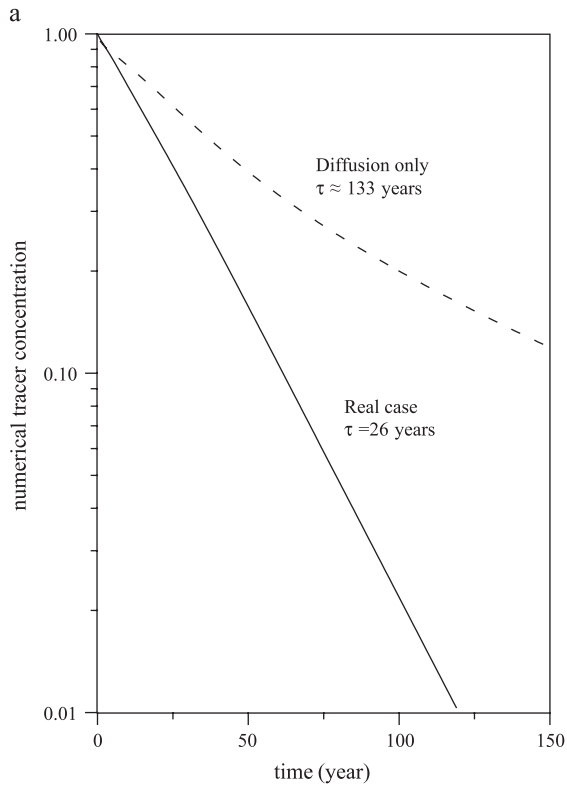
Classically, the residence time τ of a deep water body is obtained by dividing the total volume of the deep reservoir by the flux of newly formed deep water. In the reality however, the translation of a purely advective rate of deep water formation into a bulk ventilation time τ of the deep waters brings additional difficulties, due to different possible modes of deep water ventilation, including diffusive modes. Cember (1989) proposed two modes of ventilation of the Red sea, one corresponding to a deep convection mode in the north, at a rate of $0.05 \times 10^6 \text{ m}^3/\text{s}$, and a second mode called isopycnal mode, characterized by an injection of surface water at intermediate depth, below the pycnocline, at a rate of $0.11 \times 10^6 \text{ m}^3/\text{s}$. His main conclusions were supported by the work of Eshel et al. (1994). On the other hand, Kuntz (1985) concluded from the study of the bomb tritium distribution using a multi-box model, that convection was a minor mode of deep water ventilation ($0.016 \times 10^6 \text{ m}^3/\text{s}$) and that the deep Red Sea was rapidly ventilated by widespread vertical mixing responsible for 90% of the ventilation process.

In order to quantify the bulk residence time of the Red Sea deep waters in our model, we performed a run similar to the radiocarbon run described above but this time with a numerical tracer initially set to a concentration $C_0=1$ everywhere in the basin and set to zero at the air–sea interface (corresponding to layer-1 in Eshel's multibox model used in the range 0–300 m). Fig. 8a shows that the temporal decrease of the mean tracer concentration $C(t)$ below 300 m depth follows an exponential law $C(t)=C_0 \times \exp(-t/\tau)$. The time constant τ is equal to 26 years.

Table 1

Bulk residence time of Red Sea deep waters (numbers in parentheses are renewal time deduced from the sole rate of deep water formation in the north)

	Residence time (year)	Method
Manins (1973)	320	Hydrological model
Maillard (1974)	(100)	Hydrography
Wyrтки (1974)	72	Oxygen budget
Kuntz (1985)	42	Tritium, ^3He (multibox-model)
Cember (1988)	36	^{14}C , ^3He (box-model with 2 deep boxes)
Eshel et al. (1994)	35	T, S, ^3He (box-model with 6 deep boxes)
Woelk and Quadfasel (1996)	(40–90)	Hydrography
This work	26–(60)	^3He , ^{14}C (box model with 36 deep boxes)



b

62.2	62.7	65.1	63.0	62.0	59.4	57.0
56.9	64.4	62.9	61.3	59.2	58.2	56.2
57.7	62.5	62.9	62.3	61.6	60.7	60.7
52.6	57.2	61.4	62.0	61.8	61.2	60.7
44.7	54.6	58.9	61.3	61.6	60.8	
			61.4	61.8		

Fig. 8. (a) Decay rate of a numerical tracer as a function of time. The tracer is initially set to 1 in the entire basin and to 0 at the surface. As for the ^{14}C simulation, the model of Eshel et al. (1994) is used in the 0–300 m layer. The solid line shows an exponential decay with a time constant of 26 years. The dashed line corresponds to a simulation where the net advection is set to zero at all boxes interfaces (diffusion only experiment). (b) Time necessary to ventilate each box at the 90% level (in year).

What is the relationship between this time constant and the bulk residence time of the deep basin? If we consider the same numerical tracer approach in the very simple case of a reservoir of volume V (in m^3) renewed from the surface at a rate φ (in m^3/s), meaning that, per unit of time, a volume φ of water is ventilated at the surface and subsequently mixed back into the reservoir, one can easily demonstrate that the decay of the tracer concentration $C(t)$ follows the exponential law $C(t) = C_0 \times \exp(-\varphi \times t/V)$. This simple analogy shows that the time constant τ in Fig. 8a is equivalent to a ratio V/φ and therefore is indeed a measure of the bulk residence time of the deep Red Sea basin.

This value of 26 years is less than half that deduced from the rate of deep water formation alone (60 years). This shows, in agreement with the conclusions of Eshel et al. (1994), that deep water sinking in the extreme north is not an exclusive mode of ventilation of the deep Red Sea. Fig. 8b, which displays the rate of ventilation of the individual boxes, also indicates that ventilation proceeds rather uniformly within the Red Sea interior. The same numerical tracer simulation carried out by suppressing any net advection (diffusion only experiment in Fig. 8a) also shows that diffusion is not the main driver of the Red Sea ventilation, as claimed by Kuntz (1985) and already challenged by Eshel et al. (1994).

7. Conclusion

In order to describe the deep circulation of the Red Sea and estimate its ventilation rate, a linear inverse model was constructed, based on the conservation of mass and ^3He .

The main features of the deep circulation (below 300 m) deduced from the inversion include (i) in the northernmost part of the basin, a descending branch made of water entrained by the sinking plume of dense newly formed deep water. This water mass proceeds southwards below 800 m depth, (ii) in the south, an upward movement of the deep water, connected to a counterclockwise recirculation loop, which feeds a well defined return flow at intermediate depth, between 460 and 600 m.

The intensity of the deep circulation deduced from our best estimate of the ^3He sources is confirmed by the simulation of the bomb ^{14}C transient. The present

model produces deep waters at a rate of $0.09 \times 10^6 \text{ m}^3/\text{s}$, corresponding to a deep convective renewal time of 60 years. However, the model also points to an additional mode of ventilation through efficient advective exchange across the upper boundary of the domain, whereas vertical diffusion is of minor importance. The bulk residence time resulting from both modes of ventilation is of 26 years. This short residence time explains why 12 years only after the peak of the ^{14}C atmospheric injection, the 1977 Geosecs survey found that the transient signal had already reached the deepest layers, leaving no place uncontaminated.

References

- Andrié, C., 1987. Utilisation des traceurs hélium-3 et tritium en océanographie. PhD Thesis, Université Paris 6. 340 pp.
- Andrié, C., Merlivat, L., 1989. Contribution des données isotopiques de deutérium, oxygène-18 et tritium à l'étude de la circulation de la Mer Rouge. *Oceanol. Acta* 12, 165–174.
- Beauverger, C., Brunet, C., Poisson, A., 1982. Les rapports des campagnes à la mer à bord du Marion-Dufresne, MD33/MEROU, les publications de la Mission Recherche des Terres Australes et Antarctiques Françaises, vol. 82-04. 181 pp.
- Bolin, B., Bjorkstrom, A., Holmen, K., 1983. The simultaneous use of tracers for ocean circulation studies. *Tellus* 35B, 206–236.
- Cember, R.P., 1988. On the sources, formation, and circulation of the Red Sea deep water. *J. Geophys. Res.* 93, 8175–8191.
- Cember, R.P., 1989. Bomb carbon in the Red Sea: a medium-scale gas exchange experiment. *J. Geophys. Res.* 94, 2111–2123.
- Clarke, W.B., Beg, M.A., Craig, H., 1969. Excess ^3He in the sea: evidence for terrestrial primordial helium. *Earth Planet. Sci. Lett.* 6, 213–220.
- Cochran, J.R., Martinez, F., Steckler, M.S., Hobart, M.A., 1986. Conrad Deep: a new northern Red Sea deep. Origin and implications for continental rifting. *Earth Planet. Sci. Lett.* 78, 18–32.
- Craig, H., Clarke, W.B., Beg, M.A., 1975. Excess ^3He in deep water on the East Pacific Rise. *Earth Planet. Sci. Lett.* 26, 125–182.
- Dutay, J.C., Jean-Baptiste, P., Campin, J.M., Ishida, A., Maier-Reimer, E., Matear, R.J., Mouchet, A., Totterdell, I.J., Yamana, Y., Rodgers, K., Madec, G., Orr, J.C., 2004. Evaluating OCMIP-2 ocean models' deep circulation using the natural ^3He tracer field. *J. Marine Systems* 48, 15–36 (this issue).
- Eshel, G., Naik, N.H., 1997. Climatological coastal jet collision, intermediate water formation and the general circulation of the Red Sea. *J. Phys. Oceanogr.* 27, 1233–1257.
- Eshel, G., Cane, M.A., Blumenthal, M.B., 1994. Modes of subsurface, intermediate, and deep water renewal in the Red Sea. *J. Geophys. Res.* 99, 15941–15952.
- Farley, K.A., Maier-Reimer, E., Schlosser, P., Broecker, W.S., 1995. Constraints on mantle ^3He fluxes and deep-sea circulation from an oceanic general circulation model. *J. Geophys. Res.* 100, 3829–3839.
- Jähne, B., Munnich, K.O., Bosinger, R., Dutzi, A., Huber, W., Libner, P., 1987a. On parameters influencing air–water gas exchange. *J. Geophys. Res.* 92, 1937–1949.
- Jähne, B., Heinz, G., Dietrich, W., 1987b. Measurement of diffusion coefficients of sparingly soluble gases in water. *J. Geophys. Res.* 92, 10767–10776.
- Jean-Baptiste, P., 1992. Helium-3 distribution in the deep world ocean: its relation to hydrothermal ^3He fluxes and to terrestrial heat budget/isotopes of Noble Gases as Tracers in Environmental Studies. IAEA Panel Series, Vienna, pp. 219–240. STI/PUB/859.
- Jean-Baptiste, P., Poisson, A., 2000. Gas transfer experiment on a lake (Kerguelen Islands) using ^3He and SF_6 . *J. Geophys. Res.* 105, 1177–1186.
- Jean-Baptiste, P., Charlou, J.L., Stievenard, M., Donval, J.P., Bougault, H., Mevel, C., 1991. Helium and methane measurements in hydrothermal fluids from the Mid Atlantic Ridge: the SNAKE PIT site at 23°N . *Earth Planet. Sci. Lett.* 106, 17–28.
- Jean-Baptiste, P., Bougault, H., Vangriesheim, A., Charlou, J.L., Radford-Knoery, J., Fouquet, Y., Needham, D., German, C., 1998. Mantle ^3He in hydrothermal vents and plume of the Lucky Strike site (MAR $37(17^\circ\text{N})$) and associated geothermal heat flux. *Earth Planet. Sci. Lett.* 157, 69–77.
- Jean-Baptiste, P., Fourré, E., Poisson, A., 2002. Gas transfer velocities for ^3He in a lake at high wind speeds. In: Donelan, M., Drennan, W., Saltzman, E.S., Wanninkhof, R. (Eds.), *Gas Transfer at Water Surfaces*. Geophysical Monograph Series, vol. 127. American Geophysical Union, Washington DC, pp. 233–238.
- Kuntz, R., 1985. Bestimmung der Tiefenwasserzirkulation des Roten Meeres anhand einer Boxmodellauswertung von Tritium-, ^3He - und Salinitätsdaten. PhD Thesis, Ruprecht Karls Univ., Heidelberg. 87 pp.
- Lawson, C.L., Hanson, R.J., 1974. *Solving Least Square Problems*. Prentice-Hall, Englewoods Cliffs, NJ. 340 pp.
- Lupton, J.E., Weiss, R.F., Craig, H., 1977. Mantle helium in Red Sea brine. *Nature* 266, 244–246.
- Maillard, C., 1974. Eaux intermédiaires et formation d'eau profonde en Mer Rouge. *L'océanographie Physique de la Mer Rouge (IAPSO Symposium)*, vol. 2. Publications du CNEXO, Paris, pp. 105–134.
- Maillard, C., Soliman, G., 1986. Hydrography of the Red Sea and exchanges with the Indian Ocean in summer. *Oceanol. Acta* 9, 249–269.
- Manins, P.C., 1973. A filling box model of the deep circulation of the Red Sea. *Mem. Soc. Royale des Sciences de Liège, Ser. 6 IV*, 153–166.
- Martinez, F., Cochran, J.R., 1989. Geothermal measurements in the Northern Red Sea: implications for lithospheric thermal structure and mode of extension during continental rifting. *J. Geophys. Res.* 94 (IV), 12239–12265.
- Merlivat, L., Andrié, C., Jean-Baptiste, P., 1984. Distribution des isotopes de l'hydrogène, de l'oxygène et de l'hélium dans les sources hydrothermales sous-marines de la ride Est-Pacifique à 13°N . *C.R. Acad. Sc. Paris*, 299, Ser.II 17, 1191–1196.
- Metzl, N., Moore, B., Papaud, A., Poisson, A., 1989. Transport and

- carbon exchanges in the Red Sea. Inverse methodology, *Global Biogeochemical Cycles* 3, 1–26.
- Miller, A.R., Densmore, C.D., Degens, E.T., Hathaway, J.C., Manheim, F.T., Manheim, P.F., McFarlin, P.F., Pocklington, R., Jokola, A., 1966. Hot brines and recent iron deposits in deeps of the Red Sea. *Geochim. et Cosmochim. Acta* 30, 341–359.
- Morcos, S.A., 1970. Physical and chemical oceanography of the Red Sea. *Oceanogr. Mar. Biol. Ann. Rev.* 8, 73–202.
- Morcos, S.A., Soliman, G.F., 1974. Circulation and deep water formation in the northern Red Sea in winter. *L'océanographie Physique de la Mer Rouge*, (IAPSO Symposium), vol. 2. Publications du CNEXO, Paris, pp. 91–103.
- Murray, S.P., Hecht, A., 1989. Outflow from the gulfs of Aqaba and Suez and the formation of Red Sea deep water. *European Geophysical Society XIV General Assembly*, 13–17 March 1989. Book of Abstracts, Barcelona.
- Murray, S.P., Johns, W.E., 1997. Direct observation of seasonal exchange through the Bab el Mandeb strait. *Geophys. Res. Lett.* 24, 2557–2560.
- Neumann, A.C., McGill, D.A., 1962. Circulation of the Red Sea in early summer. *Deep-Sea Res.* 8, 223–235.
- Ostlund, H.G., Craig, H., Broecker, W.B., Spencer, D., 1987. *Geosecs Atlantic, Pacific and Indian Ocean Expeditions, Shore-based Data and Graphics*, vol. 7. National Science Foundation, Washington, DC.
- Patzert, W.C., 1974. Seasonal reversal in the Red Sea circulation. *L'océanographie Physique de la Mer Rouge* (IAPSO Symposium), vol. 2. Publications du CNEXO, Paris, pp. 55–90.
- Phillips, O.M., 1966. On turbulent convection currents and the circulation of the Red Sea. *Deep-Sea Res.* 13, 1149–1160.
- Quadfasel, D., 2001. Ocean currents: Red Sea. In: Steele, J.H., Thorpe, S.A., Turekian, K.K. (Eds.), *Encyclopedia of Ocean Sciences*. Academic Press, San Diego, pp. 2366–2376.
- Quadfasel, D., Baudner, H., 1993. Gyre-scale circulation cells in the Red Sea. *Oceanol. Acta* 16, 221–229.
- Sofianos, S.S., Johns, W.E., 2003. An Oceanic General Circulation Model (OGCM) investigation of the Red Sea circulation: 2. Three-dimensional circulation in the Red Sea. *J. Geophys. Res.* 108 (C3), 3066 (doi: 10.1029/2001JC001185).
- Sofianos, S.S., Johns, W.E., Murray, S.P., 2002. Heat and freshwater budgets in the Red Sea from direct observations at Bab el Mandeb. *Deep-Sea Res. II* 49, 1323–1340.
- Souvermezoglou, E., Metzl, N., Poisson, A., 1989. Red Sea budgets of salinity, nutrients and carbon calculated in the strait of Bab el Mandeb during the summer and winter seasons. *J. Mar. Res.* 47, 441–456.
- Top, Z., Eismont, W.C., Clarke, W.B., 1987. Helium isotope effect and solubility of helium and neon in distilled water and seawater. *Deep-Sea Res.* 34, 1139–1148.
- Tragou, E., Garrett, C., 1997. The shallow thermocline circulation of the Red Sea. *Deep-Sea Res. I* 44 (8), 1355–1376.
- Woelk, S., Quadfasel, D., 1996. Renewal of deep water in the Red Sea during 1982–1987. *J. Geophys. Res.* 101 (C8), 18155–18165.
- Wyrki, K., 1974. On the deep circulation of the Red Sea. *L'océanographie Physique de la Mer Rouge* (IAPSO Symposium), vol. 2. Publications du CNEXO, Paris, pp. 55–90.



Tracer age symmetry in advective–diffusive flows

Timothy M. Hall^{a,*}, Thomas W.N. Haine^b

^aNASA Goddard Institute for Space Studies, 2880 Broadway, New York, NY 10025, USA

^bJohns Hopkins University, Baltimore, MD, USA

Received 24 September 2002; accepted 17 January 2003

Available online 28 February 2004

Abstract

The “age” of a trace constituent is a common diagnostic of its transport in a geophysical flow. Deleersnijder et al. (Bull. Soc. R. Sci. Liege 70 (2001a) 5) and Beckers et al. (SIAM J. Appl. Math. 61 (2001) 1526) analyzed tracers released from point sources in unbounded advective–diffusive flows with uniform coefficients and noted a surprising feature: the “mean tracer age” (the averaged elapsed time since tracer was injected) is symmetric about the source, despite the directionality of the flow. Although the majority of tracer is swept downstream, the small fraction that diffuses upstream does so at the same average rate. We explore this symmetry physically by examining the random walk trajectories that underlie the advective–diffusive description of transport. Using physical arguments, we show that symmetry in the tracer age field is a natural consequence of symmetry in the velocity and diffusivity fields.

© 2004 Elsevier B.V. All rights reserved.

Keywords: Tracers; Age; Ocean transport; Advection–diffusion

1. Introduction

“Age” is a diagnostic timescale of transport used in geophysical systems as diverse as the ocean, stratosphere, and ground water (e.g., the review of Waugh and Hall, 2002). Common to these systems is the advective–diffusive nature of the transport. Superposed on bulk motions are mixing processes that necessitate a statistical treatment of transport. Not surprisingly, given the widely varying contexts, precise definitions vary. In one usage, age is a property of the tracer itself, and is defined as the elapsed time

since tracer was injected from a source (e.g., Delhez et al., 1999; Deleersnijder et al., 2001b). We refer to this age as “tracer age” to distinguish it from the “transit time” of an irreducible fluid element traveling to the interior from a specified boundary region, a property of the underlying fluid that Deleersnijder et al. (2001b) has called “water age” and is often simply called “age.” As a result of mixing the tracer content of a macroscopic fluid parcel is comprised of a range of tracer ages, just as the parcel’s irreducible fluid elements exhibit a range of transit times.

This note is largely motivated by recent work of Deleersnijder et al. (2001a) and Beckers et al. (2001), who analyzed tracer age in idealized unbounded advective–diffusive flows with uniform velocity and diffusivity. These authors noted the surprising result that the mean tracer age is symmetric about a point

* Corresponding author. Tel.: +1-2128785652; fax: +1-2126785552.

E-mail addresses: thall@giss.nasa.gov (T.M. Hall), Thomas.Haine@jhu.edu (T.W.N. Haine).

source, despite the strong asymmetry in the tracer concentration due to the directionality of the flow. Beckers et al. (2001) also noted the symmetry in numerical models of the North Sea. The symmetry is counterintuitive because one expects that the rate of tracer motion should reflect the relative difficulty of moving against the flow. Here, we present a physical explanation for this symmetry by analyzing the random walks that underlie advective diffusive motion. We also compare and contrast different definitions of “age” in regards to this symmetry.

2. Tracer age

2.1. Definitions

The concept of “age” as a diagnostic of transport is widely used in geophysics (Vaugh and Hall, 2002). However, definitions vary. The most direct definition in terms of tracer is what we call here “tracer age.” Tracer age is defined to be a property of the tracer itself, rather than a property of the underlying fluid. (By contrast, Hall and Plumb, (1994) and Haine and Hall, (2002) define related diagnostics as properties of the fluid, independent of particular tracers.) Each tracer particle (e.g., molecule) is imagined to have a “clock” that is turned on at the time the tracer is injected into the fluid. A macroscopic fluid parcel contains many particles with a distribution of clock times, or “tracer ages.” The tracer age distribution can be characterized by its temporal moments: the zeroeth moment (proportional to the tracer mole fraction), the first moment (the “mean tracer age”), and higher moments (e.g., the variance of tracer age). A tracer age distribution can be defined at each point in the domain. The distribution depends both on the underlying fluid flow and on the sources and sinks of the tracer.

As a concrete example, consider an inert passive tracer injected into an advective–diffusive flow by a point source at \mathbf{r}' with time-dependent source strength $S(\mathbf{r}', t)$ having units of tracer mass per time. At position \mathbf{r} and time t the tracer mole fraction $q(\mathbf{r}, t)$ is comprised of tracer injected at a range of past times. The contribution from the past time interval $t' + \delta t'$ is $S(\mathbf{r}', t')G(\mathbf{r}, t|\mathbf{r}', t')\delta t'$, where $G(\mathbf{r}, t|\mathbf{r}', t')$ is the response at (\mathbf{r}, t) to an injection at \mathbf{r}' at a single past

time t' ; that is, $S(\mathbf{r}', t) = \rho^{-1}\delta(\mathbf{r} - \mathbf{r}')\delta(t - t')$, where ρ is the fluid density. G is the Green’s function that carries tracer from (\mathbf{r}', t) to (\mathbf{r}, t) . The concentration q is the sum of these contributions:

$$q(\mathbf{r}, t) = \int_{-\infty}^t dt' S(\mathbf{r}', t')G(\mathbf{r}, t|\mathbf{r}', t') \quad (1)$$

$$q(\mathbf{r}, t) = \int_0^{\infty} d\xi S(\mathbf{r}', t - \xi)G(\mathbf{r}, t|\mathbf{r}', t - \xi), \quad (2)$$

where $\xi \equiv t - t'$ is the elapsed time since a contribution was injected into the flow, the “tracer age” of the contribution. The fraction of $q(\mathbf{r}, t)$ with tracer age in the interval ξ to $\xi + \delta\xi$ is

$$\begin{aligned} Z(\mathbf{r}, t|\mathbf{r}', t - \xi)\delta\xi \\ = \frac{S(\mathbf{r}', t - \xi)G(\mathbf{r}, t|\mathbf{r}', t - \xi)}{q(\mathbf{r}, t)}\delta\xi, \end{aligned} \quad (3)$$

thereby defining $Z(\mathbf{r}, t|\mathbf{r}', t - \xi)$, the “tracer age distribution.” This formulation is discussed in detail by Holzer and Hall (2000) and for linear tracers is related to the “concentration distribution function,” $c(\mathbf{r}, t|\mathbf{r}', t - \xi)$, of Deleersnijder et al. (2001b) simply by $Z = c/q$. By construction, $\int_0^{\infty} Z d\xi = 1$. The “mean tracer age” is the first moment of this distribution: $A(\mathbf{r}, t, \mathbf{r}') = \int_0^{\infty} \xi Z d\xi$.

We emphasize that Z and A are in general distinct from the “age spectrum,” \mathcal{G} , and “mean age,” Γ , of Hall and Plumb (1994) (also called the “transit time distribution” and “mean transit time,” respectively). \mathcal{G} and its first moment Γ are descriptors of the underlying fluid transport and are independent of the properties of any particular tracer, while Z depends explicitly on the tracer source, as seen in Eq. (3). \mathcal{G} is the distribution of transit times since a fluid parcel made last contact with some specified region, Ω , and Γ is the mean of the distribution. The relationship of Z and A to underlying timescales of the flow and the conditions under which $Z \approx \mathcal{G}$ are laid out by Holzer and Hall (2000). For example, Holzer and Hall (2000) show that for a constant uniform source on a region in a bounded domain $\Gamma(\mathbf{r}) \approx 2(A(\mathbf{r}) - A(\Omega))$. In more general cases there is no such simple relationship. Further contrast and comparison of tracer and fluid age is made in the summary and discussion sections.

2.2. Examples

In order to gain insight to tracer age and illustrate tracer age symmetry in a simple context, we consider the following model: a passive inert tracer injected into an unbounded advective diffusive flow with uniform and constant velocity \mathbf{v} and diffusivity κ . Tracer age in these simple models is also analyzed by [Deleersnijder et al. \(2001b\)](#) and [Beckers et al. \(2001\)](#). The point source is taken to be the origin, and $t' = 0$. The Green's function is

$$G(\mathbf{r}, t) = \left(\frac{1}{\sqrt{4\pi\kappa t}} \right)^n \exp\left(-\frac{|\mathbf{r} - \mathbf{v}t|^2}{4\kappa t} \right), \quad (4)$$

where n is the dimensionality of the flow, and it is assumed that $\rho = 1$, giving G units of L^{-n} . We consider the cases $n = 1$ and $n = 3$ because they permit easy analytic solution.

If the source is $S(t) = s_0$ for $t \geq 0$ and $S(t) = 0$ for $t < 0$, then the steady-state response of the tracer is $q(\mathbf{r}) = \int_0^\infty G(\mathbf{r}, t) dt$. One finds in 3-D

$$q(\mathbf{r}) = \frac{s_0}{4\pi\kappa r} \exp\left(-\frac{(rv - \mathbf{r} \cdot \mathbf{v})}{2\kappa} \right) \quad (5)$$

$$Z(\mathbf{r}, \xi) = \frac{r}{\sqrt{4\pi\kappa\xi^3}} \exp\left(-\frac{(r - v\xi)^2}{4\kappa\xi} \right) \quad (6)$$

and

$$A(\mathbf{r}) = \frac{r}{v} \quad (7)$$

where $r = |\mathbf{r}|$ and $v = |\mathbf{v}|$. In 1-D the solutions are

$$q(x) = \frac{s_0}{v} \exp\left(-\frac{v(|x| - x)}{2\kappa} \right) \quad (8)$$

$$Z(r, \xi) = \frac{v}{\sqrt{4\pi\kappa\xi}} \exp\left(-\frac{(|x| - v\xi)^2}{4\kappa\xi} \right) \quad (9)$$

and

$$A(x) = \frac{|x|}{v} + \frac{2\kappa}{v^2}. \quad (10)$$

(See also [Deleersnijder et al., 2001a,b](#) and [Beckers et al., 2001](#) for these and other related solutions.)

Several features are worth noting. The first point, constituting the main focus of this work, concerns the differences between q on the one hand and Z and A on the other. The concentration, q , is highly asymmetric. For example, in 1-D, tracer completely fills the downstream domain (i.e., $q(x) = 1$ for $x > 0$), while upstream tracer falls as $e^{-|x|v/2\kappa}$. By contrast, both Z and A are symmetric in x . This symmetry, noted by [Beckers et al. \(2001\)](#) in a study of North Sea models and by [Deleersnijder et al. \(2001a\)](#) and [Beckers et al. \(2001\)](#) in the 1-D solutions above, is counterintuitive. One expects that it is harder to move against the flow than with the flow, and therefore it should take longer. One finds, instead, that while only a small fraction of the tracer moves against the flow, this fraction requires no more time to travel an equal distance than the larger fraction moving with the flow. This symmetry is discussed in detail in the next section.

Before addressing the symmetry, however, we also note the qualitative difference between 1-D and 3-D. Tracer completely fills the domain downstream in 1-D; that is, if one waits long enough, $q = 1$ anywhere downstream. This is not the case in 3-D, where even directly downstream $q \ll 1/r$. In 3-D there is too much space to be filled by a point source. In 1-D $A(x)$ is nonzero everywhere, including at the point source. Because of diffusive motion tracer can make an excursion downstream or upstream from the point source and then return to the source, causing $A(0) > 0$. In 3-D, however, there is too much available space, and recirculation back to the origin has infinitesimal influence. (See [Appendix C of Holzer and Hall \(2000\)](#) for a related discussion.)

3. Tracer age symmetry

In order to understand physically the counterintuitive tracer age symmetry we consider a Lagrangian description of transport. Advective–diffusive transport arises from the continuum limit of such a description. Diffusion represents the aggregate effect of random motions of particles. Advection is the net drift of particles in a direction of preferred probability for individual particle steps.

For simplicity, we consider particles that move in discrete steps of unit magnitude every time step δt , selecting randomly among the six possible directions $\pm \hat{x}$, $\pm \hat{y}$, and $\pm \hat{z}$ in a 3-D rectilinear lattice; that is, the single step probability density function (pdf) consists of six spikes, one for each direction. Take the direction of the macroscopic velocity to be $+\hat{x}$. Particles are more likely to take $+\hat{x}$ steps than $-\hat{x}$ steps (i.e., the $+\hat{x}$ spike of the pdf has greater magnitude). Steps in $\pm \hat{y}$, and $\pm \hat{z}$ all have equal probability. Step probabilities are assumed to be spatially uniform, resulting in uniform macroscopic velocity and diffusivity. Because volume elements have unit magnitude, the particle concentration at $\mathbf{r}=(x, y, z)$ is equal to the particle number at \mathbf{r} . The mean tracer age, $A(\mathbf{r})$, is the average over the particles at \mathbf{r} of the elapsed times since they were injected at a source, which we take to be a point source at $\mathbf{r}'=(x', y', z')$ of magnitude $S(\mathbf{r}', t)$ (particle number per time).

Clearly q , Z , and A are symmetric in y and z , since there is no preferred direction in this plane. However, it may seem surprising that Z and A are symmetric in x , despite the directionality of the velocity (i.e., the preferred single step probability). Our physical argument for the symmetry requires two ingredients: (1) For each sequence of particle steps (a “trajectory”) connecting \mathbf{r}' to \mathbf{r} there is a “reflection” trajectory connecting \mathbf{r}' to $-\mathbf{r}$. The reflection is obtained by reversing the sign of all the steps. The existence of a reflection requires that the probability for a step in an opposite direction be nonzero, although it can be arbitrarily close to zero. (For example, the limit of small probability of a $-\hat{x}$ step is the limit of small x diffusion. The tracer age is still symmetric in x , but it is realized by a vanishingly small amount of tracer at points $x < x'$.) (2) The steps comprising a trajectory are statistically independent. In the argument that follows this independence allows us to reorder a step sequence with no impact on its overall probability. Note that if steps were not statistically independent, but instead had a finite decorrelation time, one could accumulate a sequence of steps over the decorrelation time and consider the net displacement of the accumulation as the fundamental step.

Consider a sequence of n steps w_1, \dots, w_n forming a trajectory W from \mathbf{r}' to \mathbf{r} . If $p(w_j)$ is the probability of the j th step, then $P(W)=p(w_1) \cdots p(w_n)$ is the

probability that trajectory W is sampled by a particle. Now, in every trajectory there must be a subset of steps that, when taken in sequence, forms a “sub-trajectory” directly from \mathbf{r}' to \mathbf{r} . The remaining set of steps form a sub-trajectory of zero net displacement. We consider the reordered sequence

$$W = \overbrace{w_1, \dots, w_{n-m}}^{\mathbf{r}' \rightarrow \mathbf{r}'} \overbrace{w_{n-m+1}, \dots, w_n}^{\mathbf{r}' \rightarrow \mathbf{r}} \quad (11)$$

where $R \equiv w_1, \dots, w_{n-m}$ is a “recirculation sub-trajectory” of zero net displacement and step number $n-m$, and $D \equiv w_{n-m+1}, \dots, w_n$ goes directly to \mathbf{r} in the minimum number of steps $m=|x|/\delta x$. Because of the statistical independence of steps the reordering does not affect the overall probability of W , and so $P(W)=P(R)P(D)$.

Each permutation of steps in Eq. (11) is also a trajectory from \mathbf{r}' to \mathbf{r} and has the same probability. To obtain the full probability, P , of traveling from \mathbf{r}' to \mathbf{r} in n steps, $P(W)$ must be multiplied by a factor $B(n,m)$, the number of distinct permutations of n steps that result in a net m steps in one direction. That is,

$$P = B(n,m)P(R)P(D). \quad (12)$$

$P(D)$ depends on both the magnitude of $\mathbf{r}-\mathbf{r}'$ (a longer sequence of steps is required to reach a greater $|\mathbf{r}-\mathbf{r}'|$) and its direction (steps against the flow are less likely than steps with the flow). However, $P(D)$ does not depend on the total step number n or, equivalently, on the total duration of the trajectory $n\delta t$, as long as $m \geq n$. Every trajectory to \mathbf{r} must have the sub-trajectory D , regardless of the total step number. The additional steps affect $P(R)$ but not $P(D)$.

The expected number of particles q at \mathbf{r} is the sum of the probabilities of all trajectories to \mathbf{r} of all step numbers n (equivalently, durations $n\delta t$) multiplied by the particle number, $S(\mathbf{r}', t-n\delta t)\delta t$, emitted at the time the trajectory started at \mathbf{r}' . That is,

$$q(\mathbf{r}, t) = \sum_{n=m}^{\infty} S(\mathbf{r}', t-n\delta t)\delta t B(n,m)P(R)P(D) \quad (13)$$

(Note that, compared to Section 2, q and S here have units of particle number and particle number per time, respectively.) The quantity $S(\mathbf{r}', t-n\delta t)B(n,m)$

$P(R)P(D)\delta t$ is the number of particles that took time $n\delta t$ to travel \mathbf{r}' to \mathbf{r} . Therefore, the tracer age distribution, following Eq. (3), is

$$Z(\mathbf{r}, t) = \frac{S(\mathbf{r}', t - n\delta t)B(n, m)P(R)P(D)}{\sum_{n=m}^{\infty} \delta t S(\mathbf{r}', t - n\delta t)B(n, m)P(R)P(D)}. \quad (14)$$

We now exploit the fact that $P(D)$ does not depend on the length of a trajectory by moving it outside the summation, leaving

$$Z(\mathbf{r}, t) = \frac{S(\mathbf{r}', t - n\delta t)B(n, m)P(R)}{\sum_{n=m}^{\infty} \delta t S(\mathbf{r}', t - n\delta t)B(n, m)P(R)}. \quad (15)$$

None of the factors in Eq. (15) depends on the direction from the point source at \mathbf{r}' . Because the velocity and diffusivity are assumed uniform, the probability of a trajectory of zero net displacement, $P(R)$, is actually independent of position. $B(n, m)$ is the number of trajectories that go \mathbf{r} to \mathbf{r} , and depends on $|\mathbf{r} - \mathbf{r}'|$ through the step number m , but not on the direction. Therefore Z is symmetric, as are all its temporal moments, including the mean tracer age A .

Let us summarize the essence of the tracer age symmetry. Every trajectory from \mathbf{r}' to \mathbf{r} has a reflection to $-\mathbf{r}$, formed by reversing all the steps. If single step probabilities are spatially uniform (equivalent to uniform velocity and diffusivity) and the steps are statistically independent, then the sequence of steps in a trajectory can be reordered with no impact on the trajectory's total probability. One such reordering results in a recirculation sub-trajectory about \mathbf{r}' of zero net displacement (same number of steps in all directions) followed by a direct flight to \mathbf{r} . But the recirculation is the same for the trajectory and its reflection. The difference in the trajectory probabilities comes only from the difference in probabilities of the direct flights. These direct flight probabilities do not depend on the overall trajectory duration, and thus the difference in probability of a trajectory and its reflection does not depend on the duration. In other words, the distributions by trajectory duration of trajectory probabilities to \mathbf{r} and $-\mathbf{r}$ differ by a single scaling factor, the

difference in direct flight probability to \mathbf{r} and $-\mathbf{r}$. Upon dividing by the particle number to obtain Z , the distribution among the particles present, the distribution and its reflection become identical.

3.1. One-dimensional examples

We now illustrate these arguments in a 1-D example. Consider steps of equal magnitude δx every time step δt , with a probability p of a positive step and a probability $q = 1 - p$ of a negative step; that is, a single step probability distribution function (pdf) consisting of spikes of unequal magnitude at ± 1 . (The macroscopic transport coefficients are related to the randomwalk parameters by $u = (p - q)\delta x/\delta t$ and $k = pq\delta x^2/\delta t$.) To arrive at $x > 0$ there must be $m = x/\delta x$ more positive steps than negative. Because of the statistical independence of steps, the probability of any trajectory to x in time $\xi = n\delta t$, where n is the total step number, can be written

$$P(x, \xi) = p^m p^{\frac{1}{2}(n-m)} q^{\frac{1}{2}(n-m)} \quad (16)$$

The probability for the reflection trajectory is obtained by reversing all the steps; that is, by interchanging p and q in Eq. (16):

$$P(-x, \xi) = q^m q^{\frac{1}{2}(n-m)} p^{\frac{1}{2}(n-m)} \quad (17)$$

All other trajectories of duration ξ to x and $-x$ are permutations of Eqs. (16) and (17). Note that the ratio

$$\frac{P(-x, \xi)}{P(x, \xi)} = \left(\frac{q}{p}\right)^m = \left(\frac{q}{p}\right)^{|x|/\delta x} \quad (18)$$

does not depend on ξ . Thus, the distributions by ξ of trajectory probabilities differ by the constant scaling factor $(q/p)^{|x|/\delta x}$, and Z is symmetric in x . That is,

$$Z(x, \xi) = \frac{S(t - \xi)B(n, m)p^{\frac{1}{2}(n-m)}q^{\frac{1}{2}(n-m)}}{\sum_{n=m}^{\infty} \delta t S(t - \xi)B(n, m)p^{\frac{1}{2}(n-m)}q^{\frac{1}{2}(n-m)}} \quad (19)$$

is invariant under exchange of p and q . (Here, $B(n, m) = n!/(1/2(n - m)!1/2(n + m)!)$ is the number of

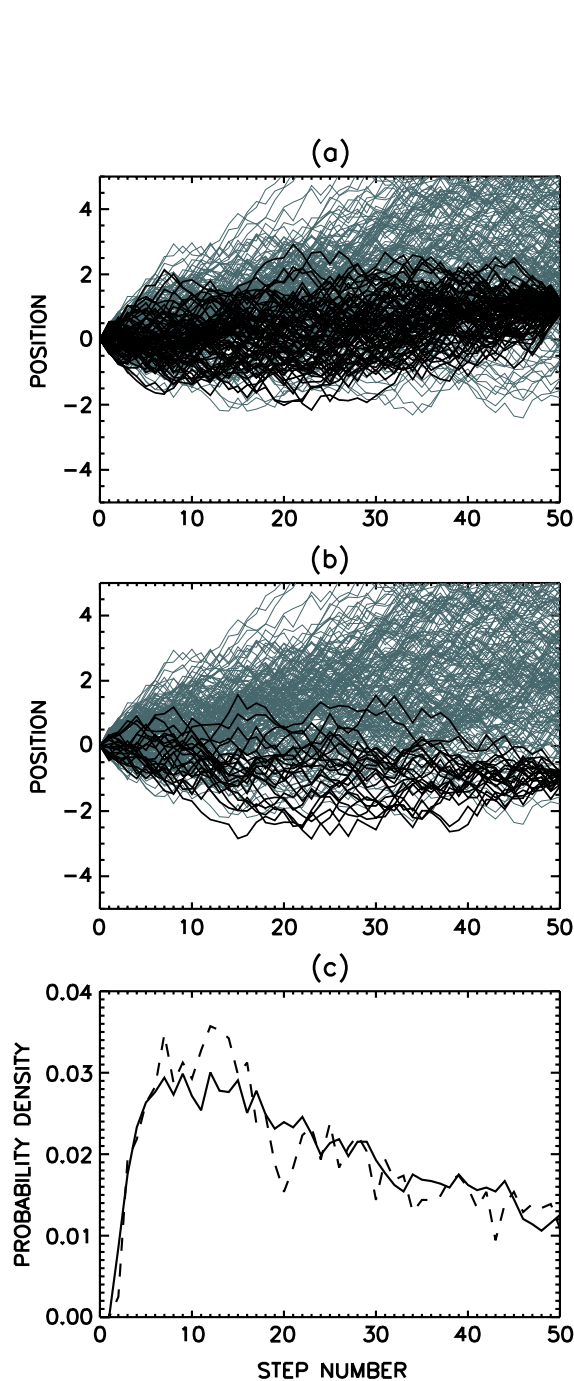


Fig. 1. Position versus step number of 1000 trajectories starting at the origin. (a) All trajectories (gray) and those that end at $x = +1 \pm 0.25$ (black). (b) All trajectories (gray) and those that end at $x = -1 \pm 0.25$ (black). (c) Tracer age distributions at $x = +1$ (solid) and $x = -1$ (dashed).

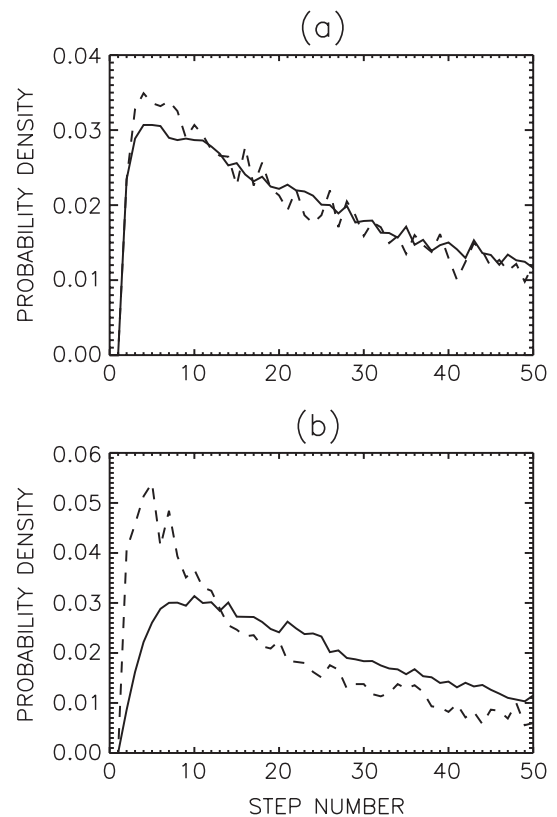


Fig. 2. Tracer age distributions at $x = +1$ (solid) and $x = -1$ (dashed) for 5000 trajectories. (a) The width of the single step pdf increases symmetrically with distance from the origin. (b) The width of the single step pdf is constant downstream but increases upstream with distance from the origin.

distinct permutations of n total steps with a net m either positive or negative.)

As an additional 1-D random walk example that relaxes the earlier restriction to quantized steps in x , consider the following: At each time step 1000 particles are given a random displacement according to a single step pdf that is equal to unity for $-0.45 < \delta x < +0.55$ and zero otherwise. Fig. 1a and b shows trajectories after 50 time steps. Also shown among all the trajectories in Fig. 1a are the subset that reach $x = 1 \pm 0.25$. Fig. 1b shows those that reach $x = -1 \pm 0.25$. More particles follow trajectories reaching $+1$ than -1 , because of the preferred direction for single steps. We now form the tracer age distributions, $Z(x, \xi)$, at $x = +1$ and $x = -1$ by binning the number of particles at these positions

according to their step number at arrival, then dividing by the total number reaching the locations. These Z , shown in Fig. 1c, are symmetric, discounting statistical fluctuations.

The symmetry of $Z(x, t)$ in the example above reflects the uniformity of the transport coefficients, expressed as velocity u and diffusivity κ macroscopically and by the single step pdf microscopically. More generally, u and κ (and the single step pdfs) need not be uniform, but merely symmetric, to result in symmetric $Z(x, \xi)$. Fig. 2a shows Z at $x = \pm 1$ resulting from a random walk with the single step pdf of Fig. 1, except that now the pdf width increases symmetrically with distance from the origin according to $1 + 3(1 - e^{-|x|})$. The symmetry of Z in x is preserved. By contrast, when the width increases upstream but remains uniform downstream, Z is asymmetric, as shown in Fig. 2b.

4. Summary and discussion

Deleersnijder et al. (2001a) and Beckers et al. (2001) noted a counterintuitive symmetry in the “age” of a tracer released from a point source in an advective–diffusive flow with uniform coefficients. We have explained this symmetry physically by analyzing random walks with statistically independent steps, a description that underlies advective–diffusive transport. Every trajectory from a source \mathbf{r}' to \mathbf{r} has a reflection to $-\mathbf{r}$. The step sequence in a trajectory and its reflection can be reordered with no effect on the probability of being sampled by a particle. One such reordering results in a recirculation about \mathbf{r}' of zero net displacement followed by a direct flight from \mathbf{r}' to \mathbf{r} . But the recirculation is the same for the trajectory and its reflection. The difference in the trajectory probabilities comes only from the difference in probability of the direct flights. These direct flight probabilities do not depend on the overall trajectory duration (transit time), and thus the difference in probability of a trajectory and its reflection does not depend on the transit time. Therefore, the normalized distributions of transit times to \mathbf{r} and $-\mathbf{r}$ are identical.

It is worthwhile contrasting the symmetry properties of two different definitions of “age.” The age symmetry of Deleersnijder et al. (2001a) and Beckers

et al. (2001) arises in the case where age is considered to be a property of the tracer itself—what we have called “tracer age”. In an alternate use of the term “age,” the symmetry does not arise. It is common in ocean tracer studies to consider the age to be a property of a water mass. One speaks of the elapsed time (or distribution of times) since a water mass was last at the ocean surface (e.g., England, 1995; Beining and Roether, 1996). (For clarity, we have referred to the “transit times” for irreducible fluid elements to travel from a specified boundary region to the interior, although simply “age” is common.) Observable tracers allow an estimation of the transit time distribution and its moments to varying degrees, depending on the tracer and the flow conditions (Waugh et al., 2003).

To make explicit, the different symmetry properties of these timescales consider an unbounded 1-D advective–diffusive system with uniform coefficients, the system analyzed by Deleersnijder et al. (2001a). The transit time of an irreducible fluid element is the time since it was last at the origin. Note the distinction: transit time is always zero at the origin, whereas tracer age is generally nonzero at the origin. In the simplest case of a tracer having a constant source, the mean tracer age $A(x)$ downstream is given by expression (10), whereas the mean transit time (also known as the “mean age” and the “ideal age”) is $\Gamma(x) = x/u$. In this idealized case the two timescales are related simply: $\Gamma(x) = A(x) - A(0)$. (Contrast this with the relationship noted in Section 2.1 for a conservative tracer with constant source in a bounded domain.)

We now ask what is the mean transit time upstream? One could attempt to construct the transit time distribution \mathcal{G} (also known as the age spectrum) following Hall and Plumb (1994) by computing the response to a $\delta(t)$ boundary condition at $x=0$ and looking at positive x with $u < 0$; i.e., the fluid flow running toward the origin from the parcel location. This yields

$$\mathcal{G}(x, \xi) = \frac{x}{\sqrt{4\pi k \xi^3}} e^{-(x+u\xi)^2/4k\xi} \quad (20)$$

However, one finds that $\int_0^\infty \mathcal{G} d\xi = e^{-2xu/k} < 1$. Unlike the case downstream, where $\int_0^\infty \mathcal{G} d\xi = 1$, the upstream transit time distribution is not normalized. A fraction of the fluid parcel that increases exponentially with x has never been at the origin. The mean transit time

solely among the fluid fraction that has been at the origin is $\int_0^\infty \xi \mathcal{G} d\xi / \int_0^\infty \mathcal{G} d\xi = x/u$, identical to the downstream solution. But over the entire fluid parcel the mean transit time since last contact with the origin is infinite, since much of the parcel has never been at the origin. It is therefore not symmetric. A second approach is to consider the steady-state solution to the equation for the ideal age, τ_{id} , which downstream is equivalent to the mean transit time (e.g., [Khatiwala et al., 2001](#)):

$$\frac{\partial \tau_{id}}{\partial t} - u \frac{\partial \tau_{id}}{\partial x} - k \frac{\partial^2 \tau_{id}}{\partial x^2} = 1 \quad (21)$$

with $\tau_{id}(0, t) = 0$. In steady-state, one finds $\tau_{id} = -x/u$, again not symmetric about $x=0$. A negative timescale upstream to describe the elapsed time since the fluid made contact with $x=0$ is as plausible as an infinite timescale: most of the upstream fluid has never been at the origin but will make contact with the origin at a future time; that is, a negative elapsed time. We conclude that upstream in an unbounded domain the mean transit time is either infinite or negative, depending on definition, but in any case is not equal to the downstream value. Eric Deleersnijder (personal communications) has recently confirmed the asymmetry of the ideal age (also known as the “water age”), extending the analysis to include the transient solution.

It is perhaps not surprising that transport timescales should have peculiar properties in an open domain (unbounded in some direction), given the continuous and unlimited source of new fluid from upstream. Although an open approximation may be useful in certain instances, all geophysical domains are ultimately closed; that is, the fluid has finite mass. This has considerable bearing on the transport timescales discussed here. Given a constant source applied on some boundary region and no sink, the tracer concentration and mean tracer age will eventually increase everywhere linearly in time if the domain is closed. This is in contrast to the steady-state tracer age in the open 1-D domain, where escape from the domain acts as an effective sink for any finite sub-domain. On the other hand, the mean transit time reaches a finite steady state even in a bounded domain, if the circulation is

stationary. Sufficiently far enough back in time, all fluid elements have made boundary contact.

Finally, we note that in a closed domain streamlines of the flow are closed. While “upstream” and “downstream” may be meaningful locally, the mean transit time upstream is not determined locally, but is rather set by the remote boundaries that cause streamlines to close. In closed domains, the mean transit time is not symmetric. Downstream, parcels are dominated by fluid that made recent boundary contact and are therefore young. In contrast, upstream parcels may have had only weak diffusive contact locally with the boundary region. The majority of their fluid elements have circulated about streamlines that may span much of the domain, and the parcels are therefore much older.

Acknowledgements

We thank Eric Deleersnijder for detailed discussions and correspondences on tracer age. This work was supported by grant OCE-9911598 from the Physical Oceanography Program of the National Science Foundation.

References

- Beckers, J.M., Delhez, E.J.M., Deleersnijder, E., 2001. Some properties of generalized agedistribution equations in fluid dynamics. *SIAM J. Appl. Math.* 61, 1526–1544.
- Beining, P., Roether, W., 1996. Temporal evolution of CFC 11 and CFC 12 concentrations in the ocean interior. *J. Geophys. Res.*, 101, 16, 455–16, 464.
- Deleersnijder, E., Delhez, J.M., Crucifix, M., Beckers, J.M., 2001a. On the symmetry of the age field of a passive tracer released into a one-dimensional fluid flow by a point source. *Bull. Soc. R. Sci. Liege* 70, 5–21.
- Deleersnijder, E., Campin, J.M., Delhez, E.J.M., 2001b. The concept of age in marine modelling: I. Theory and preliminary model results. *J. Mar. Syst.* 28, 229–267.
- Delhez, E.J.M., Campin, J.M., Hirst, A.C., Deleersnijder, E., 1999. Toward a general theory of age in ocean modelling. *Ocean Model.* 1, 17–27.
- England, M.H., 1995. The age of water and ventilation timescales in a global ocean model. *J. Phys. Oceanogr.* 25, 2756–2777.
- Haine, T.W.N., Hall, T.M., 2002. A generalized transport theory: water mass composition and age. *J. Phys. Oceanogr.* 32, 1932–1946.

- Hall, T.M., Plumb, R.A., 1994. Age as a diagnostic of stratospheric transport. *J. Geophys. Res.* 99, 1059–1070.
- Holzer, M., Hall, T.M., 2000. Transit-time and tracer-age distributions in geophysical flows. *J. Atmos. Sci.* 57, 3539–3558.
- Khatiwala, S., Visbeck, M., Schlosser, P., 2001. Age tracers in an ocean tracer GCM. *Deep-Sea Res.* 48A, 1423–1441.
- Waugh, D.W., Hall, T.M., 2002. Age of stratospheric air: theory, observations, and models. *Rev. Geophys.* 40 (doi: 10.1029/2000RG000101).
- Waugh, D.W., Hall, T.M., Haine, T.W.N., 2003. Relationships among tracer ages. *J. Geophys. Res.* 108 (doi:10.1029/2002JC001325).



Symmetry and asymmetry of water ages in a one-dimensional flow

Eric Deleersnijder^{a,*}, Eric J.M. Delhez^b

^a*Institut d'astronomie et de Géophysique G. Lemaître, Université catholique de Louvain, 2 Chemin du Cyclotron, B-1348 Louvain-la-Neuve, Belgium*

^b*Modélisation et Méthodes Mathématiques, Département ASMA, Université de Liège, Sart Tilman B37, B-4000 Liege, Belgium*

Received 29 November 2002; received in revised form 27 May 2003; accepted 9 July 2003

Available online 17 March 2004

Abstract

Hall and Haine [J. Mar. Syst., in press] briefly addressed the problem of estimating the age of irreducible fluid elements or water parcels in a one-dimensional flow with constant velocity and diffusivity. Herein further developments are achieved on this subject. The age of every water parcel is set to zero at the moment it passes through the point $x=0$, where x is an appropriate space coordinate. As time progresses, the age of the water is seen to increase unboundedly upstream of the point $x=0$, and tend to the steady-state value $|x/u|$ downstream of the point $x=0$, where u is the water velocity. By contrast, the age of the water parcels that have touched at least once the point $x=0$ is symmetric with respect to the point $x=0$ is smaller than the water age at any time and position, and tends to $|x/u|$ as time progresses. Asymptotic expansions are derived for large times.

© 2004 Elsevier B.V. All rights reserved.

Keywords: Age; Age of seawater; Ageing; Tracer

1. Introduction

Age is a diagnostic used for understanding complex geophysical flows (e.g., England, 1995; Campin et al., 1999; Hirst, 1999; Khatiwala et al., 2001; Deleersnijder et al., 2001a, 2002; Delhez and Deleersnijder, 2002; Delhez et al., 2003; Waugh and Hall, 2002; Waugh et al., in press). However, as age is the solution of a rather elaborate partial differential problem (e.g., Delhez et al., 1999, Holzer and Hall, 2000), it is also appropriate to evaluate the age in simple, idealised flows, so as to gain insight into the functioning of the

“age machinery”. This is why studies were achieved of the age of a tracer released by a point source into an infinite domain with constant velocity and diffusivity. It was found that the age is symmetric with respect to the point source (Beckers et al., 2001; Deleersnijder et al., 2001b; Hall and Haine, in press). To date, the best explanation of this rather counterintuitive property is the one given by Hall and Haine (in press), who resorted to an elegant Lagrangian approach.

Hall and Haine (in press) also briefly addressed the problem of calculating the age of irreducible fluid elements in a one-dimensional flow. At the initial time, the age of all fluid elements was assumed to be zero. The age of every fluid element increased at the same rate as time progressed, and was reset to zero every time the fluid element under consideration would pass through the point $x=0$, where x is an appropriate space

* Corresponding author. Tel.: +32-10-47-26-76; fax: +32-10-47-47-22.

E-mail addresses: ericd@astr.ucl.ac.be (E. Deleersnijder), e.delhez@ulg.ac.be (E.J.M. Delhez).

coordinate. The mean age of fluid elements contained in an arbitrarily small water sample taken at location x was seen to be unequal to the age in a water sample taken at the same time at location $-x$. Every water sample consists of fluid elements which have not yet touched the point $x=0$, and those which have passed at least once through $x=0$. The latter make up a distinct water mass, which is different from the water as such. Hall and Haine (in press) mentioned that the age of this particular water mass, unlike the water age, is symmetric with respect to point $x=0$.

Hall and Haine's (in press) concept of "irreducible fluid element" is equivalent to that of "water parcel" in the Constituent-oriented Age Theory (CAT) of Delhez et al. (1999) and Deleersnijder et al. (2001a). CAT is well suited to investigate the age of tracers (e.g., Delhez and Deleersnijder, 2002; Delhez et al., 2003) as well as that of water masses (Hirst, 1999; Deleersnijder et al., 2002). The objective of the present study is to investigate in some detail the behaviour of the two water ages considered by Hall and Haine (in press). First, in Section 2, the Eulerian equations of the problem are set. Then, their solutions are established, including asymptotic expansions for large times (Section 3).

2. Model equations

Consider a one-dimensional water flow with constant velocity u (>0) and diffusivity κ (>0) in the domain $-\infty < x < \infty$. At any time $t > 0$ and position, the age $a(t, x)$ of a passive- or inert-tracer is given by (e.g., Delhez et al., 1999; Deleersnijder et al., 2001a)

$$a(t, x) = \frac{\alpha(t, x)}{C(t, x)}, \quad (1)$$

where α and C denote the age concentration and the concentration of the tracer under study, respectively. The latter satisfy the following equations

$$\frac{\partial C}{\partial t} + u \frac{\partial C}{\partial x} = \kappa \frac{\partial^2 C}{\partial x^2}, \quad (2)$$

$$\frac{\partial \alpha}{\partial t} + u \frac{\partial \alpha}{\partial x} = C + \kappa \frac{\partial^2 \alpha}{\partial x^2}. \quad (3)$$

The concentration is a dimensionless mass fraction, which is generally much smaller than unity, except the

concentration of the water which is almost equal to 1 (Fig. 1).

It is convenient to introduce dimensionless variables (Table 1). As in Deleersnijder et al. (2001b), the time and space scales are taken to be $4\kappa/u^2$ and $4\kappa/u$, respectively. After the introduction of the dimensionless variables, it is readily seen that relation (1) is left unchanged, while Eqs. (2) Eqs. (3) transform to

$$\frac{\partial C}{\partial t} + \frac{\partial C}{\partial x} = \frac{1}{4} \frac{\partial^2 C}{\partial x^2}, \quad (4)$$

$$\frac{\partial \alpha}{\partial t} + \frac{\partial \alpha}{\partial x} = C + \frac{1}{4} \frac{\partial^2 \alpha}{\partial x^2}. \quad (5)$$

The concentration of the water being equal to 1, the age of the water $a_w(t, x)$ obeys equation

$$\frac{\partial a_w}{\partial t} + \frac{\partial a_w}{\partial x} = 1 + \frac{1}{4} \frac{\partial^2 a_w}{\partial x^2}, \quad (6)$$

which is equivalent to Hall and Haine's (in press) equation for the ideal age. On the other hand, the water parcels that have touched at least once the point $x=0$ can also be considered. The set of these water parcels bears similarities with the "surface water" studied in Deleersnijder et al. (2001a, 2002). The fraction $C_m(t, x)$ of such "marked" water parcels in water sample taken at time t and location x obeys the equation

$$\frac{\partial C_m}{\partial t} + \frac{\partial C_m}{\partial x} = \frac{1}{4} \frac{\partial^2 C_m}{\partial x^2}. \quad (7)$$

The age concentration $\alpha_m(t, x)$ of the marked particles, which will be regarded as a "water mass" created at $x=0$, satisfies

$$\frac{\partial \alpha_m}{\partial t} + \frac{\partial \alpha_m}{\partial x} = C_m + \frac{1}{4} \frac{\partial^2 \alpha_m}{\partial x^2}. \quad (8)$$

Then, the mean age of the water mass under study is $a_m(t, x) = \alpha_m(t, x)/C_m(t, x)$. No variable is allowed

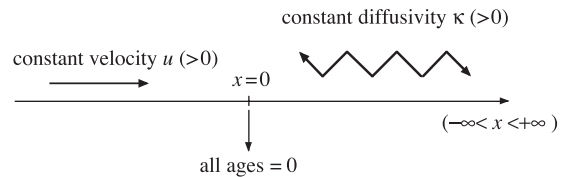


Fig. 1. Schematic representation of the characteristics of the flow in which water ages are estimated.

Table 1
Definition of the dimensionless variables used from Eq. (4) onwards

Original variable	Dimensionless variable
t	$t' = t/(4\kappa/u^2)$
x	$x' = x/(4\kappa/u)$
a_w	$a'_w = a_w/(4\kappa/u^2)$
C_m	$C'_m = C_m$
α_m	$\alpha'_m = \alpha_m/(4\kappa/u^2)$
a_m	$a'_m = [a_m/(4\kappa/u^2)] = (\alpha'_m / C'_m)$

The prime symbols are systematically omitted.

to grow exponentially in the limit $|x| \rightarrow \infty$. All variables are zero at $t=0$. The water age and the age concentration of the water mass are prescribed to be zero at $x=0$. For the concentration C_m to actually represent the fraction of the water parcels that have touched at least once the point $x=0$, it is necessary that the boundary condition $C_m(t, x=0)$ be applied.

By manipulating Eqs. (6)–(8), it may be seen that the age of the water and that of the water mass satisfy

$$a_w = a_m + (t - a_m)(1 - C_m). \quad (9)$$

This relation is similar to that established in Deleersnijder et al. (2002) for the age of the water and the age of the surface water in the World Ocean. Lagrangian arguments similar to those of Deleersnijder et al. (2002) may also be invoked to obtain Eq. (9). At any time and location, the age of the water mass that has already touched $x=0$, and its concentration are no larger than t and 1, respectively. Therefore, Eq. (9) implies that the age of the water is larger than or equal to that of the water mass under study.

3. Solution and discussion

The temporal Laplace transform of governing Eqs. (6)–(8) is evaluated, leading to ordinary differential equations involving x -derivatives only. Next, taking into account the initial and boundary conditions, the ordinary differential equations are easily solved. Finally, using a standard table of Laplace transforms, the solutions to Eqs. (6)–(8) are obtained:

$$a_w = t(1 - e^{2x}I_{3/2}) + e^{2x}I_{1/2}, \quad (10)$$

$$C_m = e^{2x}I_{3/2}, \quad (11)$$

$$\alpha_m = e^{2x}I_{1/2}, \quad (12)$$

with

$$I_\beta(t, x) = \frac{|x|}{\pi^{1/2}} \int_0^t \theta^{-\beta} e^{-\theta-x^2/\theta} d\theta. \quad (13)$$

The age of the water mass under study is

$$a_m = \frac{I_{1/2}}{I_{3/2}} \frac{\int_0^t \theta^{-1/2} e^{-\theta-x^2/\theta} d\theta}{\int_0^t \theta^{-3/2} e^{-\theta-x^2/\theta} d\theta}. \quad (14)$$

The solutions above satisfy relation (9). Clearly, the age of the water is not symmetric with respect to point $x=0$, whereas the water mass age is (Fig. 2), i.e.,

$$a_w(t, x) \neq a_w(t, -x) \quad (15)$$

and

$$a_m(t, x) = a_m(t, -x). \quad (16)$$

For $\beta = 1/2$ and $\beta = 3/2$, the integral (13) behaves as

$$I_{1/2}(t, x) \sim |x| e^{-2|x|} - \frac{|x| e^{-t-x^2/t}}{\pi^{1/2} t^{1/2}} \quad (17)$$

$$I_{3/2}(t, x) \sim e^{-2|x|} - \frac{|x| e^{-t-x^2/t}}{\pi^{1/2} t^{3/2}}, \quad (18)$$

if $t \rightarrow \infty$ and $|x|/t \rightarrow 0$ (Appendix A). Accordingly, the asymptotic behaviour for large times of the age of the water, the concentration of the water mass that has

Table 2

Dominant terms of the asymptotic expansions for $t \rightarrow \infty$ and $|x|/t \rightarrow 0$ of the age of the water a_w , the concentration C_m of the water parcels having touched at least once the point $x=0$, and the mean age of this water mass a_m

	$x < 0$	$x > 0$
$a_w(t, x)$	$(1 - e^{-4 x t})$	x
$C_m(t, x)$	$e^{-4 x }$	1
$a_m(t, x)$	$ x $	x

Variables are in their dimensionless form (see Table 1).

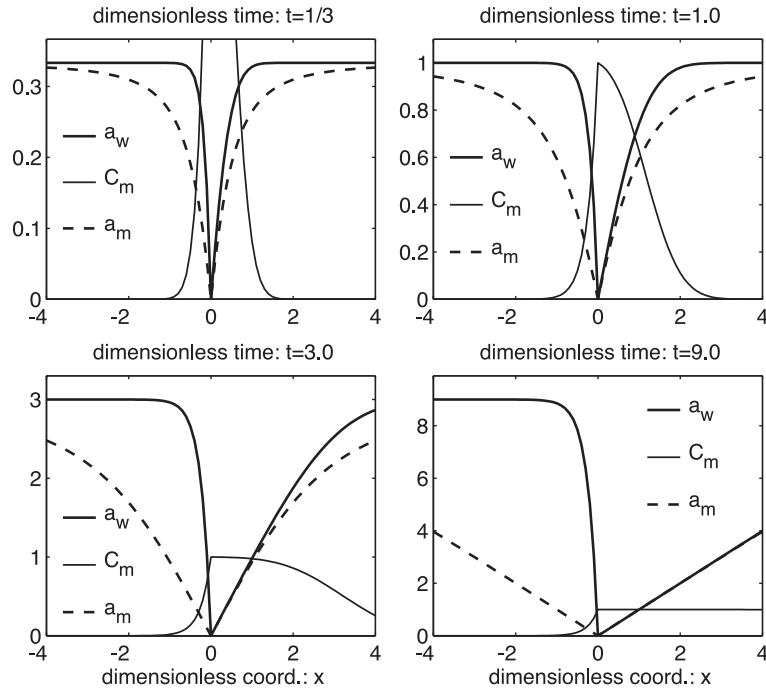


Fig. 2. Graphical representation at time $t=1/3$, $t=1$, $t=3$ and $t=9$ of the age of the water a_w (thick solid curve), the concentration C_m of the water parcels having touched at least once the point $x=0$ (thin solid curve), and the mean age of this water mass a_m (dashed curve). Variables are their dimensionless form (see Table 1).

touched at least once the point $x=0$ and the age of this water mass are

$$a_w(t, x) \sim (1 - e^{2x-2|x|})t + |x|e^{2x-2|x|}, \quad (19)$$

$$C_m(t, x) \sim e^{2x-2|x|} + \frac{|x|e^{-(x-t)^2/t}}{\pi^{1/2}t^{3/2}}, \quad (20)$$

$$a_m(t, x) \sim |x| - \frac{|x|e^{-(|x|-t)^2/t}}{\pi^{1/2}t^{1/2}}. \quad (21)$$

Upstream and downstream of the point $x=0$, these expansions exhibit significant differences (Table 2). The age of the water and that of the water mass tend to x for $x>0$, which corresponds to x/u in dimensional variables. However, in the region $x<0$, the age of the water mass tends to $|x|$ —i.e., $|x/u|$ in dimensional variables—while the water age grows unboundedly as t .

Downstream of the point $x=0$, the fraction C_m of the water parcels that have touched at least once the point $x=0$ tends to 1 as time progresses. Therefore, in the region $x>0$, the age of the water and that of the water mass under study must tend to the same limit, which, in accordance with elementary intuition, is x/u in dimensional form. Nonetheless, upstream of the point $x=0$, the larger the distance to this point, the larger the fraction of the water parcels that have not yet touched the point $x=0$ —since there is an infinite reservoir of such water parcels upstream of $x=0$, the domain of interest being infinite. This is why the age of the water tends to be equal to the time that has elapsed since the age of all water parcels was set equal to zero. By contrast, the age of the water mass that has touched at least once the point $x=0$ tends to a value that is independent of the instant at which the age of all water parcels was initialised to zero. This points to a certain ill-foundedness of the concept of water age for an unbounded domain (Hall and Haine, in press), a problem which is unlikely to

arise if the volume of the domain of interest is finite (e.g., England, 1995; Deleersnijder et al., 2002).

Obviously, for any physically relevant problem, the domain of interest is not infinite. However, the infinite-domain solutions discussed herein are believed to be a good approximation of those obtained in a finite domain, provided the latter are considered in the vicinity of the point at which the ages are prescribed to be zero and over a period of time sufficiently smaller than the timescales related to advection and diffusion over length scales comparable to the size of the domain of interest. A relevant illustration thereof is the age symmetry depicted in Fig. 1 of Beckers et al. (2001), which is obtained from a numerical model of the North Sea. A future study will focus on the time evolution of various ages in a Munk loop (Munk, 1966; Hall and Holzer, 2003), with an emphasis on the analysis of the sensitivity of the solutions to the length of the loop.

Acknowledgements

E. Deleersnijder is a Research associate with the Belgian National Fund for Scientific Research (FNRS). The authors are indebted to A. Mouchet for the useful comments she provided.

Appendix A

The integral defined by relation (10) may be regarded as the following sum:

$$I_{\beta}(t, x) = I_{\beta}(\infty, x) - \tilde{I}_{\beta}(t, x), \tag{A.1}$$

with

$$I_{\beta}(\infty, x) = \frac{|x|}{\pi^{1/2}} \int_0^{\infty} \theta^{-\beta} e^{-\theta - x^2/\theta} d\theta \tag{A.2}$$

and

$$\tilde{I}_{\beta}(\infty, x) = \frac{|x|}{\pi^{1/2}} \int_t^{\infty} \theta^{-\beta} e^{-\theta - x^2/\theta} d\theta. \tag{A.3}$$

Clearly, in the limit $t \rightarrow \infty$, the integral $I_{\beta}(\infty, x)$ is much larger than $\tilde{I}_{\beta}(t, x)$.

By using Gradshteyn and Ryzhik (2000), it is readily seen that

$$I_{\beta}(\infty, x) = |x|^{3/2-\beta} e^{-2|x|}. \tag{A.4}$$

Setting $\theta = t(1 + \xi)$, the integral $\tilde{I}_{\beta}(t, x)$ may be transformed to

$$\tilde{I}_{\beta}(t, x) = \frac{|x| t^{1-\beta} e^{-t}}{\pi^{1/2}} \int_0^{\infty} (1 + \xi)^{-\beta} e^{-t f(\xi)} d\xi, \tag{A.5}$$

where

$$f(\xi) = \xi + \frac{x^2}{t^2(1 + \xi)}. \tag{A.6}$$

In the interval $0 \leq \xi < \infty$, the maximum rate of $f(\xi)$ occurs at $\xi = 0$. Therefore, according to Laplace’s method (e.g., Bender and Orszag, 1978), using the asymptotic expansion

$$f(\xi) \sim \frac{x^2}{t^2} + \left(1 - \frac{x^2}{t^2}\right) \xi, \quad \xi \rightarrow 0, \tag{A.7}$$

the dominant term of the behaviour of $\tilde{I}_{\beta}(t, x)$ as $t \rightarrow \infty$ and $|x|/t \rightarrow 0$ is obtained

$$\tilde{I}_{\beta}(t, x) \sim \frac{|x| t^{1-\beta} e^{-t-x^2/t}}{\pi^{1/2}} \int_0^{\infty} \exp\left[-t\left(1 - \frac{x^2}{t^2}\right)\xi\right] d\xi, \tag{A.8}$$

which immediately yields

$$\tilde{I}_{\beta}(t, x) \sim \frac{|x|}{\pi^{1/2}} t^{-\beta} e^{-t-x^2/t}. \tag{A.9}$$

Combining Eqs. (A.1), (A.4) and (A.9) leads to the asymptotic behaviour of $I_{\beta}(t, x)$ as $t \rightarrow \infty$ and $|x|/t \rightarrow 0$:

$$I_{\beta}(t, x) \sim |x|^{3/2-\beta} e^{-2|x|} - \frac{|x| e^{-t-x^2/t}}{\pi^{1/2} t^{\beta}}. \tag{A.10}$$

References

- Beckers, J.-M., Delhez, E.J.M., Deleersnijder, E., 2001. Some properties of generalised age-distribution equations in fluid dynamics. *SIAM J. Appl. Math.* 61 (5), 1526–1544.
- Bender, C.M., Orszag, S.A., 1978. *Advanced Mathematical Methods for Scientists and Engineers*. McGraw-Hill.
- Campin, J.-M., Fichefet, T., Duplessy, J.-C., 1999. Problems with using radiocarbon to infer ocean ventilation rates for past and present climates. *Earth Planet. Sci. Lett.* 165, 17–24.
- Deleersnijder, E., Campin, J.-M., Delhez, E.J.M., 2001a. The concept of age in marine modelling: I. Theory and preliminary model results. *J. Mar. Syst.* 28, 229–267.
- Deleersnijder, E., Delhez, E.J.M., Crucifix, M., Beckers, J.-M., 2001b. On the symmetry of the age field of a passive tracer released into a one-dimensional fluid flow by a point-source. *Bull. Soc. R. Sci. Liege* 70 (1), 5–21.
- Deleersnijder, E., Mouchet, A., Delhez, E.J.M., Beckers, J.-M., 2002. Transient behaviour of water ages in the World Ocean. *Math. Comput. Model.* 36, 121–127.
- Delhez, E.J.M., Deleersnijder, E., 2002. The concept of age in marine modelling: II. Concentration distribution function in the English Channel and the North Sea. *J. Mar. Syst.* 31, 279–297.
- Delhez, E.J.M., Campin, J.-M., Hirst, A.C., Deleersnijder, E., 1999. Toward a general theory of the age in ocean modelling. *Ocean Model.* 1, 17–27.
- Delhez, E.J.M., Deleersnijder, E., Mouchet, A., Beckers, J.-M., 2003. A note on the age radioactive tracers. *J. Mar. Syst.* 38, 277–286.
- England, M.H., 1995. The age of water and ventilation timescales in a global ocean model. *J. Phys. Oceanogr.* 25, 2756–2777.
- Gradshteyn, I.S., Ryzhik, I.M., 2000. *Tables of Integrals. Series and Products*, 6th edition. Academic Press, San Diego.
- Hall, T.M., Haine, T.W.N., 2004. Tracer age symmetry in advective–diffusive flows. *J. Mar. Syst.* 48, 51–59 (this issue).
- Hall, T.M., Holzer, M., 2003. Advective–diffusive mass flux and implications for stratosphere–troposphere exchange. *Geophys. Res. Lett.* 30 (5), 1222 (doi:10.1029/2002GL016419).
- Hirst, A.C., 1999. Determination of water component age in ocean models: application to the fate of North Atlantic Deep Water. *Ocean Model.* 1, 81–94.
- Holzer, M., Hall, T.M., 2000. Transit-time and tracer-age distributions in geophysical flows. *J. Atmos. Sci.* 57, 3539–3558.
- Khatriwala, S., Visbeck, M., Schlosser, P., 2001. Age tracers in an ocean GCM. *Deep-Sea Res.* 48A, 1423–1441.
- Munk, W.H., 1966. Abyssal recipes. *Deep-Sea Res.* 13, 707–730.
- Waugh, D.W., Hall, T.M., 2002. Age of stratospheric air: theory, observations, and models. *Rev. Geophys.* 40 (4), 1010 (doi:10.1029/2000RG000101).
- Waugh, D.W., Hall, T.M., Haine, T.W.N., 2003. Relationships among tracer ages. *J. Geophys. Res. (Oceans)*, doi:10.1029/2002JC001325.



Ages and age spectra of Eastern Mediterranean Deep Water

Reiner Steinfeldt

Institut für Umweltp Physik, Universität Bremen, P.O. Box 330440, 28334 Bremen, Germany

Received 26 September 2002; received in revised form 27 February 2003; accepted 28 March 2003

Available online 5 March 2004

Abstract

Observations of transient tracers such as tritium, helium and CFCs can be used to obtain information on the ages of water masses. The ocean general circulation model Modular Ocean Model-Array (MOMA) is used to compute the distribution of anthropogenic tracers as well as the ‘ideal’ age and age spectra for the Eastern Mediterranean. Substantial differences between tracer concentration age, tracer ratio age and the ideal age are revealed. The reason for these discrepancies is the fact that a water parcel in the ocean interior has to be regarded as a composition of fluid elements with different ages and different tracer concentrations. Therefore the concept of age spectra (distribution of transit times), describing the composition of the water parcel, is more adequate than using a single age. The computed age spectra are analysed in how far they are reflecting the circulation of Eastern Mediterranean Deep Water, especially its spreading and upwelling velocities. The methods used for the computation of the age spectra assume a steady ocean circulation. Short- and long-term variability of the model lead to a falsification of the calculated age spectra. The comparison between tracer concentrations and ideal age derived from the age spectra with the values computed directly in the model as passive tracers allows an estimation of the accuracy of the computed age spectra. The distribution of transit times for the deep water range, which are characterized by one pronounced maximum, suggests an approximation of the deep water masses consisting of only two parts, a young and an old component. Based on this assumption, it is possible to obtain a good estimation of the ideal age derived from measured tracer data.

© 2004 Elsevier B.V. All rights reserved.

Keywords: Age; Age spectrum; Deep water; Ocean circulation; Tracers; Mediterranean

1. Introduction

The assessment of the formation and spreading of water masses is a relevant topic in oceanography. Transient tracers provide a good means for such investigations as their distribution indicates the pathways of newly ventilated water. If, however, a more quantitative analysis of tracer measurements is to be

made, difficulties arise. One aspect is to determine the characteristics of the oceanic transport such as spreading rates and velocities from the measured tracer concentrations. Another problem is due to the temporal change of the tracer concentrations at a given location in the ocean interior. Such a change may be caused both by the temporal evolution of the tracer input during water mass formation and by the variability of oceanic transport. One approach is to convert the measured tracer concentrations into ‘ages’. The ideal age of a water parcel is defined as the time elapsed

E-mail address: rsteinf@physik.uni-bremen.de (R. Steinfeldt).

since it has been last in contact with the ocean surface (England, 1995). Yet the ages derived from different tracers are not identical with the theoretical ideal age and also differ among one another (Sonnerup, 2001). The reason for the discrepancies between the different kinds of ages is the fact that a water parcel in the ocean interior has to be regarded as a composition of fluid elements with different ages and different tracer concentrations. Therefore a water parcel can be characterized more accurately by means of an age spectrum rather than by a single age. These age spectra can be calculated in a numerical model, but it is impossible to derive them from tracer measurements directly. Only some characteristics of such spectra may be inferred. Beining and Roether (1996) showed that the shape of the age spectra affect the temporal evolution of CFC-concentrations in the ocean interior.

Typical age spectra for the deep ocean have long tails towards higher ages (Khatiwala et al., 2001). Modern anthropogenic tracers such as CFCs and tritium only resolve decadal to interdecadal timescales and give no information on the higher ages. These can be resolved only by long living radioactive tracers, e.g., carbon-14 (half-life $t_{1/2} = 5370$ yr). In the little ventilated regions of the world ocean the carbon-14-age derived from measurements is close to the modelled ideal age (England, 1995).

This study analyses the ages (ideal age as well as tracer ages) and age spectra for the Eastern Mediterranean, especially for the deep water range. As the deep water in the classical situation before the 1990s has one single source, the Adriatic (Roether and Schlitzer, 1991), the connection between age spectra and circulation is rather straightforward. The ages, age spectra and concentration of transient tracers, namely CFC-12, tritium and tritogenic helium-3 are computed by an ocean general circulation model. As the renewal timescale of the Mediterranean is about 100 years, only transient tracers with decadal timescales are used in this study. The results for the simulated tracer distributions are compared with measurements from the survey of the research vessel Meteor M5/6 in 1987 (Schlitzer et al., 1991).

After a description of the model (Section 2), Section 3 provides a detailed specification how the age spectra are computed. This is done in two ways, which are mathematically identical for a steady state circulation, but since the model simu-

lation shows short- and long-term variability, the results for the two age spectra are quite different. This is shown in Section 4. In order to assess the falsification of the calculated age spectra due to the temporal variability of the model, tracer concentrations and mean ages inferred from the age spectra are compared with the values computed directly by solving the advection–diffusion equation for the respective tracers.

Section 5 gives an overview of the different kinds of tracer derived ages (concentration and ratio age). The simplification assuming that a water parcel consists of a young and an old component gives a clear explanation of the discrepancies among the different ages. Furthermore, by interpreting the ratio age as characteristic for the young component and calculating its portion from the CFC-concentration, it is possible to give a good estimation of the ideal age just by means of transient tracer data.

2. Modelling of tracers

The study on the relationship between ages and age spectra presented here deals with the ideal age as well as with the transient tracers CFC-12, tritium and tritogenic helium-3 in the Eastern Mediterranean. Before describing in more detail the ocean general circulation model (OGCM) that is used for modelling these quantities, some characteristics of the computed tracers are highlighted.

2.1. Ideal age

A conservative tracer C transported by the ocean circulation fulfills the advection–diffusion equation:

$$\frac{\partial C}{\partial t} + \mathbf{u} \cdot \nabla C = \mathcal{L}(C). \quad (1)$$

The operator \mathcal{L} refers to all mixing processes (e.g., diffusion, convection) occurring within the ocean. The ideal age τ_{id} is defined by England (1995):

$$\frac{\partial \tau_{id}}{\partial t} + \mathbf{u} \cdot \nabla \tau_{id} = \mathcal{L}(\tau_{id}) + 1. \quad (2)$$

The source term ‘1’ describes the process of aging: In the absence of advection and diffusion ($\mathbf{u}=0$, $\mathcal{L}=0$), the age grows linearly with time. The ideal age in an oceanographic sense is understood as the time elapsed since a fluid element left the ocean surface. The boundary condition for τ_{id} is: $\tau_{id}(z=0)=0$.

2.2. Transient tracers

Fig. 1 shows the temporal evolution of the atmospheric mixing ratio of CFC-12 and the concentration of tritium in Mediterranean surface waters. Low tracer concentrations before 1955 are neglected. Atmospheric mixing ratios of CFC-12 are from Walker et al. (2000), and tritium values (Roether et al., 1992) are rescaled from a surface-water time history (Dreisigacker and Roether, 1978) of the North Atlantic. Tritium has been mainly produced during atmospheric nuclear weapon testing. It becomes part of the water cycle as tritiated water (HTO) and enters the ocean via water vapor exchange, precipitation and river run-off. For CFCs, gas exchange generates near-equilibrium values with atmospheric concentrations. This equilibrium concentration can be determined from the atmospheric mixing ratio and the temperature and salinity of the surface waters using the solubility function of CFC-12 (Warner and Weiss, 1985).

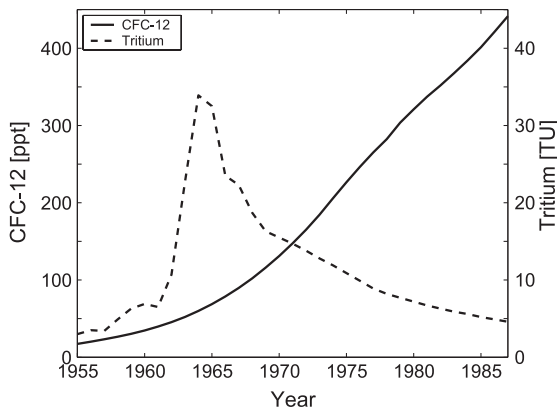


Fig. 1. Time history of the atmospheric mixing ratio of CFC-12 and concentration of tritium in Eastern Mediterranean surface waters, 1955–1987.

CFC-12 is inert in the ocean interior, i.e., conservative, and its governing equation is Eq. (1). Tritium on the other hand decays to helium-3 with a half-life of $t_{1/2}=12.43$ yr (Unterweger et al., 1980). This is accounted for by a sink/source term included into the equations for tritium (${}^3\text{H}$)/helium-3 (${}^3\text{He}$):

$$\frac{\partial [{}^3\text{H}]}{\partial t} + \mathbf{u} \cdot \nabla [{}^3\text{H}] = ([{}^3\text{H}]) - \lambda [{}^3\text{H}], \quad (3)$$

$$\frac{\partial [{}^3\text{He}]}{\partial t} + \mathbf{u} \cdot \nabla [{}^3\text{He}] = ([{}^3\text{He}]) + \lambda [{}^3\text{H}], \quad (4)$$

where λ denotes the decay constant for tritium ($\lambda = \ln 2/t_{1/2}$). Oceanic helium-3 consists of three contributions: atmospheric helium, terrigenic and tritogenic helium. By means of component separation (Roether et al., 1998), however, it is possible to isolate the tritogenic helium. At the surface the tritogenic helium escapes from the ocean, as helium isotopes tend to equilibrate rapidly with the atmosphere. Therefore the surface boundary condition for tritogenic helium, the only component of helium-3 computed in the model, is: $[{}^3\text{He}](z=0)=0$. Tritium is measured in tritium units (TU, 1 TU means a 10^{-18} $[{}^3\text{H}]/[\text{H}]$ ratio). For simplicity, throughout this paper, tritogenic helium-3 is also given in TU.

2.3. Description of the circulation model

The numerical model used in this work is the Modular Ocean Model-Array (MOMA) (Killworth et al., 1991; Webb et al., 1997), a free-surface version of the Geophysical Fluid Dynamics Laboratory Ocean Model (Bryan, 1969). The model resolution is $1/4^\circ$ horizontally and by 31 vertical levels with a spacing increasing from 10 m at the surface to 300 m below 1000 m depth. The model domain comprises the whole Mediterranean and a small Atlantic box allowing water exchange. Within this box temperature and salinity are relaxed towards climatological values (Levitus, 1982) with a 1-day timescale.

The governing equations of the model are:

$$\begin{aligned} \frac{\partial \mathbf{u}_h}{\partial t} + \mathbf{u} \cdot \nabla \mathbf{u}_h + f \times \mathbf{u}_h \\ = -\frac{1}{\rho_0} \nabla \mathbf{p} - A_h \nabla^4 \mathbf{u}_h + A_v \frac{\partial^2 \mathbf{u}_h}{\partial z^2}, \end{aligned} \quad (5)$$

$$\frac{\partial p}{\partial z} = -\rho g, \quad (6)$$

$$\nabla \cdot \mathbf{u} = 0, \quad (7)$$

$$\frac{\partial T}{\partial t} + (\mathbf{u} + \mathbf{u}^*) \cdot \nabla T = S_T, \quad (8)$$

$$\rho = \rho(T, S, p), \quad (9)$$

where \mathbf{u}_h represents the horizontal velocity, whereas \mathbf{u} is the full three-dimensional velocity vector. The vector \mathbf{f} written in components is $(0, 0, f)$ with the Coriolis parameter f . Eq. (9) is the UNESCO equation of state for sea water (Gill, 1982). For momentum, mixing owing to processes unresolved by the model is included via biharmonic terms in the horizontal and harmonic in the vertical (Eq. (5)). The viscosities are $A_h = 3.0 \times 10^{10} \text{ m}^4/\text{s}$ and $A_v = 1.5 \times 10^{-4} \text{ m}^2/\text{s}$, respectively. Eq. (8) is used for the computation of potential temperature, salinity and all passive tracers. The source or sink terms of the non-conservative tracers are described by S_T . The Gent and McWilliams (GM) scheme (Gent et al., 1995) is used to parameterise the subgrid processes in the tracer equation (\mathbf{u}^* denotes the GM velocity). The value of the GM thickness diffusion is $50 \text{ m}^2/\text{s}$. In order to improve the spreading of dense water over rough topography, a bottom boundary layer (Beckmann and Döscher, 1997) has been implemented into the model. A positive definite flux-limiting scheme (Thuburn, 1996) is also incorporated into the model and operating on the advection of all tracers.

2.3.1. Surface forcing

The model is initialized with the Levitus climatology (Levitus, 1982). A climatological forcing repeating each year is applied both for the wind stress and for the restoring of sea surface temperature and salinity. The wind stress is derived from data of the European Center for Medium Range Weather Forecast (ECMWF) (Myers et al., 1998) from the period 1986–1992.

SST and SSS values are used from the Mediterranean Oceanographic Database (MODB) (Brasseur, 1995). For the transient tracers also a relaxation towards the prescribed surface values is applied. The different relaxation time scales (applied to the uppermost 10 m thick model grid box) for temperature, salinity, CFC-12, tritium and helium-3 are given in Table 1. Note that the time scale for salinity is reduced in the Levantine to allow for the formation of saline Levantine Intermediate water (LIW) (Wu and Haines, 1996). After a model spin up of 50 years, the age and age spectra are computed for a period of 92 years. The modelling of the anthropogenic tracers CFC-12, tritium and helium-3 covers a period of only 32 years, corresponding to the period 1955–1987.

2.4. Modelled tracer distributions

Using the climatological surface forcing, the model is able to represent the thermohaline circulation of the Eastern Mediterranean as, e.g., observed on the Meteor cruise M5/6 in 1987 and described in Roether and Schlitzer (1991). The newly ventilated Eastern Mediterranean Deep Water (EMDW) can be identified by its enhanced CFC-12 concentrations. The formation region of this water mass is the Adriatic, from where the water passes the Strait of Otranto and enters the Ionian basin (the western part of the Eastern Mediterranean) as a deep western boundary current. Further on the EMDW turns to the east into the Levantine (the most eastern part of the Mediterranean), where it upwells eventually. This circulation pattern is indicated by the decrease of CFC-12 in the deep water from west to east both in the measured and in the modelled data (Fig. 2). Although the model represents the formation and spreading of EMDW quite well, the intermediate water range in the model is too shallow. This can be seen by the large CFC-12 gradient below

Table 1

Timescales for relaxation of model surface values to prescribed boundary condition

Quantity	Restoring time scale (day)
Temperature	1/12
Salinity	5 (1/12)
CFC-12	1
Tritium	180
Helium-3	3/8

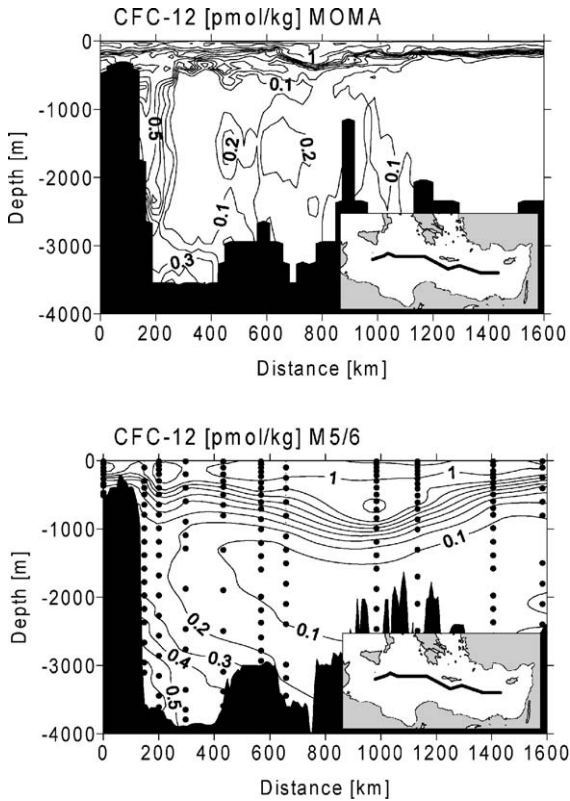


Fig. 2. CFC-12 concentration in 1987 on a west–east section from the Ionian into the Levantine (model data top, bottom observations). The orientation of the section is shown in the inset map.

the surface. As this study focuses on ages and tracers in the deep water, this shortcoming of the model is not considered further. Another model deficit is that some water originating from the Adriatic does not sink towards the bottom, but is spreading at depths about 1500 m. This leads to high tracer concentrations and quite young modelled ages compared with measured data in this depth range. On the other hand, at the western end of the section near the bottom, the modelled tracer concentrations are quite low. The boundary current at this position in the model is less pronounced than in reality.

3. Age spectrum

A fluid parcel within the ocean is considered to be a composite of irreducible, elementary fluid

elements. The fluid parcel itself represents a macroscopic volume element, such as a water sample. Because of the turbulent mixing occurring in the ocean interior, the fluid elements can have different source regions and transit times. The distribution of transit times within the water parcel can be described by means of an age spectrum (Beining and Roether, 1996) $\mathcal{G}(\mathbf{x}, t; \tau)$, which is a function of space \mathbf{x} , time t and age τ .

Mathematically, the age spectrum is a type of Green’s function propagating information from the boundary (the sea surface) into the interior (Holzer and Hall, 2000). Let $C_0(t')$ be the surface concentration of a tracer at time $t' = t - \tau$, then

$$C(\mathbf{x}, t) = \int_0^\infty \mathcal{G}(\mathbf{x}, t; \tau) C_0(t - \tau) d\tau \quad (10)$$

gives the concentration C of the tracer at location \mathbf{x} in the ocean interior and at time t .

Another quantity that can be calculated by means of the age distribution is the ideal age τ_{id} . It can be shown that first moment of \mathcal{G} , τ_m ,

$$\tau_m(\mathbf{x}, t) = \int_0^\infty \mathcal{G}(\mathbf{x}, t; \tau) \tau d\tau, \quad (11)$$

is identical with τ_{id} (Khatiwala et al., 2001).

3.1. Calculating the age spectrum in a 3-D model

In the case of one-dimensional flow with constant advection and diffusion, the age spectrum can be expressed by an analytical solution, namely an Inverse Gaussian distribution. This is, however, not possible for a realistic three-dimensional ocean circulation. In order to compute the age distribution in the 3-D model, certain properties of the integral of the age spectrum are of special interest. $\int_{n-1/2}^{n+1/2} \mathcal{G}(\mathbf{x}, t; \tau) d\tau$ gives the fraction of the water parcel that has an age between $n - 1/2$ and $n + 1/2$ years. Neglecting seasonal variations of \mathcal{G} , this can be interpreted as the portion of the water with a mean age of n years. Defining an artificial tracer C^{part} with impulse boundary condition ($C_0^{part}(t - \tau) = 1$ for $0 < t - \tau < 1$ (during the first model year) and $C_0^{part}(t - \tau) = 0$ for $t - \tau > 1$) gives the following relation between the values of C^{part} and the integral of \mathcal{G} :

$$C^{part}(\mathbf{x}, t) = \int_{t-1}^t \mathcal{G}(\mathbf{x}, t; \tau) d\tau. \quad (12)$$

That means the value of $C^{\text{part}}(\mathbf{x}, t)$ is identical with the fraction of water with an age of $\tau = t - 1/2$.

The integral $\int_0^t \mathcal{G}(\mathbf{x}, t; \tau) d\tau$ gives the fraction of water with an age between 0 and t , e.g., the part of the water that has been ventilated in the time period t prior to the observation. This integral can also be calculated in the model by means of an artificial tracer. Defining C^{tot} with the boundary conditions $C_0^{\text{tot}}(t - \tau) = 1$ for all ages τ yields:

$$C^{\text{tot}}(\mathbf{x}, t) = \int_0^t \mathcal{G}(\mathbf{x}, t; \tau) d\tau. \quad (13)$$

The age spectrum itself can be derived from the values of C^{tot} or C^{part} as follows:

$$\mathcal{G}(\mathbf{x}, t; \tau = t) = \frac{\partial}{\partial t} C^{\text{tot}}(\mathbf{x}, t) - \int_0^t \frac{\partial}{\partial t} \mathcal{G}(\mathbf{x}, t; \tau) d\tau, \quad (14)$$

$$\mathcal{G}(\mathbf{x}, t; \tau = t - 1/2) = \frac{1}{\Delta t} C^{\text{part}}(\mathbf{x}, t), \quad (15)$$

where Δt denotes a time interval of 1 year. If \mathcal{G} is independent of t (steady state), the integral in Eq. (14) vanishes. Moreover, the values of $\mathcal{G}(\mathbf{x}, t; \tau = t)$ calculated during the model run for different times t can be shifted towards a common point in time. Making use of this steady state assumption, the age spectra for ages from $\tau = 0$ up to $\tau = T$, T being the whole integration time of the model, can be calculated using the values of either C^{tot} or C^{part} . The method using C^{part} was described before, e.g., in Khatiwala et al. (2001). The quantity C^{tot} was used in England (1995), but without calculating an age spectrum by means of this artificial tracer.

In an OGCM, which never is exactly in a steady state, discrepancies will appear between the age spectra \mathcal{G}^{tot} derived from C^{tot} and $\mathcal{G}^{\text{part}}$ derived from C^{part} . It should be noted that, according to Eq. (13), the value of $C^{\text{tot}}(\mathbf{x}, t)$ is always identical with the fraction of water at location \mathbf{x} and model time t that has been ventilated throughout the model integration. For $t \rightarrow \infty$, $C^{\text{tot}}(\mathbf{x}, t) \rightarrow 1$, which means that the age spectrum \mathcal{G}^{tot} is normalized ($\int_0^\infty \mathcal{G}^{\text{tot}}(\mathbf{x}, t; \tau) d\tau = 1$). This cannot be guaranteed for the age spectra calculated from C^{part} . The values of $\mathcal{G}^{\text{part}}$ calculated according to Eq. (15) are shifted towards a common point of time, which leads to an error if the circu-

lation is not exactly in a steady state. This error is reflected in the wrong integral properties of the inferred age spectrum. In order to get the correct fraction of ventilated water at the end of the model run, the values of the age spectrum $\mathcal{G}^{\text{part}}$ can be normalized so that

$$\mathcal{G}^{\text{part-norm}}(\mathbf{x}, t = T; \tau) = \mathcal{G}^{\text{part}}(\mathbf{x}, t = T; \tau) \times \frac{\int_0^T \mathcal{G}^{\text{tot}}(\mathbf{x}, t; \tau) d\tau}{\int_0^T \mathcal{G}^{\text{part}}(\mathbf{x}, t; \tau) d\tau}. \quad (16)$$

For the calculation of the ‘exact’ age spectrum in a non-steady state, a series of artificial tracers with an impulse boundary condition like C^{part} would have to be calculated. For each of these tracers, the surface value is set to unity in one model year and to zero in all others. Each of these tracers give the fraction of water that has been ventilated during one particular model year. Then, at the end of the model run, the number of artificial tracers equals the number of years of model integration time (92 in this study). In order to avoid this high computational effort, the approximated age spectra inferred from the two tracers C^{tot} and C^{part} are calculated instead.

4. Model results

4.1. Age spectra

The artificial tracers C^{tot} and C^{part} defined in the previous sections are computed over a period of 92 years. In the further discussion, three regions and one model grid point from each of these regions will be considered in order to gain insight into the age spectra and their relation to the circulation of the Mediterranean. These regions (Fig. 3) represent the Northern Ionian, the Central Ionian and the Levantine. The newly ventilated Eastern Mediterranean Deep Water (EMDW), after leaving the Adriatic through the Strait of Otranto, flushes these regions successively. This is clearly reflected in the age spectra. Fig. 4 shows the model age spectra at grid points located at the positions of stations

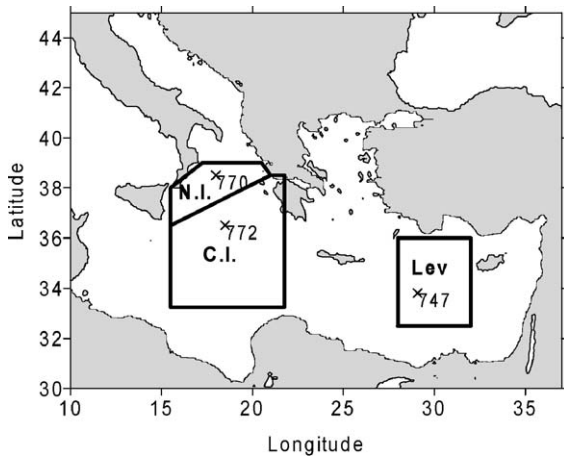


Fig. 3. Location of model grid points (coincident with stations from Meteor cruise M5/6) and regions; N.I.: Northern Ionian, C.I.: Central Ionian, Lev: Levantine.

770, 772 and 747 of Meteor cruise M5/6 for the deepest model box. The larger the distance of the stations from the Strait of Otranto, the higher is the most probable age (maximum of age spectrum) and the shape of the age spectra become broader. The maximum peak is the main contribution of the newly ventilated deep water. The most probable age can thus be interpreted as an approximation of the transit time of the deep water from its source in the Adriatic to the specific region. These time-scales are 1.5, 4.5 and about 20 years for the Northern and Central Ionian and the Levantine, respectively. The mean spreading velocity of EMDW becomes approximately 0.4 cm/s, based

upon a distance between the Adriatic and the Levantine of about 2500 km.

The upwelling of old water in the Levantine indicated by the tracer minimum layer between about 1000 and 2000 m depth (see Fig. 2) is also reflected in the age spectra. The values of G^{part} show distinct maxima in this depth range, and the most probable age decreases with depth. These maxima in the age spectra can be interpreted as a signal of the upwelling old deep water. Plotting the most probable age versus depth (Fig. 5) allows to estimate the upwelling velocity resulting in a value of about 35 m/yr or 1.1×10^{-4} cm/s.

The velocities calculated above are inferred from the propagation of a signal (the maximum of the age spectra) and can be interpreted as the mean spreading and upwelling velocities of EMDW. From observations it is well known that actual current speeds are normally higher than the effective spreading velocities due to eddies and recirculations. Andrié et al. (2001) for example calculated a spreading velocity for Upper North Atlantic Deep Water of 1.4 cm/s compared to direct current measurements which are up to 20 cm/s. The same holds true in the model simulation presented here. The velocities in the EMDW-core vary between 1 and 2 cm/s. The mean horizontal velocity in the EMDW-range in the passage south of Crete is 0.2 cm/s and the mean vertical velocity in the Levantine amounts to 1.7×10^{-4} cm/s. These mean values cover all gridpoints of the specified section/region. If only gridpoints with eastward/upward velocities are considered, the mean values increase

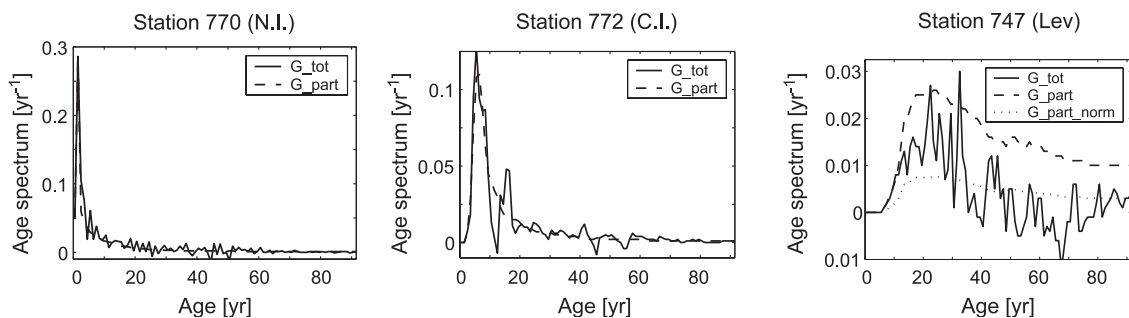


Fig. 4. Age spectra for the deepest model layer at single gridpoints coincident with stations from Meteor cruise M5/6: Station 770 in the Northern Ionian (N.I.), 772 in the Central Ionian (C.I.), and 747 in the Levantine (Lev).

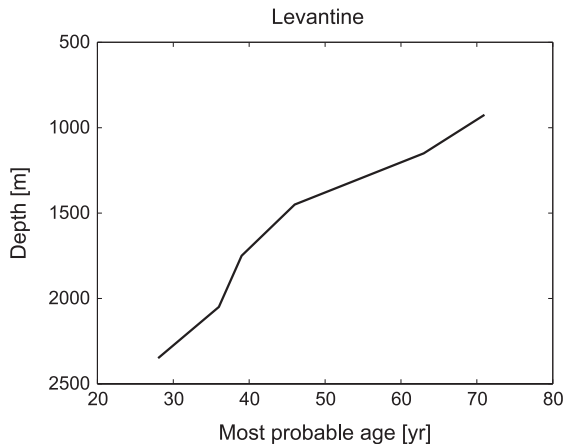


Fig. 5. Most probable age (maximum of age spectrum) versus depth in the Levantine indicating the upwelling of old water.

to 0.4 and 6.6×10^{-4} cm/s, respectively. This example demonstrates that it is not trivial to convert measured or modelled velocities into mean spreading rates.

It can be clearly seen from Fig. 4 that the age spectra calculated from the two artificial tracers C^{tot} and C^{part} are significantly different. In general, the G^{tot} curve shows more fluctuations compared with the smoother age spectra G^{part} . This is due to the neglect of the integral in Eq. (14). This integral can have negative values that may even lead to negative values of the inferred age spectrum. Another finding of Fig. 4 is that the time integral over the two age spectra can differ significantly, for example for station 747 it is much greater for the G^{part} than for the G^{tot} age spectrum. In the cases where the differences between the two time integrals are

evident, the normalized age spectrum $G^{\text{part_norm}}$ is calculated additionally as described in the previous section.

The ripples in the pointwise age spectra are due to temporal variability in the model circulation such as a meandering of the main outflow of young water from the Adriatic. To get rid of these oscillations, regional means of the age spectra have been calculated for the deep water range (Fig. 6). The regionally averaged age spectra are indeed smoother than the pointwise ones. It is also evident that they are broader with their maximum shifted towards higher ages and, especially in the Ionian, the maximum values are much smaller (note the different scales at the y-axes). The broadening of the age spectra is a direct effect of the averaging, which can be interpreted as a kind of mixing, and mixing of different water parcels makes the age spectrum wider. The young most probable ages in the pointwise distributions indicate that these grid-points are located directly in the outflow region of the newly formed EMDW. In the Levantine the age spectra G^{tot} have generally smaller values than the G^{part} spectra for ages higher than 40 years (Figs. 4 and 6, right panels). This indicates a temporal drift of the modelled circulation.

4.2. Inferring tracer concentrations and mean age from the age spectra

As shown above (Section 3), it is possible to calculate the concentration of transient tracers as well as the ideal age by means of the age spectrum. The tracer treated with are CFC-12, tritium and tritogenic helium-3. Comparing the tracer values

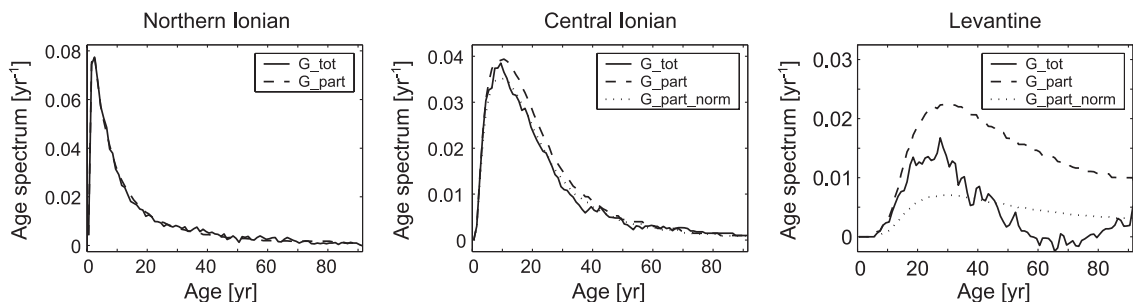


Fig. 6. Regional mean age spectra for the deep water range (EMDW) in the Northern and Central Ionian and in the Levantine.

inferred from the age spectra with the directly computed ones provides an assessment of the ‘quality’ of the age spectra and helps to decide which kind of age spectrum (\mathcal{G}^{tot} or $\mathcal{G}^{\text{part}}$) is more realistic.

Before starting the analysis, some modifications and specifications of Eqs. (10) and (11) have to be done. The ideal age τ_{id} is the first moment of the age spectrum according to Eq. (11), but the upper limit for the integration is ∞ . In the model, however, this limit is the time T over which the age tracers are calculated ($T=92$ years). Beginning with an age of zero at model time zero, the ideal age τ_{id} is approximating an equilibrium value, but in the less ventilated regions it is still increasing at the end of the numerical integration. Furthermore, the value of τ_{id} does not equal the first moment of the age spectrum as long as $C^{\text{tot}} < 1$, which means that not all water has been renewed during the model integration. This can be seen as follows: If a fluid element does not have any contact to the surface throughout the model run (between $t=0$ and $t=T$), its model ideal age equals T . The age spectrum however is zero for all ages between $\tau=0$ and $\tau=T$, which means that the first moment of the age spectrum taken between $\tau=0$ and $\tau=T$ is also zero. Now consider a water parcel consisting of ventilated and unventilated, ‘old’ fluid elements. The model age of the unventilated portion is given by the term $(1 - \int_0^T \mathcal{G} d\tau)T$. The term $1 - \int_0^T \mathcal{G} d\tau$ represents the mass fraction of unventilated water, and T is the belonging age. So the term $(1 - \int_0^T \mathcal{G} d\tau)T$ has to be added to the first moment of the age spectrum in order to yield the ideal age. For inferring the tracer concentration from the age spectrum (Eq. (10)) the finite model integration time does not matter, because the concentrations of the anthropogenic tracers used here are zero at and before the beginning of the model run and increase later on. The only change in Eq. (10) is that the undersaturation of CFC-12 and tritium in the newly formed Adriatic water is taken into account. The saturation amounts to about 80% for CFC-12 and 60% for tritium (the exact percentage is not constant during the model run and is taken from the model outflow of deep water at the Strait of Otranto). The modified formula for calculating the mean age as well as the tracers CFC-12, tritium

(^3H) and tritogenic helium-3 ($^3\text{He}_{\text{tri}}$) by means of the age distribution are:

$$\tau_{\text{id}}(\mathbf{x}, T) = \int_0^T \mathcal{G}(\mathbf{x}, T; \tau) \tau d\tau + (1 - \int_0^T \mathcal{G}(\mathbf{x}, T; \tau) d\tau) T, \quad (17)$$

$$C^{\text{CFC-12}}(\mathbf{x}, T) = \int_0^T \mathcal{G}(\mathbf{x}, T; \tau) C_0^{\text{CFC-12}}(T - \tau) d\tau, \quad (18)$$

$$C^3\text{H}(\mathbf{x}, T) = \int_0^T \mathcal{G}(\mathbf{x}, T; \tau) C_0^3\text{H}(T - \tau) e^{-\lambda\tau} d\tau, \quad (19)$$

$$C^3\text{He}_{\text{tri}}(\mathbf{x}, T) = \int_0^T \mathcal{G}(\mathbf{x}, T; \tau) C_0^3\text{H}(T - \tau) (1 - e^{-\lambda\tau}) d\tau. \quad (20)$$

The radioactive decay of tritium into helium is accounted for by the factors $e^{-\lambda\tau}$ in Eq. (19) and $1 - e^{-\lambda\tau}$ in Eq. (20).

The comparison between the tracer concentrations calculated according to Eqs. 17–20 and the directly computed ones are shown in Fig. 7 for the regional mean values. The regions ‘Northern Ionian’ and ‘Levantine’ are chosen as representative examples for the cases of young and old deep water, respectively. The averaging procedure has been performed only in the horizontal and not vertically like for the age spectra in Fig. 6, so one value for each model depth level exists. The tracer concentrations in the upper 500 m are not shown as the tracer saturation near the surface is greater than in the newly formed deep water, so that taking the saturation of about 80% for CFC-12 and 60% for tritium would result in too low values.

The concentrations of the different transient tracers calculated from the three age spectra \mathcal{G}^{tot} , $\mathcal{G}^{\text{part}}$ and $\mathcal{G}^{\text{part-norm}}$ according to Eqs. (18)–(20) are in good correspondence with the directly calculated values for the Northern Ionian. The ideal ages, however, show greater discrepancies. The better agreement of the tracer values compared with the ideal age can be understood considering the following: Transient tracers such as CFCs and tritium have high values for young ages. By calculating the integral with the age spectrum, the ‘younger’ part of the age spectrum is weighted higher than the ‘older’ part. For the mean age it is just the opposite: The old part of the age spectrum

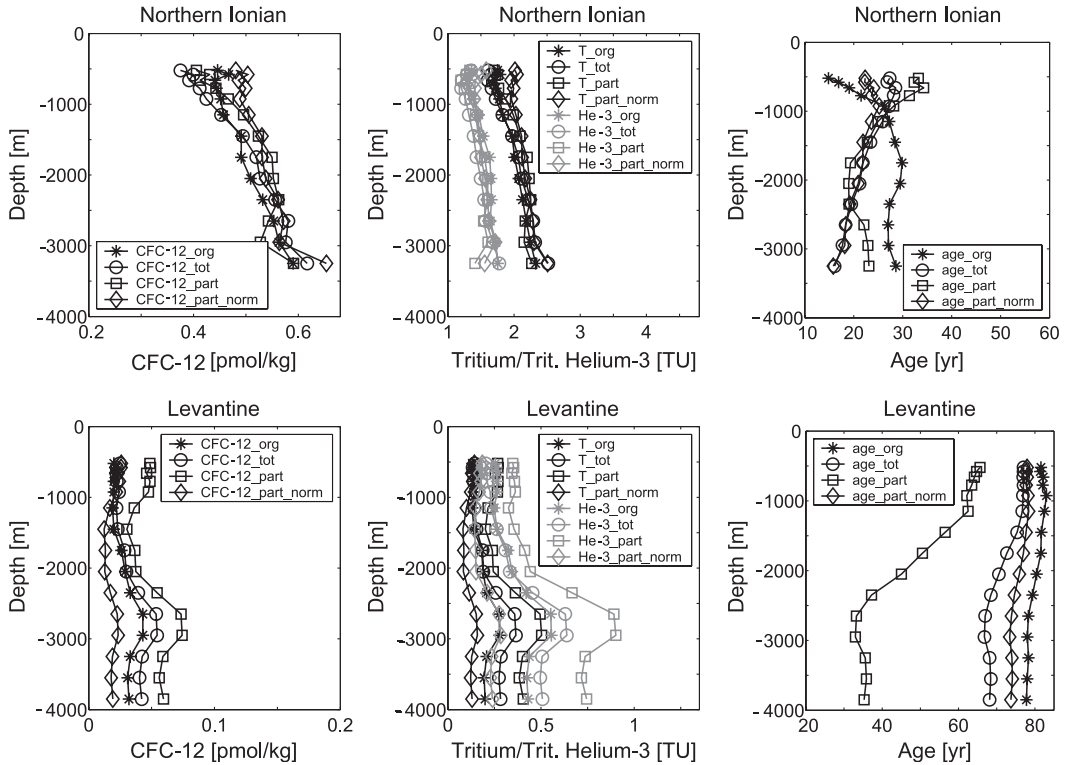


Fig. 7. Concentration of CFC-12, tritium, tritiogenic helium-3 and ideal age computed directly ($_org$) and inferred from the age spectra ($_tot$, $_part$ and $_part_norm$) as regional mean for the Northern Ionian (upper) and Levantine (lower) panel.

is multiplied with high ages and so weighted more heavily. This shows that the old part of the computed age spectra is affected and falsified by a temporal model drift. For the Levantine, the concentration of transient tracers inferred from the age spectra \mathcal{G}^{tot} , \mathcal{G}^{part} and \mathcal{G}^{part_norm} differ among each other significantly. Only the values derived from the \mathcal{G}^{tot} are in good agreement with the values computed directly as passive tracers. These differences can be explained by comparing the three kinds of age spectra. The \mathcal{G}^{part} spectra have higher values than the \mathcal{G}^{tot} spectra (see Figs. 4 and 6, right panel). This results in the high tracer concentrations inferred from the \mathcal{G}^{part} age spectra and, because the value $1 - \int_0^T \mathcal{G}^{part}(\mathbf{x}, t; \tau) d\tau$ (see Eq. (17)) is small, in the low mean ages throughout the Levantine. In contrast, the normalized age spectra \mathcal{G}^{part_norm} for the Levantine have small values for young ages. Therefore the inferred tracer concentrations are too low, whereas the mean ages in the Levantine are quite close to the directly computed ones.

The presented examples show that the age spectra computed by means of the artificial tracers C^{tot} and C^{part} may be deteriorated by temporal variability of the model. A good indicator for this kind of error are discrepancies between the values of the age spectra \mathcal{G}^{tot} and \mathcal{G}^{part} . Therefore it provides a good test for the ‘quality’ of the calculated age spectra to compute both of the artificial tracers C^{tot} and C^{part} .

5. Comparison of model and tracer-based ages

Ideal age and age distributions as described in the previous sections are theoretical quantities and cannot measured directly. As these quantities play an important role in providing information on the circulation, it is desirable to get ‘agelike’ quantities by measurements of transient tracers. Another reason for the calculation of tracer ages is that the time dependence of transient tracers is for a great part caused by the

temporal variation of their atmospheric sources. By deriving ages from tracer measurements, this variability of the source strength, which has nothing to do with the ocean circulation, can be removed.

Two concepts of tracer derived ages are covered, i.e., the concentration age and the ratio age. To calculate the concentration age the time t_{conc} has to be determined when the surface concentration C_0 of the tracer equals the measured value C in the ocean interior at time t (Doney and Bullister, 1992):

$$C(t) = C_0(t_{\text{conc}}). \quad (21)$$

The concentration age τ_{conc} is then defined as the time lag between t and t_{conc} ($\tau_{\text{conc}} = t - t_{\text{conc}}$). The ratio age τ_{ratio} is calculated in the same way, but instead of using the concentration of one single tracer, the ratio of two tracers C^1/C^2 is considered:

$$\frac{C^1}{C^2}(t) = \frac{C_0^1}{C_0^2}(t_{\text{ratio}}). \quad (22)$$

A special case of the concentration age is the tritium–helium-age $\tau_{^3\text{H}/^3\text{He}}$ (Jenkins and Clarke, 1976). As the surface concentration of tritogenic helium is zero, Eq. (22) cannot be applied. From the law of radioactive decay follows:

$$\tau_{^3\text{H}/^3\text{He}} = \lambda^{-1} \ln \left(1 + \frac{[^3\text{He}]}{[^3\text{H}]} \right). \quad (23)$$

For an irreducible fluid element which is transported from the ocean surface into the interior by purely advection without mixing, τ_{conc} and τ_{ratio} are identical and are also in agreement with the ideal age τ_{id} (the age spectrum is a delta-peak in this case). The ideal age and tracer concentration of a water sample is the mean of the ages and tracer values of all the fluid elements that make up the water sample. Because of the generally nonlinear temporal evolution of the tracer concentration at the sea surface differences between the individual tracer ages will occur. This effect of mixing is illustrated in Fig. 8. As simplification the assumption is used that the water parcel consists only of two components: an ‘old’ one (formation time 1930) and a ‘young’ component (formation time t_{young} 1987). The thick line shows the temporal evolution of the atmospheric concentration of CFC-12. The considered mixture of the

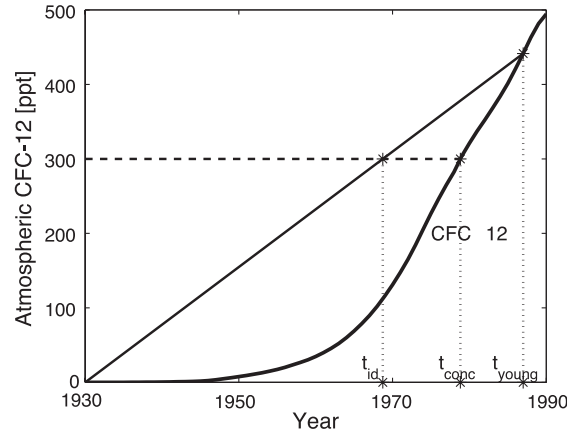


Fig. 8. Formation times according to the concept of ideal, concentration and ratio age for a water mass consisting of two components that are ventilated at 1930 and 1987.

old and young component has a formation time of $t_{\text{id}} = 1969$ (the ideal age mixes linear as the CFC-12 content). Its CFC-12 content corresponds to an atmospheric mixing ratio of 300 ppt, resulting in a formation time of $t_{\text{conc}} = 1979$ according to the concept of concentration age. The ratio age is identical with the age of the young component ($t_{\text{young}} = t_{\text{ratio}}$). This is always the case if the ‘old’ component does not contain any of the two tracers used for ratio dating, leading to large discrepancies between ideal and ratio age. The concentration of both tracers is diluted by mixing for the same amount, so the dilution factor cancels out by computing the concentration ratio. This problem is mentioned in Doney and Bullister (1992), where CFC-11/CFC-12 ratio ages are calculated for the eastern North Atlantic. According to the simplified assumption of a two component mixture of young tracer carrying and old tracer free water, and provided the second temporal derivative of the considered tracer concentration is positive, the following relation holds:

$$\tau_{\text{id}} > \tau_{\text{conc}} > \tau_{\text{ratio}} = \tau_{\text{young}}. \quad (24)$$

This result is already known, for example it is shown in Sonnerup (2001) for CFC-derived ages in observations and a 1-D model.

5.1. Model results and observations

In this section, it will be examined how far the results from the simplified assumption of a two

component mixture of a water parcel (Eq. (24)) are still valid in a full ocean circulation model and in reality. Fig. 9 shows the modelled distribution of the mean and the CFC-12 concentration age in the Eastern Mediterranean on a west–east section (same section as in Fig. 2) for the year 1987. In the less ventilated regions with the oldest waters (at 1000 m depth in the Ionian and between 1000 and 2000 m in the Levantine), the ideal age is about 80 years and has not yet reached a steady state because of the insufficient model integration time. The concentration age at these places however is only about 40 years. As the atmospheric CFC-12 concentration is almost zero before 1940, the highest concentration age that would be possible in 1987 is 47 years, close to the maximum reached in the model. Even the youngest EMDW found near the bottom at the western end of the section shows a significant difference between ideal age and concentration age (about 30 and 20 years,

respectively). Taking into account the broader age spectra with maxima at higher ages for EMDW in the Levantine compared to the Ionian, it is evident that the west–east gradient of the age in the Eastern Mediterranean is a result of both spreading and mixing of the deep water. The effect of mixing increases with the spreading time (age) and so does the difference between ideal and concentration age. This is in qualitative agreement with the assumptions made in the previous section.

In order to compare all three kinds of ages discussed here (ideal age τ_{id} , concentration age τ_{conc} and ratio age τ_{ratio}), the age profiles at station 772 of the Meteor cruise M5/6 located in the Central Ionian are considered. Fig. 10 shows these profiles for the model results (left) and for the concentration and ratio ages derived from tracer measurements (right). It can be seen that the inequality from Eq. (24) holds almost everywhere both in the model and in the observed data.

Also shown in Fig. 10 is the computed most probable age. If the two component assumptions were correct, the age spectrum of the young component would be a delta-peak. So the age of the young component should be identical with the position of this peak, which is also the maximum of the age spectrum. Fig. 10 shows that above 2000 m the most probable age is almost constant located at 3 years, whereas the tritium–helium-age is 10 years or older. In the deep-water range the discrepancies decrease but still amount a few years. This indicates that the age spectrum of the young portion of the water can be approximated by a sharp peak only for the deep water range, and even here the width of the peak amounts to a few years as is shown in Fig. 4, left and middle panel.

Between 1000 and 2000 m, τ_{conc} and τ_{ratio} are almost constant, whereas τ_{id} shows a clear maximum near 1000 m. The constant tracer derived age values as well as the most probable age of about 3 years reveal that a direct pathway from the Adriatic to the depth range between 1000 and 2000 m in the Central Ionian exists in the model, but mixing, especially with upwelling old water free of tracers leads to the high mean age. Similar features are present in the tracer ages derived from observations. There the ratio age also shows low variation with depth. The CFC-12 concentration age however exhibits a pronounced maximum at 1500 m, indicating that the portion of young water in this depth range is overestimated in the model. This

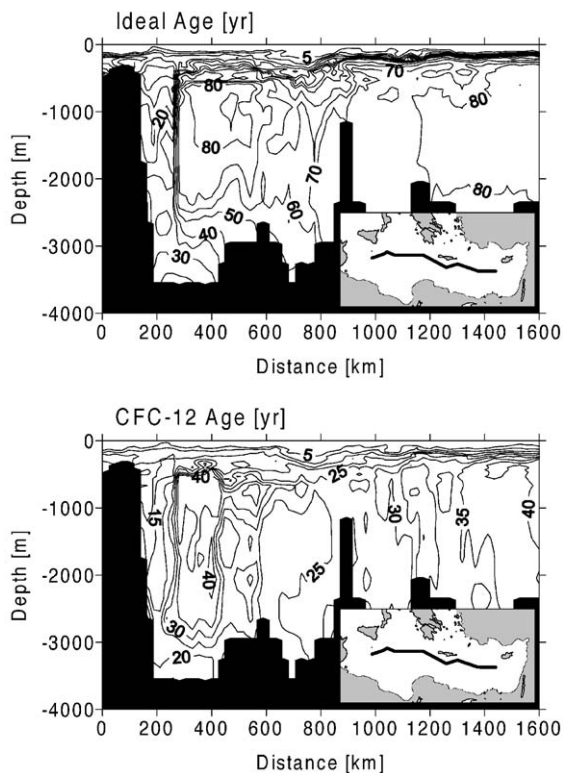


Fig. 9. Model ideal age (top) and CFC-12 concentration age (bottom) in 1987 along the same section as shown in Fig. 2.

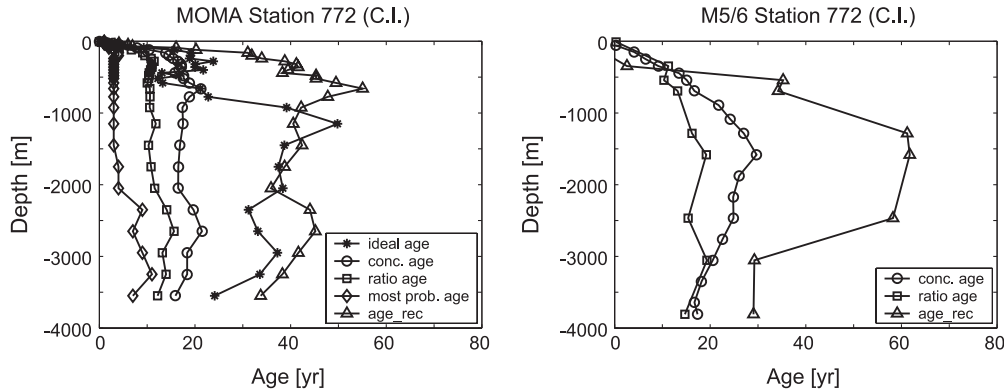


Fig. 10. Comparison of ideal age, CFC-12 concentration age, tritium–helium ratio age, most probable age and reconstructed mean age based on the two component approximation for modelled (left) and measured (right) data at station 772 in the Central Ionian.

can also be seen from the discrepancies between modelled and observed CFC-12 distributions shown in Fig. 2, which are quite large in the western part of the section (the central Ionian) at 1500 m depth.

Additionally to the ages discussed so far, a ‘reconstructed age’ τ_{rec} is computed. This age gives an approximation to the mean age and is calculated using the ratio age and the concentration of CFC-12, so it can be directly derived from measurements. The reconstructed age τ_{rec} is based again on the assumption that the water parcel is a mixture of an old and a young component, which, as shown above, is a sensible approximation for the deep water. The mean age τ_{rec} of this two-component mixture is

$$\tau_{\text{rec}} = c_{\text{young}}\tau_{\text{ratio}} + (1 - c_{\text{young}})\tau_{\text{old}}, \quad (25)$$

with c_{young} and $1 - c_{\text{young}}$ being the mass fractions and $\tau_{\text{ratio}} = \tau_{\text{young}}$ and τ_{old} being the ages of both components. Since the old water is considered to contain no anthropogenic tracers, the fraction c_{young} can be calculated by means of the tritium/helium ratio age τ_{ratio} and the measured concentration of CFC-12 [$\text{CFC-12}^{\text{sample}}(t)$]:

$$c_{\text{young}} = \frac{[\text{CFC-12}^{\text{sample}}(t)]}{[\text{CFC-12}_0(t - \tau_{\text{ratio}})]}. \quad (26)$$

The value of τ_{old} is determined as follows: Roether and Well (2001) give a turn-over time of 150 years \pm 30% for the deep regime below 1200 m in the Eastern Mediterranean. Taking into account that the mean age is at least half of the turn-over time

(Björkström, 1978) results in a minimum value for τ_{old} of 75 years. This value is used in Fig. 10 and seems to be reasonable at least for depths below 1000 m. Transferring this result to the measured data, τ_{rec} in the right panel of Fig. 10 for the deep water range can be regarded as approximation of the mean age calculated from observed tracer data.

6. Summary and conclusions

Transient tracer concentrations, ideal age and age spectra for the Eastern Mediterranean have been calculated in a fully three-dimensional circulation model. It is shown that, if the circulation is not exactly in a steady state, the age spectra can only be calculated approximatively with not unduly extended computational effort. This approximation uses two artificial tracers (C^{tot} and C^{part}) from which the age spectra are inferred. The age spectra for an individual model gridpoint show a lot of ripples originating from temporal and spatial variability of the model. For example, the main pathway of the newly produced deep water indicated by a velocity maximum changes its exact position from year to year. This is not a model artifact but is also indicated by repeated observations, e.g., in the western tropical Atlantic (Andrié et al., 2001). Therefore it is more appropriate to calculate regional means of the age spectra, by which these fluctuations are weakened.

A method to test the approximated age spectra is to infer the mean age and the concentrations of transient

tracers by means of the spectra and to compare them with the directly computed values. The agreement for the anthropogenic tracers is quite good, whereas for the mean age marked discrepancies appear. This indicates that the old parts of the age spectra, which are weighted higher by calculating the mean age, have greater errors than the younger segments. Age spectra can also be used to calculate the concentration of tracers that are not directly included into the model, if the time history of the surface concentration as well as composition/decomposition rates of the tracers are known. The agreement between directly calculated tracer concentrations and the values inferred from the age spectra suggests that the results would be good at least for tracers with higher input during the last decades (high tracer concentration for young waters). Another finding is that ideal age and tracer concentrations inferred from \mathcal{G}^{tot} are in most cases closer to the directly computed values than for the $\mathcal{G}^{\text{part}}$ age spectra. Using the normalized the $\mathcal{G}^{\text{part_norm}}$ age spectra instead of the original $\mathcal{G}^{\text{part}}$ spectra leads to a decrease of these differences. This is due to the fact that the time integrals of the \mathcal{G}^{tot} and $\mathcal{G}^{\text{part_norm}}$ age spectra give the mathematical correct value. As for a steady state circulation the age spectra derived from C^{tot} and C^{part} would be identical, deviations between the two age spectra indicate temporal model variability. Calculating both artificial tracers C^{tot} and C^{part} as described here allows to assess the temporal change of the modelled circulation and in how far the calculated age spectra are deteriorated by this effect. For example, it can be seen that temporal variability on shorter time scales (order of 1 year) causing the ripples of the pointwise age spectra in Fig. 4 increases from the Northern Ionian to the Levantine, i.e., with distance from the deep water source.

The connections between age spectra and ocean circulation are evident. The maxima in the age spectra correspond to the signal of Eastern Mediterranean Deep Water (EMDW). The most probable age (maximum of age spectrum) increases with distance from the Adriatic, the source region of EMDW. A mean velocity of 0.4 cm/s for the spreading of EMDW from the Adriatic into the Levantine is calculated thereby. In the Levantine, the age spectra reflect the upwelling of old deep water in the tracer minimum layer between 1000 and 2000 m. The depth dependency of the most probable age gives an upwelling velocity of 35 m/yr.

Different kinds of tracer-derived ages (concentration and ratio age) are compared both for modelled and observed data. If the age spectrum was a delta peak, all ages would be identical, but in reality this is not the case. The age spectra get broader with increasing distance from the source region. The ratio age is generally younger than the concentration age both in the model and observations, and in the model the ideal age has the highest values of all kinds of ages. For the deep water in question, which is replenished by a single source, the assumption of a two-component mixture can be made, e.g., the water consists of a young and an old component free of tracers. This is indicated by the maximum of the age spectrum being close to the ratio age. Based on this assumption and an estimation of the age of the old component (approximately half of the turn over time), the ideal age can be calculated by means of the ratio age and a tracer concentration. This provides an easy way to yield the ideal age from observed tracer data.

Acknowledgements

The author would like to thank Wolfgang Roether for discussions and two anonymous reviewers for their helpful comments. The Meteor cruise M5/6 was funded by the Deutsche Forschungsgemeinschaft and scientific data evaluation was supported by the European Union.

References

- Andri , C., Rhein, M., Freudenthal, S., Pl hn, O., 2001. CFC time series in the deep water masses of the western tropical Atlantic. *Deep-Sea Res., Part 1, Oceanogr. Res. Pap.* 49, 281–304.
- Beckmann, A., D scher, R., 1997. A method for improved representation of dense water spreading over topography in geopotential-coordinate models. *J. Phys. Oceanogr.* 27, 581–591.
- Beining, P., Roether, W., 1996. Temporal evolution of CFC11 and CFC12 in the ocean interior. *J. Geophys. Res.* 101, 16455–16464.
- Bj rkstr m, A., 1978. A note on the relation between average age and transit time in natural reservoirs. *Tellus* 30, 185–188.
- Brasseur, P., 1995. Free data offered to researchers studying the Mediterranean. *EOS Trans.-Am. Geophys. Union* 76, 363.
- Bryan, K., 1969. A numerical method for the study of the circu-

- lation of the world ocean. *J. Comp. Phys. Educ. Sport* 4, 347–376.
- Doney, S.C., Bullister, J.L., 1992. A chlorofluorocarbon section in the eastern North Atlantic. *Deep-Sea Res.* 39, 1857–1881.
- Dreisigacker, E., Roether, W., 1978. Tritium and ^{90}Sr in North Atlantic surface water. *Earth Planet. Sci. Lett.* 38, 301–312.
- England, M., 1995. The age of water and ventilation timescales in a global ocean model. *J. Phys. Oceanogr.* 25, 2756–2777.
- Gent, P.R., Willebrand, J., McDougall, T.J., McWilliams, J.C., 1995. Parameterizing eddy-induced tracer transports in ocean circulation models. *J. Phys. Oceanogr.* 25, 463–474.
- Gill, A.E., 1982. *Atmosphere–ocean dynamics*. International Geophysics Series, vol. 30. Academic Press. 662 pp.
- Holzer, M., Hall, T.M., 2000. Transit-time and tracer-age distributions in geophysical flows. *J. Atmos. Sci.* 57, 3539–3558.
- Jenkins, W.J., Clarke, W.B., 1976. The distribution of ^3He in the western Atlantic Ocean. *Deep-Sea Res.* 23, 481–494.
- Khatiwala, S., Visbeck, M., Schlosser, P., 2001. Age tracers in an ocean GCM. *Deep-Sea Res., Part 1, Oceanogr. Res. Pap.* 48, 1423–1441.
- Killworth, P.D., Stainforth, D., Webb, D.J., Peterson, S.M., 1991. The development of a free-surface Bryan–Cox–Semtner ocean model. *J. Phys. Oceanogr.* 21, 1333–1348.
- Levitus, S., 1982. *Climatological atlas of the world ocean*. NOAA Prof. Pap., vol. 13. U.S. Govt. Print. Off., Washington, DC.
- Myers, P.G., Haines, K., Josey, S., 1998. On the importance of the choice of wind stress forcing to the modeling of the Mediterranean Sea circulation. *J. Geophys. Res.* 103, 15729–15749.
- Roether, W., Schlitzer, R., 1991. Eastern Mediterranean deep water renewal on the basis of chlorofluoromethane and tritium data. *Dyn. Atmos. Ocean.* 15, 333–354.
- Roether, W., Well, R., 2001. Oxygen consumption in the Eastern Mediterranean. *Deep-Sea Res., Part 1, Oceanogr. Res. Pap.* 48, 1535–1551.
- Roether, W., Schlosser, P., Kuntz, R., Weiss, W., 1992. Transient-tracer studies of the thermohaline circulation of the Mediterranean. *Rep. Meteorol. Oceanogr.* 41 (II), 291–317.
- Roether, W., Well, R., Putzka, A., R uth, C., 1998. Component separation of oceanic helium. *J. Geophys. Res.* 103, 27931–27946.
- Schlitzer, R., Roether, W., Oster, H., Junghans, H.-G., Hausmann, M., Johannsen, H., Michelato, A., 1991. Chlorofluoromethane and oxygen in the Eastern Mediterranean. *Deep-Sea Res.* 38, 1531–1551.
- Sonnerup, R.E., 2001. On the relations among CFC derived water mass ages. *Geophys. Res. Lett.* 28, 1739–1742.
- Thuburn, J., 1996. Multidimensional flux-limited advection schemes. *J. Comp. Phys. Educ. Sport* 123, 74–83.
- Unterweger, M.P., Coursey, B.M., Schima, F.J., Mann, W.B., 1980. Preparation and calibration of the 1978 National Bureau of Standards tritiated water standards. *Int. J. Appl. Radiat. Isot.* 31, 611–614.
- Walker, S.J., Weiss, R.F., Salameh, P.K., 2000. Reconstructed histories of the annual mean atmospheric mole fractions for the halocarbons CFC-11, CFC-12, CFC-113, and carbon tetrachloride. *J. Geophys. Res.* 105, 14285–14296.
- Warner, M.J., Weiss, R.F., 1985. Solubilities of chlorofluorocarbons 11 and 12 in water and seawater. *Deep-Sea Res.* 32, 1485–1497.
- Webb, D.J., Coward, A.C., de Cuevas, B.A., Gwilliam, C.S., 1997. A multiprocessor ocean general circulation model using message passing. *J. Atmos. Ocean. Technol.* 14, 175–183.
- Wu, P., Haines, K., 1996. Modeling the dispersal of Levantine Intermediate Water and its role in Mediterranean deep water formation. *J. Geophys. Res.* 101, 6591–6607.



ELSEVIER

Available online at www.sciencedirect.com

SCIENCE @ DIRECT®

Journal of Marine Systems 48 (2004) 83–116

JOURNAL OF
MARINE
SYSTEMS

www.elsevier.com/locate/jmarsys

Physical and biochemical averaged vertical profiles in the Mediterranean regions: an important tool to trace the climatology of water masses and to validate incoming data from operational oceanography

B. Manca^{a,*}, M. Burca^b, A. Giorgetti^a, C. Coatanoan^c, M.-J. Garcia^d, A. Iona^e

^a *Istituto Nazionale di Oceanografia e di Geofisica Sperimentale-OGS, Borgo Grotta Gigante 42c, 34010 Sgonico, Trieste, Italy*

^b *National Institute for Marine Research and Development "Grigore Antipa", Constanta, Romania*

^c *IFREMER/SISMER, BP 70, 29280 Plouzane, France*

^d *Instituto Espanol de Oceanografia-IEO, c. Corazon de Maria 8, 28002 Madrid, Spain*

^e *National Centre for Marine Research, NCMR, Aghios Kosmas-Hellinikon, 16604 Athens, Greece*

Received 28 January 2003; received in revised form 4 September 2003; accepted 13 November 2003

Available online 26 April 2004

Abstract

Seasonally and spatially averaged vertical profiles of temperature, salinity, dissolved oxygen, nutrients and chlorophyll-*a* have been computed from in situ observations in different regions of the Mediterranean Sea using the recently released EU/MEDAR/MEDATLAS II and EU/MTPII/MATER databases. The regions have been defined according to known dynamics important in the formation, transformation and spreading of the main water masses that circulate in the upper, intermediate and deep layers. The climatological characteristics of temperature and salinity reflect the water mass structures and the general thermohaline circulation patterns. Spatial and temporal variations on a seasonal basis of nutrients and principal biological parameters are described along with some aspects of the trophic conditions of the Mediterranean Sea. The strongest signal of variability is along the vertical; however, horizontal inhomogeneities are mostly associated with the internal dynamics. The distribution of the biochemical elements, in conjunction with hydrographic measurements of temperature and salinity, may serve as appropriate tracers for the characterisation of the main water masses (Atlantic Water, Levantine Intermediate Water and Bottom Water in the eastern and eastern basins) throughout the Mediterranean Sea. In a first approach, adequate descriptors of water properties have been obtained, useful for the quality control of incoming data in large databases and in setting-up documented procedures to improve future data management practices. Secondly, the biochemical climatological characteristics addressed in this paper are verified to be consistent with the physics of the Mediterranean Sea and are conceived useful to initialise coupled physical–biological models. The full set of spatially averaged vertical profiles can be found and downloaded from the World Wide Web data server established at OGS (<http://doga.ogs.trieste.it/medar/climatologies/>).

© 2004 Elsevier B.V. All rights reserved.

Keywords: Mediterranean Sea; Hydrodynamics; Biochemical observations; Climatological fields; Marine ecosystem

* Corresponding author. Tel.: +39-40-2140201; fax: +39-40-2140266.

E-mail address: bmanca@ogs.trieste.it (B. Manca).

1. Introduction

The Mediterranean Sea is a semi-enclosed basin characterised by rough bottom topography with a narrow continental shelf (<200 m) and a steep continental slope (Fig. 1). The western and the eastern basins communicate through the relatively shallow Strait of Sicily and present peculiar topographic depressions characterised by great depths, where nutrient-rich deep-water masses are stored for long time. The most important depressions are the Algero-Provençal basin (maximum depth of ~2900 m), the Tyrrhenian Sea (~3900 m), the Ionian abyssal plain (~4200 m), and the Hellenic trench that runs from the Ionian into the Levantine basin (~5000 m); finally, in the Levantine basin, the deepest areas are the Rhodes depression (~4200 m) in the north and the Herodotus abyssal plain (~3000 m) in the south.

The Mediterranean Sea, located at mid-latitudes, is characterised by a rather sub-tropical climate with two well-defined seasons, winter and summer, and short periods of transition between them. It possesses an anti-estuarine thermohaline circulation and has an active water exchange with the northern Atlantic through the Strait of Gibraltar. As a consequence of the excess of evaporation over precipitation (~0.62–

1.16 m year⁻¹; Hopkins, 1978), Atlantic Water (AW) inflows at the surface and Mediterranean Water (MW) outflows along the bottom. In wintertime, outbreaks of cold and dry continental air masses lead to a significant negative heat budgets (~5–10 W m⁻²; Castellari et al., 2000) and buoyancy losses, initiating deep and/or intermediate dense water formation. These events are recurrent over the shelf areas and in the offshore regions, both in the western and the eastern basins (MEDOC Group, 1970; Ovchinnikov et al., 1985; Malanotte-Rizzoli, 1991; POEM Group, 1992).

In a climatological sense, for physical and biogeochemical studies, the thermohaline circulation may be schematically described as follows (Robinson et al., 2001; Béthoux et al., 1992): (i) at the surface (0–150 m), relatively fresh AW (~36.5 psu) circulates from the Strait of Gibraltar to the easternmost part of the Levantine basin; (ii) in the intermediate layer (150–600 m), the saline Levantine Intermediate Water (LIW), regularly formed in the Levantine basin with a salinity of ~39.10 psu, spreads westwards and constitutes the non-returning flow towards the Strait of Gibraltar, and then into the Atlantic Ocean; (iii) in the deep layer, two internal thermohaline cells circulate dense water masses formed via convective events in the northern

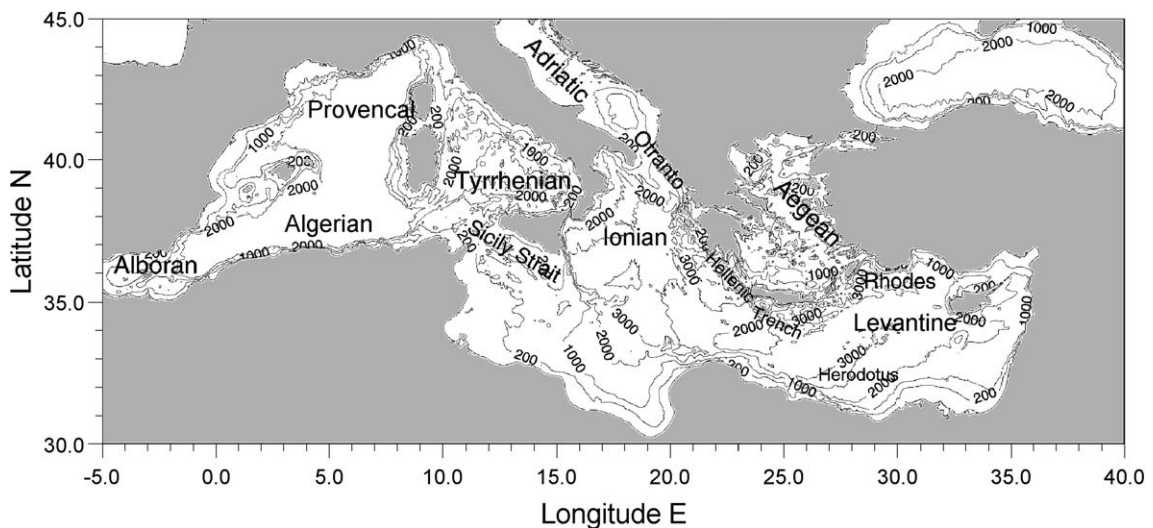


Fig. 1. Mediterranean Sea geography showing the names of the major sub-basins and the bottom topography. Depth contours are indicated in metres.

regions, mainly in correspondence to topographically controlled cyclonic gyres both in the Western and in the Eastern Mediterranean Sea. It has been generally accepted that the Western Mediterranean Deep Water (WMDW) forms in the Gulf of Lions (Leaman and Schott, 1991), and the Eastern Mediterranean Deep Water (EMDW) originates in the southern Adriatic Sea (Schlitzer et al., 1991). Transitional waters (i.e. between the intermediate and the deep layers) may be recognised everywhere as a product of the transformation of the intermediate and deep waters. These latter may participate in the outflow into the western basin through the Strait of Sicily (Sparnocchia et al., 1999; Astraldi et al., 2002), and into the Atlantic Ocean through the Strait of Gibraltar (Kinder and Parilla, 1987). Thus, the Mediterranean Sea influences, to a large extent, the global oceanic circulation (Reid, 1979).

Improvements in monitoring and numerical modelling have provided new insights into the general thermohaline circulation, which results much more complex than the one based on large-scale patterns. Atmospheric forcing and strong topographic constraints generate permanent and recurrent sub-basin scale cyclonic and anticyclonic motions. At the same time, the most energetic mesoscale activities play a major role in enhancing the internal dynamics and mixing processes (Millot, 1991; Robinson et al., 1991). In addition, seasonal characteristics and interannual variations of the circulation elements, verified by model simulations (Rousenov et al., 1995; Pinardi et al., 1997), affect the distribution of the biochemical species such as dissolved oxygen and nutrients, as well as the magnitude and the composition of phytoplankton biomass (Crise et al., 1999).

It has been demonstrated that the Mediterranean Sea is in a non-steady-state situation. A marked long-term warming trend and salinity increase in the deep water of the Western Mediterranean has been detected since 1960, i.e. from the period when the accuracy of the observations have revealed differences significantly greater than possible instrumental errors. These variations have been mostly attributed to changes in climate (Béthoux et al., 1990). These trends have been estimated to be about 0.027 °C and 0.019 units per decade in temperature and salinity, respectively (Leaman and Schott, 1991). However, since most of the

water transformation occurs during winter by convective events with a large participation of the LIW, these trends have been also related to an increase in the LIW properties due to man-induced reduction of the freshwater inflow for agricultural purposes (Rohling and Bryden, 1992).

Most dramatically, hydrographic observations conducted over the last decade in the Eastern Mediterranean have revealed a major transition event, due to an additional source of dense waters established in the Aegean Sea (Roether et al., 1996). More saline, warmer and denser waters ($S \cong 38.85$, $\theta \cong 13.80$ °C, $\sigma_\theta \cong 29.22$ kg m⁻³; Klein et al., 1999) than the EMDW of Adriatic origin ($S \cong 38.66$, $\theta \cong 13.30$ °C, $\sigma_\theta \cong 29.18$ kg m⁻³; Schlitzer et al., 1991), flowing out through the Cretan Arc Straits, sank to the bottom layer of the central Mediterranean regions, replacing almost 20% of the dense water below 1200 m. This event, named as Eastern Mediterranean Transient (EMT), has been attributed to an important meteorological anomaly that occurred in the Eastern Mediterranean at the beginning of the 1990s (Lascaratos et al., 1999). Changes in the distributions of salt (Malanotte-Rizzoli et al., 1999) and of the biogeochemical materials have also been observed in the intermediate and deep layers of the Eastern Mediterranean (Klein et al., 1999).

Many projects have produced significant amounts of multidisciplinary hydrographic data both in the Western and the Eastern Mediterranean Sea, i.e. MEDIPROD (Coste et al., 1972), PRIMO (Millot, 1995), POEM (Robinson and Malanotte-Rizzoli, 1993), ALMOFRONT 1 (Prieur and Sournia, 1994), EROS 2000 (Martin and Milliman, 1997), EU/MAST/MTP (Lipiatou et al., 1999), MTP II/MATER (Monaco and Peruzzi, 2002). Individual hydrographic experiments were specifically designed to investigate physical processes and the impact on nutrients and biological production. Nutrient enrichment has been observed at the surface in the presence of convective chimneys in the Gulf of Lions (Coste et al., 1972), in the southern Adriatic gyre (Gacic et al., 2002) and during severe winters in the area of the northern Levantine occupied by the cyclonic Rhodes Gyre (Yilmaz and Tuğrul, 1998); whereas low nutrient values have been detected in the neighbouring anticyclones (Kress and Herut, 2001). In the upper layer, nitrate concentrations are higher in winter than

in summer, when oxygen rich and very low nutrient surface waters are rapidly capped creating conditions of high oligotrophy in the subsurface layer. Differences in nutrient concentration and changes in biodiversity between the Eastern and Western Mediterranean, due to the different physiography of the two interconnected basins, have been verified from a fully coupled physical and biochemical cycling model (Crise et al., 1999). The inverse estuarine circulations cause a net loss of nutrients in the eastern and western basins through the Sicily and the Gibraltar Straits, respectively (Béthoux et al., 1992).

In this paper, the most complete data set of archived historical data collated within the framework of the EU/MEDAR/MEDATLAS II and the basin-scale measurements obtained from the EU/MTPII/MATER project have been used. Since the data sets cover the interval from the beginning of the last century to the present, these data are analysed to calculate climatological profiles on a seasonal basis and to characterise the main water masses, providing a basis for describing their spatial variability. The same profiles can be used for checking the quality of historical and incoming data from operational oceanography, as well as for the initialisation of coupled hydrodynamical–biological models and sensitivity analyses.

The main purpose of the study is to deduce physical properties and biochemical characteristics of the principal water masses, taking into account vertical transfers and the general thermohaline circulation. This is done by analysing the vertical climatological profiles of temperature, salinity, dissolved oxygen, primary nutrient elements (nitrate, phosphate, silicate) and chlorophyll-*a*, calculated in different regions of the Mediterranean Sea. It should be stressed that the dissolved oxygen, nutrient and chlorophyll-*a* values have been employed merely as straightforward descriptors of the spatial and temporal variability of the water column structure, without any consideration of the underlying biochemical processes that are involved. The biochemical properties, although non-conservative have been used in the past to get supplementary information on the water masses (Coatanoan et al., 1999); the non-conservative aspects of these properties will not be discussed in the present study, but will be the object of future investigations into the functioning of the Mediterranean marine ecosystem.

The paper is organised as follows: in Section 2, we assess the quantitative content of the hydrographic data mentioned above and the quality control adopted within the framework of the data management practices. In Section 3, the data distributions and the statistical analyses performed to deduce the climatological characteristics of the physical and biochemical properties in the different regions of the Mediterranean Sea are described. In Section 4, we present typical climatological vertical profiles for some regions in the western and eastern basins. Some scientific frameworks are discussed analysing the results with emphasis on the properties of the most significant water masses circulating in the Mediterranean Sea. The concluding remarks of the present work are summarised in Section 5.

2. Data sets

2.1. Data archived within EU/MEDAR/MEDATLAS II and EU/MTP II/MATER projects

Earlier efforts in collecting historical data sets and mapping climatological fields in the Mediterranean Sea include those of Miller et al. (1970), Levitus (1982), Guibout (1987), Picco (1990) and Levitus et al. (1998). The twin EU/MAST/MODB and MEDATLAS projects provided quality controlled data sets of temperature and salinity in the Mediterranean Sea and produced an updated version of the horizontal climatologies and combined error field estimates (MODB Group, 1996; MEDATLAS Consortium, 1997).

The EU/MEDAR/MEDATLAS II project has improved the volume of available physical data and extended the database to include some biological and geo-chemical parameters in the Mediterranean and Black Seas (MEDAR Group, 2002). The project involved the majority of the scientific institutions of the bordering countries, thereby obtaining the best coverage of biochemical data in the whole Mediterranean. The core parameters comprise hydrographic data relating to temperature, salinity, dissolved oxygen, seawater nutrients (nitrates, phosphates and silicates), pH, alkalinity and chlorophyll-*a*.

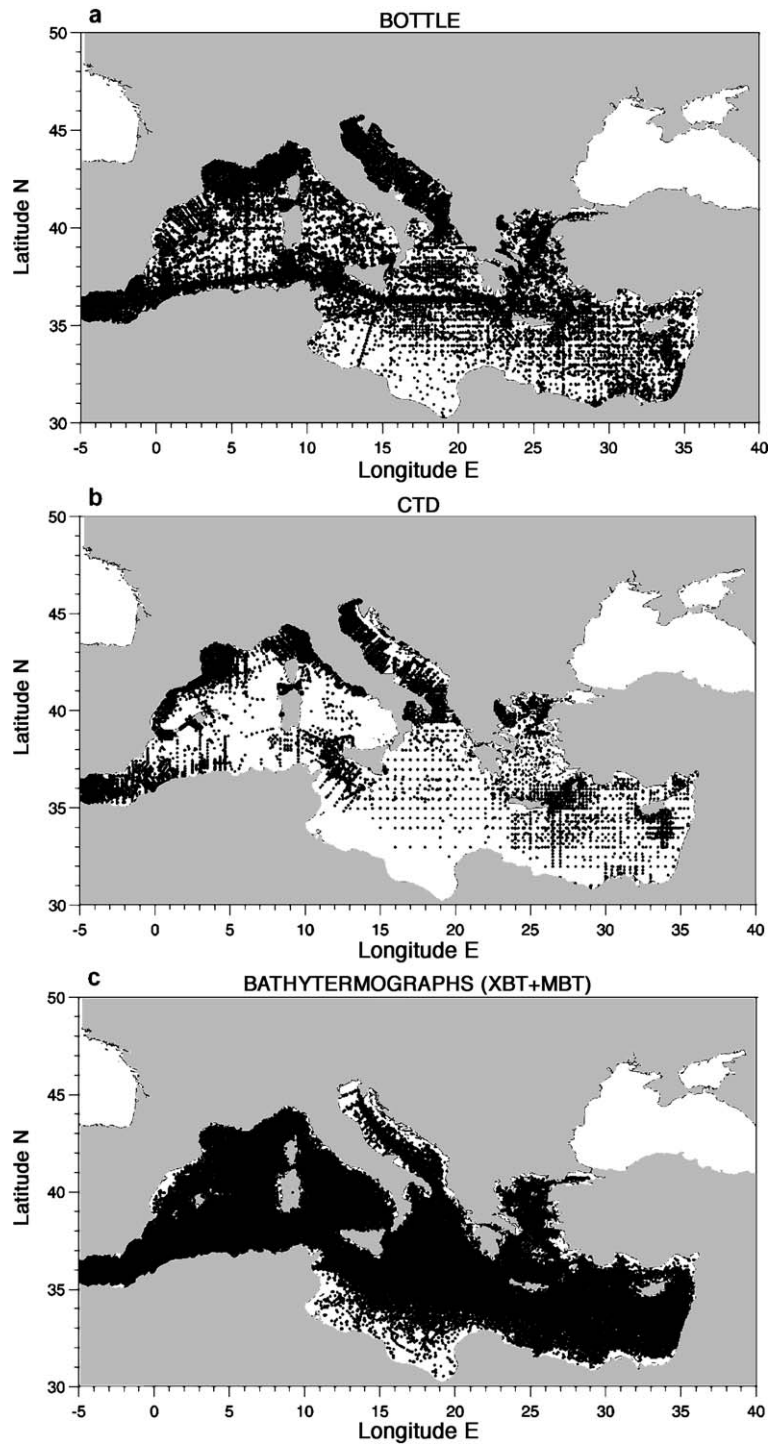


Fig. 2. Maps showing the locations of the hydrographic stations globally assembled in the MEDAR/MEDATLAS II database: (a) bottle casts (Nansen/Niskin), (b) CTD casts, (c) MBT and XBT probes.

The MEDAR/MEDATLAS II database consists of 286,397 vertical profiles, including bottle, CTD, MBT and XBT casts. Fig. 2 illustrates the distribution of the hydrological stations by data type, while Fig. 3 shows the distribution per year. Despite the good coverage of the Mediterranean Sea, the space and time distributions of the considered parameters are rather heterogeneous. The bottle stations display a fairly regular coverage of the western and eastern basins, with the exception of the southern coastal region in the Eastern Mediterranean, but the majority of them contain temperature and salinity data, exclusively. The CTD stations cover the period from the early seventies onward (Fig. 3), providing a major concentration in some regions of the Mediterranean Sea. The temperature and salinity profiles obtained with CTD probes reach down to the bottom layer and are useful to detect small variations of the temperature and salinity

fields. In contrast, the MBT and the XBT profiles extend vertically to a depth of about 250 and 700 m, respectively. These measurements, being less accurate (~ 0.1 °C) than the conventional measurements obtained by reversing thermometers (~ 0.02 °C) and CTD probes (~ 0.005 °C), can capture the seasonal variability in the upper thermocline or changes in the intermediate layer only in the presence of significantly strong dynamics.

Together with the historical MEDAR/MEDATLAS II database, the most recent data set collected in limited areas of the Mediterranean Sea within the framework of the MTP II/MATER project has also been considered (Maillard et al., 2002). The EU/MTP II/MATER database deals with an additional 3141 CTD profiles, 634 XBT probes and 1327 bottle casts of multidisciplinary biochemical samples collected during a series of oceanographic cruises

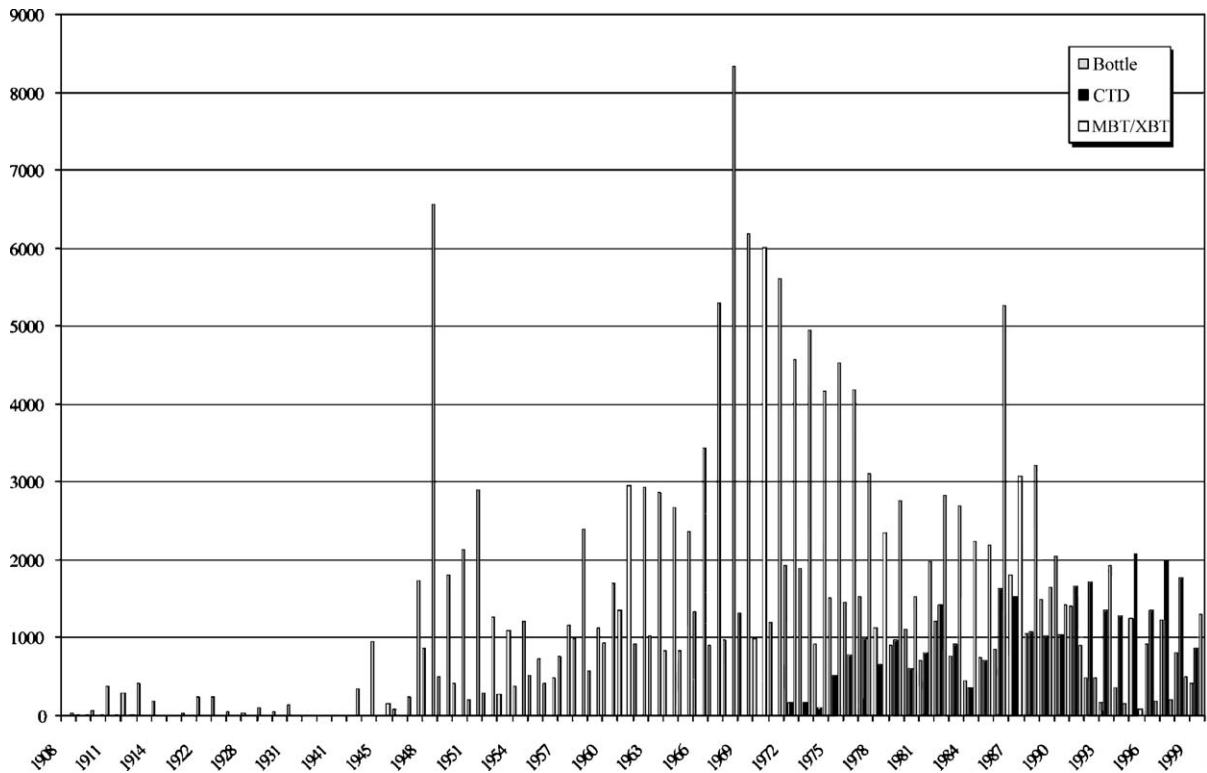


Fig. 3. Temporal distribution of the hydrological stations since the beginning of the last century that were used for the climatological analyses: CTD (black scale), bottles (grey scale) and bathythermographs (white scale).

from 1996 to 1999. It provides for the first time a good resolution in the vertical distribution of oxygen and nutrients (nitrate, phosphate and silicate) in the Algerian basin, in the Strait of Sicily and in the southern Adriatic. Hydrographic bottle casts were collected also in the Ionian Sea, in the Levantine basin and in the Aegean Sea.

The quantity of hydrological casts analysed in this work, i.e. with the exclusion of the stations pertinent to the Black Sea and the adjacent region in the Atlantic Ocean (Fig. 2), is synthesized in Table 1. The overall distributions of hydrological stations (Nansen/Niskin bottles, CTD, XBT and MBT) for temperature, salinity, dissolved oxygen, nutrients (nitrate, phosphate, silicate) and chlorophyll-*a* in the Mediterranean Sea used to reconstruct the spatially averaged vertical profiles addressed in this work are shown in Fig. 4. The density of hydrological stations decreases from North to South; the distribution of casts with chlorophyll-*a* measurements shows that the large majority of the data is located in the Western Mediterranean (along the Catalan, Spanish and Algerian coastlines) and in the Adriatic Sea; few stations cover the offshore regions in the Eastern Mediterranean.

2.2. Data quality control within MEDAR/MEDATLAS II project

The data quality control adopted within the MEDAR/MEDATLAS II data management work was based on specific protocol (Maillard et al.,

2001) designed according to international methods and standards (UNESCO, 1993). The procedure was as follows: (i) data and metadata (ancillary information) are checked and reformatted in a unique format, (ii) numerical checks are performed by the comparison of the incoming data with prescribed ranges (e.g. broad ranges values) and reference statistics (e.g. spatially averaged vertical profiles and standard deviations), and (iii) the behaviour in the water column and the acceptability of consecutive values are checked testing the hydrostatic stability and searching for spikes and artefacts. Successively, a quality flag is added to the station header (meta-data information), and to each of measured numerical values also.

The temperature and salinity data have been fully quality checked in this way. For the biochemical data, a preliminary analysis of the major sources of existing data was performed to determine broad range values, which could then be confidently used to qualify incoming data from historical or unknown field investigations.

The major difficulty in the process of data validation arises from the fact that the marine environment exhibits some trends and/or interannual variations. The incoming data might or might not fit the existing climatologies (MODB Group, 1996; MEDATLAS Consortium, 1997; Levitus et al., 1998), which are representative of the mean and variance of the oceanographic fields but is time-independent. Consequently, the model for data validation described above may fail and trend evaluations should be included to improve the methods for data quality control. However, these requirements are quite difficult to fulfil due to the scarcity of systematic information and the lack of long time series in many areas. Therefore, the final action of flagging inconsistencies was decided visually and corrected manually, i.e. subjectively, to account for quality control flags that may be incorrect due to the characteristics of the used climatologies, which might not be adequately representative. The data with quality flag 1 (i.e. good data) and quality flag 2 (i.e. outside one standard deviation of the used climatologies) were retained for the following analyses. From the total number of profiles that were available for each parameter (Table 1), we finally retained about 99% of the temperature, 98% of the

Table 1

Number of hydrographic stations globally assembled for the Mediterranean Sea within the framework of the MEDAR/MEDATLAS II and MTP II/MATER projects that were used for the climatological analyses

Data type	Data sets no.	Profiles no.	Period
Bottle	1633	52,068	1908–1999
CTD	561	29,663	1970–1999
MBT and XBT	894	141,110	1908–1999
Total	3088	222,841	

Bottle cast parameters are depth, temperature, salinity, oxygen, phosphate, nitrate, nitrite, ammonium, silicate, pH, alkalinity, and chlorophyll-*a*.

CTD cast parameters are depth, temperature, salinity and sometimes, oxygen.

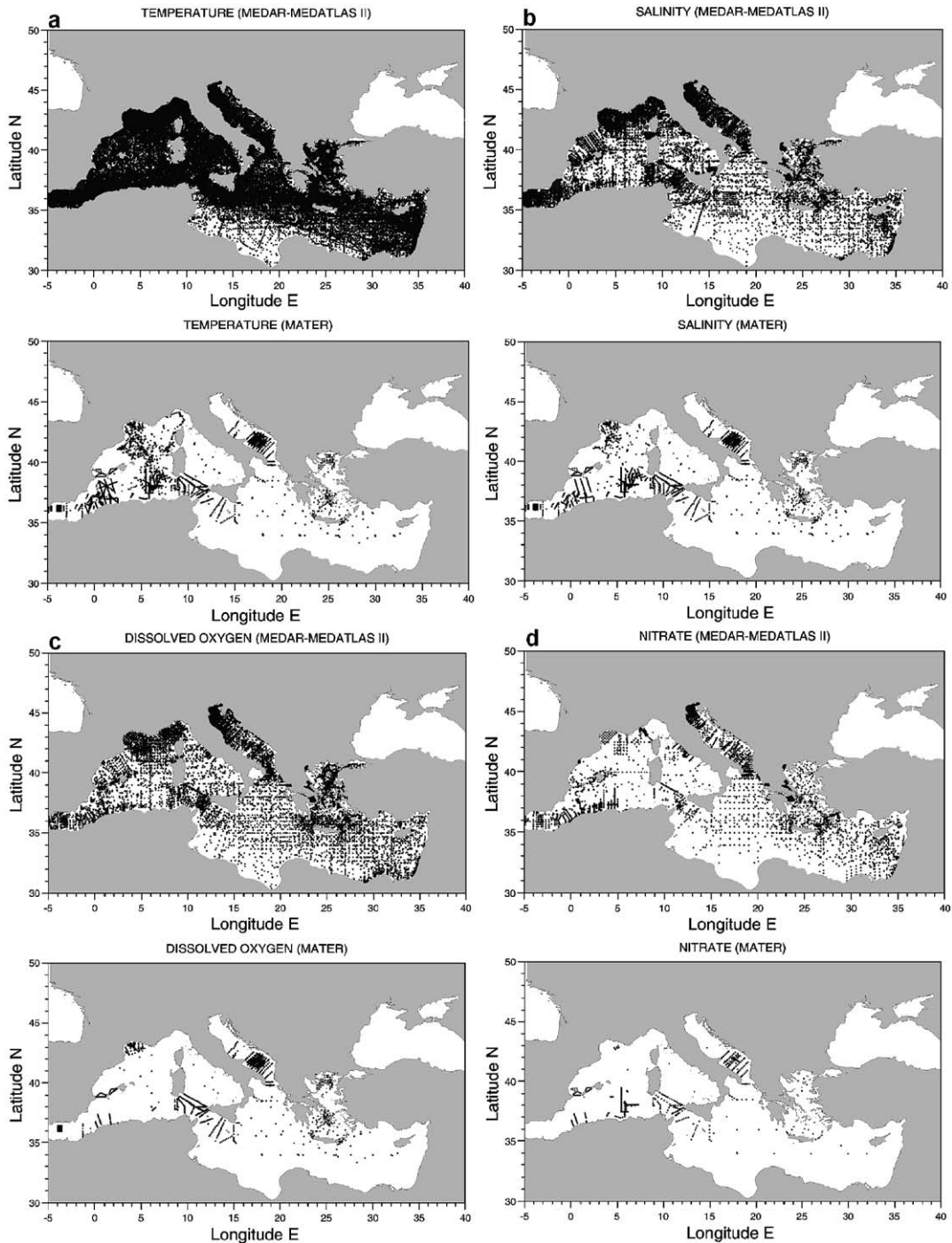


Fig. 4. Distribution of sampling stations originated in the context of the EU/MAST/MEDAR-MEDATLAS II and EU/MTPHII/MATER projects for (a) temperature, (b) salinity, (c) dissolved oxygen, (d) nitrate, (e) phosphate, (f) silicate, and (g) chlorophyll-*a* used to reconstruct the averaged vertical profiles addressed in this work.

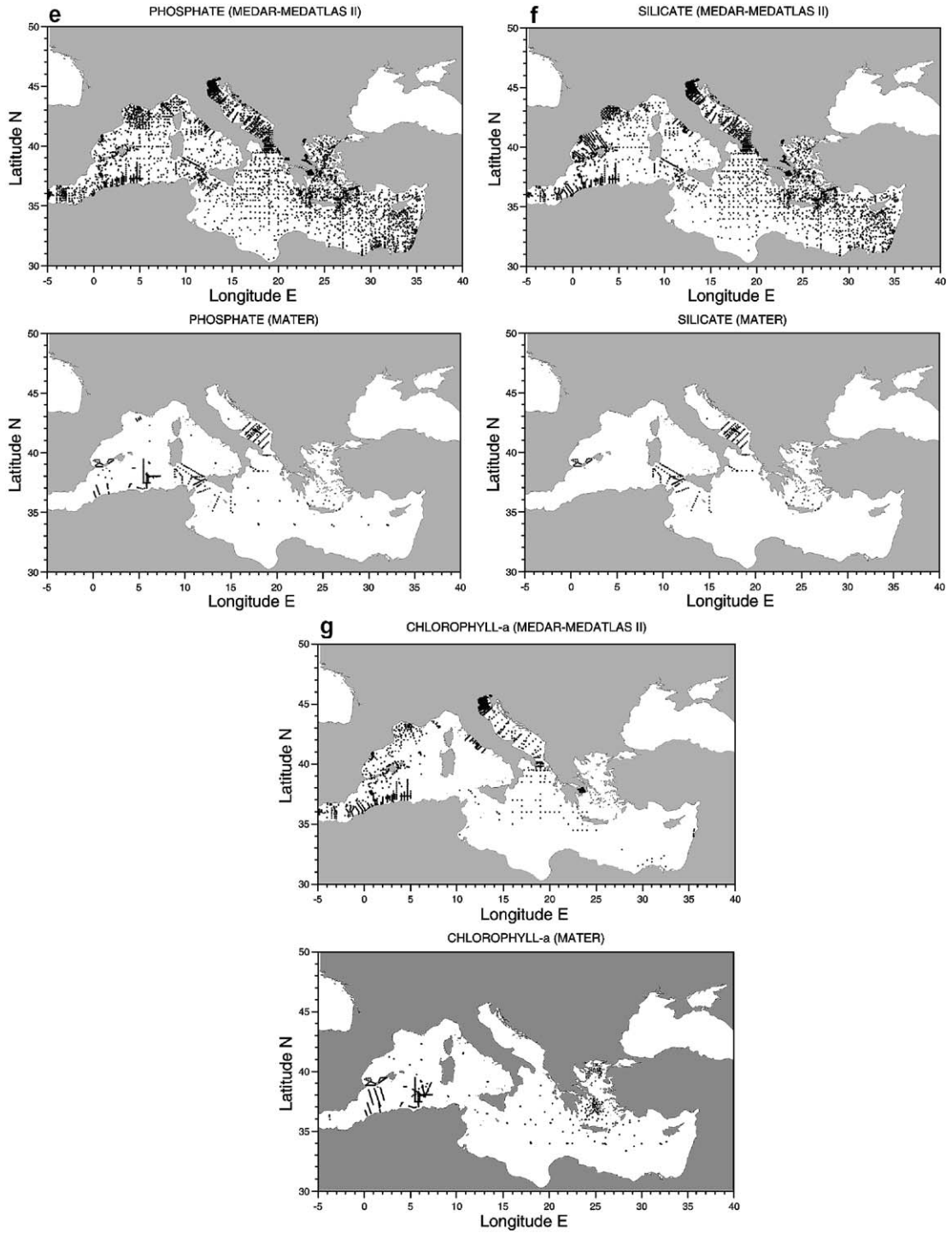


Fig. 4 (continued).

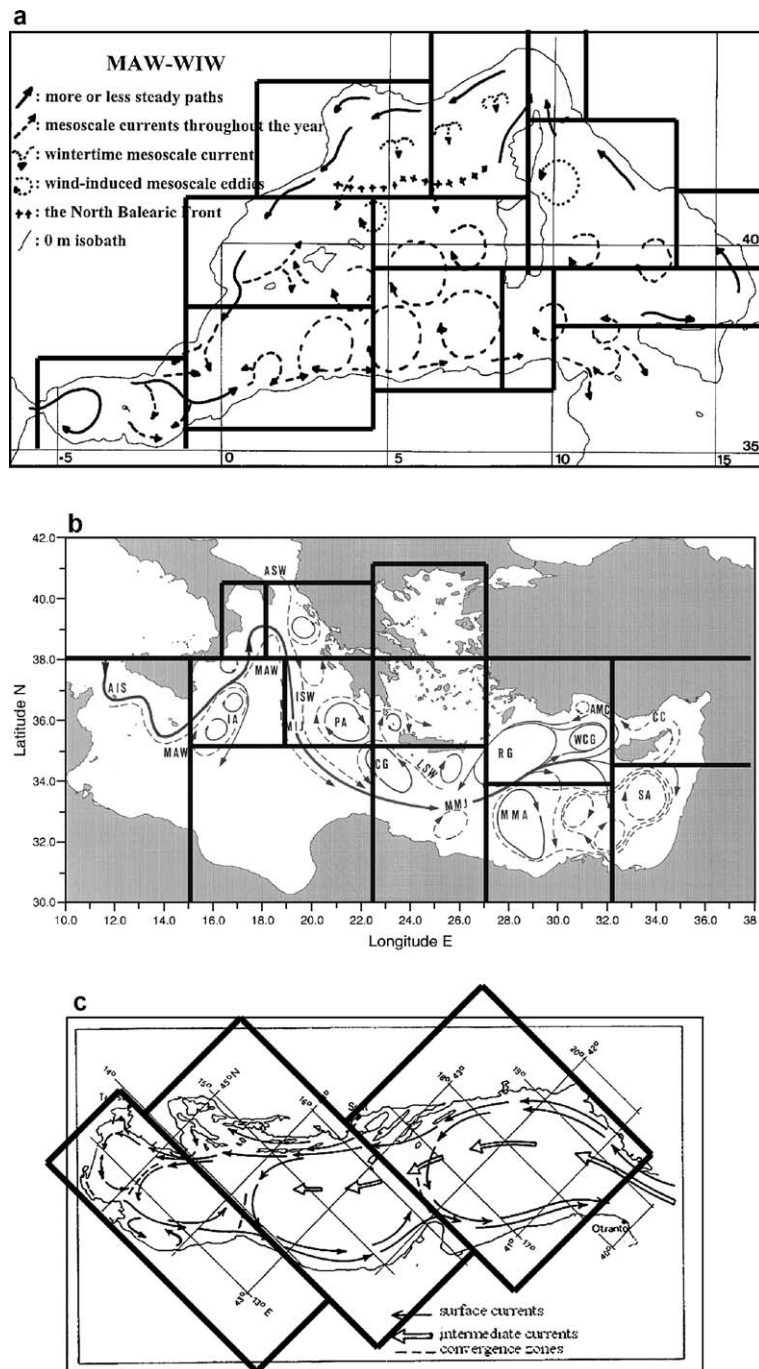


Fig. 5. Mediterranean regions defined according to the schematic representation of the upper thermohaline circulation in (a) Western Mediterranean (redrawn from Millot, 1999), (b) Eastern Mediterranean (redrawn from Robinson et al., 1991; Malanotte-Rizzoli et al., 1999) and (c) Adriatic Sea (redrawn from Mosetti, 1983).

salinity, 97% of the dissolved oxygen, 94% of the nitrate, 98% of the phosphate, 97% of the silicate, and 98% of the chlorophyll-*a* profiles.

3. Methods of analysis

3.1. Mediterranean regions defined according to general circulation patterns

Detailed hydrographic surveys conducted during the last two decades have assessed reliable schemes of the sub-basin scale thermohaline circulation and water mass pathways. Mesoscale phenomena have been traced by means of fragmentary evidence from specific surveys. Some gaps still exist, specifically over large areas in the southern regions of the Eastern Mediterranean. However, the dynamics in the regions have been recently filled with complementary information from model simulations and satellite images (Wu and Haines, 1998; Marullo et al., 1999). The schemes shown in Fig. 5 roughly represent the typical permanent features in the upper layer (0–200 m). On the basis of these schemes, the Mediterranean Sea has been subdivided into sub-regions (Fig. 5), which exhibit typical features (e.g. regions mostly affected by convective mixing vs. other regions where advective processes prevail). Fig. 6 and Table 2 summarise the nomenclatures used in the text and the basic physiography of the sub-regions defined above. It should be stressed that

the utilised circulation diagrams represent the upper sub-basin scale dynamics, exclusively. One may consider that the two deep/internal thermohaline cells in the western and eastern basin certainly possess larger scale features; therefore, the above sub-regions oversample the deep dynamics and they can be also considered to characterise the spatial variability that affect the deep layers.

3.2. Spatially and seasonally averaged vertical profiles at standard depths

Spatially and temporally averaged vertical profiles of physical and chemical parameters (i.e. temperature, salinity, dissolved oxygen, nitrate, phosphate, silicate and chlorophyll-*a* concentrations) were constituted considering hydrological casts within the above-defined regions, separately and over seasonal periods. Table 3 summarises the total amount of hydrological stations available in each region and for each considered parameter to conduct the present analysis. Thirty-four standard levels (0, 5, 10, 20, 30, 40, 50, 75, 100, 125, 150, 200, 250, 300, 400, 500, 600, 700, 800, 900, 1000, 1100, 1200, 1300, 1400, 1500, 1750, 2000, 2500, 3000, 3500, 4000, 4500, 5000), which resemble the major standard levels defined in the Climatological Atlas of the World Ocean (Levitus et al., 1998) and in the MEDAR/MEDATLAS II protocols (Maillard et al., 2001), were defined to obtain more accurate “images” of the water column structure.

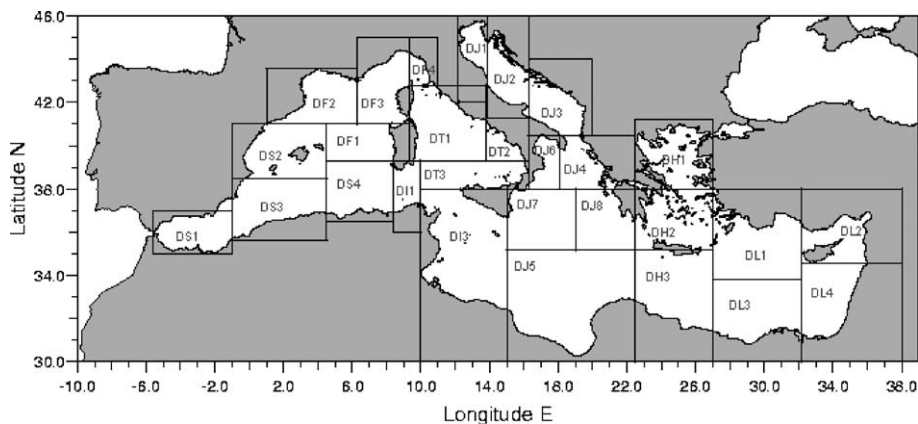


Fig. 6. Map of the Mediterranean Sea showing the geographical limits and the nomenclatures of the regions defined in Fig. 5 (cf. Table 2).

Table 2

Geographic limits and basic physiography of the Mediterranean regions defined according to the schematic thermohaline circulation features (cf. Fig. 5)

Code	Region	Lat N (min)	Lat N (max)	Lon E (min)	Lon E (max)	Depth (m)	Volume (km ³)
<i>Western Mediterranean</i>							
DF2	Gulf of Lions	41 00'	43 36'	01 00'	06 18'	2642	117,629
DF3	Liguro-Provençal	41 00'	45 00'	06 18'	09 18'	2791	151,632
DF4	Ligurian East	42 48'	45 00'	09 18'	11 00'	1146	3592
DS2	Balearic Sea	38 30'	41 00'	−01 00'	04 30'	2653	105,501
DF1	Algero-Provençal	39 18'	41 00'	04 30'	09 18'	2791	140,658
DS1	Alboran Sea	35 00'	37 30'	−05 36'	−01 00'	2583	48,954
DS3	Algerian West	35 36'	38 30'	−01 00'	04 30'	2728	208,249
DS4	Algerian East	36 30'	39 18'	04 30'	08 24'	2799	209,205
DT1	Tyrrhenian North	39 18'	42 48'	09 18'	13 48'	3991	185,963
DT2	Tyrrhenian East	39 18'	41 18'	13 48'	16 16'	3451	26,888
DT3	Tyrrhenian South	38 00'	39 18'	10 00'	16 16'	3446	114,422
DI1	Sardinia Channel	36 00'	39 18'	08 24'	10 00'	2529	24,477
DI3	Sicily Strait	30 00'	38 00'	10 00'	15 00'	1611	54,624
<i>Eastern Mediterranean</i>							
DJ1	Adriatic North	42 00'	46 00'	12 10'	13 50'	63	548
DJ2	Adriatic Middle	41 18'	46 00'	13 50'	16 16'	258	4344
DJ3	Adriatic South	40 36'	44 00'	16 16'	20 00'	1211	24,425
DJ6	Ionian North–West	38 00'	40 30'	16 16'	18 05'	2758	36,387
DJ4	Ionian North–East	38 00'	40 30'	18 05'	22 30'	3647	75,994
DJ7	Ionian Middle West	35 10'	38 00'	15 00'	19 00'	3991	290,358
DJ8	Ionian Middle East	35 10'	38 00'	19 00'	22 30'	4653	239,530
DJ5	Ionian South	30 00'	35 10'	15 00'	22 30'	3949	422,804
DH1	Aegean North	38 00'	41 12'	22 30'	27 00'	1747	23,088
DH2	Aegean South	35 10'	38 00'	22 30'	27 00'	4424	72,987
DH3	Cretan Passage	30 00'	35 10'	22 30'	27 00'	4007	264,455
DL1	Levantine North	33 50'	38 00'	27 00'	32 10'	4227	291,136
DL2	Levantine North–East	34 35'	38 00'	32 10'	38 00'	2452	47,918
DL3	Levantine South	30 00'	33 50'	27 00'	32 10'	3133	238,281
DL4	Levantine South–East	30 00'	34 35'	32 10'	38 00'	2650	116,332

The months allocated to each season were as follows: January–March for winter, April–June for spring, July–September for summer, and October–December for autumn. Vertical temperature, salinity and dissolved oxygen profiles were computed seasonally for the entire water column in all the Mediterranean regions, while for nutrients seasonal means were considered reliable for the first 0–200 m and annual means in the layer below. However, in some regions where the winter convection may play a major role in vertical water column homogenisation, as in the Gulf of Lions, in the Adriatic Sea and in the Rhodes gyre area, the amount of the available data allowed us to calculate seasonal profiles over the entire water column.

The observed levels for each hydrographic cast were converted to the standard depths using a weighted parabolic interpolation method (Reiniger and Ross, 1968). The final composition of the climatological profiles included the averaged vertical profiles along with the relevant computed standard deviation. In order to avoid the influence of extreme and possibly erroneous values or large biases derived from the coastal stations, the statistical analysis was reiterated once. After computing primary means and standard deviations, the data departing from the mean by more than one standard deviation, in absolute value, were rejected. The rejected data were less than 20–30% of the total measurements. The graphic representation of the

Table 3

Total number of hydrological casts used to calculate the spatially averaged vertical profiles of TEMP=temperature, PSAL=salinity according to the practical salinity scale, DOX1=dissolved oxygen, NTRA=nitrate, PHOS=phosphate, SLCA=silicate, and CPHL=chlorophyll-*a*, in the different regions of the Mediterranean Sea (data from CD-ROMs MEDAR/MEDATLAS II, 2002 and MTP II/MATER, 2001)

Code	Region	TEMP	PSAL	DOX1	NTRA	PHOS	SLCA	CPHL
<i>Western Mediterranean</i>								
DF2	Gulf of Lions	13,859	12,625	10,517	4998	6498	11,613	11,955
DF3	Liguro-Provençal	16,800	16,380	12,281	15,345	12,350	12,650	11,739
DF4	Ligurian East	3254	3180	3127	38	1288	498	0
DS2	Balearic Sea	7768	7523	6296	4937	4710	6484	6497
DF1	Algero-Provençal	3694	3641	3499	2053	2507	2455	2536
DS1	Alboran Sea	15,374	14,235	10,361	9148	10,304	9687	10,578
DS3	Algerian West	11,909	9482	6150	7456	7318	6642	9797
DS4	Algerian East	7670	6417	4250	4253	4199	2739	4023
DT1	Tyrrhenian North	10,495	10,386	9172	7026	8622	6508	1059
DT2	Tyrrhenian East	1475	1470	1231	0	822	0	0
DT3	Tyrrhenian South	7804	6662	5784	4573	4705	4472	10
DI1	Sardinia Channel	4134	3640	2784	1176	1681	1162	3
DI3	Sicily Strait	10,410	9934	9557	8545	8513	8398	6951
<i>Eastern Mediterranean</i>								
DJ1	Adriatic North	8253	8169	6129	5896	5406	6129	638
DJ2	Adriatic Middle	4832	4721	2868	2581	2451	3323	428
DJ3	Adriatic South	7379	6906	4611	4041	4193	4079	1230
DJ6	Ionian North–West	1834	1670	1591	597	795	597	0
DJ4	Ionian North–East	4023	3848	3624	2998	3150	3233	1156
DJ7	Ionian Middle West	17,226	16,694	13,727	13,386	13,347	14,196	5
DJ8	Ionian Middle East	7608	7078	7035	6007	6007	5610	7
DJ5	Ionian South	5953	5879	5832	4496	4464	3777	25
DH1	Aegean North	6784	6362	6144	4183	4950	4717	3014
DH2	Aegean South	10,558	10,230	10,100	9737	9777	9580	5549
DH3	Cretan Passage	8353	8256	8148	7826	6119	7871	14
DL1	Levantine North	7992	7698	7650	5794	6791	5436	22
DL2	Levantine North–East	1640	1636	1642	932	933	1181	0
DL3	Levantine South	5312	5159	5156	2410	3280	4089	1434
DL4	Levantine South–East	9151	9136	8941	6563	7107	6418	5081
Total		221,544	209,017	178,207	146,995	152,287	153,544	83,751

spatially averaged vertical profiles of dissolved oxygen and nutrients, as shown in the following, have been obtained after a three-point “running average” smoothing filter.

4. Results and discussion

4.1. Western Mediterranean regions

The spatial variability in the Western Mediterranean is discussed by comparing the averaged vertical profiles in three regions: the Gulf of Lions (region-DF2), the Tyrrhenian Sea (region-DT1) and the Algerian basin (region-DS4).

The Gulf of Lions is mainly characterised by a permanent cyclonic circulation and manifests strong seasonal variations of the physical and biochemical properties (Fig. 7) due to convective movements and deep mixing during the wintertime. The seasonal thermocline extends to a depth of 50 m in summer (Fig. 7a); it is deeper in autumn reaching down to 100 m. In summer, stratification conditions and the prevailing northwesterlies allow the spreading of the less saline AW (Fig. 7b) transported by the Ligurian Current (Millot, 1999). In winter, the deep convection sets the homogenisation of the water column (Fig. 7a) bringing saline water from the intermediate layer close to the surface (Fig. 7b). Typical values indicate a salinity increase of about $\Delta S=0.55 \pm 0.32$ at the sur-

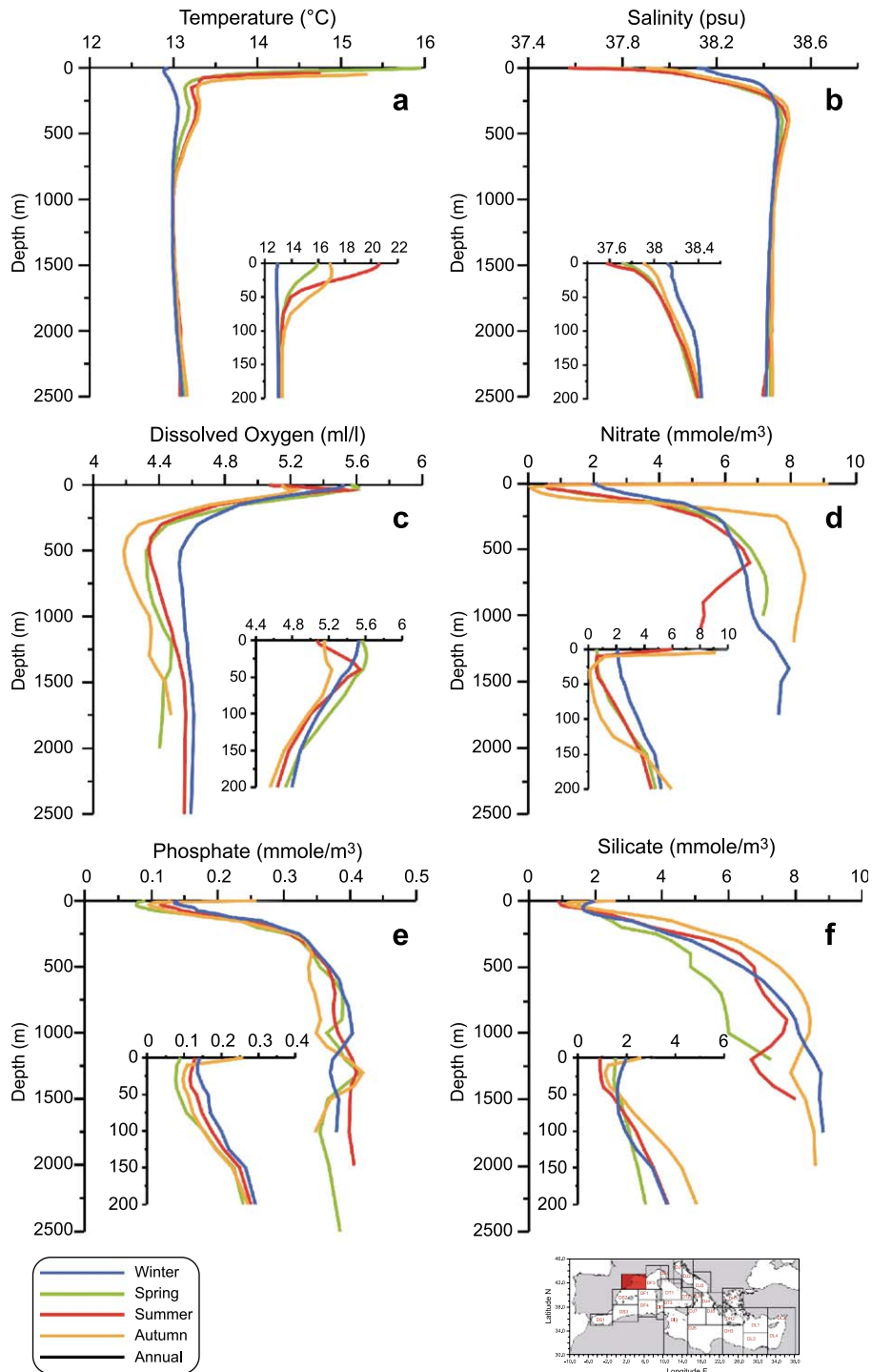


Fig. 7. Seasonally averaged vertical profiles of (a) temperature, (b) salinity, (c) dissolved oxygen, (d) nitrates, (e) phosphates, and (f) silicates in the NW region of the western Mediterranean (DF2—Gulf of Lions). The insets indicate the shallower portion of the profiles.

face and $\Delta S = 0.16 \pm 0.09$ at a depth level of 100 m; on the contrary, the salinity decreases ($\sim 0.04 \pm 0.03$) in the LIW layer, which occupies the 200- and 800-m depth interval.

Similar patterns also appear in the oxygen and nutrient profiles (Fig. 7c–f). In winter, a rather high ventilation (oxygen content $> 5.4 \text{ ml l}^{-1}$) and enrichment of nutrients ($\sim 2.1 \text{ mmol m}^{-3}$ for nitrate and $\sim 0.14 \text{ mmol m}^{-3}$ for phosphate) is evident in the upper water column, whilst an almost nutrient depleted layer is established in summer and autumn. In summer, the upper water column is topped by relatively low-oxygen layer; a shallow oxygen maximum located at 40–50 m retains the same concentration as in winter. However, biological activity cannot be neglected, and the oxygen increase derives from the general phytoplankton bloom that occurs at the beginning of spring (Coste et al., 1972). Nutrients are consumed between winter and summer and phosphates appear utilised more rapidly. During the stratification period, the highest nutrient concentrations appear at the surface and sharply decreases to a depth of about 5–10 m; this is clearly due to the Rhone river discharge that constitutes the major runoff to the western basin (Béthoux et al., 1992). The permanent nutricline is well established at 100–150 m during the stratification seasons, whilst it moves upward to the base of the euphotic zone in winter. Deep waters reveal an oxygen minimum ($\text{O}_2 \sim 4.2\text{--}4.6 \text{ ml l}^{-1}$) at about 500 m associated with the LIW layer; below this layer, abnormally high nutrient concentrations ($\text{NO}_3 = 8.1 \text{ mmol m}^{-3}$; $\text{PO}_4 = 0.40 \text{ mmol m}^{-3}$; $\text{Si} = 8.5 \text{ mmol m}^{-3}$) result from terrestrial inputs, and from the mineralization processes related to the oxidation of the organic matter precipitating from the euphotic zone (Béthoux et al., 1992).

Seasonally averaged vertical profiles of temperature and salinity in the Algerian basin and in the Tyrrhenian Sea are depicted in Figs. 8 and 9, respectively. The temperatures in the upper water column display similar behaviour in the two regions over the entire annual cycle. In summer, the surface waters are essentially stratified and attain the same temperature values; in the winter months, the thermocline disappears almost completely leading to the formation of a vertically homogenised water column down to the bottom; the surface temperatures reach climatological values of $\sim 14.0 \text{ }^\circ\text{C}$ in the Tyrrhenian Sea and ~ 14.5

$^\circ\text{C}$ in the Algerian basin. Note also the strong north–south gradient, considering the very low climatological value of $\sim 13 \text{ }^\circ\text{C}$ in the northern convection region (Fig. 7a). The salinity profiles reflect the advective explanation of salinity changes in the Western Mediterranean given by Millot (1999); it is mainly dictated by the westward propagation of Atlantic water, which results relatively fresher in the Algerian basin than in the Tyrrhenian Sea.

In the intermediate layer, the water column structures between 250 and 750 m emphasise the presence of relatively high temperature and salinity values indicating the LIW. These features are much more pronounced in the Tyrrhenian basin (Fig. 9) than in the Algerian basin (Fig. 8), in agreement with the circulation pattern of the LIW schematically depicted by Millot (1999) in his Fig. 2. However, in the Tyrrhenian Sea the LIW properties change during the year displaying a maximum of salinity in autumn. In winter, the salinity in the LIW core decreases (Fig. 9b) due to the vertical mixing in the nearly permanent cyclonic gyre (Sparnocchia et al., 1994).

Hydrographic properties in the deep part of the Tyrrhenian Sea (Tyrrhenian Deep Water—TDW) exhibit higher climatological temperature and salinity values ($\Delta t \sim 0.17 \text{ }^\circ\text{C}$; $\Delta S \sim 0.04$) than those observed for the WMDW at the formation site. These results are in agreement with the observations of Sparnocchia et al. (1999), which indicated that significant amounts of Eastern Mediterranean transitional and deep waters flow through the Strait of Sicily below the LIW into the Tyrrhenian basin where they sink and mix with the ambient Western Mediterranean waters.

Fig. 10 addresses the spatial variability of the hydro-chemical properties in the Western Mediterranean, showing the differences between the annually averaged vertical profiles for the three regions mentioned above. The purpose of this analysis is to assess the role of the upper/external and the deep/internal ‘conveyor belts’ in defining the biochemical characteristics of the water masses throughout the Western Mediterranean. The oxygen minimum layer is found at $\sim 500 \text{ m}$ and it is more pronounced in the Algerian basin, in agreement with the decrease in the salinity of the LIW core, because more time is needed for the LIW to flow into the Algerian basin after its recirculation in the Tyrrhenian Sea. In the layer below, the oxygen content shows more pronounced positive

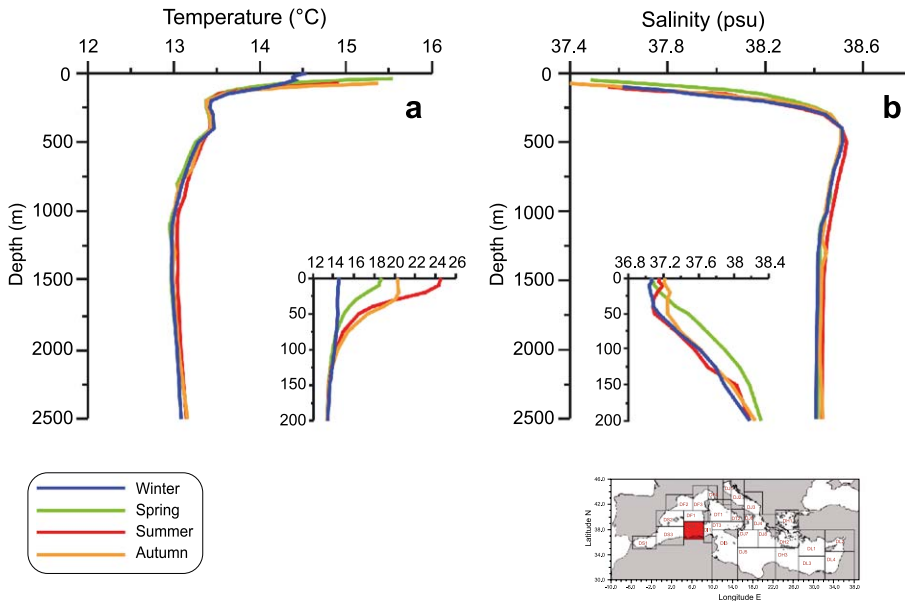


Fig. 8. Seasonally averaged vertical profiles of (a) temperature, and (b) salinity in the southern region of the western Mediterranean (DS4—Algerian basin). The insets indicate the shallower portion of the profiles.

anomalies in the northwestern basin, indicative of the region prone to the deep convection. The WMDW formed there moves into the Algerian basin and then into the Tyrrhenian Sea. The profiles of nutrients (Fig.

10b–d) exhibit remarkable spatial variations. The upper waters overlying the permanent nutricline (<200 m) are generally poor in nutrients; however, their values are higher in the Gulf of Lions. In the

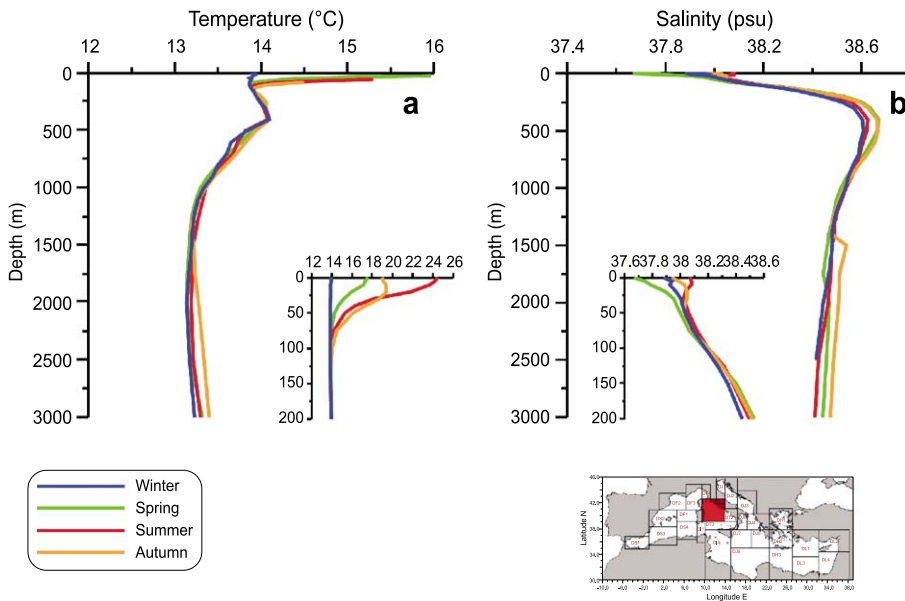


Fig. 9. As for Fig. 8 but for the Tyrrhenian Sea (DT1).

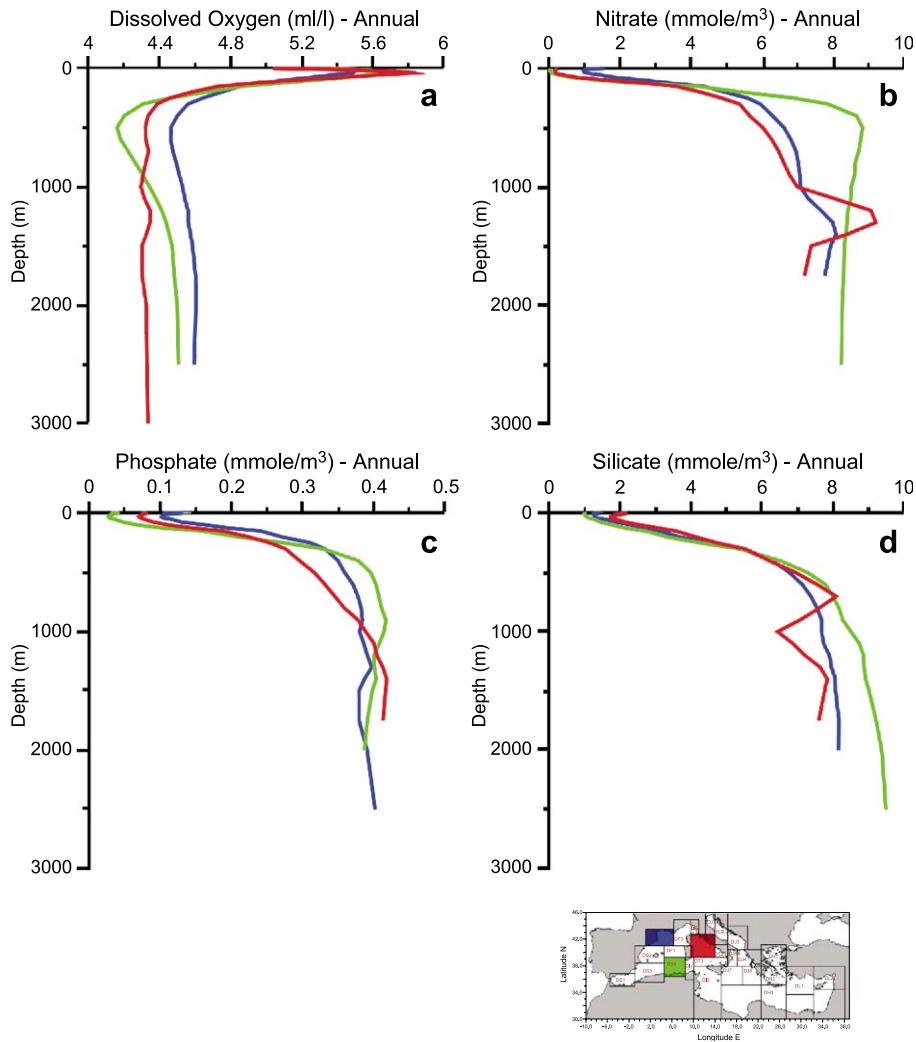


Fig. 10. Superimposed annually averaged vertical profiles of hydrographic parameters for selected regions (see inset map) in the western Mediterranean: (a) dissolved oxygen, (b) nitrate, (c) phosphate, and (d) silicate.

other regions, the photic zone exhibits lower nutrient concentrations, close to the detectable limits, generally attributed to phytoplankton consumption and the scarce supply of nutrient-rich waters from the deep layer. The vertical profiles of nutrients are almost mirror images of those of the dissolved oxygen. The high spatial variability mostly reflects the advective process of the involved water masses. The highest values of nitrate and phosphate concentrations (Fig. 10b and c) are at ~ 500 m, i.e. at the same depth of the oxygen minimum, and are higher in the Algerian basin than in other areas. These features may elucidate

some questions raised by many authors about the preferential pathway of the LIW in the Western Mediterranean (Millot, 1999; Sparnocchia et al., 1999); the climatological fields of the oxygen and nutrient concentrations confirm the results obtained from the analysis of the salinity profiles earlier. The silicates in the deep waters (>500 m) always exceed 7 mmol m^{-3} throughout the year (Fig. 10d). The highest values above 9 mmol m^{-3} in the Algerian basin imply long residence times and poor ventilation, whilst lower silicates ($\sim 8 \text{ mmol m}^{-3}$) in the convection region are representative of the WMDW of more

recent formation. The poor estimates for this parameter in the deep Tyrrhenian basin are in large part due to the lack of data in this region.

The chlorophyll-*a* data contained in the databases are scarce and did not allow the elaboration of seasonal profiles for all the regions in the Western Mediterranean due to gaps in the spatio-temporal distributions. In order to infer the seasonal variation, we present the vertical profiles relative to the Gulf of Lions (Fig. 11a), which exhibits strong differences with respect to other regions, while Fig. 11b illustrates the spatial variability among the three regions indicated in the inset map during spring.

In the Gulf of Lions, the highest surface phytoplankton biomass develops in winter and spring due to the violent mixing and vertical injections of nutrient-rich deep waters in the open-sea convective region; the vertical profiles also show sustained phytoplankton activity at depth in winter, while during the rest of the year, the depletion of dissolved inorganic nutrients in the photic zone reflects low chlorophyll-*a* concentrations. In late winter and early spring, the phytoplankton growth is indicated in the subsurface waters, as shown by the peaks of the chlorophyll-*a* maximum at ~ 10 m. Peak concentrations are found at depths of

50–70 m in summer and in autumn, the so-called Deep Chlorophyll Maximum (DCM) typical of the oligotrophic character of the Mediterranean Sea (Crise et al., 1999), corresponding to the subsurface oxygen maximum. The basic behaviour of the vertical chlorophyll-*a* distribution, characterised by the presence of the DCM, is also maintained in other regions (Fig. 11b). The vertical profiles shown in Fig. 11b refer only to spring, since the database contains very little chlorophyll-*a* data relating to the summer, and does not contain any data at all for winter and autumn. Away from the Gulf of Lions, the DCM seems much weaker and deeper (~ 50–75 m) and closely follows the depth of the nutricline.

4.2. Eastern Mediterranean regions

4.2.1. The Adriatic Sea

The Adriatic Sea has been subdivided into three sub-basins, which exhibit different general oceanographic characteristics (Fig. 5c). A collection of an unprecedented amount of hydrological data in the Southern Adriatic Sea allows a more refined analysis than that performed by Zavatarelli et al. (1998) of the seasonal variability of water mass structures and

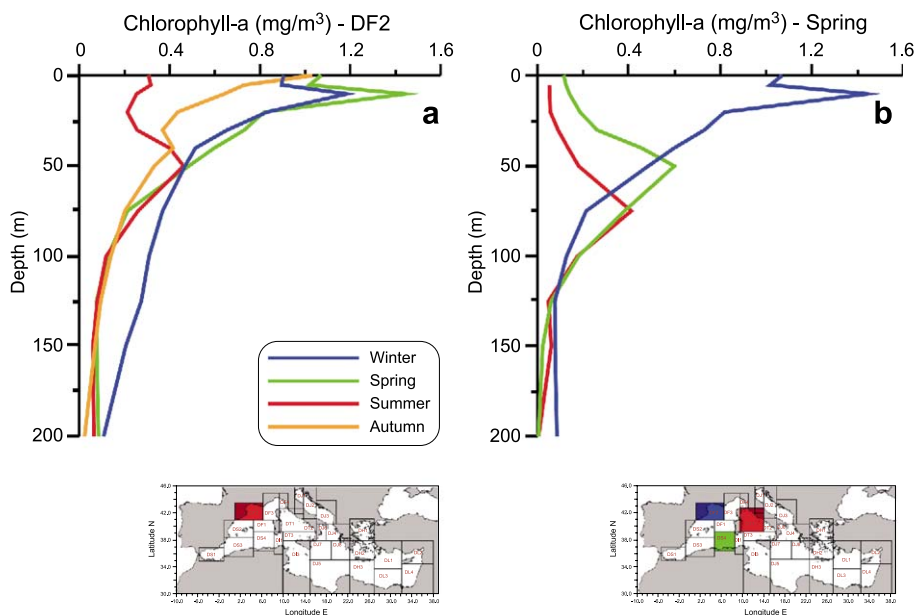


Fig. 11. Superimposed averaged vertical profiles of chlorophyll-*a*: (a) seasonal variations in the Gulf of Lions; (b) spring climatology for the regions indicated in the inset map.

biochemical properties. Fig. 12 shows the seasonally averaged vertical profiles of temperature, salinity, oxygen and nutrients in the southern region (DJ3). The temperature and salinity profiles (Fig. 12a and b) manifest a three-layer thermohaline structure. In the surface layer (0–150 m), the temperature profiles reflect basically the seasonal cycle. The surface waters are periodically exposed during wintertime to convective processes (Ovchinnikov et al., 1985) able to homogenise the entire water column to a temperature of ~ 13.5 °C. In spring, the seasonal thermocline develops at approximately 75 m and extends to 100 m in summer. At the surface, an excess of the relatively fresh waters advected from the north sustains the very low static stability during winter months (Artegiani et al., 1997). The positive anomalies of temperature and salinity located between 100 and 400 m identify the LIW, which manifests its salinity maximum in autumn. The distinguishing feature in the deep layer is the decrease of temperature and salinity, which testifies either a large contribution of the cold and less saline (but dense) waters from the northern shelf in replenishing the deep trench in the Southern Adriatic Sea or a sufficient buoyancy loss of the less saline surface water during wintertime convection that would permit mixing to large depths.

The dissolved oxygen and nutrient profiles (Fig. 12c–f) display characteristics which result from the convection activity in this region during wintertime. In winter, more oxygenated water masses extend from the surface down to ~ 600 m (Fig. 12c) due to the fast convective ventilation; in contrast, less ventilated and nutrient-rich (Fig. 12d–f) waters reside beneath. In summer, it seems that the contribution of oxygen from atmosphere is not able to overcome the biological consumption. The occurrence of pronounced subsurface oxygen maxima at a depth of about 30 m accompanied by the minimum nitrate values at the same depth are, however, mostly indicative of strong biological activity. Below 50 m, the concentrations show a strong gradient zone towards low values of dissolved oxygen and high values of nutrients. The nutrient enrichment in the intermediate and deep layers (Fig. 12 d–f) reflects the advection of the LIW (Civitaresi et al., 1998), which manifests its maximum in autumn as in the case of the salinity values. In addition, contrary to the results showed by Zavatarelli et al. (1998), in large part due to the lack of

data, the convective mixing during winter has been demonstrated to be an important mechanism for the significant transfer of nutrients to the surface layer and the development of the spring phytoplankton bloom in the centre of the gyre (Gacic et al., 2002).

Interestingly, the oxygen profiles show in general an increase in the 800–1000-m depth interval during spring and summer periods accompanied by a decrease in the nutrients. This is an indication of freshly ventilated and dense waters advected from the northern shelf region rather than dense waters formed by convection to a depth greater than 600 m. These waters flow southwards driven by a bottom density current and may reach the southern latitudinal sections later in the year (Artegiani et al., 1997). There, having a density higher than the ambient water masses, they partly sink into the deep layer at the shelf break (Bignami et al., 1990; Manca et al., 2002) and partly flow against the continental slope. Both branches constitute the main component of the deep Adriatic outflow (ADW) over the sill depth (~ 850 m) through the Strait of Otranto (Manca and Giorgetti, 1998). Subsequently, the ADW sinks into the adjacent Ionian Sea and fills the bottom layer of the Eastern Mediterranean (Schlitzer et al., 1991).

The bottom water in the southern Adriatic exhibits low oxygen and high nutrient values due to the longer residence time of this water mass in the deep trench at ~ 1200 m. The silicates show a pattern similar to that of the other nutrients; the highest silicate values (~ 10 – 15 mmol m⁻³) imply a long residence time and poor ventilation.

4.2.2. The Ionian Sea

The Ionian Sea stands out as the region of the Eastern Mediterranean mainly characterised by the transit and transformation of the major water masses, i.e. the relatively fresh AW, the highly saline LIW and the colder and denser EMDW, which characterise the general thermohaline circulation in the upper, intermediate and deep layers, respectively (Malonotte-Rizzoli et al., 1997). In the Southern Ionian (region-DJ5, Fig. 6), the upper waters are mostly typified by the transit of the AW and the LIW that drive the well-known anti-estuarine circulation, whilst the properties of the deep waters are essentially determined by the deep/internal ‘conveyor belt’ driven by the dense waters of Adriatic origin. The spatially averaged deep

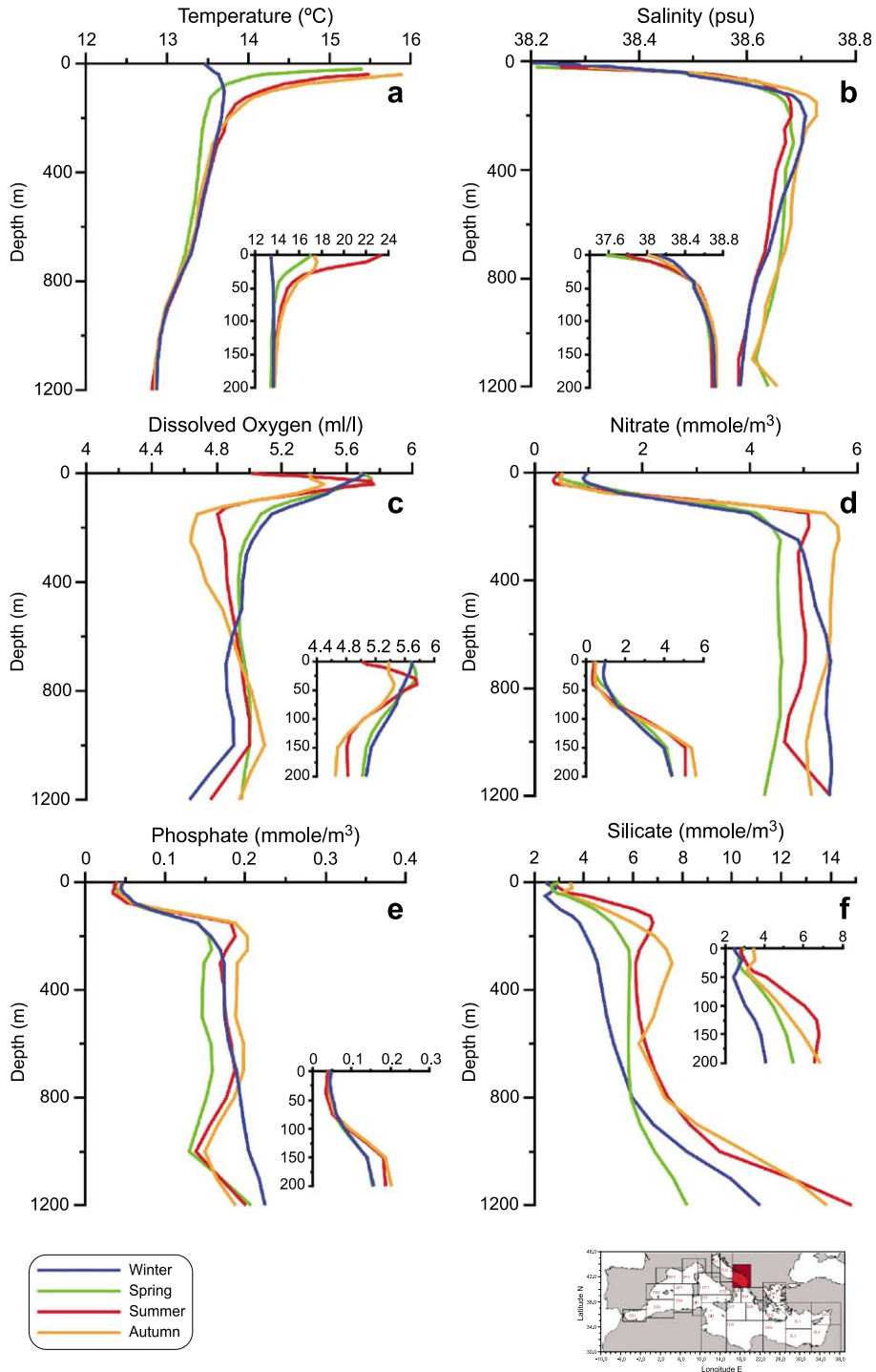


Fig. 12. Seasonally averaged vertical profiles of (a) temperature, (b) salinity, (c) dissolved oxygen, (d) nitrates, (e) phosphates, and (f) silicates in the southern Adriatic (DJ3). The insets indicate the shallower portion of the profiles.

profiles calculated from the data available in this region are shown in Fig. 13.

In the surface layer (0–150 m), the lowest salinity indicates AW that, after passing the Strait of Sicily, undergoes substantial modification along the way towards the Levantine basin. The seasonal thermocline extends down to 50–75 m (Fig. 13a); the most prominent feature appears during the stratified seasons when the excess of evaporation isolates less saline AW in the sub-surface layer at ~50 m (Fig. 13b). Below 100 m, the water column exhibits almost permanent conditions of stratification mostly sustained by the sharp salinity gradient. The seasonal oxygen cycle (Fig. 13c) exhibits a subsurface maximum in summer and in autumn at about 50 m. The nutrient distributions (Fig. 13d and e) show that the photic layer is almost nutrient depleted throughout the year without appreciable seasonal variations indicating weak vertical mixing from the deep layer in winter months. However, the feeble mixing and ventilation processes occurring during the wintertime cause the nutrients to become available in the photic layer where they are quickly utilised in phytoplankton production processes that in the Ionian may occur rather early in the year (Napolitano et al., 2000). Moreover, the subsurface production has been seen in model simulations to occur below the thermocline also in June with a maximum of biomass in addition to that of the phytoplankton bloom in spring, giving conditions of higher oxygen concentrations and very low nitrate contents in the subsurface layer (Fig. 13c–e). The silicates (Fig. 13f) display some artefacts in the upper layer in winter and summer despite the selection of the data with specific quality flags, while in the other two seasons the profiles overlap, showing a behaviour that is very similar to those of nitrates and phosphates.

The intermediate layer is dominated by the LIW (~200–600 m), typified by the salinity maximum that develops below the well-pronounced thermocline. The salinity in the LIW layer displays strong seasonal variability; in summer and autumn it spreads westward towards the Strait of Sicily purer than in the other seasons. The decrease of salinity manifests during the seasons prone to the mixing and it is certainly due to the vertical exchange with the less saline AW above. An upper limit of about 8 years has been estimated for the apparent travel time of LIW to

the Strait of Sicily from CFC ages distribution (Roether et al., 1998). The water masses below the LIW layer (~600–1200 m) present almost steady seasonal conditions, mostly characterised by the slow decrease of both temperature and salinity, due to the mixing of the LIW with the relatively fresh EMDW of Adriatic origin (Schlitzer et al., 1991). This layer, named the transitional layer in recent literature (Malonotte-Rizzoli et al., 1997), is mostly characterised by the ‘oldest’ water mass and the highest nutrient content, essentially due to a high oxygen consumption rate and very low convective renewal (Roether and Well, 2001).

In the deep layer, one would expect almost steady seasonal conditions with the exception of the convective regions; on the contrary, the more heterogeneous deep waters have multiple sources, which include the Adriatic, the Aegean and, on some occasions, the Rhodes Gyre region (Sur et al., 1992). The major complication in the assessment of the value of the temperature and salinity climatologies is the effect of the profound changes in the status of the Eastern Mediterranean which have occurred since the early 1990s (Roether et al., 1996). The large deviations below 1200 m, as shown in Fig. 13a and b, reflect water intrusions due to the EMT, and the seasonal variations depend on when the cruises were carried out.

Retrospective analyses of the historical deep profiles have been conducted by many authors (Özsoy and Latif, 1996; Lascaratos et al., 1999; CIESM, 2002) considering different regions in the Eastern Mediterranean, with the objective of distinguishing the climatic event and in particular with the attempt to identify further events that could have influenced the properties of the most important water masses in the past regime. In this study, the temperature and salinity data pertinent to the entire Ionian and Levantine basins were grouped separately in 1-year intervals since 1950 and volume-averaged in the depth interval from 1200 to the bottom (i.e. the deep layer mainly influenced by the transient event; Roether et al., 1996) to produce a time series. In Fig. 14, we illustrate the time sequence of the averaged potential temperature and salinity in the deep Ionian Sea. It is notable that, with the exception of some suspect values of salinity in terms of accuracy, the salinity field has fluctuated at least three times in the last 50 years, i.e. in the 1960s,

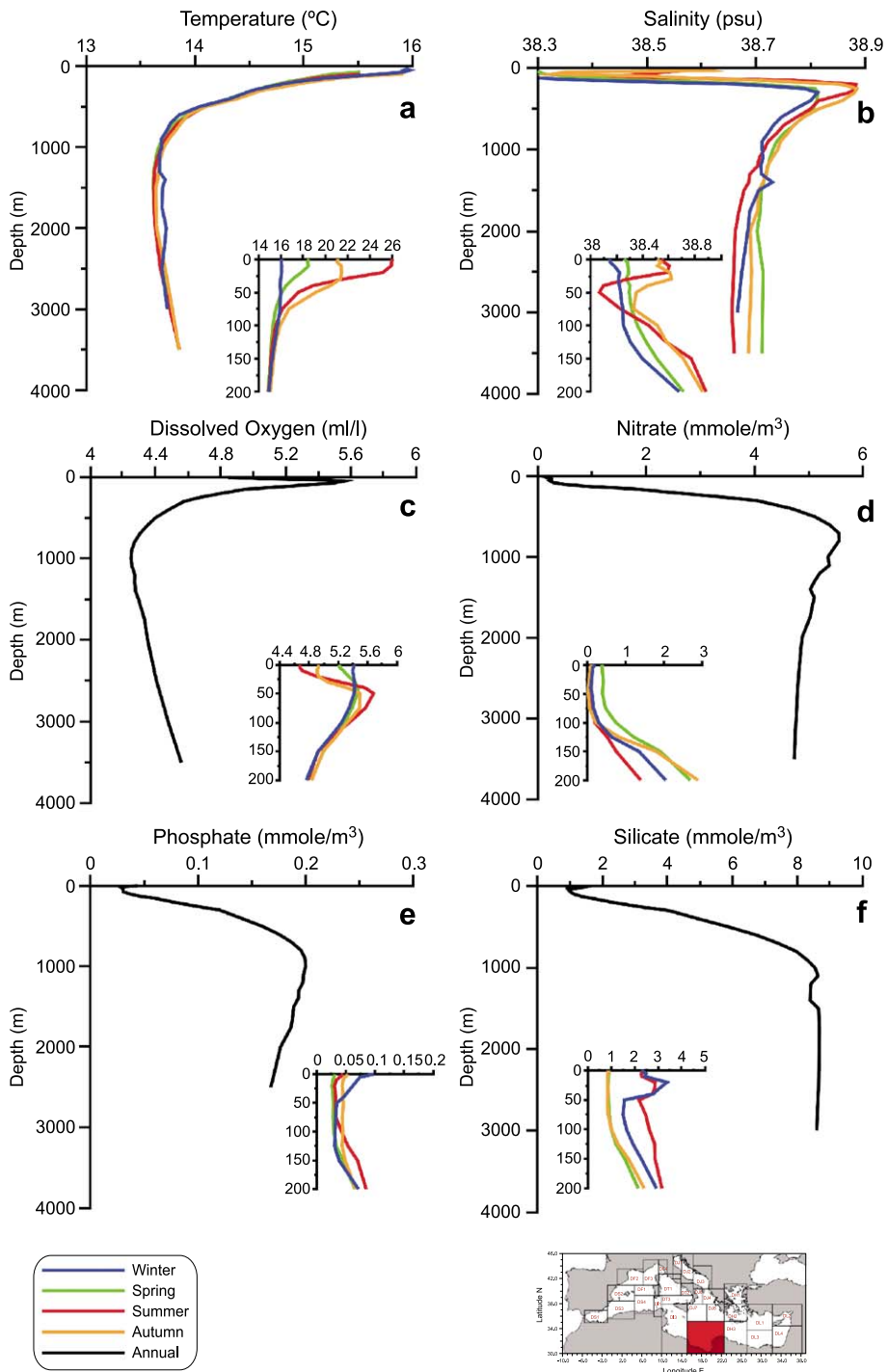


Fig. 13. Seasonally averaged vertical profiles of (a) temperature, (b) salinity. Annual-averaged vertical profiles of (c) dissolved oxygen, (d) nitrates, (e) phosphates, and (f) silicates in the southern region of the Ionian Sea (DJ5—South Ionian). The insets indicate seasonal variations in the shallower portion of the profiles.

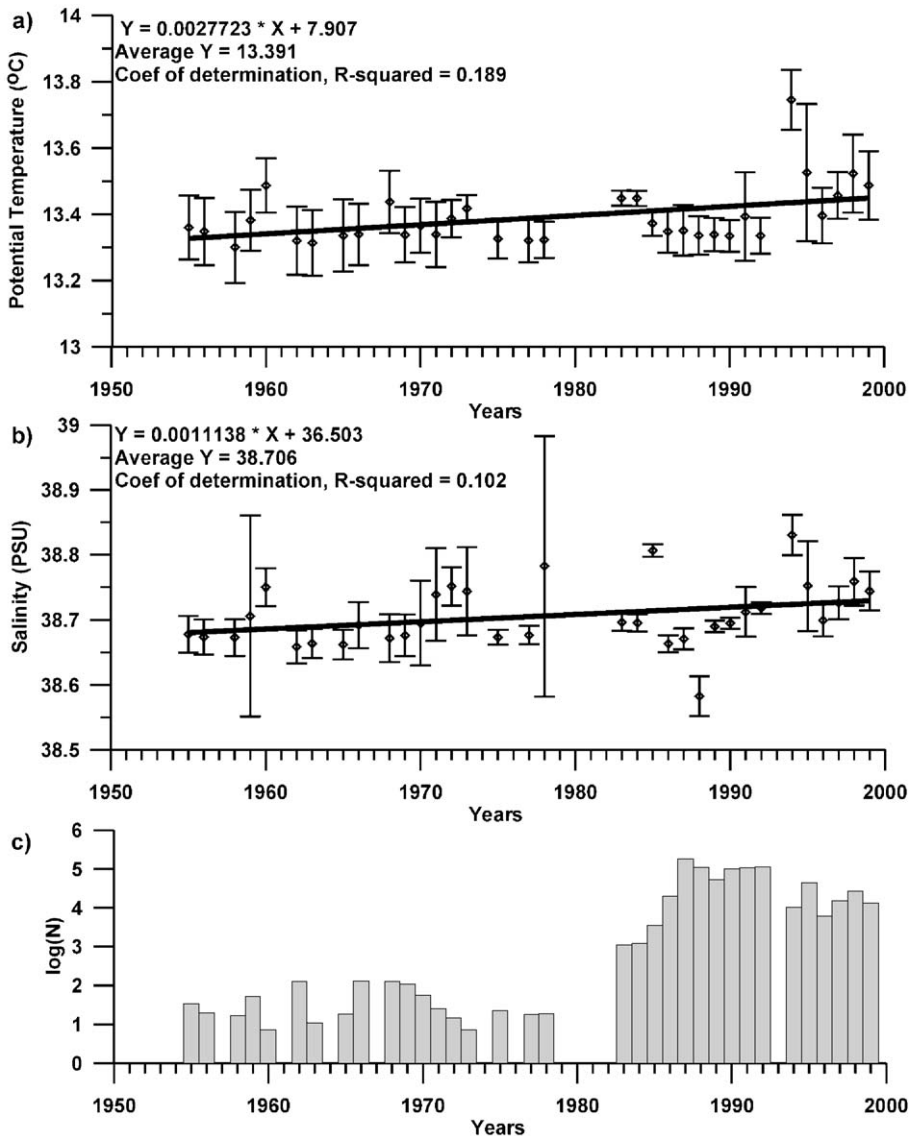


Fig. 14. Long-term changes in (a) potential temperature (°C) and (b) salinity. Number of data points (c) in the Ionian deep waters (>1200 m) obtained by grouping the hydrological profiles annually. The vertical bars denote one standard deviation confidence intervals. The linear regression lines and the r^2 correlation coefficients are indicated.

in the 1970s and in the 1990s, starting with the last increase in 1986. However, an overall trend of about 0.001 per year can be inferred for the salinity. The temperature shows a positive trend with an annual increment of about 0.003 °C per year. In order to reach firm conclusion in using the climatologies for future narrow range checks in the deep layer, we propose the combined use of seasonal climatologies

for the upper and intermediate layer, while the annual-averaged vertical profiles may be adopted for the deep waters; the actual climatological values can be further adjusted by trends.

4.2.3. The Levantine basin and the Rhodes gyre

A number of studies based on quasi-synoptic basin-wide surveys conducted in the Levantine basin

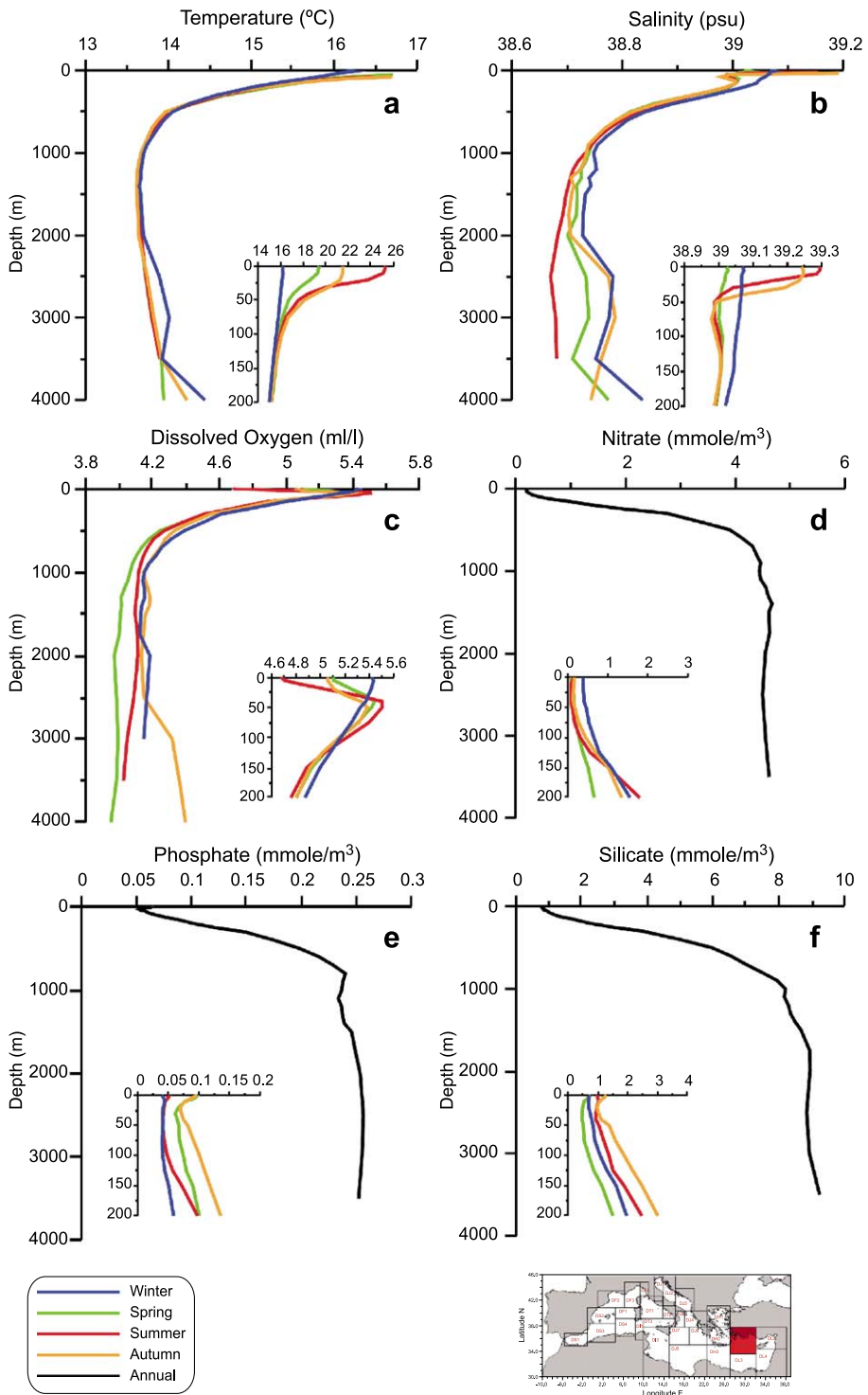
have shown that the thermohaline circulation is mainly characterised by a cyclonic region in the north and a series of anticyclones in the south (POEM Group, 1992 and Fig. 5b). In the northern cyclonic region, under prolonged winter conditions, the upper water column presents a well mixed layer which extends down to about 200 m. Typical isopycnals at surface are in the range of 29.00–29.05 kg m^{-3} ; therefore, a moderate dense water forms, i.e. the LIW, regarded as the most important water mass of the Mediterranean (Özsoy et al., 1993). Deeper and more efficient mixing conditions were observed during severe winter leading to the formation of a variety of Eastern Mediterranean deep water, the Levantine Deep Water (Sur et al., 1992), which results warmer and saltier than the EMDW. In this region, during winter, the nutricline reaches the photic zone bringing relatively nutrient-poor deep-water masses close to the surface for biological consumption. These features in addition to a very limited external input of nutrients essentially make the Levantine basin one of the most oligotrophic regions of the Mediterranean (Yilmaz and Tuğrul, 1998). On the other hand, stratified conditions prevail in the southern region; under the influence of anticyclonic motion, the pycnocline deepens to ~450 m, creating fairly constant distributions of high temperature, salinity and dissolved oxygen, and low nutrients (Krom et al., 1992). In the deep layer, no seasonal variations and spatial differences were noticed in nutrient concentrations, apart from a weak eastward oxygen decrease and silicate increase (Kress and Herut, 2001).

Fig. 15 depicts the climatological profiles in the northern region of the Levantine basin. In the upper layer, climatological temperatures span over a wide range from 16 to 25.5 °C (Fig. 15a). The salinities at the surface reflect the conspicuous effect of the high evaporation rate, reaching values higher than 39.2 in summer and in autumn. During the warm seasons, the highly saline Levantine Surface Water (LSW) forms in the surface layer up to ~50 m. In the layer below, a strong halocline exists between the LSW and the AW; the latter may be recognised

in the subsurface layer by the minimum of salinity (<39.0) at ~75 m (Fig. 15b). In winter and spring, the salinity decreases due to winter mixing of the LSW with the less saline water of Atlantic origin that upwells in the Rhodes cyclonic gyre. However, most of the salt accumulated at the surface by strong evaporative processes is transferred into the layer below (0–500 m) due to the intensification of the Rhodes gyre and continuous water column overturning.

In the deep layer, below 1000 m, the large difference in the seasonal profiles of temperature and salinity mostly derives from the dense water of Aegean origin. As for the Ionian Sea, we investigated the evolution of the water mass properties in the deep Levantine basin (1200–bottom) by constructing time series of potential temperature and salinity from yearly volume-averaged vertical profiles (Fig. 16). Evidence of a warming trend and an associated salinity increase emerges from these analyses; however, the linear correlations were not significant. On the other hand, despite the larger error bars during the era of the bottle casts, two very distinct episodes of large fluctuations in salinity can be noted, i.e. in the 1960s and in the 1990s. The latter starts in 1987 as in the Ionian Sea. It has been speculated that, while the second episode in the early 1990s is clearly related to the EMT, the one which occurred in the early 1970s seems to originate in the Levantine basin where it has shown the maximum signal (Theocharis et al., 2002). In brief, the climatological characteristics of the physical properties (temperature and salinity) show seasonal differences that depend on the EMT. However, this may be largely due to the fact that a great part of the seasonal data were obtained from specific surveys conducted more recently, i.e. following the appearance of the EMT, whereas very little relevant data is available for the earlier years in the historical database. Therefore, for future application of the climatological profiles in data quality checks related to the deep waters in the Eastern Mediterranean, we propose the use of regional climatologies computed on an annual basis from the entire data set.

Fig. 15. Seasonally averaged vertical profiles of (a) temperature, (b) salinity, and (c) dissolved oxygen. Annually averaged of (d) nitrates, (e) phosphates, and (f) silicates in the NE region of the eastern Mediterranean (DL1—North Levantine). The insets indicate seasonal variations in the shallower portion of the profiles.



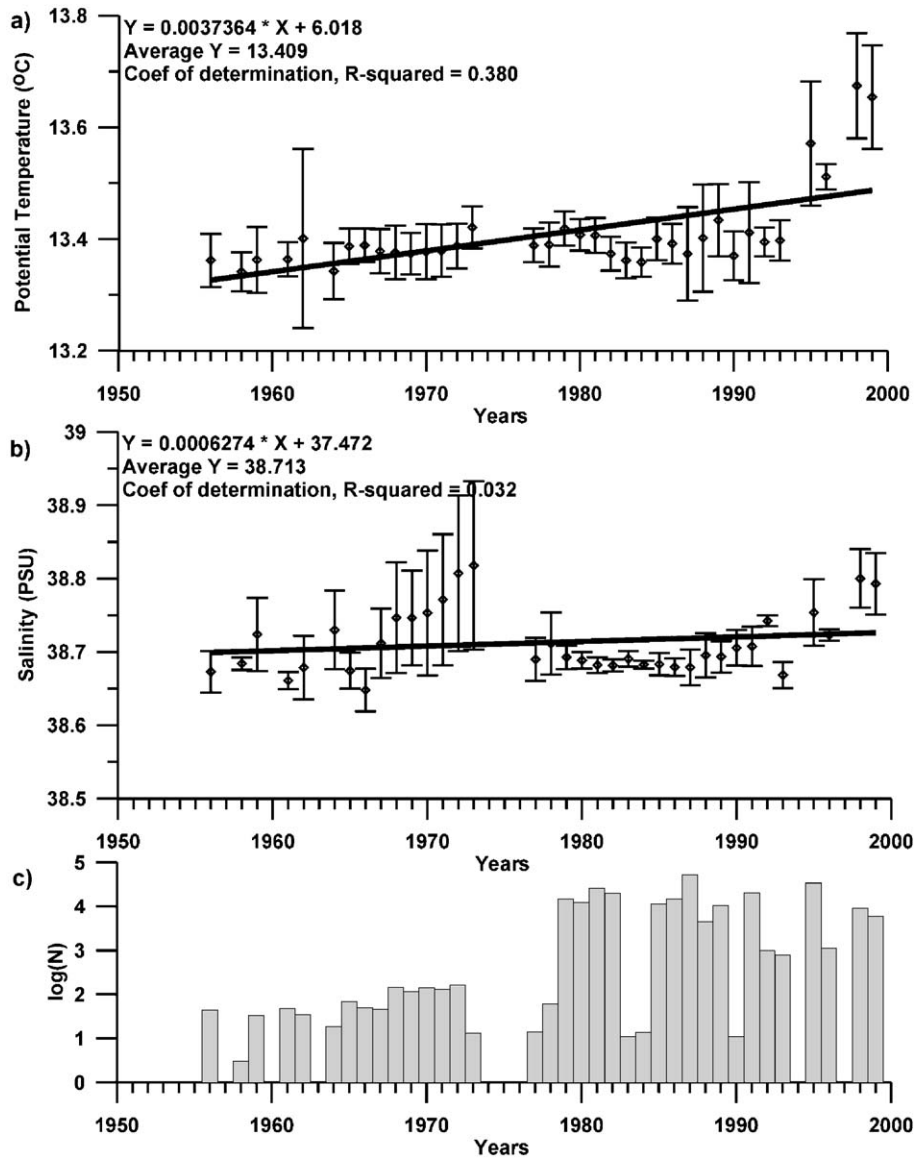


Fig. 16. As for Fig. 14 but for the Levantine basin.

Fig. 15c–f provides a general overview of the vertical distributions of oxygen and nutrients. In the upper layer, seasonal variations of the primary nutrient elements follow hydrographic features appropriate for a cyclonic region. In winter, the dissolved oxygen is of comparable magnitude as in other convective regions (e.g. the Gulf of Lions and the southern Adriatic gyre), emphasising the effect of the surface ventilation, whilst at depth, the observed profiles

differ greatly with respect to other basins. During the stratified seasons, the concentrations present a shallow oxygen maximum at about 50 m, poor in nutrients due to photosynthetic consumption. A sharp nutricline essentially characterises the transition to the deep layer; the tendency of the nutricline to disappear during winter is less pronounced than in other convective regions. In the northern Levantine, the convective movements usually reach the intermediate

layer and a limited mixing with the nutrient-enriched and less saline deep waters occurs (Yilmaz and Tuğrul, 1998).

Spatial differences of biochemical properties distribution from west to east have been demonstrated by many authors on the basis of basin-wide climatological observations from earlier cruises (Miller et al., 1970). These differences indicate a longitudinal gradient of increasing oligotrophy in terms of phytoplankton production and stocks of biomass from the Ionian towards the easternmost part of the Levantine basin. Conceptual and statistically models applied to large quasi-synoptic databases (Denis-Karafistan et al., 1998) as well as coupled hydrodynamic–ecological model simulations (Crise et al., 1999) have reconstructed the East–West trophic gradient in the Mediterranean. Here, we are able to quantify the main spatial characteristic of trophic levels in the Eastern Mediterranean from vertical climatologies.

Fig. 17 shows composite profiles of oxygen, nutrients and chlorophyll-*a* calculated in three selected regions of the Eastern Mediterranean: two regions are in the northern and southern Levantine basin, and are mainly affected by cyclonic and anticyclonic eddies, respectively; the third region is in the Southern Ionian mainly characterised by lateral advection. The employed plotting method is useful to confirm the spatial differences among these regions due to different dynamics.

Some preliminary elements of the seasonal variability in the upper water column, mostly attributed to photosynthetic consumption, have been discussed above; here, some key elements of the spatial characterization of deep-water masses emerge from the comparison of the deep profiles which reflect different ecosystems and dynamics. In the deep layer, the dissolved oxygen concentrations decrease gradually from the Ionian towards the southern Levantine and are lowest in the northern Levantine (Fig. 17a). This is a clear manifestation of the spreading of the EMDW that has been supplied by the Adriatic inflow. In the Ionian, below a broad oxygen minimum at mid depths (~1000 m), the concentrations increase slightly towards the bottom indicating more ventilated bottom waters. This increase, still evident in the southern Levantine, disappears in the north where the deep convective mixing rarely extends

down to 1000 m in the Rhodes gyre (Özsoy et al., 1993), indicating a rather ‘older’ and stagnant situation in the deep layer.

Nutrient concentrations exhibit remarkable differences with depths and regions. The photic layer (~120 m) exhibits almost nutrient-depleted conditions; on an annual basis the photosynthetic consumption seems higher in the Levantine basin than in the southern Ionian. In the layer beneath, the nitrate concentrations increase sharply (Fig. 17b), reaching extreme values that result higher in the southern Ionian (~5.7 mmol m⁻³) than in the Levantine basin (~4.7 mmol m⁻³). This enhances the trophic gradient in the intermediate layer attributed to the spreading of LIW and subsequent export of nutrient-associated materials into the Ionian Sea. However, the enrichment of the LIW by nitrate as it moves westwards cannot be excluded, because of the mineralization of the detritus from the upper layer and mixing with deep waters (Crise et al., 1999). Moreover, the nitracline is shallower (200–750 m) in the Ionian than in the Levantine convective region (200–1000 m). In contrast, the phosphates (Fig. 17c) are higher in the Levantine (~0.25 mmol m⁻³) than in the southern Ionian (<0.18 mmol m⁻³).

The link between nitrates and phosphates has also been briefly explored by N/P molar ratios calculated from the volume-averaged concentrations in the deep layer (>1500 m). They result 27.17 for the southern Ionian, 18.36 for the northern Levantine and 14.71 for the southern Levantine basin (the averaged concentrations are listed in Table 5). From a systematic standpoint, these values are certainly in contrast to the well known N/P ratio anomaly in the Eastern Mediterranean Sea (Krom et al., 1991; Kress and Herut, 2001). It should be stressed that the primary aim of this study is the construction of climatological profiles for checking the quality of future incoming data and at the present time, the scope was not to establish whether the phosphorus is a limiting factor for the pelagic waters across the Eastern Mediterranean. In order to elucidate these discrepancies, we have simply divided our data set in two periods: (i) from the beginning of historical data up to 1985, and (ii) from 1985 onwards (i.e. from the starting of basin wide systematic observations conducted in the Eastern Mediterranean within

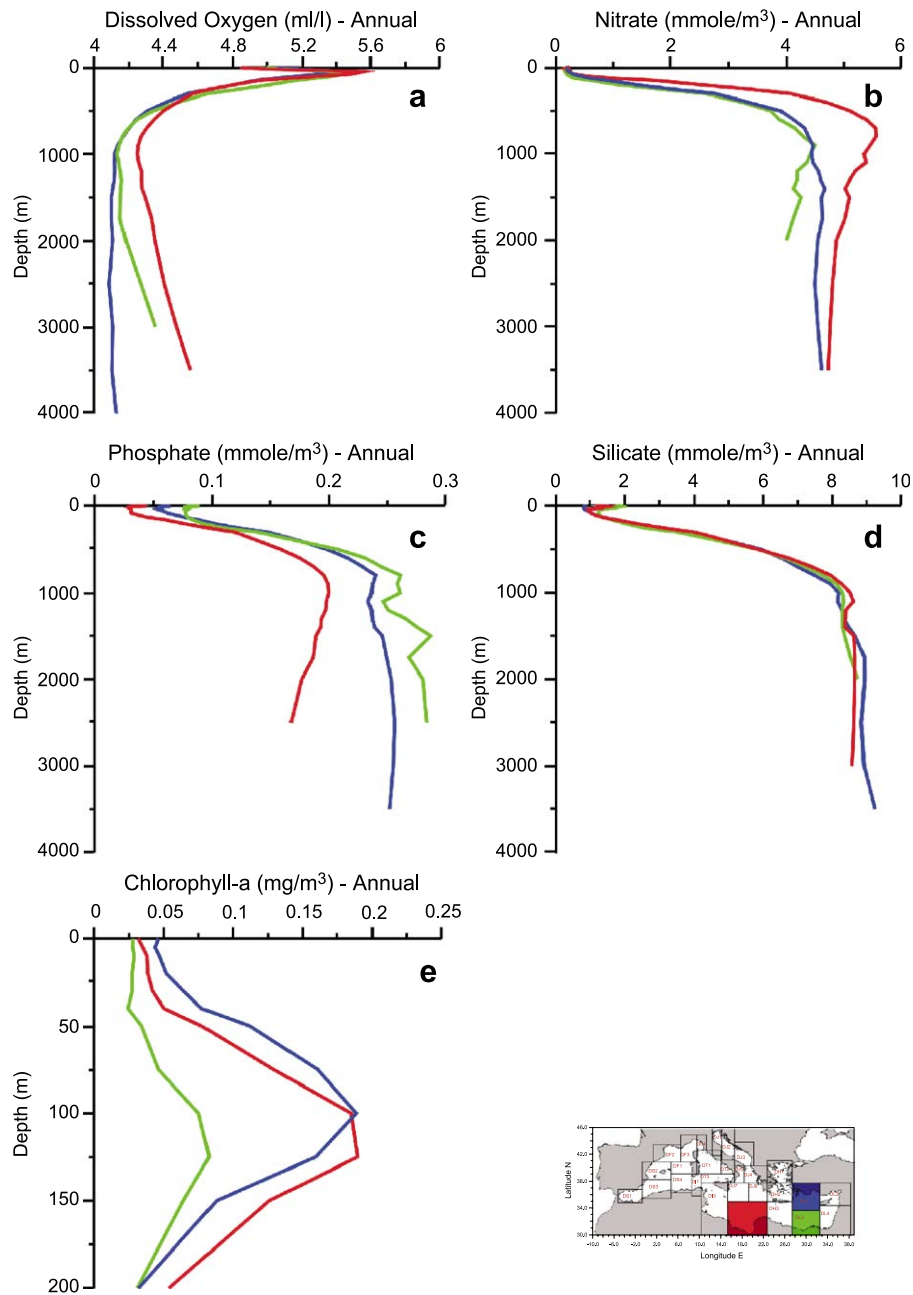


Fig. 17. Annually averaged vertical profiles of hydrographic parameters: (a) dissolved oxygen, (b) nitrate, (c) phosphate, (d) silicate, and (e) chlorophyll-*a* concentrations in three selected regions of the Eastern Mediterranean (see inset map).

the framework of the POEM programme). In the northern Levantine basin, the nitrate concentrations before 1985 result appreciably lower and phosphate higher than those obtained during the more recent

expeditions, i.e. after 1985. The reason is not known and may be due to the limited accuracies of the measurements and poor spatial coverage. On the other hand, the nitrates and phosphates in the Ionian

have resulted to be of comparable magnitude. Civitarese et al., 1998 have hypothesised that the large excess of nitrates in the Ionian Sea could be a direct consequence of the enriched dense waters of Adriatic origin that may support high molar ratios in the Eastern Mediterranean.

Comparable profiles are observed in the silicate content (Fig. 17d) that may be explained by slower decay of siliceous biogenic materials than nitrogenous components (Yilmaz and Tuğrul, 1998). The silicate gradient zone extends down to ~1000 m, the depth level which defines the upper boundary of the EMDW; however, the general thermohaline circulation in the deep layer does not permit to distinguish EMDW masses of different ages from silicate concentrations.

The averaged maxima of chlorophyll-*a* vary spatially and they range on an annual basis between 0.05 and 0.20 mg m⁻³. A distinct chlorophyll-*a* maximum is observed in all regions, and it is shallower in the northern Levantine basin than in the other regions, in agreement with the major dynamical features (Yacobi et al., 1995).

5. Summary and conclusions

Seasonally averaged vertical profiles of temperature, salinity, dissolved oxygen, nutrients (nitrate, phosphate and silicate) and chlorophyll-*a* have been computed for different regions of the Mediterranean Sea, following the joint effort in rescuing, quality

Table 4
Spatially averaged water properties in four regions of the Western Mediterranean

Water mass	Temperature (°C)	Salinity (psu)	Oxygen (ml l ⁻¹)	Nitrate (mmol m ⁻³)	Phosphate (mmol m ⁻³)	Silicate (mmol m ⁻³)
<i>Gulf of Lions—DF2</i>						
Surface water (0–5 m)	17.61±2.30 (14,218)	37.88±0.45 (9472)	5.44±0.24 (2182)	1.45±2.10 (352)	0.13±0.12 (757)	1.37±1.01 (820)
LIW (400 m)	13.17±0.11 (3101)	38.48±0.03 (2306)	4.48±0.17 (610)	6.31±0.58 (55)	0.34±0.08 (208)	6.26±1.02 (87)
WMDW (≥1500 m)	13.04±0.02 (3218)	38.42±0.01 (3473)	4.60±0.07 (1214)	7.78±0.51 (17)	0.39±0.04 (184)	8.16±0.71 (128)
<i>Tyrrhenian North—DT1</i>						
Surface water (0–5 m)	18.90±2.54 (11,208)	37.91±0.25 (2867)	5.55±0.26 (576)	0.24±0.22 (110)	0.08±0.07 (282)	2.17±0.59 (168)
LIW (500 m)	13.88±0.13 (593)	38.65±0.03 (391)	4.29±0.13 (179)	5.91±0.56 (32)	0.31±0.07 (61)	6.85±0.79 (29)
TDW (≥1500 m)	13.21±0.04 (277)	38.47±0.02 (185)	4.32±0.13 (139)	7.32±0.74 (10)	0.42±0.08 (20)	7.73±0.66 (12)
<i>Algerian East—DS4</i>						
Surface water (0–5 m)	19.56±2.52 (7684)	37.12±0.14 (1112)	5.31±0.33 (340)	0.05±0.10 (207)	0.04±0.05 (307)	0.99±0.33 (90)
LIW (500 m)	13.30±0.09 (988)	38.52±0.02 (459)	4.14±0.12 (168)	8.90±0.40 (36)	0.40±0.07 (81)	7.58±0.89 (26)
WMDW (≥1500 m)	13.04±0.04 (778)	38.42±0.02 (548)	4.49±0.12 (287)	8.28±0.11 (39)	0.39±0.05 (73)	9.29±0.27 (29)
<i>Alboran Sea—DS1</i>						
Surface water (0–5 m)	17.85±0.616 (18,874)	36.57±0.28 (7122)	5.44±0.33 (1877)	0.44±0.49 (733)	0.11±0.11 (1046)	1.33±1.20 (642)
LIW (500 m)	13.07±0.08 (2014)	38.45±0.04 (1588)	4.21±0.17 (320)	8.49±0.89 (126)	0.37±0.07 (121)	8.36±1.22 (112)
WMDW (≥1500 m)	13.08±0.03 (176)	38.44±0.01 (170)	4.50±0.09 (21)	9.13±3.91 (6)*	0.41±0.06 (8)*	8.381±0.99 (7)

Average and standard deviation for physical and biochemical parameters (the number of data used are indicated within brackets) for three layers, which essentially characterize the water column structure. The regions are those defined according to the scheme in Figs. 5 and 6.

* The deepest values are at 1400 m.

checking and archiving hydrographic and biochemical data within the EU/MEDAR/MEDATLAS II and EU/MTPII/MATER data management activities. The regions are defined according to the schematic representation of the sub-basin scale dynamics, mostly representative of the upper/external thermohaline cell circulation. This method overcomes the pure definition of climatologies based on a regular grid, which, if coarsely defined, may be inadequate to resolve the complicate geometry of the Mediterranean basin. On the other hand, high-resolution gridded climatologies may result poor in statistics due to a limited number of hydrological casts in some oceanic domains.

The inhomogeneous distribution of historical data as well as coastal data can introduce biases in the seasonally averaged vertical profiles, resulting in enlarged and unrealistic variations along the vertical. For this reason, an iterative process in computing first-order statistics and annual means for the deep waters have been used, considering that some anomalous values exist in the databases. Data departing from the mean by more than one standard deviation were rejected for the computed climatologies. In addition,

data relevant to particular periods have revealed large differences with respect to the past climatologies, as for example, the large climatic shift in the temperature and salinity caused by the EMT. Analyses of measurements made since the early 1950s allowed to evidence warming trends and salinity increases in the Ionian and Levantine basin, which have resulted to be of the same order of magnitude as similar changes observed by Béthoux et al. (1990) in their pilot study in the Western Mediterranean.

A synthetic description of the dominant features in the vertical distributions of the hydrographic fields is presented on a seasonal basis from the climatological profiles in the upper waters (0–200 m). The hydrological structures along the vertical reflect the water mass distributions and their circulation patterns with satisfying accuracy. The chemical profiles follow the well-known ventilation mechanisms of the convection regions in the Gulf of Lions, in the southern Adriatic Sea and in the northern Levantine basin. In addition, several important aspects of the advective processes that transport water masses among the adjacent basins are easily identified from the transformation of water characteristics.

Table 5
As for Table 4 but in three regions of the Eastern Mediterranean

Water mass	Temperature (°C)	Salinity (psu)	Oxygen (ml l ⁻¹)	Nitrate (mmol m ⁻³)	Phosphate (mmol m ⁻³)	Silicate (mmol m ⁻³)
<i>Ionian South—DJ5</i>						
Surface water (0–5 m)	20.26±2.49 (6208)	38.40±0.19 (545)	4.85±0.20 (531)	0.23±0.29 (103)	0.04±0.04 (244)	1.22±1.01 (139)
LIW (250 m)	14.72±0.18 (2390)	38.85±0.06 (284)	4.67±0.13 (279)	3.24±0.73 (49)	0.10±0.04 (108)	3.22±0.97 (68)
EMDW (≥1500 m)	13.70±0.02 (878)	38.69±0.02 (410)	4.40±0.11 (418)	4.89±0.37 (103)	0.18±0.04 (146)	8.65±0.49 (95)
<i>Levantine North—DL1</i>						
Surface water (0–5 m)	21.72±2.20 (8816)	39.16±0.10 (1995)	5.06±0.26 (1395)	0.21±0.24 (450)	0.06±0.05 (513)	0.89±0.78 (465)
LIW (125 m)	15.69±0.44 (4479)	39.02±0.05 (1087)	5.05±0.20 (720)	0.62±0.54 (237)	0.08±0.07 (313)	1.36±0.99 (262)
EMDW (≥1500 m)	13.77±0.04 (1973)	38.73±0.05 (972)	4.10±0.17 (1191)	4.59±0.92 (351)	0.25±0.07 (383)	8.94±1.47 (396)
<i>Levantine South—DL3</i>						
Surface water (0–5 m)	23.05±2.26 (5890)	38.97±0.39 (1116)	5.00±0.40 (1240)	0.21±0.42 (157)	0.09±0.04 (444)	1.86±1.70 (329)
LIW (125 m)	15.60±0.29 (2461)	38.97±0.06 (311)	5.03±0.15 (296)	1.13±0.63 (54)	0.09±0.05 (152)	1.92±1.23 (127)
EMDW (≥1500 m)	13.70±0.03 (632)	38.72±0.04 (309)	4.22±0.11 (385)	4.12±1.20 (90)	0.28±0.09 (129)	8.55±1.65 (96)*

*The deepest values are at 1400 m.

Table 4 summarises the layer-averaged hydrographic properties and nutrient concentrations calculated for four regions in the Western Mediterranean, i.e. the Gulf of Lions, the Tyrrhenian Sea and the Algerian basin, discussed in the text. The Alboran Sea, through which the entire Mediterranean Sea exchanges water with the Atlantic Ocean across the Strait of Gibraltar, has been also included. In Table 5, a summary of the most important water mass properties and their vertical and spatial differences in three regions of the Eastern Mediterranean, i.e. the Southern Ionian, the northern Levantine basin and the southern Levantine basin, is presented. The hydrochemical properties in the marginal basins of the Eastern Mediterranean, i.e. in the southern Adriatic Sea and in the Strait of Sicily are summarised in Table 6. The characteristics and transformations of the main water masses mentioned in the text (i.e. AW, LIW, TDW, WMDW and EMDW) can be traced from the source regions through the basin interior by a comparative analysis of the averaged values. The water column has been schematised in three layers, which essentially characterise the thermohaline circulation. The surface layer (0–5 m) may be considered representative of the AW, the properties in the LIW layer are those corresponding to the depth of the salinity maximum and finally, the properties in the deep layer (i.e. the layer essentially occupied by the TDW, WMDW and EMDW) are those calculated for depths greater than

1500 m where the waters exhibit rather homogeneous behaviour during the entire annual cycle.

The layer-averaged water mass properties and the averaged vertical profiles may be used as a basis for validating incoming data from operational oceanography and to initialise coupled physical–biological models. The full set of spatially averaged hydrological profiles can be found and downloaded from the World Wide Web data server at the OGS (<http://doga.ogs.trieste.it/medar/climatologies/>).

New optimisation criteria may reduce the effects of errors and uncertainties in quality control of historical data of unknown origin before incorporating them into large databases. Trend evaluations could be effective in reducing subjective choices, especially in the deep waters, when sufficiently long time-series will be available to the scientific community.

Acknowledgements

This work was not possible without the large amount of oceanographic data rescued within the framework of the EU/MEDAR/MEDATLAS II project with the partial financial support of the EC (contract MAS3-CT98-0174 and ERBIC20-CT98-0103). The authors gratefully acknowledge the financial support of the Ministry of Education, Universities and Research (MIUR) in Italy. The International Centre

Table 6

As for Table 4 but in two marginal regions of the Eastern Mediterranean: the Southern Adriatic and the Strait of Sicily

Water mass	Temperature (°C)	Salinity (psu)	Oxygen (ml l ⁻¹)	Nitrate (mmol m ⁻³)	Phosphate (mmol m ⁻³)	Silicate (mmol m ⁻³)
<i>Adriatic South—DJ3</i>						
Surface water (0–5 m)	16.58±2.53 (14,218)	37.93±0.69 (9739)	5.47±0.26 (3000)	0.57±0.47 (1665)	0.04±0.03 (2442)	2.86±1.43 (1201)
LIW (200 m)	13.63±0.18 (1351)	38.70±0.04 (1039)	4.97±0.22 (372)	4.98±0.70 (235)	0.18±0.05 (244)	5.38±1.32 (210)
ADW (≥1000 m)	12.88±0.05 (812)	38.59±0.01 (768)	4.89±0.18 (272)	5.25±0.65 (208)	0.19±0.05 (245)	9.67±2.61 (193)
<i>Sicily Strait—DI3</i>						
Surface water (0–5 m)	19.23±2.59 (11,709)	37.47±0.20 (3476)	5.25±0.37 (1468)	0.48±0.76 (455)	0.06±0.06 (526)	1.09±0.59 (189)
LIW (400 m)	14.02±0.13 (1823)	38.75±0.02 (678)	4.30±0.13 (215)	5.46±0.87 (54)	0.20±0.05 (64)	7.25±1.33 (47)
EMDW (≥1500 m)	13.83±0.04 (12)	38.73±0.01 (10)	4.21±0.01 (4)	5.00±0.31 (2)*	0.18±0.04 (4)*	5.89±1.29 (4)**

* The deepest value is at 1200 m.

** The deepest value is at 1000 m.

for Theoretical Physics in Trieste granted the fellowship to M. Burca within the Training Research in Italian Laboratory (TRIL) Programme. We thank the reviewers for their precious comments which helped us to improve the manuscript.

References

- Artegiani, A., Bregant, D., Paschini, E., Pinardi, N., Raicich, F., Russo, A., 1997. The Adriatic Sea general circulation: Part I. Air–sea interaction and water mass structure: Part II. Baroclinic circulation structure. *J. Phys. Oceanogr.* 27, 1492–1532.
- Astraldi, M., Gasparini, G.P., Vetrano, A., Vignudelli, S., 2002. Hydrographic characteristics and interannual variability of water masses in the central Mediterranean: a sensitivity test for long-term changes in the Mediterranean Sea. *Deep-Sea Res., Part 1, Oceanogr. Res. Pap.* 49, 661–680.
- Béthoux, J.P., Gentili, B., Raunet, J., Taillez, D., 1990. Warming trend in the Western Mediterranean deep water. *Nature* 347, 660–662.
- Béthoux, J.P., Morin, P., Madec, C., Gentili, B., 1992. Phosphorus and nitrogen behaviour in Mediterranean Sea. *Deep-Sea Res.* 39, 1641–1654.
- Bigami, F., Salusti, E., Schiarini, S., 1990. Observations on a bottom vein of dense water in the Southern Adriatic and Ionian Seas. *J. Geophys. Res.* 95, 7249–7259.
- Castellari, S., Pinardi, N., Leaman, K., 2000. Simulation of water mass formation processes in the Mediterranean Sea: influence of the time frequency of atmospheric forcing. *J. Geophys. Res.* 105, 24157–24181.
- CIESM, 2002. Tracking long-term hydrological change in the Mediterranean Sea. In: Briand, F. (Ed.), 2002. CIESM Workshop Series, vol. 16, p. 134.
- Civitarese, G., Gacic, M., Vetrano, A., Boldrin, A., Bregant, D., Rabitti, S., Souvermezoglou, E., 1998. Biochemical fluxes through the Strait of Otranto (Eastern Mediterranean). *Cont. Shelf Res.* 18, 773–789.
- Coatanoan, C., Metzl, N., Fieux, M., Coste, B., 1999. Seasonal water mass distribution in the Indonesian throughflow entering the Indian Ocean. *J. Geophys. Res.* 104, 20801–20826.
- Coste, B., Gostan, J., Minas, H.J., 1972. Influence des conditions hivernales sur les productions phyto-et zooplanctoniques en Méditerranée Nord-Occidentale: I. Structures hydrologiques et distribution des sels nutritifs. *Mar. Biol.* 16, 320–348.
- Crise, A., Allen, J.I., Baretta, J., Crispi, G., Mosetti, R., Solidoro, C., 1999. The Mediterranean pelagic ecosystem response to physical forcing. *Prog. Oceanogr.* 44, 219–243.
- Denis-Karafistan, A., Martin, J.M., Minas, H., Brasseur, P., Nihoul, J., Denis, C., 1998. Space and seasonal distributions of nitrates in the Mediterranean Sea derived from a variational inverse model. *Deep-Sea Res., Part 1, Oceanogr. Res. Pap.* 45, 387–408.
- Gacic, M., Civitarese, G., Miserocchi, S., Cardin, V., Crise, A., Mauri, E., 2002. The open-ocean convection in the Southern Adriatic: a controlling mechanism of the spring phytoplankton bloom. *Cont. Shelf Res.* 22, 1897–1908.
- Guibout, P., 1987. Atlas Hydrographique de la Méditerranée IFRMER, Brest.
- Hopkins, T.S., 1978. Physical Processes in the Mediterranean basins. In: Kjerfve, B. (Ed.), *Estuarine Transport Processes*. Univ. of South Carolina Press, Columbia, SC, pp. 269–310.
- Kinder, T.H., Parilla, G., 1987. Yes, some of the Mediterranean outflow does come from great depth. *J. Geophys. Res.* 92, 2901–2906.
- Klein, B., Roether, W., Manca, B., Bregant, D., Beitzel, V., Kovacevic, V., Luchetta, A., 1999. The large deep transient in the Eastern Mediterranean. *Deep-Sea Res., Part 1, Oceanogr. Res. Pap.* 46, 371–414.
- Kress, N., Herut, B., 2001. Spatial and seasonal evolution of dissolved oxygen and nutrients in the Southern Levantine basin (Eastern Mediterranean Sea): chemical characterization of the water masses and inferences on the N:P ratios. *Deep-Sea Res., Part 1, Oceanogr. Res. Pap.* 48, 2347–2372.
- Krom, M.D., Kress, N., Brenner, S., Gordon, L.I., 1991. Phosphorus limitation of primary productivity in the E. Mediterranean sea. *Limnol. Oceanogr.* 36, 424–432.
- Krom, M.D., Brenner, S., Kress, N., Neori, A., Gordon, L.I., 1992. Nutrient dynamics and new production in a warm-core eddy from the Eastern Mediterranean Sea. *Deep-Sea Res.* 39, 467–480.
- Lascaratos, A., Roether, W., Nittis, K., Klein, B., 1999. Recent changes in deep water formation and spreading in the Eastern Mediterranean Sea. *Prog. Oceanogr.* 44, 5–36.
- Leaman, K.D., Schott, F.A., 1991. Hydrographic structure of the convective regime in the Gulf of Lions: Winter 1987. *J. Phys. Oceanogr.* 21, 573–596.
- Levitus, S., 1982. Climatological atlas of the world ocean. NOAA Professional Paper, vol. 13. U.S. Gov. Printing Office, Washington, DC. 173 pp.
- Levitus, S., Boyer, T., Conkright, M., O'Brien, T., Antonov, J., Stephens, C., Stathopoulos, L., Johnson, D., Gelfed, R., 1998. World Ocean Database 1998, vol. 1: Introduction. NOAA Atlas NESDIS 18, Washington, DC. 346 pp.
- Lipiatou, E., Heussner, S., Mosetti, R., Tintoré, J., Tselepidis, A. (Eds.), 1999. Progress in oceanography of the Mediterranean Sea. *Spec. Issue, Prog. Oceanogr.*, vol. 44, p. 468.
- Maillard, C., Fichaut, M., MEDAR/MEDATLAS Group, 2001. MEDAR-MEDATLAS Protocol (V3) Part I: Exchange Format and Quality Checks for Observed Profiles; *Rap. Int. IFREMER, Brest. TMSI/IDM/SISMER/SIS00-084*.
- Maillard, C., Balopoulos, E., Giorgetti, A., Fichaut, M., Iona, A., Larour, M., Latrouite, A., Manca, B., Maudire, G., Nicolas, P., Sanchez-Cabeza, J.-A., 2002. An integrated system for managing multidisciplinary oceanographic data collected in the Mediterranean Sea during the basin-scale research project EU/MAST-MATER (1996–2000). *J. Mar. Syst.* 33–34, 523–538.
- Malanotte-Rizzoli, P., 1991. The Northern Adriatic Sea as a prototype of convection and water mass formation on the continental shelf. In: Chu, P.C., Gascard, J.C. (Eds.), *Deep Convection and Deep Water Formation in the Oceans*. Elsevier Oceanography Series, vol. 57. Elsevier, Amsterdam, pp. 229–239.

- Malanotte-Rizzoli, P., Manca, B.B., Ribera d'Alcalà, M., Theocharis, A., Bergamasco, A., Bregant, D., Budillon, G., Civitarese, G., Georgopoulos, D., Michelato, A., Sansone, E., Scarazzato, P., Souvermezoglou, E., 1997. A synthesis of the Ionian Sea hydrography, circulation and water mass pathways during POEM-Phase I. *Prog. Oceanogr.* 39, 153–204.
- Malanotte-Rizzoli, P., Manca, B.B., Ribera d'Alcalà, M., Theocharis, A., Brenner, S., Budillon, G., Özsoy, E., 1999. The Eastern Mediterranean in the 80s and in the 90s: the big transition in the intermediate and deep circulations. *Dyn. Atmos. Ocean.* 29, 365–395.
- Manca, B., Giorgetti, A., 1998. Thermohaline properties and circulation patterns in the Southern Adriatic Sea from May 1995 to February 1996. In: Piccazzo, M. (Ed.), *Atti del 12° Congresso dell'Associazione Italiana di Oceanografia e Limnologia (Isola di Vulcano, 18–21 Settembre 1996)*, vol. II. A.I.O.L., Genova, 399–414.
- Manca, B.B., Kovacevic, V., Gacic, M., Viezzoli, D., 2002. Dense water formation in the Southern Adriatic sea and spreading into the Ionian Sea in the period 1997–1999. *J. Mar. Syst.* 33–34, 133–154.
- Martin, J.-M., Milliman, J.D., 1997. EROS 2000 (European River Ocean System). The western Mediterranean: an introduction. *Deep-Sea Res., Part 2, Top. Stud. Oceanogr.* 44, 521–529.
- Marullo, S., Santoleri, R., Malanotte-Rizzoli, P., Bergamasco, A., 1999. The sea surface temperature field in the Eastern Mediterranean from AVHRR data: Part I. Seasonal variability: Part II. Interannual variability. *J. Mar. Syst.* 20, 63–112.
- MEDAR Group, 2002. MEDATLAS 2002 Mediterranean and Black Sea database of temperature, salinity and biochemical parameters climatological atlas, 4 CD-ROM. European Commission Marine Science and Technology Programme (MAST). Ed. IFREMER (sismer@ifremer.fr), Brest.
- MEDATLAS Consortium, 1997. Mediterranean Hydrological Atlas of temperature and salinity. A MAST support initiative for ocean data and information management, Contr. No. MAS2-CT93-0074, Coordinating Center IFREMER/SISMER Centre de Brest, France (C. Maillard), three CD-ROM, IFREMER Ed.
- MEDOC Group, 1970. Observation of formation of deep water in the Mediterranean Sea. *Nature* 277, 1037–1040.
- Miller, A.R., Tchernia, P., Charnock, H., Mc Gill, D.A., 1970. Mediterranean Sea Atlas of temperature, salinity, oxygen profiles and data from cruises of R.V. Atlantis and R/V chain with distribution of nutrient chemical properties. Woods Hole Oceanographic Institution Atlas Series, vol. 3. Woods Hole Oceanographic Instit., Woods Hole, MA.
- Millot, C., 1991. Mesoscale and seasonal variabilities of the circulation in the western Mediterranean. *Dyn. Atmos. Ocean.* 15, 179–214.
- Millot, C., 1995. PRIMO-0 and related experiments. *Oceanol. Acta* 18, 137–138.
- Millot, C., 1999. Review paper circulation in the Western Mediterranean Sea. *J. Mar. Syst.* 20, 423–442.
- MODB Group (The), 1996. Climatological Atlas of the Mediterranean Sea. Scientific Report of the MAST-MODB initiative for ocean data and information management, Contr. No. MAS2.0093.0075. BE, University of Liège, Liège.
- Monaco, A., Peruzzi, S., 2002. The Mediterranean targeted project MATER—a multiscale approach of the variability of a marine system—overview. *J. Mar. Syst.* 33–34, 3–21.
- Mosetti, F., 1983. Fundamental features of the Adriatic Sea hydrology. In: Università degli studi di Trieste (Ed.), *Atti del convegno internazionale 'I problemi del mare Adriatico'*, Trieste, 26–27 Settembre 1983. Università degli studi di Trieste, Trieste, pp. 209–239.
- Napolitano, E., Oguz, T., Malanotte-Rizzoli, P., Yilmaz, A., Sansone, E., 2000. Simulations of biological production in the Rhodes and Ionian basins of the eastern Mediterranean. *J. Mar. Syst.* 24, 277–298.
- Ovchinnikov, I.M., Zats, V.I., Krivosheya, V.G., Udodov, A.I., 1985. Formation of Deep Eastern Mediterranean waters in the Adriatic Sea. *Oceanology* 25 (6), 704–707.
- Özsoy, E., Latif, M.A., 1996. Climate variability in the Eastern Mediterranean and the great Aegean outflow anomaly. In: Denis, M. (Ed.), (Ed.), *POEM-BC Workshop, Molitg les Bains, France, 1–5 July 1996*. Centre d'Océanologie de Marseille, Marseille, pp. 69–86.
- Özsoy, E., Hecht, A., Unluata, U., Brenner, S., Sur, H.I., Bishop, J., Latif, M.A., Roentraub, Z., Oguz, T., 1993. A synthesis of the Levantine Basin circulation and hydrography, 1985–1990. *Deep-Sea Res., Part 2, Top. Stud. Oceanogr.* 40, 1075–1119.
- Picco, P., 1990. Climatological Atlas of the Western Mediterranean. ENEA, Roma. 224 pp.
- Pinardi, N., Korres, G., Lascaratos, A., Roussenov, V., Stanev, E., 1997. Numerical simulation of the interannual variability of the Mediterranean Sea upper ocean circulation. *Geophys. Res. Lett.* 24, 425–428.
- POEM Group (The), 1992. General circulation of the Eastern Mediterranean Sea. *Earth-Sci. Rev.* 32, 285–308.
- Prieur, L., Sourmia, A., 1994. 'Almofront-1' (April–May 1991): an interdisciplinary study of the Almaria-Oran geostrophic front, SW Mediterranean Sea. *J. Mar. Syst.* 3–5, 187–203.
- Reid, J.L., 1979. On the contribution of the Mediterranean Sea outflow to the Norwegian–Greenland Sea. *Deep-Sea Res.* 26A, 1199.
- Reiniger, R.F., Ross, C.K., 1968. A method of interpolation with application to oceanographic data. *Deep-Sea Res.* 15, 185–193.
- Robinson, A.R., Malanotte-Rizzoli, P. (Eds.), 1993. Physical Oceanography of the Eastern Mediterranean. *Deep-Sea Res., Part 2, Top. Stud. Oceanogr.*, vol. 40, pp. 1073–1332.
- Robinson, A.R., Golnaraghi, M., Leslie, W.G., Artegiani, A., Hecht, A., Lazzoni, E., Michelato, A., Sansone, E., Theocharis, A., Ünlüata, Ü., 1991. The eastern Mediterranean general circulation: features, structure and variability. *Dyn. Atmos. Ocean.* 15, 215–240.
- Robinson, A.R., Leslie, W., Theocharis, A., Lascaratos, A., 2001. Mediterranean Sea circulation. *Encyclopedia of Ocean Science*, vol. 3. Academic Press, San Diego, CA, pp. 1689–1705.
- Roether, W., Well, R., 2001. Oxygen consumption in the Eastern Mediterranean. *Deep-Sea Res., Part 1, Oceanogr. Res. Pap.* 48, 1535–1551.
- Roether, W., Manca, B., Klein, B., Bregant, D., Georgopoulos, D.,

- Artegiani, A., Kovacevic, V., Luchetta, A., 1996. Recent changes in Eastern Mediterranean deep waters. *Science* 271, 333–335.
- Roether, W., Klein, B., Beitzel, V., Manca, B.B., 1998. Property distributions and transient-tracer ages in Levantine Intermediate Water in the Eastern Mediterranean. *J. Mar. Syst.* 18, 71–87.
- Rohling, E.J., Bryden, H.L., 1992. Man-induced salinity and temperature increase in the western Mediterranean deep water. *J. Geophys. Res.* 97, 11191–11198.
- Roussenov, V., Stanev, E., Artale, V., Pinardi, N., 1995. A seasonal model of the Mediterranean Sea general circulation. *J. Geophys. Res.* 100, 13515–13538.
- Schlitzer, R., Roether, W., Oster, H., Junghans, H.-G., Hausmann, M., Johannsen, H., Michelato, A., 1991. Chlorofluoromethane and oxygen in the Eastern Mediterranean. *Deep-Sea Res.* 38, 1531–1551.
- Sparnocchia, S., Manzella, G.M., La Violette, P., 1994. The inter-annual and seasonal variability of the MAW and LIW core properties in the Western Mediterranean. In: La Violette, P.E. (Ed.), *The Seasonal and Interannual Variability of the Western Mediterranean Sea*. Coastal and Estuarine Studies, vol. 46. AGU, Augsburg, pp. 177–194.
- Sparnocchia, S., Gasparini, G.P., Astraldi, M., Borghini, M., Pistek, P., 1999. Dynamics and mixing of the Eastern Mediterranean outflow in the Tyrrhenian basin. *J. Mar. Syst.* 20, 301–317.
- Sur, H.I., Özsoy, E., Ünlüata, Ü., 1992. Simultaneous deep and intermediate depth convection in the northern Levantine Sea, winter 1992. *Oceanol. Acta* 16, 33–43.
- Theocharis, A., Lascaratos, A., Sofianos, S., 2002. Variability of sea water properties in the Ionian, Cretan and Levantine seas during the last century. In: Briand, F. (Ed.), *Tracking long-term hydrological change in the Mediterranean Sea*. CIESM Workshop Series, vol. 16, pp. 73–76.
- UNESCO, 1993. CEC/DG XII, MAST and IOC/IODE, Manual of Quality Control Procedures for Validation of Oceanographic Data. IOC Manual and Guides, vol. 26, p. 436.
- Wu, P., Haines, K., 1998. The general circulation of the Mediterranean Sea from 100-year simulation. *J. Geophys. Res.* 103, 1121–1135.
- Yacobi, Y.Z., Zohary, T., Kress, N., Hecht, A., Robarts, R.D., Waiser, M., Wood, A.M., Li, W.K.W., 1995. Chlorophyll distribution throughout the southeastern Mediterranean in relation to the physical structure of the water mass. *J. Mar. Syst.* 6, 179–190.
- Yilmaz, A., Tuğrul, S., 1998. The effect of cold- and warm-core eddies on the distribution and stoichiometry of dissolved nutrients in the northeastern Mediterranean. *J. Mar. Syst.* 16, 253–268.
- Zavatarelli, M., Raicich, F., Bregant, D., Russo, A., Artegiani, A., 1998. Climatological biochemical characteristics of the Adriatic Sea. *J. Mar. Syst.* 18, 227–263.



Application of inverse technique to study radioactive pollution and mixing processes in the Arctic Seas

L.M. Ivanov^{a,*}, T.M. Margolina^a, A.I. Danilov^b

^a Marine Hydrophysical Institute, The Ukrainian National Academy of Sciences, Kapitanskaya 2, Sevastopol 99011, Ukraine

^b Arctic and Antarctic Research Institute, Saint Petersburg, Russia

Received 25 September 2002; received in revised form 28 March 2003; accepted 28 May 2003

Available online 20 February 2004

Abstract

Rare noisy observations of the dissolved and suspended Cs^{137} , and the dissolved Sr^{90} collected for years 1985 and 1994, respectively, are utilized through an inverse method to estimate the radionuclide pollution and the mixing time scale, namely the age, of the White and Kara Seas. We demonstrate how uncertainties, such as measurement noise, inhomogeneous station disposition and others depress the identification utility of the radioactive observations in the Arctic Seas to validate regional radioecological models. The special approach estimates the current and mean radionuclide pollution from the rare observations. We found the mean integral amount of cesium (strontium) pollution of the White Sea (in 1985) and Kara Sea (in 1992) did not exceed ~ 70 (41) TBq and ~ 16 (9) TBq, respectively, and radioactive background of these seas is low in comparing to the Black and Barents Seas. Estimations of the age confirm the fact of the rapid ventilation of the Kara Sea, but not the White Sea. The age ranges from 1–2 years for the Kara Sea till 5–6 years for the White Sea. That factually says about the possibility of the long-term accumulation of radionuclides in the White Sea.

© 2004 Elsevier B.V. All rights reserved.

Keywords: Cs^{137} ; Sr^{90} ; Inverse methods; Age; Renewal; Mixing processes; Kara Sea; White Sea

1. Introduction

The problem of radionuclide pollution of the Arctic Seas is of considerable interest from the theoretical, practical and political points of view. The following circumstances determine such an interest:

- First of all, the former Soviet Union used the Siberian Arctic as the polygon for the testing nuclear weapon

(Novaya Zemlya), dumped the nuclear wastes in shallow areas of the Arctic Seas and poured liquid radioactive wastes of radiochemical plants, such as Mayak-30, Chelyabinsk-90 and others directly into Siberian rivers flowing to the Arctic Ocean (see, for example, the so-called “Yablokov Report”, Yablokov et al., 1993). Thus, the Russian Arctic Seas can be considered as a demonstrative example of how artificial radioactivity is dispersed in nature and depresses coastal ecosystems.

- A lot of non-utilized old nuclear submarines are also kept in the Russian Arctic. The last fact certainly

* Corresponding author. Fax: +380-692-554-253.

E-mail address: lmivanov@alpha.mhi.iuf.net (L.M. Ivanov).

produces a dangerous threat for the civil population of the Russian Siberia, American Alaska and Canadian North. Although the former Soviet Union broke up more than 10 years ago, for the present time there is no total clarity where, when and how much radioactive wastes were dumped.

- It is generally accepted that the major contributor to the Arctic waters radioactive contamination are nuclear-fuel reprocessing discharges from the British Nuclear Fuels Plant at Sellafield on the northeast coast of the Irish Sea and, to a lesser degree, from the French plant at Cap de la Hague on the Normandy coast (see, for example, [Livingston, 1988](#)). These sources have caused a significant input of artificial radionuclides to the Arctic ([Kershaw and Baxter, 1995](#)). The analysis of isotope pathways provides vast information on the large-scale circulation variability at seasonal and interannual scales.

Thus, it seems to be very important to get well-grounded estimations of radionuclide pollution of water, land and air in the Arctic Region.

Another possibility is to use artificial isotopes as tracers offering a unique opportunity to observe directly the ventilation process of the Arctic Seas. These tracers clearly mark the penetration of radionuclide from sea surface to deep layers by both subduction and deep convection, across-shore transport of fresh water, mixing and stirring of water mass by currents, wavelike structures and meso-scale eddies. The tracers clearly indicate the qualitative picture of these ventilation pathways, but the quantitative interpretation is complicated by the same property that leads to their utility: concentrations vary over both space and time. Therefore, the second goal of the present investigation is to develop a mathematical method for the estimation of mixing time scales for water quality. We will estimate the age characterizing the long-term trend in behavior of radionuclide pollution.

The remainder of the paper is structured as follows. Sections 2–4 discuss the theoretical aspects of the so-called utility of radionuclide measurements for model validations, estimations of radionuclide pollution of sea region and open boundary modeling applied in these goals. We will demonstrate that even for models with high forecast skill we can expect estimates for only limited model input because, in the White and Kara Seas, the quality of radioactive observations is

usually low (due to high measurement errors) and the number of available observations is poor. To overcome these lacks we develop the original approach producing the balance equations and estimations of the integral amounts of radionuclide in a sea region from the rare observations.

Section 5 is devoted to discussion of the mixing time scales, which can be useful for the analysis of the radionuclide background variability in the Russian Arctic Seas. Although presently there are a lot of different definitions connecting tracer distribution and tracer-independent transport properties of seawater, not all of them are suitable for the analysis of radionuclide observations. Reasons for choice of the applied method are given in Section 5.

Sections 6 and 7 involve the result of estimating integral balances for the dissolved Cs^{137} and Sr^{90} in the White Sea for 1985 and the same radionuclides with the suspended Cs^{137} in the Kara Sea for 1992. The age of the lower (deep) layer (from 30 to 300 m) of the White Sea and for the whole Kara Sea basin is estimated.

Section 8 discusses the sensitivity of estimated integral balances in the White and Kara Seas. We theoretically pointed out that our results are robust to variations of model input, such as the river discharge, inflow and outflow fluxes. The integral estimations also demonstrate the robust feature to variations of observation sampling lengths. Section 9 summarizes the obtained results.

2. Identification utility of radionuclide observations

The goal of the present section is to explain theoretically how much model input can be extracted (identified) from (by) the radionuclide observations. This measure may be called “the identification utility”. Our estimations will demonstrate that for the sparse and noisy observations, such as the concentrations of Cs^{137} , Cs^{134} and Sr^{90} , the volume of useful hydrodynamic information about currents, turbulent mixing, etc., accompanying these observations, is not large even for a quite representative numerical model applied to identify free model input.

The identification utility depends on the quantity of used isotopes and in general can be estimated by

several non-dimensional numbers. First two numbers are

- (i) η_1 —the ratio of the assimilation period (τ_{assim}) to the predictability period (τ_{pred})

$$\eta_1 = \frac{\tau_{\text{assim}}}{\tau_{\text{pred}}} \quad (2.1)$$

where τ_{assim} and τ_{pred} are the time periods, within which observations are assimilated by a model and without which the model loses the forecast skill, respectively; and

- (ii) η_2 —the ratio of the predictability period to the correlation time scale of radionuclide concentration field τ_{cor}

$$\eta_2 = \frac{\tau_{\text{pred}}}{\tau_{\text{cor}}} \quad (2.2)$$

The last non-dimensional number indicates the quality of observations and model ability to filtrate noise. This is the ratio of the noise variance σ^2 to the square of mean concentration (P^2):

$$\eta_3 = \frac{\sigma^2}{P^2} \quad (2.3)$$

Using all these non-dimensional numbers we estimate the identification utility in the following way. Let the time interval between successive assimilations (the discretization interval) be Δt . The number of observations assimilated to identify model output is estimated by

$$P = \frac{\tau_{\text{assim}}}{\Delta t} P_0 \quad (2.4)$$

here, P_0 is the number of observations utilized in a single assimilation event.

The following relationship between the model input parameter quantity (K) and the quantity of assimilation events within the assimilation period (P) is pointed out in the theory of statistical estimations (Stratonovich, 1973; Vapnik, 1983 and others)

$$K = f(\eta_3)P \quad (2.5)$$

where the function $f(\eta_3)$ is determined by the specificity of a used model and our request to obtain the robust estimations in the root mean square sense. However, for $\eta_3 \ll 1$, independently from a used model, $f(\eta_3) \sim 0.5-0.6$ (Vapnik, 1983). There are no

exact estimations of this function for $\eta_3 \sim 1$. The empirical estimations of Stratonovich (1973) for a large level of noise is $f(\eta_3) \sim 10^{-2}-10^{-3}$.

The value of Δt correlates with τ_{cor} as

$$\Delta t = (0.2 \div 0.3) \tau_{\text{cor}} \quad (2.6)$$

Estimation (2.6) reflects a clear physical idea: to resolve any chaotic or stochastic process of correlation scale τ_{cor} , at least three observations along the length of this scale are requested.

Originally, relationship (2.6) was suggested by Broomhead and King, 1986 for the reconstruction of dynamical attractors (the robust regimes) from the temporal observations series. Bytkovsky and Kravtsov (2001) have generalized this approach for processes with the wideband spectrum containing a dominant frequency. That allowed applying Eq. (2.6) to the real geophysical processes.

Substituting Eq. (2.6) into Eq. (2.4) and taking into account Eqs. (2.1), (2.2), (2.3) and (2.5) we get

$$K = (3 \div 5) f(\eta_3) P_0 \eta_1 \eta_2 \quad (2.7)$$

Eq. (2.7) determines the identification utility of radionuclide observations. If the number of isotopes is more than 1, we need to multiply K by this number.

Let us apply the general ideas discussed above to estimate a model input, for example, such as horizontal and vertical viscosity coefficients used in the model. We illustrate our approach for the Kara Sea and choose τ_{pred} , τ_{assim} , τ_{cor} and P_0 in the following way.

It is typical for circulation models that the model prediction time τ_{pred} be estimated as (Kravtsov, 1989; Robinson et al., 1996; Chu et al., 2002)

$$\tau_{\text{pred}} \sim \frac{2}{(\lambda_{\text{lyap}} + I_{\text{bound}}^2)} \ln \left(\frac{\varepsilon}{\sigma_{\text{int}}} \right) \quad (2.8)$$

where λ_{lyap} is the leading Lyapunov exponent; I_{bound}^2 and σ_{init}^2 are uncertainties of initial and open boundary conditions; ε is an accepted prediction error (the tolerance).

The leading Lyapunov exponent strongly depends on the spatial resolution of a model and prediction metrics, i.e. on how we measure the prediction error. The simplest way is to determine the prediction metrics as a root mean square error between the prediction and observations. How can the leading

Lyapunov exponent be estimated for a numerical model? The best way is to apply the ensemble prediction technique (Toth and Kalnay, 1997). For semi-closed marginal seas such as the Kara or Barents Sea, the prediction skill of a high-resolution model determined by the prediction time is not expected to exceed 40–60 days (Robinson et al., 1996). Low-resolution (climatic) models have a higher prediction skill up to 1 year. However, the prediction skill of climatic models considerably deteriorates while transition from seasonal to inter-annual predictions (Robinson et al., 1996). Thus, our estimation of the prediction time equals to 1 year.

The value of assimilation period $\tau_{\text{assim}} \sim 1$ month is determined by the length of summer navigation period in the Kara Sea when the sea is ice-free.

Usually, for the real marine radioecological observations $P_0 \sim 2$ –100 depending on a geographical region. The low and upper boundaries of this estimation correspond to the real situations in the Russian Arctic Seas and in European Seas, such as the Irish Sea or English Channel, where the total number of radionuclide observations is high, up to several thousands. This conclusion is confirmed by the analysis of the Data Base of Marine Environment Laboratory in Monaco (International Atomic Energy Agency) and Regional Data Bank “Contamination of Arctic Basin” (Arctic and Antarctic Research Institute, Saint-Petersburg). For the Kara Sea we take the lowest estimation, i.e. $P_0 \sim 2$, because here the total number of observations collected in the sea has never exceeded a few dozen for a single navigation period.

The correlation time τ_{cor} strongly depends on the spatial resolution of the numerical model and assimilated observations. Basing on estimations of Pavlov and Pfirman (1995) and accounting that now there are no high-resolution radionuclide observations in the Kara Sea, we take $\tau_{\text{cor}} \sim 2$ years.

Two kinds of error contribute into the variance σ^2 : measurement errors of radiochemical analytical techniques and unresolved scales. The first kind of error can easily be estimated. If we measure the concentration of a radionuclide dissolved in marine water, the measurement error in mean does not exceed 50%. For example, error in determination of the dissolved Cs¹³⁷ concentration is about 10–15%. For the suspension form this error may be much larger, up to 100–150%.

The contribution of unresolved scales strongly depends on a geographic region and the horizontal resolution of an observation grid. Accounting that most radioecological observations were realized on the grid with low spatial resolution, we suggest that the impact of this error is not less than 100–150%. Therefore, let us take that in mean $\eta_3 \sim 1$. This estimation may be improved through the effective filtration of radionuclide data and reducing measurement error of radiochemical methods.

So, to estimate climatic values of the viscosity coefficients for a high-resolution model we should take $\eta_1 \sim 1/2$, $\eta_2 \sim 1/2$, $f(\eta_3) \sim 10^{-2}$ and $P_0 \sim 2$. Substituting these values in Eq. (2.7), we get $K \ll 1$, i.e. we cannot use the radionuclide observations collected within a 1-month assimilation period to estimate the climatic model input. This is a quite reasonable result.

Let us limit the model prediction to 1 month, filtrate the radionuclide observations and estimate the mean coefficients only for the assimilation period. Here, $\eta_1 \sim 1$, $\eta_2 \sim 1$, $f(\eta_3) \sim 0.5$, $P_0 \sim 2$. That gives $K \sim 1$ and $K \sim 2$ for one and two radionuclides, respectively. Thus, there are high chances that the model can be verified through radionuclide observations in the Kara Sea.

Of course, our estimations may vary from case to case. However, in general we cannot expect their order to be considerably improved.

3. Reconstruction utility of radionuclide observations

Usually, the radionuclide data are collected only within a short observation period, the length of which depends on weather in a region, the financial cost of a ship voyage and observations. Often observations are rare and sometimes even solitary. That in general makes impossible to provide the estimate of climatic radioactive background in a sea. There is an important problem to be decided. What kind of estimations may be realized from rare and noisy radionuclide observations?

First, if the observations are rare and noisy, the best way is to reduce from spatial distributed estimations to integral estimations. That is explained in the following way.

Let the concentration of a radionuclide at z^* th horizon $c(\mathbf{x}_\perp, z^*, t)$ be decomposed as

$$c(\mathbf{x}_\perp, z^*, t) = \sum_{m=1}^M A_m(t, z^*) \Psi_m(\mathbf{x}_\perp, z^*), \quad \mathbf{x}_\perp, z \subset V \quad (3.1)$$

where Ψ_m is a set of basis functions or modes ($m=1, \dots, M$), $\mathbf{x}_\perp=(x, y)$ is the horizontal spacing, and V is the calculation domain bounded by the bottom topography and surface sea elevation.

Knowledge of the spectral coefficient A_m calculated from the observations allows determining the radionuclide concentration in any point (\mathbf{x}_\perp, z) of V . The technique to calculate the spectral coefficients and to estimate the optimal number of the basis functions $M_{\text{opt}} \leq M$ in Eq. (3.1) was developed by Ivanov et al. (2001) and Chu et al. (2002). Usually, $M_{\text{opt}} \sim (0.25-0.5)P_0$.

It was pointed out by Ivanov et al. (2001) that for the integral amount of radionuclide in sea

$$Q(z^*) = \sum_{m=1}^{M'_{\text{opt}}} A_m(t, z^*) \iint_S \Psi_m(\mathbf{x}_\perp, z^*) d\mathbf{x}_\perp \quad (3.2)$$

the optimal number of mode M'_{opt} should be considerably less than M_{opt} . Here, S is the domain generated by the intersection of the bottom topography surface and the plane $z^* = \text{const}$. Therefore, the estimate of Q needs only in knowledge of a portion of spectral coefficients A_m .

Ivanov et al. (2001) developed the effective method for determining only this portion of coefficients through filtrating contributions of other modes numbered from $(M'_{\text{opt}} + 1)$ to M_{opt} . Therefore, if even the quality and quantity of radionuclide observations do not allow to reconstruct the spatial structure of c , more coarse integral estimations are quite available.

Second, usually the integral estimations (Eq. (3.2)) indicate the current radioactive background of the sea. However, in practice the climatic estimate is the most important thing. In order to obtain such estimations from the current observations we suggest to combine the linear regression model (Eq. (3.2)) and radioactive balance equations.

Specificity of radionuclides to decay with time and the fact that before nuclear bomb tests in the Russian Arctic the integral amount of radionuclides in the

Kara, White and Barents Seas was scornfully small in comparing with 1980–2000 allow to introduce the mean amount of radionuclides in seawater for the reference period $T=t-t^*$, where t is “the current time” when observations were collected, and t^* is the moment of time, before which the radioactivity in the Arctic Seas was very low.

Choosing t^* equal to August 15, 1960 and integrating the balance equation for a radionuclide from t^* to t , we easily obtain the correlation of the mean $\bar{Q} = \frac{1}{T} \int_{t^*}^t Q(t') dt'$ and “the current” $Q(t)$. We will apply such an approach for the climatic estimate in the White and Kara Seas.

4. Open boundary modeling

Another problem is how to apply Eqs. (3.1) and (3.2) for estimating Q in a domain with an open boundary. To do so the basis functions Ψ_m need to be specified.

Let a sea region be bounded by the surface $S \cup S_{\text{open}}$. Here, S and S_{open} are the rigid and open segments of the boundary, respectively. Accordingly to Eremeev et al., 1994, the basis function $\Psi_m(\mathbf{x}_\perp, z^*)$ in Eq. (3.1) can be calculated as the eigenfunctions of the following spectral problem

$$\Delta_\perp \Psi_m(\mathbf{x}_\perp, z^*) = -\lambda_m \Psi_m(\mathbf{x}_\perp, z^*), \quad (4.1)$$

where λ_m are appropriate eigenvalues, Δ_\perp is the plane Laplacian operator.

The homogeneous conditions on the rigid segments of the boundary can be taken as

$$\frac{\partial \Psi_m}{\partial \mathbf{n}} = 0 \quad (4.2)$$

where \mathbf{n} is the external normal to the boundary.

Sometimes if inflow or outflow is dominated by advection, conditions (4.2) are also sufficient to be applied for open boundary modeling (Eremeev et al., 1994; Buffoni et al., 1997). They stated that at the open segment of the boundary, there is no diffusive flux, so that the isotopes leave the basin or pump into it only under the action of advection.

More sufficient open boundary conditions for open boundary modeling were developed in Chu et al. (2003). Accordingly to their approach the Robinson

boundary conditions are introduced on the open boundary

$$\frac{\partial c}{\partial \mathbf{n}} + \alpha(l)c = 0 \quad (4.3)$$

here, $\alpha(l)$ is the regularization function approximated by the power polynomials along the boundary and estimated by the observation within the region; l is a point moving along the open segment.

Using Eq. (4.3) allows formulating the open boundary conditions for Eq. (4.1) in the following form:

$$\frac{\partial \Psi_m}{\partial \mathbf{n}} + \alpha(l)\Psi_m = 0 \quad (4.4)$$

If a hydrodynamic model accompanies radionuclide observations, we can specify the regularization function α from the model. An approach to specify $\alpha(l)$ without knowledge of advection across the open segment of the boundary is described in [Chu et al. \(2003\)](#).

All details of such an approach can be found in that paper. However, the general recommendations for using Eqs. (4.2) and (4.4) can be formulated as follows. Boundary condition (4.4) is more preferable than Eq. (4.2) if the level of observation noise is very high, i.e. $\eta_3 \geq 1$. It is inherent for the Kara Sea. For weak noises, when $\eta_3 \ll 1$ we should apply Eq. (4.2) because it is more computational feasible and at the same time does not reduce the reconstruction accuracy considerably. In the present paper we use both Eqs. (4.2) and (4.4) for calculating the basis functions Ψ_m for open boundary domains.

5. The age

Because we may estimate only coarse characteristics of radionuclide concentration fields but not spatial distribution of isotopes, only one mixing time scale can be introduced to characterize the dynamical features of water mass. The definition given here are of simple conceptual nature.

Let us define this time scale as

$$\tau_{\text{age}}(T) = \int_{t^*}^T \frac{dQ/d\tau(\tau-t^*)d\tau}{Q(t)} \quad (5.1)$$

or in the following form

$$\tau_{\text{age}}(T) = T[1 - \bar{Q}/Q(t)] \quad (5.2)$$

$\tau_{\text{age}}(T)$ reduces into the age introduced by [Hirst \(2000\)](#) (see also [Prandle, 1984](#)) if $T \rightarrow \infty$. Note Eq. (5.2) characterizes the large-scale variability of the seawater and/or a radionuclide field in a sea region.

Two comments are principal to be done before using Eq. (5.2). Because a priori $\tau_{\text{age}} \geq 0$, $\bar{Q} < Q(t)$. This limits using Eq. (5.2) only for Q with monotonically behavior.

Another specificity of Eq. (5.2) is that for $T \rightarrow \infty$, in general $\tau_{\text{age}} \rightarrow \infty$. This confirms the local feature of τ_{age} .

More universal conception of age in marine modeling was developed by [Deleersnijder et al. \(2001\)](#) and [Delhez and Deleersnijder \(2001\)](#). However, its application requests higher quantity of observations than we have.

Let us apply the theoretical approach developed in Sections 4 and 5 for estimating radionuclide pollution and the age in the White and Kara Seas.

6. The White Sea

The White Sea is a semi-enclosed basin to the south of the Arctic Circle (between $63^{\circ}47'$ and $68^{\circ}4'N$). This sea was the closed region of the former USSR because of actively use for the conservation of old nuclear submarines and ships. Therefore, in comparing with other European Seas the hydrology and ecology of the White Sea were not well studied.

We will demonstrate how the approach described above could be useful to improve understanding hydrology and pollution of the White Sea. New estimations of cesium and strontium pollution of the White Sea are made. Using cesium-137 and strontium-90 as the indicator of water and radionuclide exchanges between different layers of the sea we will also estimate the mean time for the water renewal of its deep part.

6.1. Hydrological regime

The complex coastal geometry of the sea and its topography determine the generally accepted division

of the White Sea into several districts (see Fig. 1). The detailed survey of the White Sea hydrological regime can be found, for example, in Sukhovey (1986).

A deep-water part of the White Sea includes Pool and Kandalakshskiy Bay where the depth reaches 330 m. The north part of the sea is shallower, with depths less than 50 m. The deep-water exchange with the Barents Sea is here restricted by a sill in the Throat with a depth of about 40 m. This circumstance specifies a two-layer vertical structure of the White Sea water body: existence of surface and depth water masses separated by a permanently existing pycnocline.

The salinity of the upper 30–40 m layer (UL) does not exceed 27–28‰ due to the significant impact of fresh river water. The White Sea has a positive freshwater balance with an annual river runoff of about 215 km³. More than 75% of this amount is contributed by Mezen, Onega and Dvina rivers. The

seasonal variation of water inflow from these rivers has one distinct maximum during the spring melting in May to beginning of June. During this period the White Sea receives about 60–70% of its annual average river-off water. The rest of the year is marked by relatively low river flows, except a minor increasing in autumn, just before the winter freeze. In contrast, the rivers flowing in the Kandalakshskiy Bay have a relatively invariant seasonal distribution of water discharge. In addition to the large river runoff, the difference between precipitation and evaporation in the White Sea is positive as well. The surplus of incoming freshwater exceeding 200 km³ per year flows into the Barents Sea. On the other hand, there is an intensive mixing of White Sea and Barents Sea water masses in the Throat. The resultant dense water mass fills the deep part of the White Sea by descending the bottom slope and partially displacing the deep water towards the sea surface. Such a

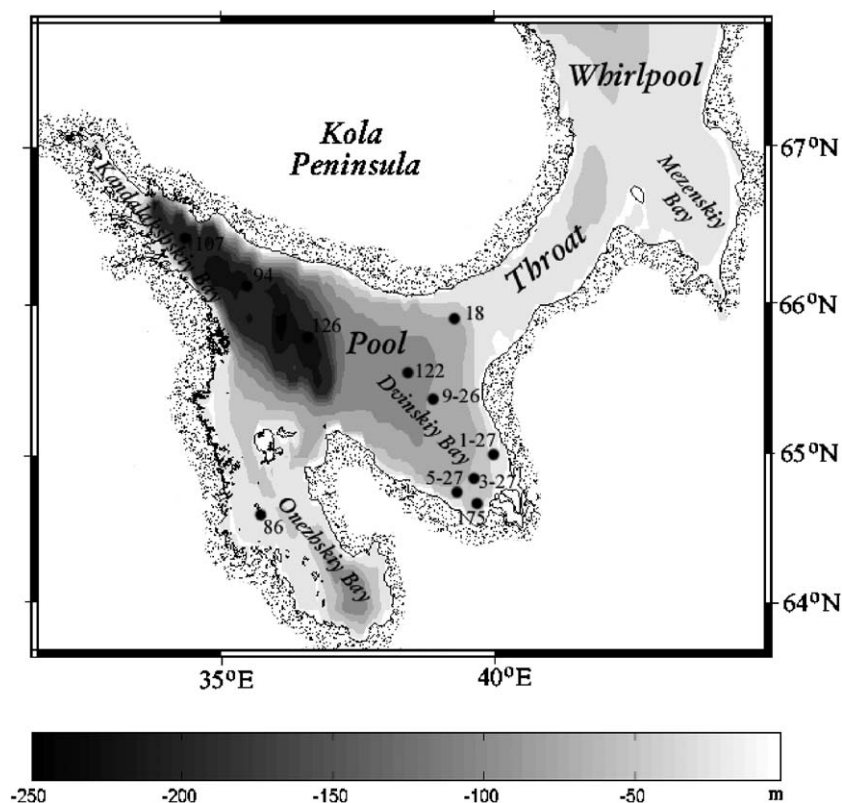


Fig. 1. Disposition of radioecological stations (black circles) in the White Sea. The measurements were provided by the Scientific Industrial Association “Taifun” (Vakulovsky et al., 1988).

process of the White Sea water renewal takes place every winter season.

6.2. Data array

The most detailed observations of radionuclide pollution of the White Sea were provided by [Vakulovskiy et al. \(1988\)](#). During the summer period of 1985 they have measured concentrations of the dissolved Cs^{137} and Sr^{90} on 11 radioecological stations. All the used field data are presented in [Table 1](#). Station dispositions are shown in [Fig. 1](#).

Table 1
Measurements of Cs^{137} and Sr^{90} concentrations in the White Sea water in 1985

Station number	Date of sampling	Horizon of sampling, m	Concentration, Bq/m ³	
			Cs^{137}	Sr^{90}
1–27	August 9	0	16	
		18	19	
3–27	August 9	0	15	
		30	18	
		50	20	
5–27	August 9	0	12	
		13	18	
		30	18	
175	August 10	0	12	10
		11	20	11
9–26	August 11	0	18	11
		30	17	
		79	19	11
122	August 12	0	11	13
		20	16	10
		40	14	10
		60	21	
		80	15	
126	August 13	100	21	11
		0	13	10
		30	19	11
		90	17	10
		150	18	9
94	August 14	200	18	11
		0	13	10
		50	16	10
		100	19	11
		150	17	10
18	August 18	200	16	10
		0	15	10
		20	18	
107	August 20	39	15	9
		0	17	12
86	August 22	0	13	8

6.3. Inverse model

The following mathematical model was used to calculate the mean amount of radionuclides Cs^{137} and Sr^{90} in the upper (UL) and lower (LL) layers of the White Sea. This model accounted the peculiarities of the hydrological regime in the sea described in Section 6.1 and some assumptions on radionuclide dynamics.

The impact of direct global fall-outs from the atmosphere and radionuclide swallowing by marine biota was a priori neglected. As it was shown by us and other investigators for the western Arctic Seas ([Matishov et al., 1994](#); [Danilov et al., 1996](#)), the global atmospheric fall-outs contribute less than several percents in total inflow both of the dissolved Cs^{137} and Sr^{90} . Also, in our opinion, marine biota accumulates scornfully small amount of the dissolved Cs^{137} and Sr^{90} (see, for example, [Eremeev et al., 1993, 1995](#)). Also we proposed that there are not strong radioactive sources on the bottom of the White Sea. This assumption is substantiated by numerous scientific publications (see, for example, [Matishov et al., 1994](#)).

It would be natural to utilize the known estimations of the fluxes from Sellafield and La Hague nuclear reprocessing plants. It is an unquestionable fact that these sources have given rise to activities generally in the Arctic waters and particularly at the entrance to the Barents Sea. However, a question arises: what part of these activities gets through into the White Sea. Besides, the Barents Sea artificial radioactivity has been induced not only by the Sellafield and La Hague fluxes. Therefore we account for the total Barents Sea radionuclide input, which in general is the resultant of all the existing sources, into the White Sea through the Throat.

Then, the balance equations connecting the current on August 1985 and the mean between 1960 and 1985 amounts of the dissolved Cs^{137} and Sr^{90} can be written as

$$\frac{Q_{\text{UL}}^i}{T} + \bar{W}^i - v_{\text{UL}} \delta_{i1} \bar{Q}_{\text{UL}}^i + \gamma \bar{Q}_{\text{LL}}^i - (1 - \eta \delta_{i1}) \bar{F}^i = \lambda^i \bar{Q}_{\text{UL}}^i \quad (6.1)$$

$$\frac{Q_{\text{LL}}^i}{T} - v_{\text{LL}} \delta_{i1} \bar{Q}_{\text{LL}}^i - \gamma \bar{Q}_{\text{UL}}^i + (1 - \theta \delta_{i2}) \bar{G}^i = \lambda^i \bar{Q}_{\text{LL}}^i \quad (6.2)$$

$$Q_{UL}^i(t) = \sum_{m=1}^8 \int_{0m}^{30m} A_m^i(t, z) \Psi_m(\mathbf{x}_\perp, z) d\mathbf{x}_\perp dz \quad (6.3)$$

$$Q_{LL}^i(t) = \sum_{m=1}^8 \int_{30m}^{300m} A_m^i(t, z) \Psi_m(\mathbf{x}_\perp, z) d\mathbf{x}_\perp dz \quad (6.4)$$

$$Q_{UL}^i(t) \geq 0, \quad \bar{Q}_{UL}^i \geq 0 \quad (6.5)$$

$$Q_{LL}^i(t) \geq 0, \quad \bar{Q}_{LL}^i \geq 0 \quad (6.6)$$

where Q_{UL}^i , Q_{LL}^i and \bar{Q}_{UL}^i , \bar{Q}_{LL}^i are the current and mean amounts of i th isotope in the upper (0–30 m) and lower (30–300 m) layers, respectively; $i=1,2$ correspond to the dissolved Cs^{137} and Sr^{90} ; δ_{ij} —Croneker symbol; λ^i is the natural decay period for the i th isotope; γQ_{LL}^i —parameterized inflows of i th isotope due to displacing the deep water towards the upper layer; $(1 - \eta)$ is a ratio of Cs^{137} concentrations in the seawater flowing out and in the White Sea; $(1 - \theta)$ is the same as $(1 - \eta)$, but for Sr^{90} ; v_{UL} and v_{LL} characterize sedimentation of the dissolved Cs^{137} , t corresponds to August 15, 1985, $T=25$ years, \bar{F}^i , \bar{G}^i , \bar{W}^i are fluxes of the i th isotope through the Throat, between UL and LL in this strait and with river runoff, respectively. The following estimations for γ , η and θ have been obtained from non-negativity condition for Q_{UL}^i , Q_{LL}^i : $\gamma \geq 0.5$; $\eta = 0.4$; $\theta = 0.5$; $[(1 - \eta)/\gamma] \geq 1$. The balance model (Eqs. (6.1–6.6)) is described in detail by Margolina (2000).

The regularized solution of Eqs. (6.1–6.6) was numerically obtained by the classical Tikhonov’s method applied to the variation problem

$$\sum_{p=1}^{11} \sum_{j=1}^5 \left[c^i(\mathbf{x}_\perp^p, z_j, t) - \sum_{m=1}^8 A_m^i(t, z_j) \Psi_m(\mathbf{x}_\perp^p, z_j) \right]^2 \rightarrow \min \quad (6.7)$$

with a priori limitations formulated as Eqs. (6.1–6.4) and inequalities (6.5) and (6.6). Summing in Eq. (6.7) is made over all the utilized radioecological stations and horizons. In detail, the Tikhonov’s method is discussed in Engl et al. (1996). We used open bound-

ary conditions (Eq. (4.2)) in the Throat and empirically determined $M'_{opt}=8$.

6.4. Radionuclide pollution of the White Sea

Table 2 summarizes quantitative estimations of the radioactive balance components from Eqs. (6.1–6.7).

These results revealed the following peculiarities of the White Sea cesium and strontium pollution. First, the major portions of radioactive cesium and strontium are pumped into the White Sea from the Barents Sea through the Throat. Second, the total amount of Cs^{137} in the White Sea water body is considerable less than the one evaluated for the Black Sea basin after the Chernobyl accident. Third, radioactive cesium in the White Sea is accumulated in bottom sediments due to transition of the dissolved Cs^{137} onto suspension. Basing on balance value on sedimentation rate in assumption on the 25-year-long cesium sedimentation in the upper 10 cm bottom layer of the White Sea, we can roughly estimate the largest possible amounts of Cs^{137} to be accumulated in sediments of the White Sea deep part with the mean concentration up to 10–15 Bq/kg. That agrees with Matishov et al. (1994).

Table 2
The mean radioactive balance of the White Sea in 1985

Isotope Fluxes and quantities in 1985	Cs^{137}		Sr^{90}	
	UL (0–30 m)	LL (30–300 m)	UL (0–30 m)	LL (30–300 m)
Total amount [TBq]	13.8	56.4	9.5	31.9
With the river runoff [TBq/year]	1.25	–	0.84	–
Inflow from the Barents Sea [TBq/year]	–	33.4	–	16.7
Outflow into the Barents Sea [TBq/year]	27.6	–	16.5	–
Accumulated by sediments [TBq/year]	1.2	3.8	–	–
Natural decay [TBq/year]	0.36	1.47	0.24	0.78

6.5. The age

Knowledge of radionuclide exchange between the upper and lower layers of the White Sea allows estimating the seawater age. It was presented in Section 6.1 that “old” deep water of the sea is periodically replaced by “new” Barents Sea water. The simplest (but not quite accurate) estimations immediately give that the mean replacement time is about 2 years if this time is determined through the ratio of the annual amount Sr^{90} in the LL to outflow of this isotope from the Barents Sea. In reality, the “old” deep White Sea water permanently mixes with more “new” water of the Barents Sea during a year. Therefore, the part of “new” water is also pushed out from the LL.

We use the radioactive Sr^{90} , which is more soluble than Cs^{137} , as an “ideal” tracer for the estimation of the seawater age (τ_{age}^1), whereas the radioactive Cs^{137} characterizes the age of the cesium field (τ_{age}^2).

Using Eqs. (5.1) and (5.2) both the ages are estimated as

$$\tau_{\text{age}}^1 \approx 5 \text{ years} \quad \tau_{\text{age}}^2 \approx 4 \text{ years} \quad (6.8)$$

So, the analysis of the characteristic mixing scales for the White Sea indicates the existence of two evolution processes in the sea. First, the salt heavy Barents Sea water transports the radionuclide Sr^{90} and Cs^{137} into the deep part of the White Sea. The mixing process renews the deep water in the White Sea approximately every 5 years. Other processes stimulate removing activity from the sea basin. However, in comparing with Sr^{90} , Cs^{137} is quite rapidly connected by sediments and suspension and then accumulated on the sea floor.

In comparing to the southern North Sea and the English Channel where the mean age reached 1 year (Delhez and Deleersnijder, 2001), the White Sea is a less ventilated basin. Our estimation is more close to the result obtained by Prandle (1984) for the age of the whole North Sea.

7. The Kara Sea

7.1. Geographical description

The Kara Sea represents the semi-enclosed ocean basin located between the Barents and Laptev Seas,

and adjoins the Arctic Ocean proper to the north (Fig. 2). The detailed survey of the Kara Sea hydrological regime can be found in Sukhovey (1986). The western boundary of sea passes along the eastern shores of Novaya Zemlya and Vaigach Island, crossing the Matochkin Shar, Kara Gate and Yugorsky Shar Straits. The Kara Sea is separated from the Laptev Sea by the Northern Land Archipelago, with the boundary passes along the eastern periphery of the Shokal'sky and Vil'kitsky Straits. The northern and southern boundaries of the Kara Sea proceed from Kol'zat Cape to the Arktichesky Cape in the Northern Land and along the mainland coast, respectively.

The Kara Sea floor is mainly a series of platform stepping downward from the southeast to the north and west. The most prominent features are Saint Anna (up to 610 m deep) and Voronin (up to 450 m deep) Troughs as well as the Novosemel'skaya depression (about 400 m deep) along the Novaya Zemlya coast. Between the former two is the Central Kara Plain with depths less than 50 m. In general, a shelf zone with depths less than 200 m constitutes about four fifths of the Kara Sea area and volume.

The coastline of the Kara Sea is complicated and irregular. It is formed by rugged eastern shores of Novaya Zemlya with numerous fiords, and mainland coast intended by the Baidaratskaya and Ob' Gulfs and three large bays, Gydansky, Yenisey and Pyasinsky.

A significant feature of the Kara Sea is the large input of freshwater from rivers, the largest of which are the Ob', Yenisey, Pyasina, Pur and Taz. The total fresh water input of the Kara Sea is about 1523 km³.

Three sources of radionuclide pollution of the Kara Sea present potential dangers: (1) transport of more polluted Barents Sea waters through the Kara Gate Strait, (2) pollution caused by run off of Siberian rivers and (3) liquid and solid radionuclide wastes dumped in the shallow-water coast of Novaya Zemlya. We will estimate the mean radioactive background of the Kara Sea, the short- and long-term trends in behavior of isotopes and impacts of potential sources of the Kara Sea radionuclide pollution.

7.2. Data array

In order to detect radionuclide sources from the field of artificial radioactivity, as well as to estimate

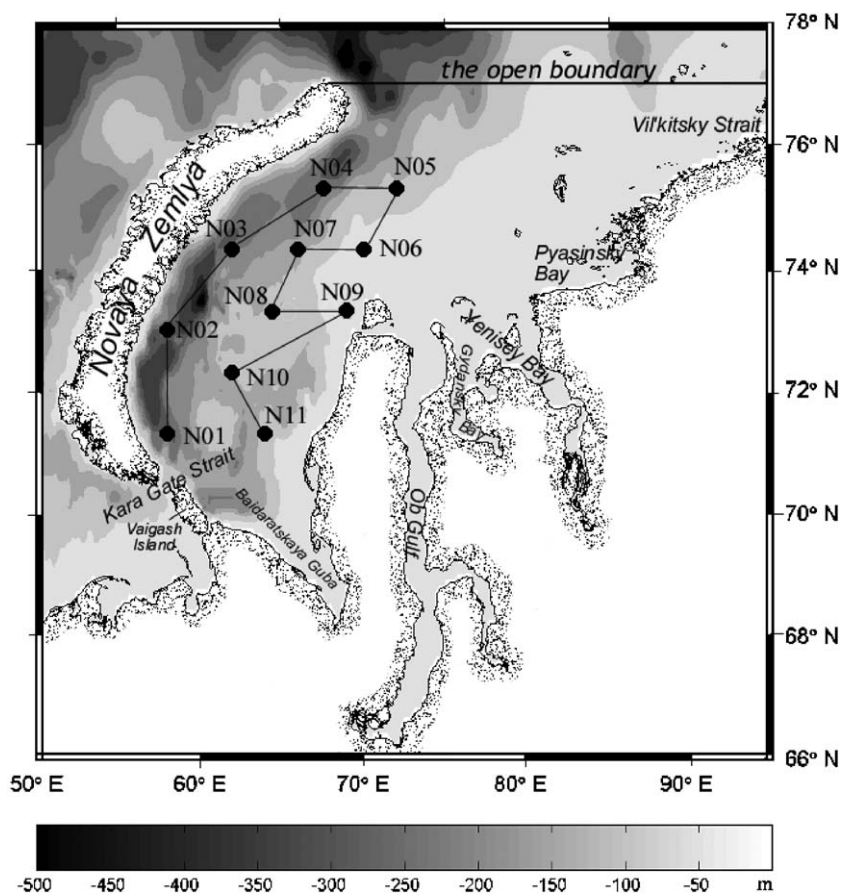


Fig. 2. Disposition of radioecological stations (black circles) in the Kara Sea. Vessel “Victor Byinitski”, the voyage 1992.

the age for the Kara Sea, we utilized observations of the dissolved and suspended Cs^{137} and dissolved Sr^{90} collected during the Russian–Norwegian 1992 expedition on the stations disposed as in Fig. 2. Table 3 presents all the used field data.

The integral amounts of Cs^{137} and Sr^{90} were calculated for the domain bounded by Novaya Zemlya and Russian Siberian coasts from 57°E to 100°E and the open boundary along 77°N from 67°E to 100°E (Fig. 2). To construct the radioactive balance we a priori utilized information on the annual currents modeling in the Kara Sea provided by Dr. M. Kulakov (the Arctic and Antarctic Research Institute, Russia), and the following climatic outflow and inflow components of the Kara Sea water balance (Table 4).

7.3. Inverse model

Radioactive cesium and strontium in the Kara Sea can come from several sources. A few major ones include effluents from other areas transported to the Kara Sea from the Barents Sea through the Kara Gate Strait; river runoff containing eroded fall-out from the land and leached materials from nuclear waste sites; released radioactive contaminants from nuclear materials dumped in the Kara Sea since 1959. Here the same comments about possibility of accounting for known fluxes from reprocessing wastes discharged into northwest European waters, as for the White Sea are valid. As it was commented by Guéguéniat et al. (1997) in the case of La Hague contribution to the radioactive contamination, one needs to have a longer

Table 3
Measurements of Cs¹³⁷ and Sr⁹⁰ concentrations in the Kara Sea water in 1992

Station number	Date of sampling	Horizon of sampling	Concentration, Bq/m ³	
			Cs ¹³⁷	Sr ⁹⁰
N01	August 21	0	8.1	3.8
		28	11.2	3.6
		70	6.3	3.8
N02	August 23	170	12.6	5.6
		0	5.3	3.7
		80	4.6	3.7
		190	10.8	3.8
N03	August 25	0	3.5	3.5
		80	4.7	4.7
		323	6.4	6.4
N04	August 27	0	5.5	11.4
		70	12.1	5.3
		250	18.3	6
N05	August 28	0	3.8	8.3
		7	3.7	12.1
		85	10.1	4.5
N06	August 29	120	10.7	4.8
		0	3.3	6.7
		16	11	5.1
N07	August 30	0	7.7	5.5
		75	11.9	4
		170	9.8	4.5
N08	August 31	0	6.5	4.3
		70	9.3	4
		124	8.8	3.9
N09	September 1	0	7.6	6.3
		10	10	5.7
		20	12.7	3.8
N10	September 3	0	7.2	3.1
		50	10.4	3
		115	8.6	3.5
N11	September 5	0	7.3	3.8
		40	7.7	3.5
		87	7.8	3.6

time series of analyses to assess the dilution between the entrance to the Barents Sea and the entrance to the Kara Sea. Thus, the composite flux into the Kara Sea through the Kara Gate Strait was incorporated in the model. The decrease of radioactivity is influenced by isotope outflow through the Vil'kitsky Strait and open sea boundary, as well as sedimentation for Cs¹³⁷ and accumulation by the marine biota for Sr⁹⁰.

Accordingly to Danilov et al. (1996) we a priori neglect isotope fluxes from atmosphere and from dumped containers with the liquid radioactive wastes. Also, it is confirmed by our experience for the Black Sea (Eremeev et al., 1994, 1995), the Kara Seas

(Danilov et al., 1996) and the White and Barents Sea (Margolina, 2000) that in comparing with other physical absorption processes marine biota accumulates negligible amount of Cs¹³⁷ and Sr⁹⁰.

Accounting these approximations let us formulate the balance equations for the Kara Sea in the following form:

$$\frac{Q_i}{T} = \bar{R}_1 \bar{c}_{\text{gate}}^i + \bar{R}_2 \bar{c}_{\text{riv}}^i - \lambda^i \bar{Q}_i + \bar{F}_i, \quad (7.1)$$

$$Q_i(t) = \sum_{m=1}^8 \int_{0m}^{200m} A_m^i(t, z) \Psi_m(\mathbf{x}_{\perp}, z) d\mathbf{x}_{\perp} dz, \quad (7.2)$$

$$\bar{c}_{\text{gate}}^i \geq 0 \quad (7.3)$$

$$\bar{c}_{\text{riv}}^i \geq 0 \quad (7.4)$$

$$\bar{Q}_i \geq 0 \quad (7.5)$$

$$Q_i \geq 0 \quad (7.6)$$

Here Q_i and \bar{Q}_i is the “current” and climatic integral amounts of i th isotope, respectively; $i=1, 2$ and 3 correspond to the dissolved Cs¹³⁷, Sr⁹⁰ and the suspended Cs¹³⁷, respectively; \bar{c}_{gate}^i , \bar{c}_{riv}^i are the mean concentration of i th isotope in the Kara Gate Strait and estuaries of the Enisey and Ob' rivers; \bar{F}_i is the outcoming of the i th isotope from the Kara Sea. S is the area generated by the intersection of the bottom topography surface and the plane $z = \text{const}$.

The regularized solution of Eqs. (7.1–7.6) was numerically obtained by the classical Tikhonov's method applied to the variation problem

$$\sum_{p=1}^{11} \sum_{j=1}^7 \left[c^j(\mathbf{x}_{\perp}^p, z_j, t) - \sum_{m=1}^8 A_m^i(t, z_j) \Psi_m(\mathbf{x}_{\perp}^p, z_j) \right]^2 \rightarrow \min \quad (7.7)$$

with a priori limitations formulated as Eqs. (7.1) and (7.2) and inequalities (7.3)–(7.6). Summing in Eq.

Table 4
Climatic inflows and outflows for the Kara Sea

Inflow (Sv)		Outflow (Sv)		
\bar{R}_1	the Kara Gate Strait	0.3	\bar{R}_4 the Vil'kitsky Strait	–0.2
\bar{R}_2	the Ob' river	0.012	\bar{R}_5 the open boundary	–0.13
\bar{R}_3	the Enisey river	0.018		

(7.7) is made over all the utilized radioecological stations and horizons. In detail, the Tikhonov's method is discussed in Engl et al. (1996). We used open boundary conditions (Eq. (4.4)) and empirically determined $M'_{\text{opt}} = 8$.

7.4. The radionuclide pollution of the Kara Sea

Table 5 summarizes the results of estimations of incoming and outgoing radioactivity for the Kara Sea.

Analyzing the presented results, the following conclusions can be made.

First, the radioactive contamination of the Kara Sea is lower in comparing with the Barents and Black Seas. To be more specific, the mean integral amount of dissolved cesium-137 in these seas is about 390 TBq (Margolina, 2000) and 2500–3000 TBq (Eremeev et al., 1995), respectively.

Second, the principle contributor of the Kara Sea radioactivity background is the Barents Sea through the Kara Gate Strait. Note that the annual incoming radioactivity through this Strait is much larger than the integral amount of isotopes in the sea. Therefore, we may expect that the Kara Sea should be well

Table 6

The activity ratio for the Kara Sea in 1992

Location	Activity ratio
Ob' and Enisey river estuaries	0.5
The Kara Gate Strait	2.36
The open boundary	1.21
The mean over the sea surface	0.79
The mean over the sea volume	1.30

“ventilated” through the open boundary and the Vil'kitsky Strait.

Third, the previous estimations of the Ob' and Enisey contributions in the Kara Sea radioactive background are overestimated at least by one order.

7.5. The age

Similar to the discussed above for the White Sea, the appropriate ages were estimated as

$$\tau_{\text{age}}^1 \approx 1 - 2 \text{ years} \quad \text{and} \quad \tau_{\text{age}}^2 \approx 1 \text{ year} \quad (7.8)$$

Note, that our estimations (Eq. (7.8)) agree very well with the results of Pavlov et al. (1993) who estimated the ventilation rate of the Kara Sea as 3.5 years, estimates of the mean residence time of water on the Siberian shelves from tritium/helium data of 3.5 ± 1.5 years (Schlosser et al., 1994) and computations of a freshwater residence time for river input of 2.5 years in the Kara Sea provided by Hanzlick and Aagaard (1980).

All these estimations confirm our assumption on high ventilation features of the Kara Sea and indicate that any pollution initially localized within a limited area of the Kara Sea be rapidly delocalized and transferred into the Arctic Ocean.

Another interesting result on the vertical mixing of the Kara Sea water mass can be revealed through the analysis of activity ratio determined as $v = \bar{c}_1/\bar{c}_2$. Table 6 lists the activity ratio calculated for different areas of the Kara Sea.

Analyzing this table we note that the river waters are rich in Sr^{90} . More salt and radioactive water of the Barents Sea contains more considerable amount of Cs^{137} . The activity ratio of this water equals to 2.36 and indicates its carrying a tracer signal from the Sellafield discharges (Livingston, 1988; Kershaw and Baxter, 1995). However, the mean activity ratio for the Kara Sea surface equals to about 0.79. It is close to

Table 5
Radioactive pollution of the Kara Sea in 1992

Fluxes and quantities in 1992	Cs^{137}		Sr^{90}
	The dissolved form	The suspended form	The dissolved form
Integral amount (TBq)	15.8	0.20	8.62
Through the Kara Gate Strait [TBq/year]	53.6	0.24	23.4
With the Enisey and Ob' river water [TBq/year]	1.84/3.80 ^a	0.028	3.87/38.0 ^a
Through the Vil'kitsky Strait, the open boundary and due to transition into the suspended form (for Cs^{137}) [TBq/year]	30.1	0.3	24.1
Due to natural decay [TBq/year]	0.5	0.007	0.3

^a Here we also give the previous estimations obtained from personal communication with Dr. A.I. Nikitin (the Scientific Industrial Association “Taifun”).

the activity ratio for the estuaries of Ob' and Enisey rivers equal to 0.5. More rich in Cs¹³⁷ Barents Sea water are mixed only in deep layers.

8. Sensitivity of inverse modeling

The inverse calculations discussed in Sections 6 and 7 are generally to obtain the best solution using the r.m.s. criteria. Thus, an important question arises: how high is sensitivity of the obtained estimations to variations of observation sampling lengths, level of noise corrupting the data and the model input, such as the river discharge, inflow and outflow fluxes?

Both inverse models (6.1)–(6.7) and models (7.1)–(7.7) resulted into solving ill-posed systems of linear algebraic equations (SLAE). The coefficients and right-hand sides of these systems are determined by the model input and the data. Any perturbations of both the model input and the data, i.e. reducing observation sampling lengths, can result in a new solution. Thus, the special methods stabilizing the solution should be applied.

In these goals the present study utilizes the Tikhonov's regularization technique. It is well known (Engl et al., 1996) that a priori the regularized solution of any SLAE is robust to small perturbations of system coefficients and right hand side of such a system. The robustness to finite size perturbations of the system can be improved through reducing the spatial resolution of the reconstructed field (Ivanov et al., 2001).

In principle, our estimations are expected to be most sensitive to limited observation sampling sizes and level noise corrupting observations. However, Ivanov et al. (2001) found that the integral amount of radionuclides and chemical substances in the Black and Kara Seas are weakly sensitive to variations of length of observation samplings and ratio of noise to signal up to 0.5–1.0. Note that this conclusion may be not true if we reconstruct the spatial structure of radionuclide fields.

9. Conclusions

In this paper we have aimed to demonstrate that even the rare and noisy radioecological observations can be useful for the analysis of the long- and short-term trends in behavior of marine radioactivity. How-

ever, we call in question identifying a significant free model input from the radionuclide data which are now accessible for the Arctic Seas. We theoretically defined the so-called identification utility of such radionuclide observations (Eq. (2.7)) and demonstrated that even for regional numerical models with a good forecast skill this value is low.

From our point of view it is more perspective to apply the rare and noisy radioecological observations for the construction of the radioactive balance for the sea or its part. We developed the special approach allowing to do this even from "solitary" observations. This approach is reduced to the analyzing of linear regression models with a priori limitations formulated as the balance equations and positive features of balance variables.

The ages characterizing variability of the seawater and radionuclide fields were estimated from knowledge of separate components of radionuclide balance. The obtained estimations range approximately from 1 to 5 years for the Kara and White Seas, respectively. That demonstrates the existence of the long-term trends in radionuclide pollution of the White Sea while the Kara Sea is a well-ventilated region.

Acknowledgements

The work described in this paper was reported by Dr. L. Ivanov on the 34th Liege Colloquium on Ocean Dynamics—Tracer Methods in Geophysical Fluids (Liege, May 6–10, 2002). Dr. L. Ivanov thanks the Scientific Organizing Committee for the support of his visit to the University of Liege. We appreciate the helpful comments from two anonymous reviewers allowed to substantially improve the manuscript.

References

- Broomhead, D., King, G.P., 1986. Extracting qualitative dynamics from experimental data. *Physica*, D 20, 217–239.
- Buffoni, G., Falco, P., Griffa, A., Zambianchi, E., 1997. Dispersion processes and residence times in a semi-closed basin with recirculating gyres: an application to the Tyrrhenian Sea. *J. Geophys. Res.* 102 (C8), 18699–18713.
- Bytkovsky, O.Ya., Kravtsov, Yu.A., 2001. On the rational choice of discretization interval for processes with spectrum containing dominant frequency. *Appl. Nonlinear Dyn.* 9 (3), 54–59.

- Chu, P.C., Ivanov, L.M., Margolina, T.M., Melnichenko, O.V., 2002. Probabilistic stability of a simple atmospheric model to differently scales perturbations. *J. Atmos. Sci.* 59 (19), 2860–2873.
- Chu, P.C., Ivanov, L.M., Korzhova, T.P., Margolina, T.M., Melnichenko, O.V., 2003. Analysis of sparse and noisy data using flow decomposition. Part 1: Theory, Part 2: Applications to Eulerian and Lagrangian data. *J. Atmos. Ocean. Technol.* 20, 478–512.
- Danilov, A.I., Ivanov, L.M., Kulakov, M.Yu., Margolina, T.M., Pavlov, V.K., 1996. Modern radioactive climate of the Kara Sea: geophysical reports. *Russ. Acad. Sci.* 346 (4), 545–548 (in Russian).
- Deleersnijder, E., Camprin, J.M., Delhez, E., 2001. The conception of age in marine modeling: 1. Theory and preliminary model results. *J. Mar. Syst.* 28, 229–267.
- Delhez, E., Deleersnijder, E., 2001. The conception of age in marine modeling: 2. Concentration distribution in the English Channel and the North Sea. *J. Mar. Syst.* 31, 279–297.
- Engl, H.W., Hanke, M., Neubauer, A., 1996. *Regularization of Inverse Problems*. Kluwer Academic Publishing, Dordrecht.
- Eremeev, V.N., Chudinovskikh, T.V., Batrakov, G.F., 1993. Artificial radioactivity of the Black sea. Contribution to the UNESCO/Chernobyl project. UNESCO Reports in Marine Science, vol. 59. UNESCO.
- Eremeev, V.N., Ivanov, L.M., Kirwan Jr., A.D., Margolina, T.M., 1994. Amount of Cs-137 and Cs-134 radionuclides in the Black Sea produced by the Chernobyl disaster. *J. Environ. Radioact.* 26, 49–63.
- Eremeev, V.N., Ivanov, L.M., Kirwan Jr., A.D., Margolina, T.M., 1995. Analysis of caesium pollution in the Black Sea by regularization method. *Mar. Pollut. Bull.* 30 (7), 460–462.
- Guéguéniat, P., Kershaw, P., Herrmann, J., Bailly du Bois, P., 1997. New estimation of La Hague contribution to the artificial radioactivity of Norwegian waters (1992–1995) and Barents Sea (1992–1997). *Sci. Total Environ.* 202, 249–266.
- Hanzlick, D., Aagaard, A., 1980. Freshwater and Atlantic water in the Kara Sea. *J. Geophys. Res.* 85, 4937–4942.
- Hirst, C.A., 2000. Determination of water component age in ocean models: application to the fate of North Atlantic Deep Water. *Ocean Model.* 92, 81–94.
- Ivanov, L.M., Kirwan Jr., A.D., Margolina, T.M., 2001. Filtering noise from oceanographic data with some applications for the Kara and Black Seas. *J. Mar. Syst.* 28 (1-2), 113–139.
- Kershaw, P.J., Baxter, A.J., 1995. The transfer of reprocessing wastes from NW Europe to the Arctic. *Deep-Sea Res., Part II* 42 (6), 1413–1448.
- Kravtsov, Yu.A., 1989. Randomness, determinativeness and predictability. *Usp. Fiz. Nauk* 158, 93–123 (in Russian).
- Livingston, H.D., 1988. The use of Cs and Sr isotopes as tracers in the Arctic Mediterranean Seas. *Trans. R. Soc. Lond.* A325, 161–176.
- Margolina, T.M., 2000. *Radioactive Pollution of the Black, Kara, Barents and White Seas: the Analysis Through the Method of Spectral Reconstruction*. PhD Thesis, Marine Hydrophysical Institute, Ukrainian National Academy of Sciences, Sevastopol, Ukraine. Unpublished (in Russian).
- Matishov, G., Matishov, D., Schipa, E., Rissanen, K., 1994. Radionuclides in the Ecosystem of the Barents and Kara Seas' Region. Russian Academy of Sciences, Apatity. In Russian.
- Pavlov, V.K., Pfirman, S.L., 1995. Hydrophysic structure and variability of the Kara Sea: implications for pollutant distribution. *Deep-Sea Res., Part II* 42 (6), 1369–1390.
- Pavlov, V.K., Kulakov, M.Yu., Stanovoy, V.V., 1993. Report to the International Arctic Seas Assessment Program. International Atomic Energy Agency, Vienna, Austria.
- Prandle, D., 1984. A modeling study of the mixing of Cs-137 in the seas of the European continental shelf. *Philos. Trans.* A310, 407–436.
- Robinson, A.R., Arango, H.G., Warn-Varnas, A., Leslie, W.G., Miller, A.J., Haley, P.J., Lozano, C.J., 1996. Real-time regional forecasting. In: Malanotte-Rizzoli, P. (Ed.), *Modern Approaches to Data Assimilation in Ocean Modeling*. Elsevier Oceanography Series Elsevier, The Netherlands, pp. 337–409.
- Schlosser, P., Bauch, D., Fairbanks, R., Bonisch, G., 1994. Arctic river run-off: mean residence time on the shelves and in the haloline. *Deep-Seas* 41, 1053–1068.
- Stratonovich, R.L., 1973. *Principles of Adaptive Reception*. Sov. Radio, Moscow. In Russian.
- Sukhovoy, V.F., 1986. *Seas of the World Ocean*. Hydrometeoizdat, Leningrad. In Russian.
- Toth, Z., Kalnay, E., 1997. Ensemble forecasting at NCEP and the breeding method. *Mon. Weather Rev.* 125, 3109–3297.
- Vakulovsky, S.M., Nikitin, A.I., Chumichev, V.B., 1988. The contamination of the White Sea by the radioactive wastes of the West Europe countries. *At. Energ.* 65 (1), 66–67 (in Russian).
- Vapnik, V.H., 1983. *Reconstruction of Empirical Laws from Observations*. Nauka, Moscow. In Russian.
- Yablokov, A.V., Krasev, V.K., Rumyantsev, V.M., Kokeyev, M.Y., Petrov, O.I., Lystsov, V.N., Yemelyanenko, A.F., Rubtsov, P.M., 1993. *Facts and Problems Related to Radioactive Waste Disposal in Seas Adjacent to the Territory of the Russian Federation*. Office of the President of the Russian Federation, Moscow, Russia.



ELSEVIER

Available online at www.sciencedirect.com

SCIENCE @ DIRECT®

Journal of Marine Systems 48 (2004) 133–157

JOURNAL OF
MARINE
SYSTEMS

www.elsevier.com/locate/jmarsys

Sea ice fluxes and drift trajectories from potential pollution sources, computed with a statistical sea ice model of the Arctic Ocean

Vladimir Pavlov^{a,*}, Olga Pavlova^a, Reinert Korsnes^b

^a *Norwegian Polar Institute, Polar Environmental Center, N-9296 Tromsø, Norway*

^b *Norwegian Defence Research Establishment (FFI), P.O. 25, NO-2027 Kjeller, Norway*

Received 10 October 2002; received in revised form 20 June 2003; accepted 13 November 2003

Available online 14 March 2004

Abstract

Using satellite ice drift and ice concentration data, observed sea surface temperature and sea level pressure data we have developed a statistical sea ice model (ISMO) and computed the vectors of ice velocity for the period 1899–2000 and ice concentration for the period 1966–2000. On the basis of the ISMO results, we estimate the sea ice fluxes through the main straits of the Arctic Ocean and simulate trajectories of the ice drift from the locations of potential sources of contaminants. The ISMO is verified by comparing with the observational results of the sea ice fluxes and extents, and with the historical drift data from the International Arctic Buoy Programme. For example, the relation between the observed (not satellite data) and calculated April ice extent in the Nordic seas for the period 1966–1998 ($R=0.57$) has good agreement, and the pathways of simulated and observed trajectories are quite close; origins derived from calculated backward trajectories are generally consistent with actual buoy drifts. We also compare the modelling sea ice flux through Fram Strait with the estimation using ice motion from satellite passive microwave data for the period 1978–1996, finding a significant correlation ($R=0.71$) between the calculated and observed time series of the monthly area flux. We estimate the average sea ice export from the Arctic Ocean through Fram Strait and the strait between Svalbard and Franz Josef Land over the 35-year simulated record (1966–2000) as 639,000 and 70,000 km² year⁻¹, respectively. Estimation of the ice flux from the Kara Sea to the Barents Sea through the strait between Franz Josef Land and Novaya Zemlya gives 104,000 km² year⁻¹ for the same period. The average sea ice import from the Kara, Laptev and East Siberian seas to the Arctic Ocean over the same period is about 332,000 km² year⁻¹. The average sea ice export from the Arctic Ocean through the strait between Wrangel Island and Cape Barrow is 7000 km². The difference between the annual mean ice fluxes estimated by ISMO and most previous estimations for Fram Strait is 0.1–30%. We investigate the seasonal and interannual variability of the sea ice flux through the main straits of the Arctic Ocean, and show strong seasonal variability and significant variations from year to year (e.g., in Fram Strait from a minimum of 435,000 km² year⁻¹ in 1985 to a maximum of 940,000 km² year⁻¹ in 1995). Calculation of forward trajectories shows that sea ice from most potential sources of contaminant can reach the open Polar Basin and Fram Strait. Contaminated sea ice from potential sources in the Kara and Laptev seas can reach Fram Strait within 2–4 years, and from the East Siberian, Chukchi and Beaufort seas within 6–11 years. Based on simulated trajectories from different potential sources

* Corresponding author. Fax: +47 77 75 05 01.

E-mail address: vladimir.pavlov@npolar.no (V. Pavlov).

in the Arctic Ocean, we conclude that the most important regions for monitoring contaminants are Fram Strait and the Barents Sea Opening.

© 2004 Elsevier B.V. All rights reserved.

Keywords: Arctic Ocean; Marginal seas; Sea ice flux; Sea ice drift; Contaminants; Modelling

1. Introduction

The study of ice conditions and pollutant transport in the Arctic Ocean is one of the most important lines of inquiry in modern polar oceanography and ecology. These investigations are of primary practical importance as well as theoretically significant for the development of the theory of ice formation, mechanisms of pollutant transport and climate variations in the Arctic Ocean. A knowledge of the specific features of ice conditions in the Polar Basin and marginal seas is necessary to resolve the problems of human activity and polar ecology.

The geographical position and climatic features of the Arctic seas mean that their ecological balance is sensitive to disturbance by inputs of man-made pollutants. The Arctic seas represent natural accumulation and transport zones between regions of active exploitation of natural resources and pollution and the ecologically clean regions of the central Polar Basin. Processes involved in transport, transformation and accumulation of contaminants from different potential sources are particularly important in assessing the fate of potential pollutant releases.

Transport via sea ice, which occurs in the Arctic seas throughout the year, is one of the major mechanisms of transport and redistribution of pollutants (Weeks, 1994; Pfirman et al., 1995; Chernyak et al., 1996). Sea ice may be contaminated by atmospheric deposition or by entrainment from the marine environment (Pfirman et al., 1997a). Deposition of atmospheric pollutants (Melnikov, 1991) transported in Arctic haze is likely to increase the contaminant load of the snow and ice (Pfirman et al., 1995).

The ice cover of the Arctic seas is contaminated by many types of pollutants: from oil hydrocarbons (Izmailov, 1988) to suspended matter transported with river runoff (Komov and Spichkin, 1981). The drift and melting of polluted ice contribute to redistribution of the concentrations of pollutants in seawater. Thus, the export of drifting ice from the region of its formation

results in partial cleansing of this region and in pollution of the region where the ice melts (Pavlov and Stanovoy, 2001). On ice melting, pollutants are released and come to the sea surface with the meltwater.

The basic problem guiding research into the processes of Arctic Ocean contamination via sea ice lies in the estimation of ice area and volume flux through the boundaries, trajectories and regions of origin of the polluted sea ice.

Sea ice motion derived from buoys in the International Arctic Buoy Programme (IABP), beginning in 1979, and the observational sea ice data derived from the satellite passive-microwave record from the SMMR and SSM/I, beginning October 1978, have given a large amount of data on the drift and the spatial and temporal variability of the sea ice cover in the Arctic Ocean. The data collected within these programs initiated a large number of studies of ice motion and variability of ice conditions in the Arctic Ocean, including the problem of pollutant transport by sea ice.

Colony and Thorndike (1984) have applied the procedure of optimal interpolation to obtain a spatially smoothed field of motion from the buoy-data and thus derived the field for mean ice motion of the Arctic Ocean. Earlier, Thorndike and Colony (1982) have tried to find a relationship between the ice velocity, geostrophic winds and mean ocean currents based on data from the buoys. The authors have shown that in the central Polar Basin the relationship between ice velocity and geostrophic wind is very strong. At a distance of 400 km or more from the coasts, the squared correlation coefficient (ρ^2) between geostrophic wind and ice velocity is about 0.75 ± 0.05 in winter and spring and 0.80 ± 0.06 in summer and autumn. However, within 400 km of the coasts, ρ^2 is generally smaller with values of 0.50 ± 0.20 in the winter and spring. During the summer and autumn, these low correlations persist near the Canadian Archipelago and north of Spitsbergen, but north of Alaska, ρ^2 reached 0.80 ± 0.10

(Thorndike and Colony, 1982). Similar results have been presented by Serreze et al. (1989) in a more detailed analysis of the relationship between geostrophic wind and sea ice motion in the Canadian Basin for 1979–1985.

This result is not unexpected, since in the shelf zone, with its complicated coastline and the presence of islands, geostrophic balance in the ice velocity can be weakened or completely absent. At the same time, ice motion data in shelf areas are most important for investigation of ice fluxes and transport of polluted sea ice.

Based on the research of Thorndike and Colony (1982), Colony and Thorndike (1984, 1985) and observational drift data from the International Arctic Buoy Programme, many studies concerning the problems of pollutant transport in the Arctic Ocean have been carried out. For example, Colony (1986) modelled transport of oil by sea ice in the Chukchi and Beaufort Seas; Pfirman et al. (1997b) presented a method of reconstructing the forward and backward trajectories of sea ice in the Arctic Ocean and showed the use of these reconstructed trajectories for understanding of Arctic sediment flux; Rigor and Colony (1997), using in addition a simple empirical relation between ice thickness and “freezing degree days” (Zubov, 1943), simulated sea ice production and export of the polluted ice from the Laptev Sea in the period from 1979 to 1993.

Buoy positions have high spatial accuracy and temporal resolution. However, the spatial distribution is generally rather coarse, so that buoy data provide only a highly restricted view of the temporal and spatial variability of the large-scale sea ice drift patterns. Buoy data provided by the IABP cover mostly the central part of Arctic Ocean, so in significant areas of the Siberian seas, where there are potential sources of pollution, the buoy data are absent.

Another method of deriving the ice motion is the analysis of sequences of images obtained from polar-orbiting satellites (e.g. Ninnis et al., 1986; Emery et al., 1991, 1997a,b; Kwok et al., 1998; Martin and Augstein, 2000). Kwok et al. (1998) and Martin and Augstein (2000) reported a good correlation between ice vectors derived from the satellite passive-microwave imagery and those derived from buoy data. The high spatial and temporal resolution and relatively large number of ice motion data from satellite

images allow these data to be applied in the study of regional processes, such as the sea ice fluxes through straits in the Arctic Ocean (Martin and Augstein, 2000), the transport of ice by the East Greenland current (Martin and Wadhams, 1999) and the transport of contaminants (Emery et al., 1997b; Korsnes et al., 2002).

In Korsnes et al. (2002), the attempt has been made to reveal the statistical relation between atmospheric forcing and ice motion, derived from the satellite images, in the Kara and Barents seas, and in Fram Strait. Ice statistical model (ISMO) developed in this paper allowed the authors to reconstruct ice drift, estimate the sea ice fluxes through the straits in the Kara and Barents seas, and Fram strait for the 1899–1998, and also calculate the most probable trajectories of the ice drift from the potential sources of pollution in the Kara Sea for the same period. In spite of the fact that these estimations have been made assuming climatic monthly ice extend and 100% concentration, the obtained results were quite realistic.

This study is a continuation of the paper of Korsnes et al. (2002). We have expanded computing domain to all Arctic Basin and Arctic seas and have made attempt to find relationship between atmospheric parameters and ice concentration. Based on the modelling results, we have given estimate of annual and interannual variability of sea ice flux cross the main straits of the Arctic seas. We also have simulated the trajectories of sea ice drift from regions of potential pollution sources in the Arctic seas using velocity vectors of ice drift and ice concentration that obtained as a result of modelling.

2. Data and methods

These estimates are based on the improvement and implementation of the ice statistical model (ISMO) developed at the Norwegian Polar Institute (Korsnes et al., 2002). At the present time, ISMO can be used for simulating ice drift (as in Korsnes et al., 2002) and ice concentration. Moreover, the domain of the model was extended and now includes the entire Arctic Ocean and its marginal seas. Thus, it has allowed us to make a more correct estimate of the ice flux through the main straits of the marginal seas of the

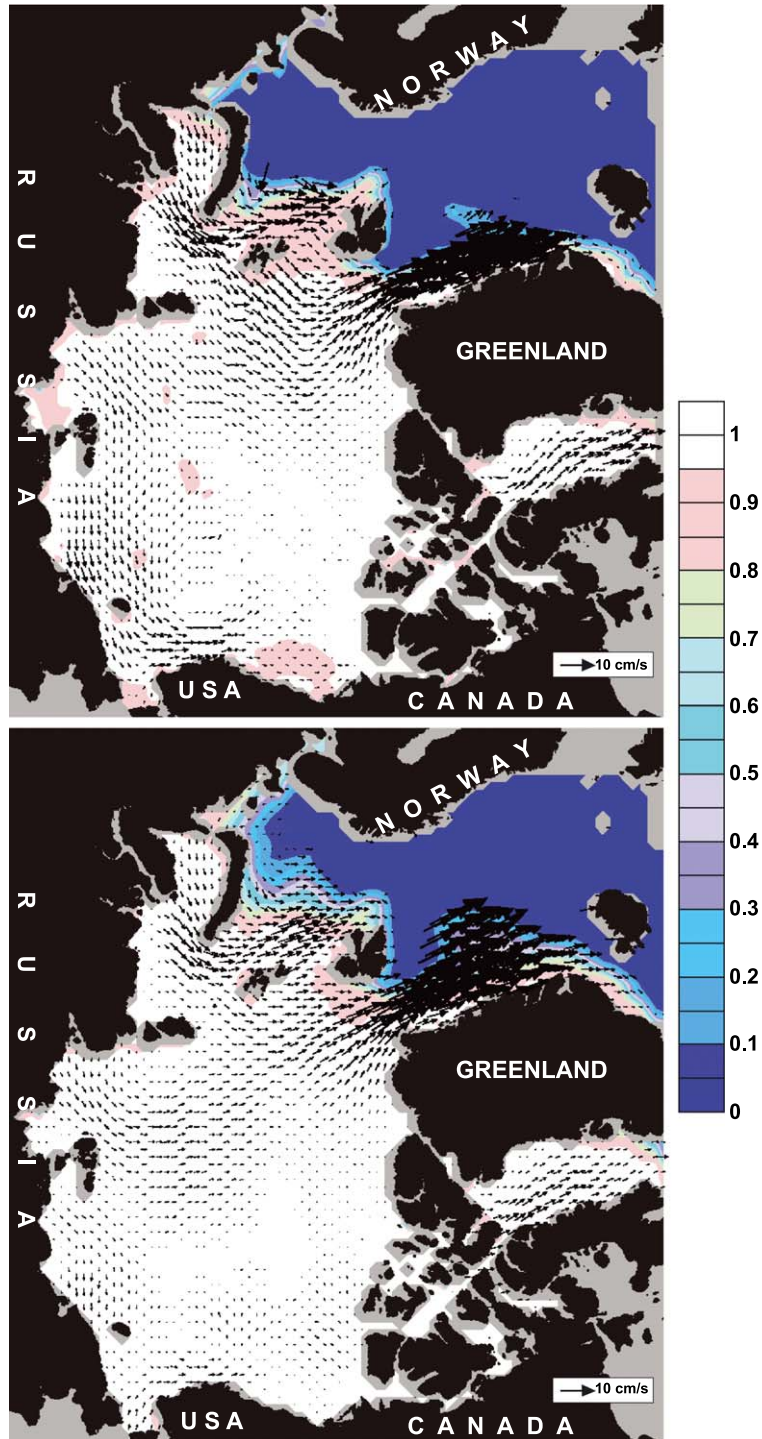


Fig. 1. Observed (top) and simulated (bottom) ice drift and ice concentration for January 1993.

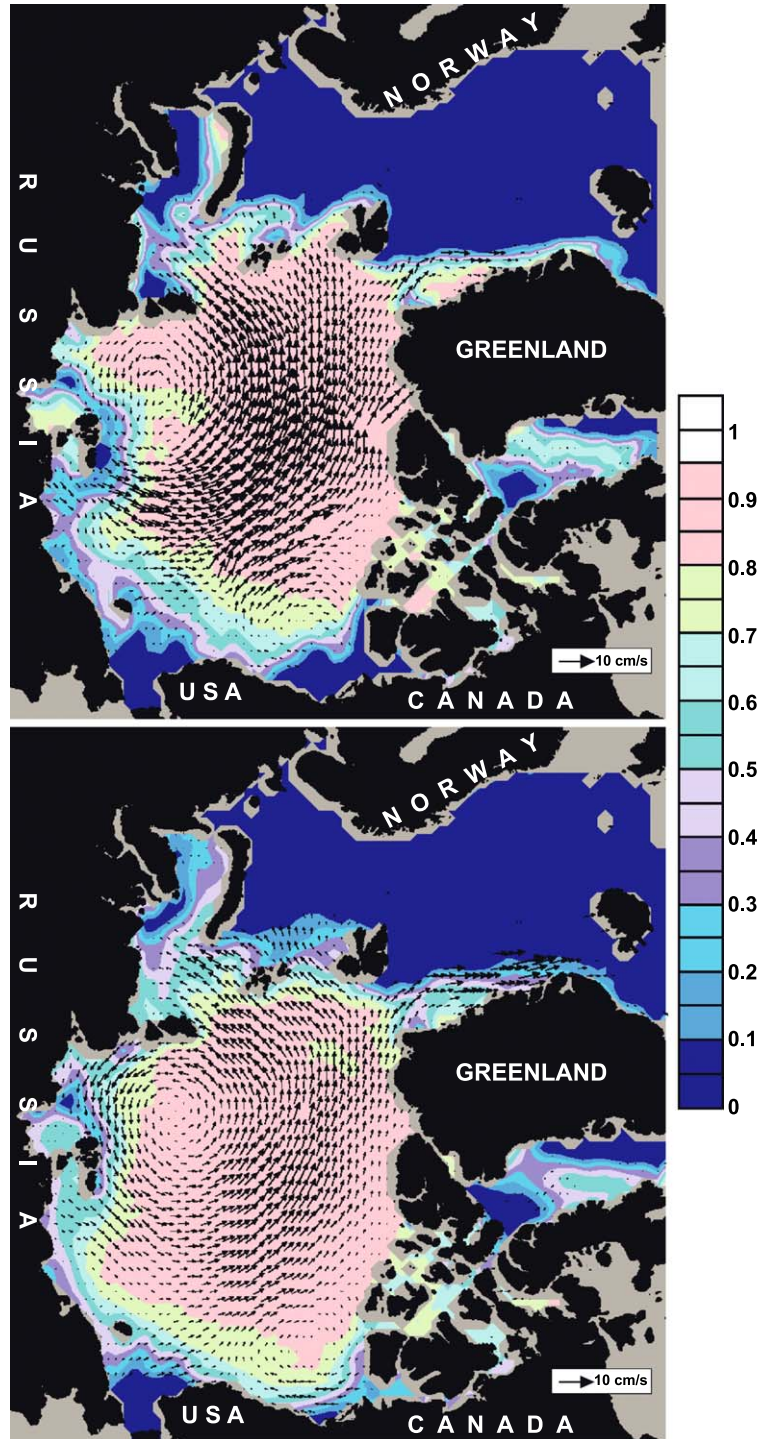


Fig. 2. Observed (top) and simulated (bottom) ice drift and ice concentration for July 1993.

Arctic Ocean. We applied this model to the simulation of the seasonal and interannual variability of the ice conditions in the Arctic Ocean. Implementation of this model allows us to simulate ice conditions not only for the period when satellite observations were available, but also for the decades when such observations were absent.

For the statistical analysis, we used the following observational data:

Monthly mean gridded sea level atmospheric pressure (SLP) fields for the northern hemisphere (20–90°N) over the hundred-year period from 1899 to 2000 (spatial resolution 5° latitude and longitude). For the period 1947–2000, we used the NCEP/NCAR SLP data set, <http://dss.ucar.edu/datasets/ds010.1/>. The time series from 1899 until 1947 is produced by Proshutinsky et al. (1999) in a reanalysis of the pressure field over the Arctic.

Mean monthly sea surface temperature (SST) comes from NCEP/NCAR data set for the period 1966–2000 (spatial resolution 5° latitude and longitude).

Monthly mean sea ice drift information was derived from the Special Sensor Microwave/Imager (SSM/I) data set and was available for the period from 1988 to 1994 from the EOS Distributed Active Archive Center (DAAC) at the National Snow and Ice Data Center, University of Colorado, Boulder, CO. The spatial resolution of the sea ice drift data set is 1° latitude.

Monthly averaged sea ice concentrations were derived from the DMSP SSM/I Daily and Monthly Gridded Sea Ice Concentration. These data are available from 1978 through 2000, gridded at a resolution of 25 × 25 km and were obtained from the EOSDIS NSIDC Distributed Active Archive Center (NSIDC

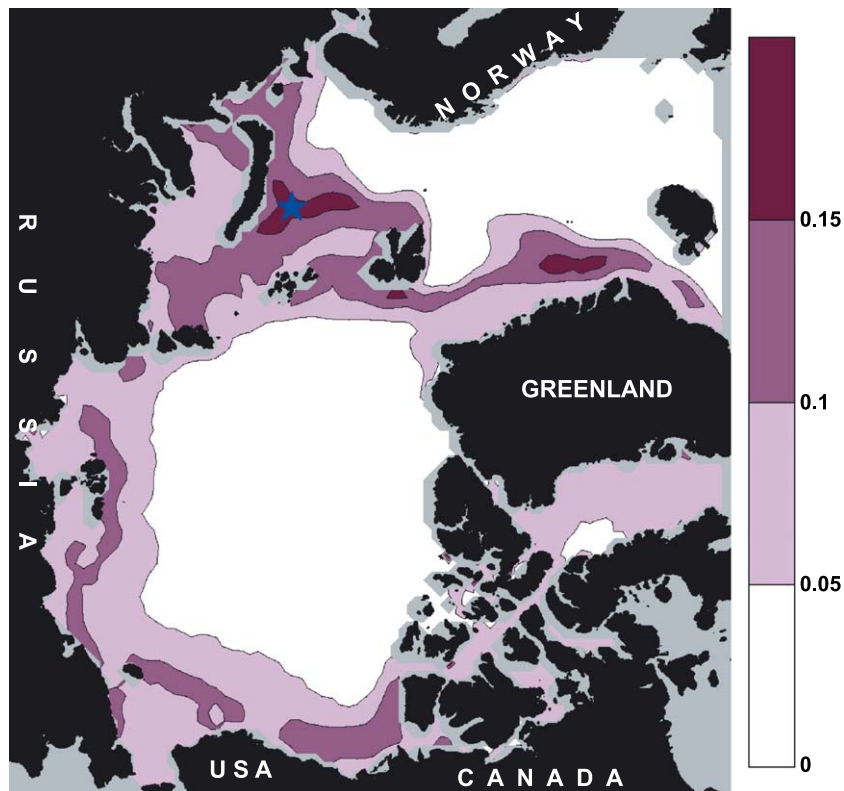


Fig. 3. The average error for ice concentration. ★Location of selected point for Fig. 4.

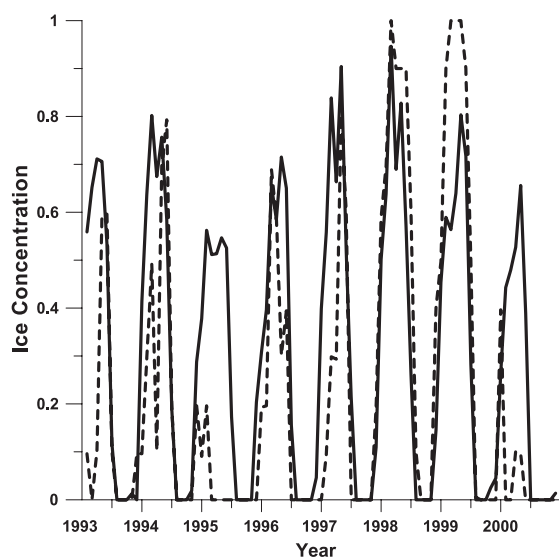


Fig. 4. Difference between observed (broken line) and simulated (solid line) ice concentration at the point where the average errors for the validation period (1993–2000) reach their maximum. The location of this point is given in Fig. 3.

DAAC), <http://nsidc.org/NSIDC/CATALOG/ENTRIES/nsi-0002.html/>.

For the calculation, we use the 88×96 rectangular grid overlays the North Pole with equal area projection. The spatial resolution is 0.5° latitude. All these observational data have been interpolated into the 88×96 rectangular grid using the *Kriging* method (Cressie, 1990, 1991). SST and SLP data have been interpolated onto each grid point in the domain, and ice concentration and components of ice velocity have been interpolated onto the grid points corresponding the ocean surface. The region of missing ice concentration and ice motion data is fully covered by interpolated data surrounding the data hole. Thus, for the statistical analysis we have obtained monthly average fields of atmospheric data (SST and SLP) and sea ice data (ice concentration and ice drift) on the same grid.

Spatial variations of air pressure (gradients) produce wind, which is the main driving force for ice drift. However, in contrast Thorndike and Colony (1982), Thomas and Rothrock (1993), Martin and Augstein (2000) and others, who have used a relationship between ice motion and geostrophic wind with a seasonally dependent drag factor and turning

angle, we have used the linear estimator $v_p(t)$ of the ice drift for each position p of observations and time t of the monthly mean ice drift:

$$v_p(t) = A_p x_p(t) + b_p \quad (1)$$

The vector $x_p(t)$ has, in this case, five components representing pressure at the grid point nearest to the point p , and the pressure at the four grid points surrounding this centre pressure grid point. These five components are thought to include information about the local wind and wind curl. The matrix A_p and the vector b_p minimize the average (or total) observed prediction error squared, i.e.:

$$\sum_{t \in O} |v'_p(t) - v_p(t)|^2 = \sum_{t \in O} |v'_p(t) - A_p x_p(t) - b_p|^2$$

where $v'_p(t)$ is observed drift velocity at position p and time t (which is within the set O of times of observations).

The matrix A_p statistically includes the effects of many parameters such as drag coefficients, ice thickness, the effect of coasts and others; the vector b_p statistically includes information about the mean ocean current at each grid point.

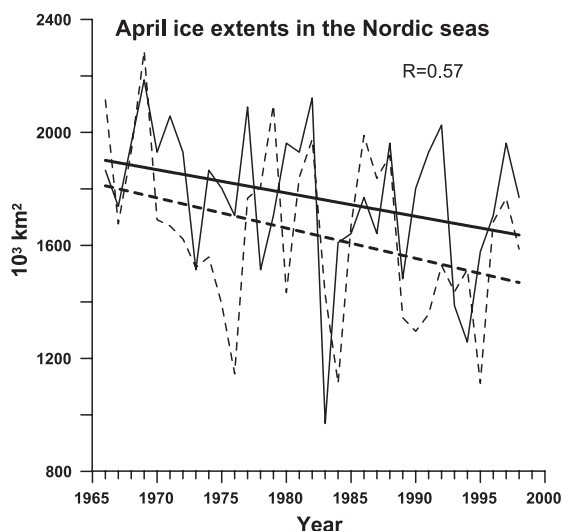


Fig. 5. Comparison between observed (broken line—Vinje, 2001a) and simulated (solid line—present results) April ice extents for the period 1966–1998.

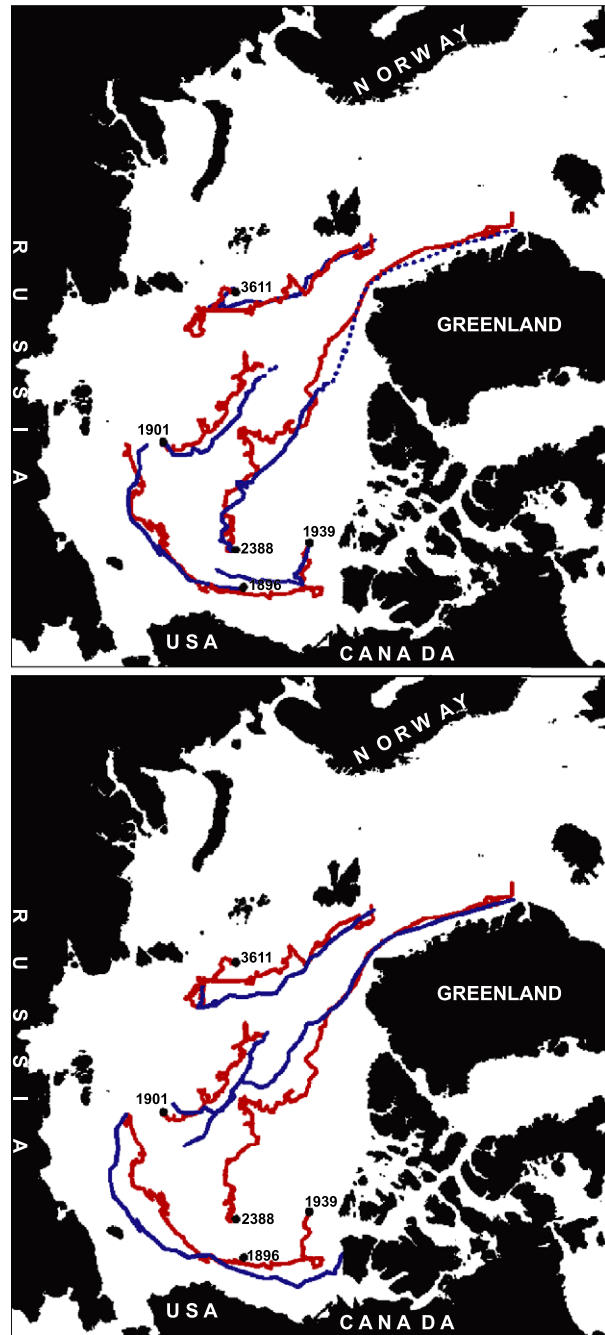


Fig. 6. Examples of simulated forwards trajectories (blue lines) and actual trajectories (red lines) of buoy drift (top), and examples of simulated backwards trajectories (blue lines) and actual trajectories (red lines) of buoy drift (bottom) in the different regions of Arctic Ocean. The buoy numbers correspond with the numbers from the data on the CD, IABP and Arctic Buoy Data, 1979–1999, version 1.0, MEDS-SDMM 2000 (<http://iabp.apl.washington.edu>).

Using Eq. (1) and the values of the matrix A_p and vector b_p obtained for each grid point, we have reconstructed the vectors of ice drift for each grid point for each month of the period when we have had SLP data, i.e. from 1899 to 2000.

In the development of ISMO, following the approach suggested in Chen and Chen (1999), we have used a multiple linear regression model to establish the statistical linkage between the ice concentration and both SST and the spatial structure of the SLP in the each point of simulating domain.

We consider ice concentration C to be a sum of two components:

$$C = C_{cl} + C_{an}$$

where C_{cl} is the climatic concentration for each month, and C_{an} is the anomaly of the ice concentration.

For anomalies of ice concentration, we use following linear function:

$$C_{an} = F(T_s, P, P_x, P_y, P_{xx}, P_{yy}, P_{xy})$$

where F is the linear function, T_s is the anomaly of SST and P is the anomaly of SLP. $P_x, P_y, P_{xx}, P_{yy}, P_{xy}$ are derivatives with respect to coordinates x and y .

The first two derivatives are responsible for the wind vectors. The last three derivatives are responsible for the wind field vorticity, divergence and convergence.

Therefore, we have a linear regression equation (Eq. (3)) for the anomalies of ice concentration for each point of our simulation domain. We have divided the SSM/I ice concentration data into two periods: the period 1978–1992 for model development and the period 1993–2000 for model validation. Using anomalies of ice concentration calculated from SSM/I data for the period from 1978 to 1992 and also anomalies of SST and SLP for the same period, we have obtained the coefficient of the linear regression equation (Eq. (3)) for each grid point. These coefficients allow us to simulate ice concentration anomalies in the each grid point depending on the anomalies of SLP and SST (Eq. (3)). According to Eq. (2), we have combined the values of ice concentration anomalies C_{an} and the climatic ice concentration C_{cl} calculated from SSM/I data.

Finally, we have calculated the ice concentration for the each grid point. Using the obtained coeffi-

Table 1

Comparison between observed (IABP data) and simulated (ISMO results) trajectories

Buoy	Date start	Initial buoy position		Date end	Buoy travel time (days)	Final buoy position ^c		Distance ^a (km)	Final calculated position ^d		Distance (km) ^b	
		Latitude	Longitude			Latitude	Longitude		Latitude	Longitude		
1896	01.01.87	73.24°N	209.92°	30.07.88	77.30°N	157.90°	72.89°N	200.75	299	78.33°N	162.01	149
1901	22.08.97	79.47°N	164.34°	22.02.99	88.25°N	133.90°	80.59°N	168.23	145	86.01°N	167.34	311
1939	25.04.80	76.55°N	227.95°	08.04.81	73.07°N	202.31°	74.82°N	232.22	224	74.31°N	202.72	139
2388	13.09.92	76.04°N	203.65°	20.09.95	70.38°N	342.76°	81.16°N	168.57	809	86.47°N	275.52	2331
3611	21.05.94	83.97°N	74.67°	08.02.96	79.02°N	4.55°	83.47°N	76.94	61	78.86°N	3.41	30

^a Distance (km) between the final calculated position of the simulated backward trajectory and initial buoy position.

^b Distance (km) between the final calculated position of the simulated forward trajectory and final buoy position.

^c Final calculated position of the simulated backward trajectory. The start position of the simulated backward trajectory is the final buoy position.

^d Final calculated position of the simulated forward trajectory. The start position of the simulated forward trajectory is the initial buoy position.

cients, Eqs. (2) and (3), we have reconstructed the sea ice concentration for each month of the period when we have had both SST and SLP data, i.e. from 1966 to 2000.

3. Verification

Figs. 1 and 2 show examples of the comparison between simulated and observed ice condition (ice drift and ice concentration) for winter and summer 1993. Observed and simulated ice conditions in general are quite close.

In January 1993, the maximum ice drift velocities based both on the observational data and the simulation results were seen in Fram Strait, in the north of the Barents Sea and in the Kara Sea (Fig. 1). Ice efflux prevailed from the Kara Sea, through the straits between Franz Josef Land and Novaya Zemlya, and between Franz Josef Land and Severnaya Zemlya. In the Laptev, East Siberian, Chukchi and Beaufort seas the sea ice drifted from west to east. In Baffin Bay, the sea ice drifted from north to south. In the central part of the Arctic Ocean and in the coastal zone of the Kara, Laptev and East Siberian seas, ice drift was practically absent. The ISMO has reproduced well all of these features. However, the calculated velocities of

the ice drift are lower than observed, by 10–15% on average. The calculated ice concentrations in the Barents and Greenland seas are higher than observed, by 10–15% on average.

The ice drift in July 1993 was cyclonic (Fig. 2). The centre of the cyclonic rotation was in the northern part of the Laptev Sea. The maximum ice drift velocities were observed in the central part of the Arctic Ocean. The ice drift through Fram Strait was very weak. The model has also reproduced very well all these features of the structure of the ice drift. However, in the winter period, the calculated velocities of ice drift are slightly less than observed. The position of the ice edge zone and ice concentration based on the observational data and modelling results are quite similar. However, in the Kara and the Barents seas, the calculated ice concentration is higher than observed, by about 10%.

The average error for ice concentration was calculated as the difference between observed and simulated values for the period of model verification (1993–2000). The averaged errors are almost everywhere less than 15% for ice concentration (Fig. 3). This is very similar to the accuracy of the observed data. The largest errors are distributed in the zone of the summer ice edge in the Nordic seas and the East Siberian, Chukchi and Beaufort seas (Fig. 3). Significant errors in the sea ice concentrations also occur in the central

Table 2
Observations of ice reaching Fram Strait

Station	Initial position	Time interval ^a	50% interval ^b (C&Th)	Observed time (months) (C&Th)	Calculated time (months) (ISMO)
NP-1	89°N, 0°E	May to December 1937	9–21	7	8
Arlis 2	74°N, 162°E	July 1961 to January 1965	51–81	42	71
1905	83°N, 36°E	February to May 1979	4–10	3	5
1915	85°N, 37°E	November 1979 to April 1980	5–10	5	7
1926	86°N, 9°E	November 1979 to February 1980	4–10	3	4
1900	83°N, 14°E	March to May 1981	1–2	2	2
1936	82°N, 3°E	February 1981	1–2	1	1
1899	84°N, 21°E	April to July 1981	4–10	4	4
3816	84°N, 45°E	May to December 1982	5–10	7	9
3819	88°N, 50°E	May to December 1982	7–14	7	10
3800	90°N	May 1981 to March 1982	10–22	10	14
3817	84°N, 19°E	May to August 1982	4–10	3	4
3814	88°N, 93°E	May 1981 to February 1982	12–25	9	13

C&Th—results of Colony and Thorndike (1985).

ISMO—the results of the Ice Statistical Model.

^a The time interval ends when station crosses 81°N (exits Fram Strait).

^b The modeled interval was chosen such that 25% of the futures were less than the lower bound and 25% of the futures were greater than the upper bound. These model results are for $\tau = 30$ days.

part of the Barents Sea, to the north and east of Svalbard and to the east of Greenland. This is probably connected with the fact that the heat flux from warm Atlantic waters, which are distributed in these areas, is not taken into account in the model. In the future, we are planning to include this effect in ISMO to improve its accuracy.

However, even in zones where the average errors reach their maximum (15–20%), the ISMO reproduces the annual and interannual variability quite well. Fig. 4 shows the variability of ice concentration in the northwest part of the Barents Sea at the point where the average error reaches its maximum for the model-verification period. The minimum ice concentration, based on both the observational and modelling results, was in 1995, and maximum ice concentration in winter 1998. The calculated periods of sea ice absence in the summer are nearly coincident with the observational. Average observed ice concentration for this period is 0.23 (standard deviation 0.32), mean simulated ice concentration is 0.32 (standard deviation 0.30). The average error of the model at this point is 17%. The correlation coefficient between observed and model ice concentration at this point is 0.65 (significance level $\sim 10^{-4}$).

We have also compared modelling results with the observational (not satellite) data of Vinje (2001a), which have not been used in the model development. Fig. 5 shows the variability of the ice extent in the

Nordic seas based on the observational (Vinje, 2001a) and our modelling data for the period 1966–1998. The correlation coefficient between observed and calculated April ice extent is quite high ($R=0.57$, significance level $\sim 10^{-3}$). Linear trends of the observed and simulated April ice extends are similar.

To examine the simulated vectors of ice drift, we have used the trajectories of five drifting buoys started at different times and at different positions in the Arctic Ocean (Fig. 6). We have not used IABP data to construct the ISMO and therefore it is possible to use them to test our results. We have tested the accuracy of the simulated vectors of ice drift by comparing with the actual trajectories of the buoys and calculated forward and backward tracks. For example, Fig. 6 shows the actual trajectories of the five buoys as red lines and the calculated forward and backward trajectories from the model results as blue lines. Numbers, positions, start time and travel time of the each buoy are shown in Table 1. We have calculated forward and backward tracks during actual travel time of the each buoy. The simulated and observed trajectories are quite close. For buoys 1896, 1901, 1939 and 3611, the differences between the actual end position and the simulated end position (forward trajectory) are 149, 311, 139 and 30 km correspondingly (Table 1). For buoy 2388, the difference between the actual and predicted position is very large (2331 km). It can be

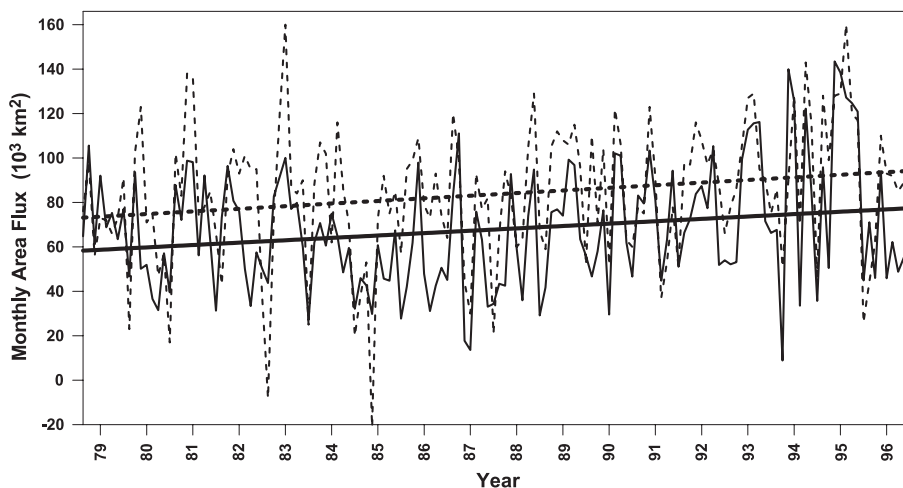


Fig. 7. Time series of monthly winter (October–May) ice area flux through Fram Strait, 1978–1996. Solid line—model results (present study), broken line—results of Kwok and Rothrock (1999).

Table 3
 Winter (October through May) ice area flux (10^3 km^2) through Fram Strait, 1978–1996

Year	October		November		December		January		February		March		April		May		Total		Average	
	ISMO	K&R	ISMO	K&R	ISMO	K&R	ISMO	K&R	ISMO	K&R	ISMO	K&R	ISMO	K&R	ISMO	K&R	ISMO	K&R	ISMO	K&R
1978–1979	64.8	76	105.6	98	61.1	56	92.1	73	68.8	72	75.3	66	63.5	73	77.0	91	608.1	605	76.0	76
1979–1980	46.7	23	93.5	103	50.2	123	52.0	71	36.6	75	31.6	47	57.1	57	39.6	17	407.2	516	50.9	64
1980–1981	87.8	102	72.0	83	98.8	138	98.2	136	56.2	74	92.2	78	63.0	85	31.3	66	599.5	762	74.9	95
1981–1982	73.1	43	96.5	92	80.8	104	76.1	93	50.0	101	33.4	95	57.5	95	50.1	37	517.4	661	64.7	83
1982–1983	43.8	–8	82.8	74	91.4	119	100.1	160	77.1	87	79.9	84	60.0	90	27.2	25	562.2	630	70.3	79
1983–1984	62.0	88	70.7	107	60.6	102	75.0	62	65.0	116	48.5	86	59.6	70	32.1	20	473.5	650	59.2	81
1984–1985	45.9	38	42.7	53	29.8	–21	60.7	73	45.7	92	44.8	75	67.4	85	27.7	57	364.8	452	45.6	57
1985–1986	42.1	95	61.9	99	97.9	109	47.9	79	31.1	73	42.6	93	50.6	74	45.1	64	419.2	686	52.4	86
1986–1987	83.1	120	111.0	100	17.7	44	13.6	30	75.9	93	63.2	77	33.1	82	34.3	21	432.0	566	54.0	71
1987–1988	43.4	66	42.5	94	92.8	83	59.3	60	36.0	63	73.8	105	94.8	129	29.1	67	471.8	666	59.0	83
1988–1989	41.7	59	75.6	105	76.9	112	74.1	108	99.3	106	96.8	115	63.5	96	55.8	52	583.7	755	73.0	94
1989–1990	46.7	110	58.0	71	76.5	104	29.6	52	102.1	122	101.0	106	62.0	63	46.6	60	522.6	689	65.3	86
1990–1991	83.1	78	79.5	75	103.4	123	81.1	91	44.8	37	63.2	53	94.3	78	51.1	51	600.5	587	75.1	73
1991–1992	66.4	98	72.6	97	83.8	116	87.4	108	77.4	97	105.3	104	51.9	88	54.0	66	598.8	774	74.9	97
1992–1993	52.1	78	53.2	86	99.5	106	112.8	127	115.6	129	116.2	95	71.6	90	66.3	75	687.3	787	85.9	98
1993–1994	67.7	86	8.9	51	139.9	90	125.6	128	33.6	70	122.2	143	84.8	115	35.7	47	618.3	731	77.3	91
1994–1995	95.9	128	50.5	99	143.4	128	138.5	129	127.2	160	124.7	120	120.9	117	44.9	26	846.0	906	105.8	113
1995–1996	71.1	44	46.0	62	93.9	110	45.9	93	62.2	92	48.8	85	55.3	89	34.9	55	458.1	632	57.3	79
Average	62.1	73	68.0	86	83.2	97	76.1	93	66.9	92	75.7	90	67.3	87	43.5	50	542.8	670	67.9	84
S.D.	17.6	35	25.6	18	32.1	38	32.6	34	28.9	28	30.7	24	20.1	19	13.8	21	116.4	108	14.5	13

ISMO—the results of the Ice Statistical Model.

K&R—the results of Kwok and Rothrock (1999).

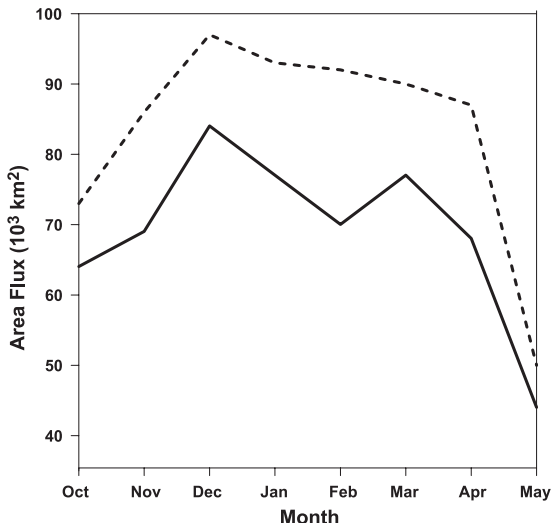


Fig. 8. Mean monthly ice area flux through Fram Strait, 1978–1996. Solid line—model results (present study), broken line—results of Kwok and Rothrock (1999).

related with large errors in simulated vectors of the ice drift near North Pole, where vectors derived from SSM/I data are absent and for statistical analysis we have used interpolated vectors. The other reason for

such a large difference is the anomalously high velocity of the East Greenland Current in that year. If we extend this forward trajectory 18 months longer than the actual buoy travel time, its trajectory will be very close to the actual trajectory of buoy 2388 (dotted blue line in Fig. 6, top). Simulated backward trajectories (Fig. 6, bottom) are also close to actual buoy trajectories for buoys 1896, 1901, 1939 and 3611 (Table 1). The differences between the starting position of these buoys and position at the end of the predicted backward trajectory are 299, 145, 224 and 61 km correspondingly. For buoy 2388, this difference is large again (809 km).

Colony and Thorndike (1985) give comparison between the travel time obtained from their model and actual travel time of several buoys and drifting stations. We have also calculated the travel time for the same buoys and drifting stations and compared our results with observed and model estimations of Colony and Thorndike (1985). The results of this comparison are given in Table 2. The ISMO gives travel times close to Colony and Thorndike (1985), but agrees slightly better with the observed times (see Table 2).

For simultaneous verification of the two components (ice drift and ice concentration) of the ISMO, we

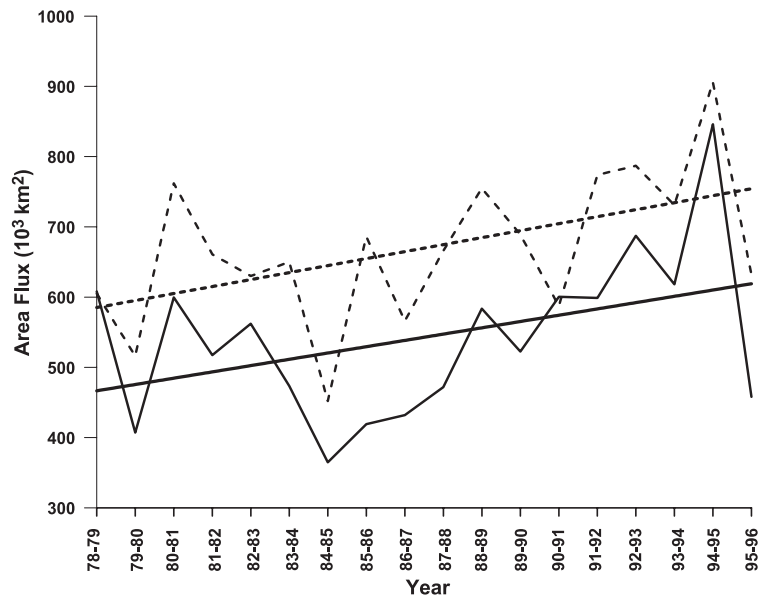


Fig. 9. Time series of average ice area flux through Fram Strait over the winter (October–May) for 1987–1996. Solid line—model results (present study), broken line—results of Kwok and Rothrock (1999).

have compared the variability of Fram Strait ice flux based on the results of the ISMO and the results of Kwok and Rothrock (1999), hereafter K&R. We discuss the monthly, seasonal and interannual variability of the ice flux estimates across Fram Strait. We have used the gate 81°N, the same as “gate a” in K&R. Fig. 7 shows the monthly winter (October–May) area flux from 1978 to 1996. The time series of the monthly area flux in K&R and ISMO are close (correlation coefficient between these two time series is 0.71, significance level $\sim 10^{-4}$). The difference between K&R and ISMO results is mostly positive (see Table 3), but in general, variability is about the same. Therefore, the minimum total ice area flux through this gate is in winter 1984–1985 (452,000 and 364,800 km², K&R and ISMO, respectively). The maximum was obtained in the winter 1994–1995 in both estimations (906,000 and 846,000 km², K&R and ISMO, respectively). Average value for the whole period of comparison (1978–1996) according to K&R is 670,000 km², and the ISMO gives 542,800 km². The difference between these two values (128,000 km²) is very close to the standard deviation of both the results (108,000 km² and 116,000 km², K&R and ISMO, respectively).

Fig. 8 shows the comparison between K&R and ISMO results of the mean month area fluxes in the wintertime (October–May) for the period 1978–1996. Both results give a maximum in December (97,000 km²—K&R and 83,000 km²—ISMO), and a minimum in May (50,000 km²—K&R and 43,000 km²—ISMO). In general, ISMO estimations are less than K&R results. The maximum difference is in February (23,000 km²) when ISMO gives local minimum of the ice area. The same minimum in January–February and local maximum in March of the seasonal sea ice transport through Fram Strait was calculated by Harder et al. (1998) using a numerical model.

The comparison between the results of K&R and ISMO for the total winter (October–May) area fluxes each year (1978–1996) is shown in the Fig. 9. The features of variability of these comparable results are fairly close. Both series have similar linear trends and similar positions of the minimum and maximum values. But the K&R estimation is 15–20% higher than ISMO result. The reason for this difference probably lies in the assumption of 100% ice concentration within the 15% ice edge, in the calculation of

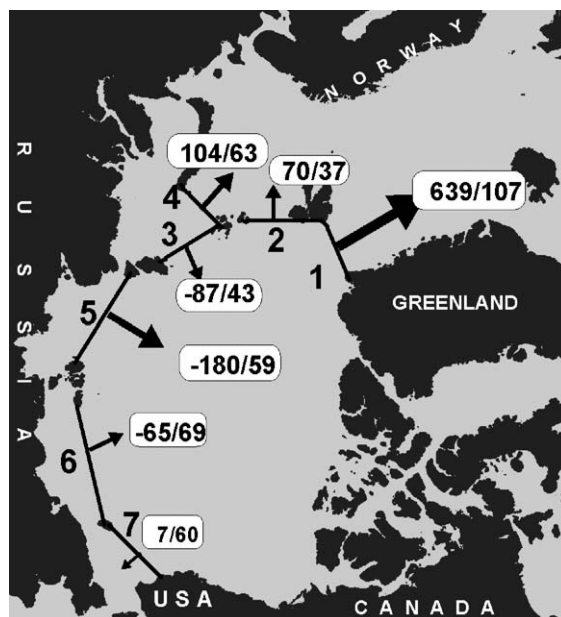


Fig. 10. Simulating domain and positions of transects. Mean annual sea ice area flux averaged for the period 1966–2000: Area flux/STD (10^3 km²).

the ice area flux by K&R. By contrast, we have used the full range (0.05–1.0) of the ice concentration which was simulated by ISMO.

The presented comparisons have shown quite good agreement of the ISMO results with the observational data, and with the results of other models.

4. Results and discussion

4.1. Arctic Ocean transboundary fluxes

The ISMO model was applied to the estimation of sea ice exchange between the marginal Arctic seas which have potential sources of pollution and the Polar Basin. The simulations were made for seven transects (Fig. 10). A positive value implies a flux from the Arctic Ocean. These estimates are based on the modelling results for ice concentration and ice drift during the period 1966–2000.

The sea ice flux through these seven transects has a strong seasonal variability (Fig. 11). In Fram Strait (Transect 1), the maximum import of the sea ice into the Greenland Sea (more than 2500 km²/day) takes place

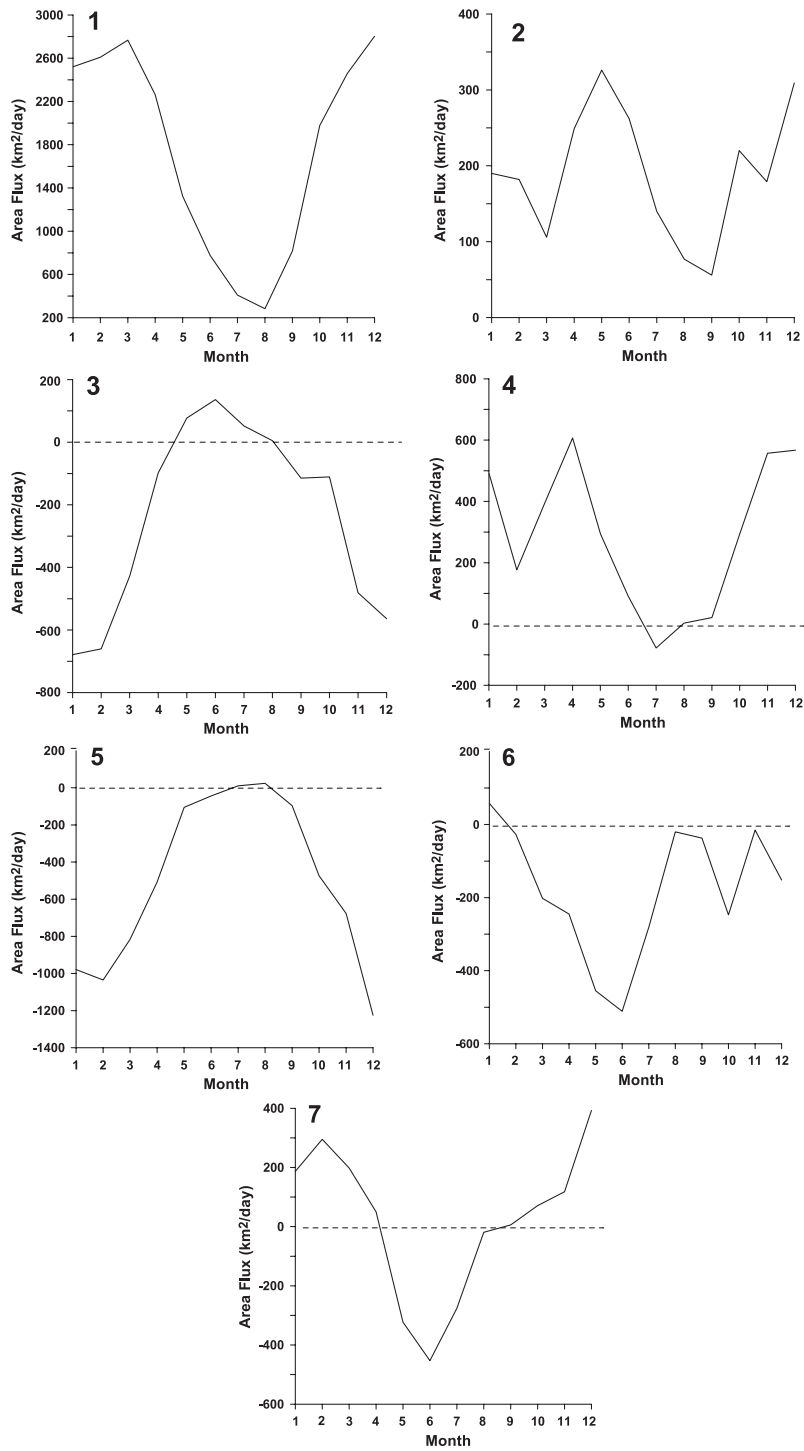


Fig. 11. Seasonal variability of the sea ice flux through the transects averaged for the period 1966–2000 (km^2/day). Geographical locations of the numbered transects are given in Fig. 10.

during the winter from December through April. After May, the ice flux decreases sharply and in July reaches its minimum (less than 500 km²/day). In the strait between Svalbard and Franz Josef Land (Transect 2), the ice flux on average over the year has the same direction (from the Polar Basin to the Barents Sea). The simulated minimum values (about 50 km²/day) are in September and the simulated maximum values (more than 300 km²/day) are in May. In the strait between Franz Josef Land and Novaya Zemlya (Transect 4) in the summer months, from June to September, the average ice flux is close to zero. In the other seasons of year, it is directed from the Kara Sea to the Barents Sea reaching maxima (about 600 km²/day) in April, November and December. In the straits between Franz Josef Land and Severnaya Zemlya (Transect 3), and Severnaya Zemlya and the Novosibirskie islands (Transect 5), the ice fluxes are directed into the Polar Basin over the whole year, except during three summer months, thus the maximum ice flux in November–January from the Kara Sea is 500–700 km²/day and from the Laptev Sea is 1000–1400 km²/day. In the summer, there is a small ice flux to the Kara Sea through the strait between Franz Josef Land and Severnaya Zemlya (from 0 to 100 km²/day). In the strait between Severnaya Zemlya and the Novosibirskie islands in summer, the average ice flux is close

to zero. The opposite situation is seen on the northern boundaries of the East Siberian and Chukchi seas. Through the transects between the Novosibirskie islands and Wrangel Island (Transect 6) and also between Wrangel Island and Cape Barrow (Transect 7), the maximum ice fluxes into the Polar Basin are seen in the period from May to June. In wintertime, the export of sea ice from the East Siberian Sea to the Polar Basin is much less, and on the northern boundary of the Chukchi Sea the ice flux changes direction and the export of sea ice from the Polar Basin to the Chukchi Sea during this period reaches 200–400 km²/day.

Mean annual climatic ice fluxes over the 35-year simulated record (1966–2000) are presented in Fig. 10. The average sea ice export from the Arctic Ocean through Fram Strait (Transect 1) is 639,000 km² year⁻¹ (average winter (October–May) flux is 569,000 km² year⁻¹, standard deviation is 103,000 km²), and through the strait between Svalbard and Franz Josef Land (Transect 2) is 70,000 km² year⁻¹ (average winter flux is 54,000 km² year⁻¹, standard deviation is 32,000 km²). The summer months (June–September) contribute about 11% and 23% of the ice area to the annual area exported Transect 1 and Transect 2, respectively. Estimation of the ice flux from the Kara Sea to the Barents Sea through the strait between Franz Josef Land and Novaya Zemlya (Transect 4) gives

Table 4
Comparison of annual flux estimates through the transects

Transect	Period	Previous results, area flux (10 ³ km ² /year)	Sources of the previous results	ISMO results, area flux (10 ³ km ² /year)
Transect 1	1966–2000	–	–	639
	1978–1996	919	Kwok and Rothrock (1999)	617
	1988–1994	584	Korsnes et al. (2002)	640
	1990–1996	1100	Vinje et al. (1998); Vinje (2001b)	681
	1993–1994	715	Martin (1996)	720
	1976–1985	830	Thomas and Rothrock (1993)	584
	1979–1984	840	Moritz (1988)	612
	1976–1984	1210	Vinje and Finnekasa (1986)	600
	1967–1977	750	Vinje (1982)	649
Transect 2	1966–2000	–	–	70
	1988–1994	75	Korsnes et al. (2002)	67
	1978–1996 (October–May)	47	Kwok (2000)	55
Transect 3	1966–2000	–	–	–87
	1978–1996 (October–May)	–65	Kwok (2000)	–82
Transect 4	1966–2000	–	–	104
	1978–1996 (October–May)	126	Kwok (2000)	112
	1988–1994	86	Korsnes et al. (2002)	88

104,000 km² year⁻¹ (average winter flux is 102,000 km² year⁻¹, standard deviation is 51,000 km²). The summer months contribute only about 1% to the ice flux from the Kara Sea because of significant year to year variations in the ice flux direction across this transect in summer. The average sea ice import from the Kara, Laptev and East Siberian seas to the Arctic Ocean over the same period through the straits between Franz Josef Land and Severnaya Zemlya (Transect 3), between Severnaya Zemlya and Novosibirskie islands (Transect 5) and between Novosibirskie islands and Wrangel Island (Transect 6) are -87,000 km² year⁻¹ (average winter flux is -89,000 km² year⁻¹, standard deviation is 45,000 km²), -180,000 km² year⁻¹ (average winter flux is -174,000 km² year⁻¹, standard deviation is 57,000 km²) and -65,000 km² year⁻¹ (average winter flux is -41,000 km² year⁻¹, standard deviation is 61,000 km²), respectively. For Transect 3, the summer months contribute only about 2% to the ice flux from the Kara Sea because of annual variations the ice flux direction, but ice flux averagely has positive direction (from the Arctic Ocean). The same variation in summer ice flux is observed across Transect 5 (less than 1%), but ice flux here has an average negative direction (to the Arctic Ocean). The contribution Transect 6 during summer months is 39% and ice flux has the same direction as the winter and annual fluxes (from the East Siberian Sea). The average sea ice export from the Arctic Ocean through the strait between Wrangel Island and Cape Barrow (Transect 7) is quite small (7000 km² year⁻¹), and has very strong variability in its direction from year to year. The average winter flux from the Arctic Ocean is 29,000 km² year⁻¹ (standard deviation is 60,000 km²), while the summer ice flux is 22,000 km² year⁻¹ (standard deviation is 8000 km²) and has the opposite direction. This figure shows that the ice flux from all the marginal seas, except the Chukchi and Barents seas, has a direction into the Polar Basin, so that the average export to the Polar Basin over a year is 332,000 km². The total import to the Greenland, Barents and Chukchi seas from the Polar Basin is 716,000 km². The sea ice import (104,000 km²) from the Kara Sea to the Barents Sea through the strait between Franz Josef Land and Novaya Zemlya should also be noted.

Table 4 compares the recent estimates of mean ice fluxes through the transects T1 to T4 with previous estimates. The estimates for Transect 1 concur most

closely with the results of Vinje (1982), Moritz (1988), Thomas and Rothrock (1993), Martin (1996) and Korsnes et al. (2002). The difference between these results ranges from 0.1% to 30%. The greatest difference (about 50%) is between our results and results of Vinje et al. (1998) and Vinje and Finnekasa (1986) for Transect 1 (Fram Strait). Possible reasons for the large ice flux obtained in these previous studies are discussed in Thomas and Rothrock (1993). In their opinion, it may be connected to differences in the sea ice velocities. Vinje and Finnekasa (1986) base their velocity estimates on buoy data, which is sparse for the eastern side of the strait, and do not include the West Spitsbergen Current. In our work, we have estimated the ice flux by integrating the ice motion and ice concentration over the 10 points along the whole flux gate from Svalbard to Greenland. The estimates for Transects 2, 3 and 4 match the results of Kwok (2000) most closely. For these transects, the difference between the ISMO results and previous estimates ranges from 2% to 21%.

Fig. 12 shows the interannual variability of annual mean (total, winter and summer) ice area fluxes over the 35-year simulated record (1966–2000) in the seven straits mentioned above. In Fram Strait (Transect 1), there is a significant variations from year to year from a minimum of 435,000 km² year⁻¹ in 1985 to a maximum of 940,000 km² year⁻¹ in 1995. The winter ice area flux ranges from a minimum of 364,800 km² in 1985 to a maximum of 846,000 km² in 1995. The summer area flux through this transect ranges from a minimum of 33,000 km² in 1990 to a maximum of 107,000 km² in 1999. In Transect 2, variations from year to year ranges from a minimum of -3000 km² year⁻¹ in 1999 (direction to the Arctic Ocean) to a maximum of 152,000 km² year⁻¹ in 1968. Only in 1999 the total area flux has direction to the Arctic Ocean (-3000 km² year⁻¹). The winter area flux ranges from a minimum of 2000 km² in 1985 to a maximum of 119,000 km² in 1968. The summer area flux ranges from a minimum of 253 km² in 1994 to a maximum of 32,000 km² in 1968. In Transect 3, total ice area flux has a direction into the Arctic Ocean during the whole period and has a minimum of 7000 km² year⁻¹ in 1969 and a maximum of 203,000 km² year⁻¹ in 1983. Only in 1993 the total area flux has direction from the Arctic Ocean (17,000 km² year⁻¹). The winter area flux ranges from a minimum of 2000

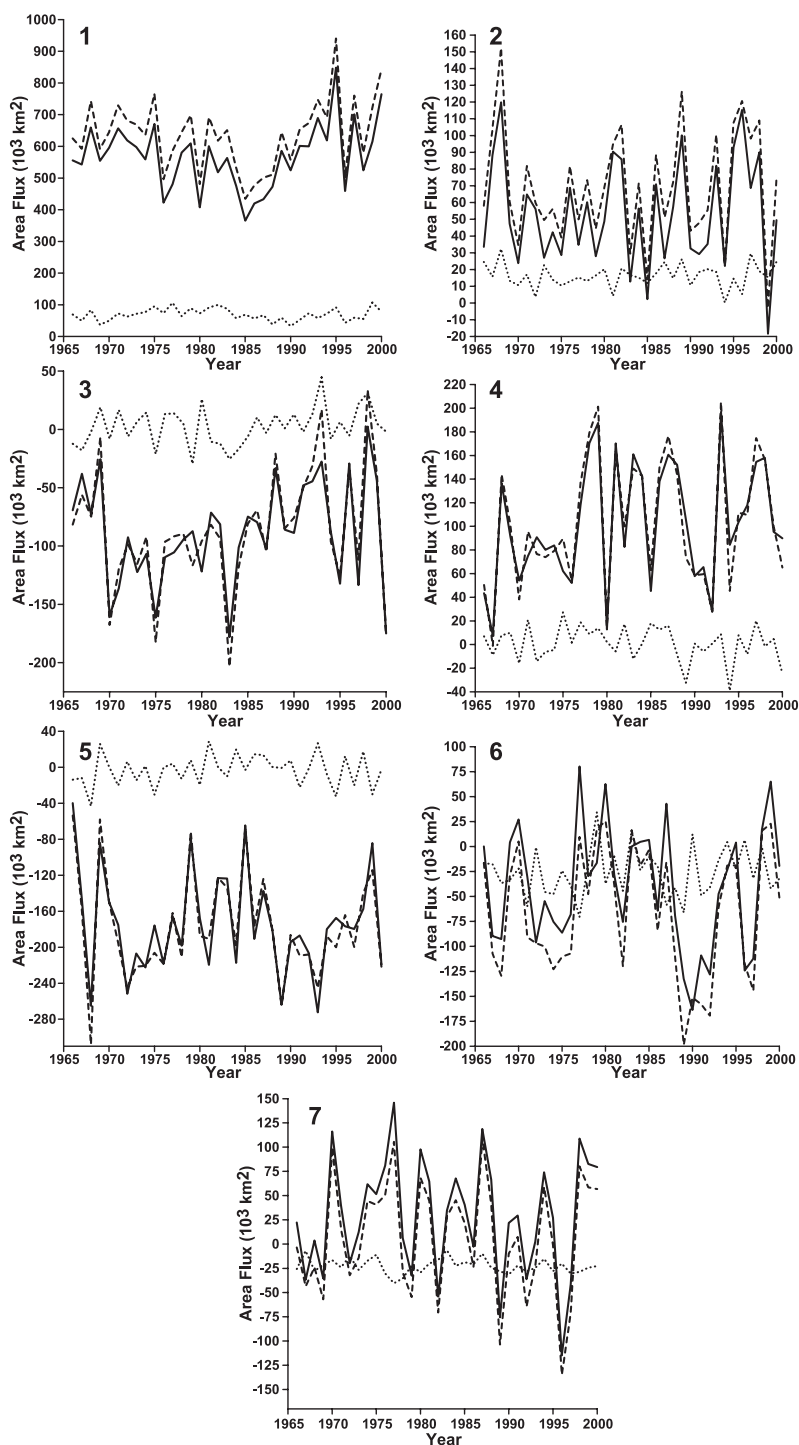


Fig. 12. Interannual variability of annual mean ice flux in the transects for the period 1966–2000 (10^3 km^2). Geographical locations of the numbered transects are given in Fig. 10. Solid line—winter area flux (October–May); dotted line—summer area flux (June–September); broken line—total area flux.

km² in 1998 (direction from the Arctic Ocean) to a maximum of 178,000 km² in 1983 (direction to the Arctic Ocean). However in summer, the area flux changes its direction from year to year, ranging from a minimum of 900 km² in 1989 to a maximum of 45,000 km² in 1993 (both directions are from the Arctic Ocean). In Transect 4, ice fluxes from the Kara Sea to the Barents Sea practically during the whole period (except 1967). In 1967, there is a minimum (1000 km² year⁻¹) and in 1993 there is a maximum (205,000 km² year⁻¹). The winter area flux ranges from a minimum of 8000 km² in 1967 to a maximum of 197,000 km² in 1993. In summer, area flux changes its direction from year to year and ranges from a minimum of 700 km² in 1992 to a maximum of 39,000 km² in 1994 (direction is to the Arctic Ocean). In Transect 5, the total ice area flux has a direction to the Arctic Ocean during the whole period and has a minimum of 54,000 km² year⁻¹ in 1966 and a maximum of 308,000 km² year⁻¹ in 1968. The winter ice area flux has a direction to the Arctic Ocean within the whole period and ranges from a minimum of 40,000 km² in 1966 to a maximum of 265,000 km² in 1968. In summer, area flux changes its direction from year to year, ranging from a minimum of 200 km² in 1976 to a maximum of 43,000 km² in 1968 (both directions are to the Arctic Ocean). The ice area flux through Transect 6 has a high degree of interannual variability, changing its direction from year to year. The total area flux has a minimum in 1983 (3000 km² year⁻¹) and a maximum in 1989 (199,000 km² year⁻¹), with its direction to the Arctic Ocean. The winter area flux averagely for the period 1966–2000 has a direction to the Arctic Ocean, and ranges from a minimum of 170 km² in 1983 (from the Arctic Ocean) to a maximum of 164,000 km² in 1990 (to the Arctic Ocean). Summer area flux changes its direction from year to year, and ranges from a minimum of 700 km² in 1972 to a maximum of 70,000 km² in 1977 (both directions are to the Arctic Ocean). The ice area flux in the Transect 7 has also complicate interannual variability. The total area flux has a minimum in 1995 (900 km² year⁻¹), and a maximum in 1996 (134,000 km² year⁻¹), both directions are to the Arctic Ocean. The winter area flux averagely for the period 1966–2000 has a direction from the Arctic Ocean and ranges from a minimum of 3000 km² in 1993 to a maximum of 118,000 km² in 1987. Summer area flux during this period has mostly direction to the Arctic

Ocean and ranges from a minimum of 6000 km² in 1983 to a maximum of 40,000 km² in 1977.

The analysis of interannual variability has shown that in Fram Strait and the straits between Svalbard and Franz Josef Land and between Severnaya Zemlya and the Novosibirskie islands, the ice fluxes for all intents and purposes do not change direction during the period of the simulation (1966–2000). In the other straits, in isolated years the ice flux changes direction. Especially strong variability is estimated on the northern boundary of the Chukchi Sea. Here, the ice flux changes direction from north to south every 5 to 7 years. On the northern boundary of the East Siberian Sea, the change of flux direction is estimated to take place in 1970, 1976, 1977, 1979, 1985 and 1998. An especially large import of ice from the Polar Basin to the East Siberian Sea (about 90,000 km²) was simulated for 1979.

4.2. Sea ice transport from potential sources of contaminant

To estimate the drift route of the sea ice from the areas containing potential sources of pollution in the Arctic Ocean, trajectories of the ice drift from several locations were simulated. By way of examples, the following regions were chosen: in the Kara Sea—the regions of the Ob and Yenisey rivers mouths and along the eastern coastal zone of Novaya Zemlya, where there were earlier sources of contamination connected with the nuclear trials at the Novaya Zemlya test site; in the Laptev Sea—the region of the Lena river mouth; in the East Siberian Sea—the region of the Kolyma river mouth; in the Chukchi Sea—the region near the Bering Strait; and in the Beaufort Sea—the mouth of the Mackenzie river.

For these simulations, the reconstructed ice drift data for the period 1899–2000 were used. The trajectories were started each month of a year on the condition that the ice concentration at the starting position was more than 10%, i.e. most of the trajectories were launched in the arctic wintertime. There is assumed to be no melting in the present approach so the following statistics are conditional on ice particles surviving over the actual time periods. This assumption may be fairly realistic since the drift positions (release in arctic wintertime) are far from open water.

Fig. 13a,b shows trajectories of sea ice drift from areas of shallow burial of radioactive waste

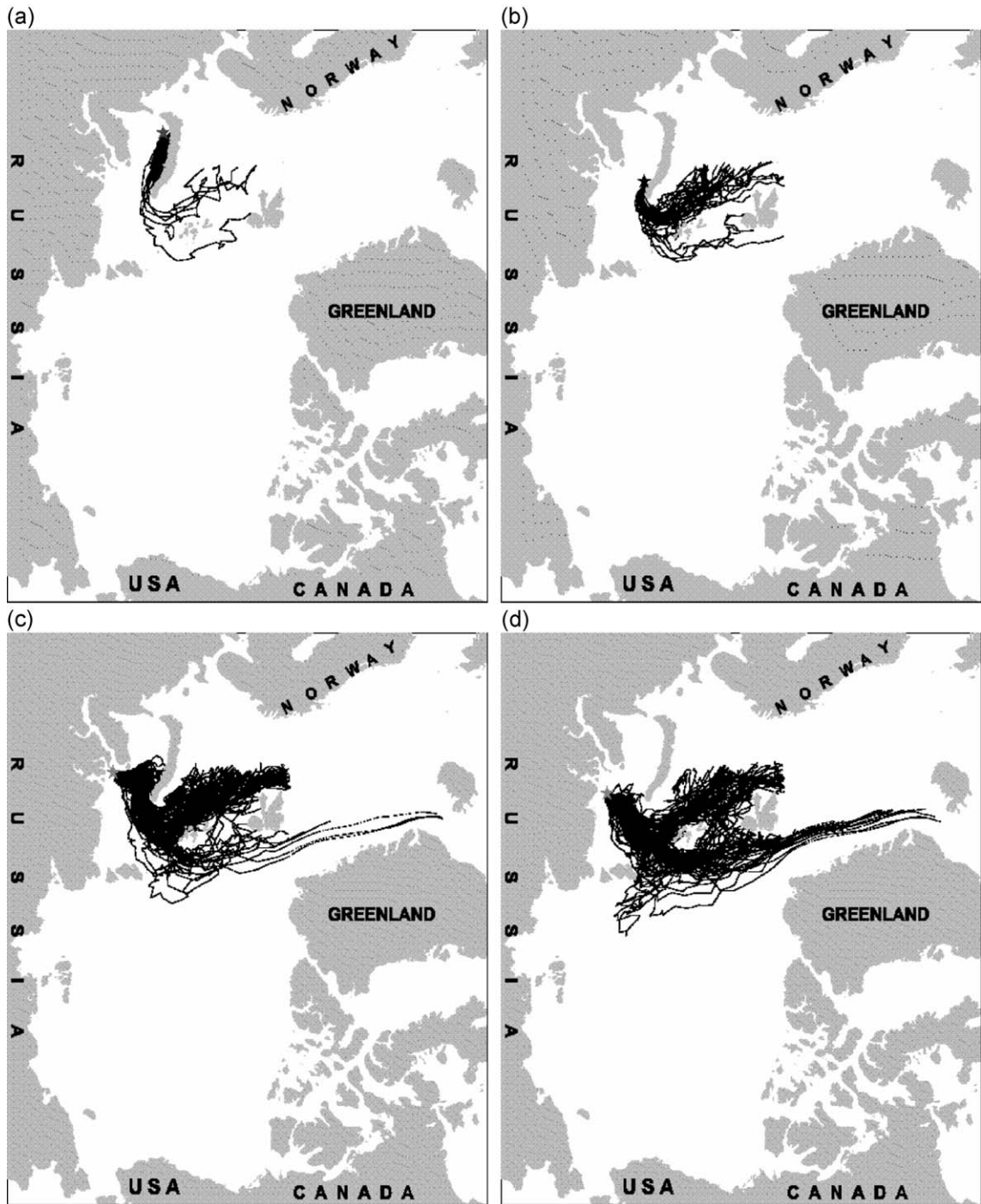


Fig. 13. (a, b) Trajectories of sea ice drift from the eastern coast of Novaya Zemlya. (c) Trajectories of sea ice drift from the Ob mouth region. (d) Trajectories of sea ice drift from the Yenisey mouth region. (e) Trajectories of sea ice drift from the Lena mouth region. (f) Trajectories of sea ice drift from the Kolyma mouth region. (g) Trajectories of sea ice drift from the region near the Bering Strait. (h) Trajectories of sea ice drift from the Mackenzie mouth region.

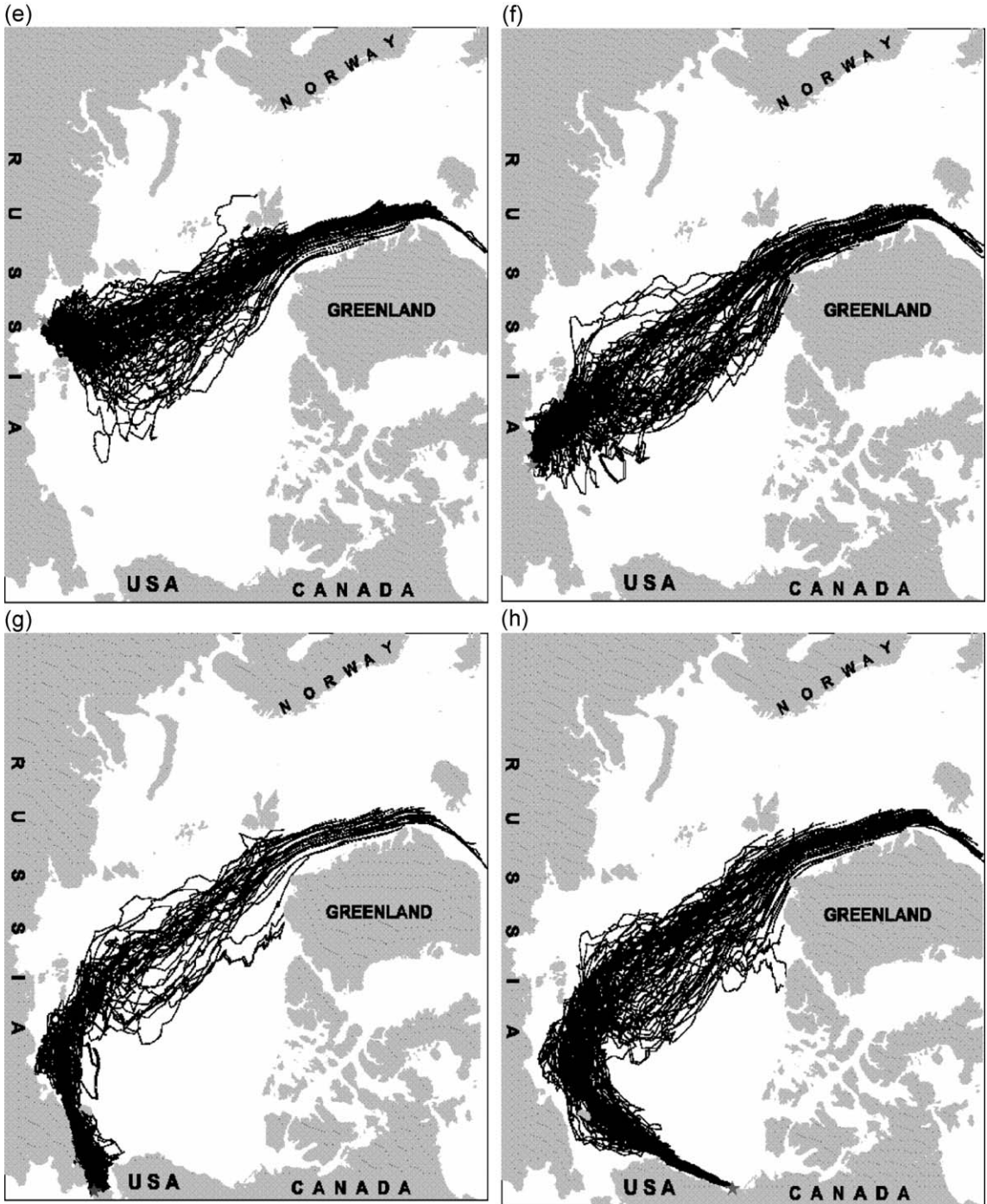


Fig. 13 (continued).

(Rumyantsev, 1993; Yablokov et al., 1993) at the eastern coast of Novaya Zemlya. The ice drift trajectories are mainly limited to the western part of the Kara Sea. And only in the isolated years can the ice from these areas reach the northern part of the Barents Sea, mainly through the strait between Franz Josef Land and Novaya Zemlya. For example, according to the estimations by Korsnes et al. (2002) an ice particle formed in this area has a probability of 26% of reaching the Barents Sea within 2 years.

Ice from the Ob mouth region (Fig. 13c) has three basic drift routes. The most probable trajectory of the ice drift from this area is to the north, around of northern coast of Novaya Zemlya, further to the west, through the strait between Franz Josef Land and

Novaya Zemlya and to the northern part of the Barents Sea Opening. Under certain atmospheric conditions connected with the extreme development of an anticyclonic circulation above the Arctic Ocean, the trajectories of ice drift from this area can pass through the strait between Franz Josef Land and Severnaya Zemlya and further to Fram Strait, finishing near the coast of Greenland. Under an extreme cyclonic regime the ice drift trajectories lie within the central part of the Kara Sea, near the eastern coast of Novaya Zemlya.

The ice drift from the area of the Yenisey gulf has two main, approximately equal, routes (Fig. 13d). During amplification of the anticyclonic regime of atmospheric circulation, the ice drifts from this area

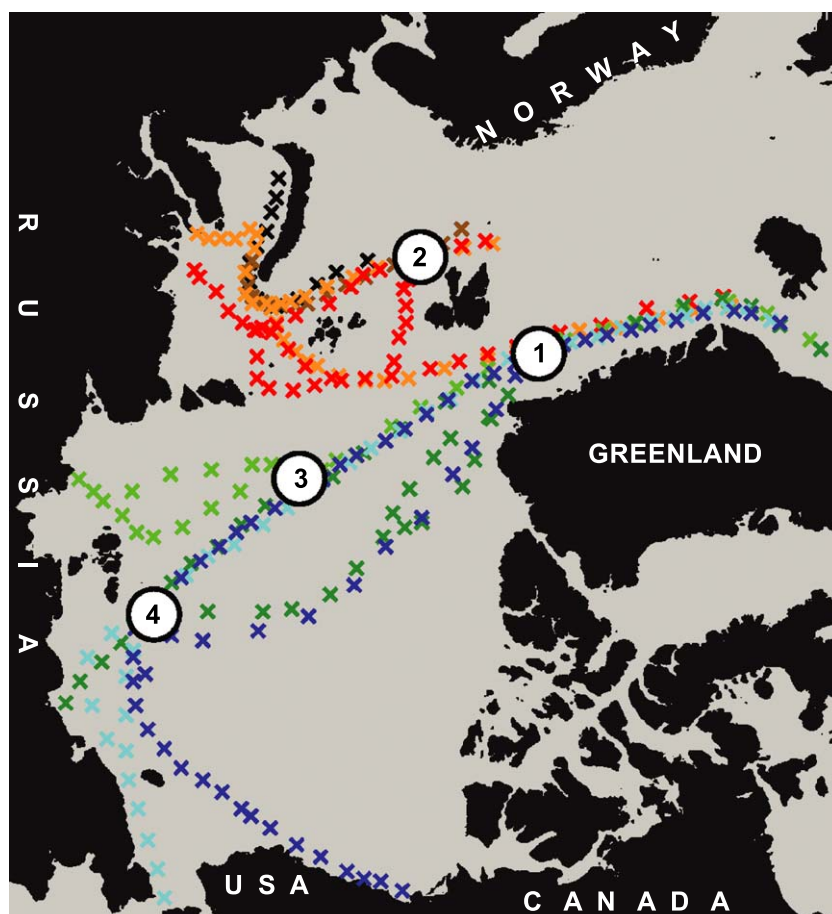


Fig. 14. The most probable routes of ice drift from the potential sources of pollution given in Fig. 13a–h. The most representative places for monitoring contaminants are marked: (1) Fram Strait; (2) the northern part of the Barents Sea Opening; (3) the northern part of the Laptev Sea; (4) the area to the northeast of the Novosibirskie islands.

to the north through the strait between Franz Josef Land and Severnaya Zemlya island and further to Fram Strait and coast of Greenland. Under a more cyclonic regime, the sea ice drifts through the northern part of the strait between Franz Josef Land and Novaya Zemlya and further to the northern part of the Barents Sea Opening. In a few years, the sea ice generated in this area can reach the northwest part of the Laptev Sea. The ice drift trajectories from the area of the Lena river delta mainly pass the Laptev Sea and continue to the northeast and Fram Strait (Fig. 13e). During amplification of the cyclonic regime, ice drifting from this area, can reach the northern part of the East Siberian Sea.

The most probable drift of ice from the region of the Kolyma river mouth is to north, to Fram Strait and further along the coast of Greenland (Fig. 13f). The ice from southern part of the Chukchi Sea drifts along coast of Siberia, through the De Long Strait, further to the north and Fram Strait and along the coast of Greenland (Fig. 13g). The ice from the area of the Mackenzie river mouth drifts mainly to the west along the northern coast of Alaska and further to the north of Wrangel Island up to the central part of the East Siberian Sea (Fig. 13h). Here, the ice drift changes direction to the north and continues through the central Polar Basin to Fram Strait and further along the eastern coast of Greenland.

Fig. 14 shows the most probable routes of ice drift from all the above-mentioned potential sources of pollution. We can see that in the Arctic Ocean and Nordic seas there are four areas where the trajectories of ice drift from several potential sources of pollution converge. It is reasonable to assume that these areas (the northern part of the Barents Sea Opening, Fram Strait, the northern part of the Laptev Sea and the area to the northeast of the Novosi-

Table 5
Travel times of sea ice drift from the potential sources of pollution to Fram Strait

Location of potential sources of pollution	Mean (years)	Min (years)
Novaya Zemlya eastern coastal zone	4.3	2
Ob river mouth	4.5	2
Yenisey river mouth	2.1	2
Lena river mouth	4.6	3
Kolyma river mouth	8.8	6
Bering Strait region	10.7	6
Mackenzie river mouth	6.7	4

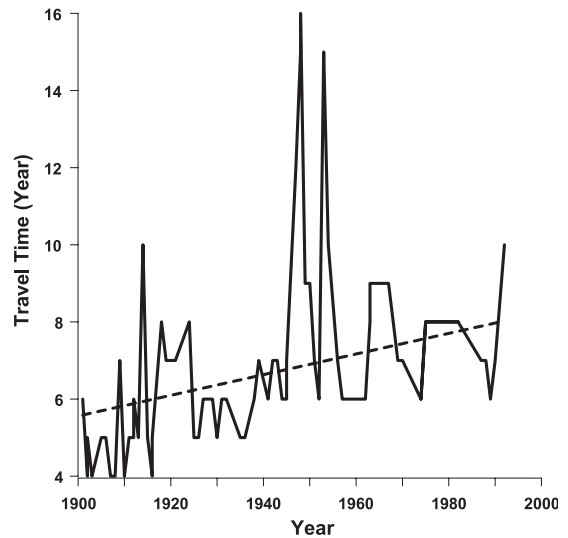


Fig. 15. Changes from year to year of the ice drift travel time from the area of the Mackenzie river mouth to Fram Strait (Transect 1) in the last century (1899–2000).

birskie islands) can be the most representative places for monitoring contaminants.

The most important are Fram Strait and the northern part of the Barents Sea Opening, because: (a) in these areas the trajectories of ice drift from the most of the potential sources of pollution converge; (b) these areas are accessible for carrying out observations from vessels during the whole year.

Table 5 shows the travel time (mean and minimum) during which the sea ice from selected potential sources can reach the region of Fram Strait. For example, sea ice from the Kara Sea region reaches Fram Strait from 2 to 4 years (min 2 years) on average, and while sea ice from the Laptev Sea takes roughly 4–6 years (min 3 years) to reach Fram Strait. The longest travel times are from the Kolyma river mouth and the Bering Strait region. These estimations have very good agreement with the results of Pfirman et al. (1997b), which were obtained based on statistics of the Arctic ice buoy motions for the period 1979–1994.

In the light of climate change in the Arctic, it is interesting to consider the interannual variability of the travel time of ice drift through the Arctic Ocean. Fig. 15 shows the changes from year to year of the ice drift travel time from the area of the Mackenzie river mouth to Fram Strait (Transect 1) in the last century (1899–2000). We

have obtained a general positive trend of the travel time. The minimum travel time (4 years) was in the first two decades of the last century. In the last four decades, the travel time was not less than 6 years. Maximum values of the travel time (15–16 years) were obtained at the end of 1940s and mid-1950s. This structure of interannual ice drift variability might be connected with the increasing cyclonic circulation in the Arctic.

5. Conclusion

Comparison of the ISMO results with the observational data and simulating results obtained from the other models have shown that ISMO gives quite realistic estimations of the sea ice conditions in the Arctic Ocean and Nordic seas, and can also be used for reconstruction of the vectors of ice drift and ice concentration.

Based on the reconstructions of the sea ice drift and sea ice concentration for the period 1966–2000, seasonal and interannual variability of the ice fluxes through the main straits of the Arctic Ocean were simulated and analysed. The sea ice flux through the all straits has a strong seasonal variability. The maximum amplitude of the annual cycle is in Fram Strait (about 2500 km²/day), and the minimum is in the strait between Svalbard and Franz Josef Land (270 km²/day). In almost all the straits, the ice fluxes are sharply decreased in the summer time but keep their direction during the whole year. Ice flux from the Chukchi Sea has opposite directions in winter and summer.

The difference between the annual mean ice fluxes through Fram Strait estimated by ISMO and most previous estimations is 0.1–30%. The difference between estimations for Transects 2, 3 and 4 ranges from 2% to 21%. Analysis of interannual variability has shown that only in the East Siberian and Chukchi seas is there a change in the direction of ice flux during the simulation period. Such changes in the Chukchi occurred every 5–7 years. In the other straits, winter ice flux does not change its direction.

The calculated trajectories of ice drift from areas of potential sources of pollution allow us to evaluate the character of pollutant transport and the areas of their release and redistribution. The simulation of backward trajectories allows us to reveal the probable area of the origin of a contaminant. From the results of the ISMO

simulation, we can conclude that sea ice from most potential sources of contaminant can reach the open Polar Basin and Fram Strait. Contaminated sea ice from potential sources in the Kara and Laptev seas can reach Fram Strait within 2–4 years, and from the East Siberian, Chukchi and Beaufort seas within 6–11 years. Analysis of the interannual variability of the sea ice travel time, for example from the Mackenzie river to Fram Strait has shown a significant positive trend in the last century.

The results of the simulation can also give useful information for the selection of the most representative areas for monitoring contaminants in the Arctic Ocean. Based on simulated trajectories from different potential sources in the Arctic Ocean, we can conclude that most important region for monitoring of contaminants are Fram Strait and Barents Sea Opening.

Acknowledgements

The authors wish to thank Jane O'Dwyer for her careful editing of the manuscript, and constructive and helpful comments. Support for this work, and attendance at the 34th International Liege Colloquium on Ocean Hydrodynamics, was provided by the Transport and Effects Programme, Phase 2 (financed by the Norwegian Ministries of Environment and of Foreign Affairs), and by the European Commission Project CONVECTION, contract no. EVK2-CT-2000-00058. Partly the work was supported by Barents Sea Production Licenses 182, 225 and 228 (Norsk Hydro, Statoil, Agip, Chevron, Enterprise, Petero - contract No. 9000000465).

References

- Chen, D., Chen, Y., 1999. Development and verification of a multiple regression downscaling model for monthly temperature in Sweden. In: Chen, D., Hellstrom, C., Chen, Y. (Eds.), Preliminary analysis and statistical downscaling of monthly temperature in Sweden SWECLIM (Swedish Regional Climate Modelling Programme) Department of Physical Geography, Gothenburg University, Gothenburg, pp. 60–76. C16 Rapport.
- Chernyak, S., Rice, C., McConnell, L., 1996. Evidence of currently-used pesticides in air, ice, fog, seawater and surface microlayer in the Barents and Chukchi Seas. *Mar. Pollut. Bull.* 5 (32), 410–419.
- Colony, R., 1986. The random transport of oil by sea ice. *Water Sci. Technol.* 18, 25–39.

- Colony, R., Thorndike, A.S., 1984. An estimate of the mean field of Arctic Sea ice motion. *J. Geophys. Res.* 89 (C6), 10623–10629.
- Colony, R., Thorndike, A.S., 1985. Sea ice motion as a drunkard's walk. *J. Geophys. Res.* 90 (C1), 965–974.
- Cressie, N.A.C., 1990. The Origins of Kriging. *Mathematical Geology* 22, 239–252.
- Cressie, N.A.C., 1991. *Statistics for Spatial Data*. Wiley, New York.
- Emery, W.J., Fowler, C.W., Hawkins, J., Preller, R.H., 1991. Fram Strait satellite image derived ice motions. *J. Geophys. Res.* 96 (C3), 4751–4768.
- Emery, W.J., Fowler, C.W., Maslanik, J.A., 1997a. Satellite-derived maps of Arctic and Antarctic sea ice motion: 1988 to 1994. *Geophys. Res. Lett.* 24 (8), 897–900.
- Emery, W.J., Fowler, C.W., Maslanik, J.A., Pfirman, S., 1997b. New satellite derived sea ice motion tracks Arctic contamination. *Mar. Pollut. Bull.* 35 (7–12), 345–352.
- Izmailov, V., 1988. Transformation of oil slicks in the ocean–ice–atmosphere system. *Problems of Chemical Pollution of Water in the World Ocean*. Gidrometeoizdat, St. Petersburg, pp. 1–145. In Russian.
- Harder, M., Lemke, P., Hilmer, M., 1998. Simulation of sea ice transport through Fram Strait: natural variability and sensitivity to forcing. *J. Geophys. Res.* 103 (C3), 5595–5606.
- Komov, N., Spichkin, V., 1981. Formation of polluted ice in the Arctic Seas. *Trudi AARI* 384, 130–134 (in Russian).
- Korsnes, R., Pavlova, O., Godtliebsen, F., 2002. Assessment of potential transport of pollutants into the Barents Sea via sea ice—an observational approach. *Mar. Pollut. Bull.* 44 (9), 861–869.
- Kwok, R., 2000. Recent changes in Arctic Ocean sea ice motion associated with the North Atlantic Oscillation. *J. Geophys. Res.* 104 (C3), 5177–5189.
- Kwok, R., Rothrock, D.A., 1999. Variability of Fram Strait ice flux and North Atlantic Oscillation. *Geophys. Res. Lett.* 27 (C6), 775–778.
- Kwok, R., Schweiger, A., Rothrock, D.A., Pang, S., Kottmeier, C., 1998. Sea ice motion from satellite passive microwave imagery assessed with ERS SAR and buoy motions. *J. Geophys. Res.* 103 (C4), 8191–8214.
- Martin, T., 1996. Sea ice drift in the East Greenland Current. *Proc. of Fourth Symposium on Remote Sensing of the Polar Environments*. Eur. Space Agency Spec. Publ. 391, 101–391.
- Martin, T., Augstein, E., 2000. Large-scale drift of Arctic sea ice retrieved from passive microwave satellite data. *J. Geophys. Res.* 105 (C4), 8775–8788.
- Martin, T., Wadhams, P., 1999. Sea-ice flux in the East Greenland current. *Deep-Sea Res., Part 2, Top. Stud. Oceanogr.* 46, 1063–1082.
- Melnikov, S., 1991. Report on heavy metal. *Tech. Rep. 2*, Arct. Cent., Univ. of Lapland, Rovaniemi, Finland.
- Moritz, R.E., 1988. The ice budget of the Greenland Sea. *Tech. Rep. APL-UW TR 8812*, Seattle, 117.
- Ninnis, R.M., Emery, W.J., Collins, M.J., 1986. Automated extraction of pack ice motion from Advanced Very High Resolution Radiometer imagery. *J. Geophys. Res.* 91 (C6), 10725–10734.
- Pavlov, V., Stanovoy, V., 2001. The problem of transfer of radionuclide pollution by sea ice. *Mar. Pollut. Bull.* 4, 319–323.
- Pfirman, S., Kogler, J., Anselme, I., 1995. Coastal environments of the western Kara Sea and eastern Barents Sea. *Deep-Sea Res., Part 2, Top. Stud. Oceanogr.* 42 (6), 1391–1412.
- Pfirman, S., Kogler, J., Rigor, I., 1997a. Potential for rapid transport of contaminants from the Kara Sea. *Sci. Total Environ.* 202, 111–122.
- Pfirman, S., Colony, R., Numberg, D., Eicken, H., Rigor, I., 1997b. Reconstructing the origin and trajectory of drifting Arctic sea ice. *J. Geophys. Res.* 102 (C6), 12575–12586.
- Proshutinsky, A., Johnson, M., Proshutinsky, T., 1999. Arctic atmosphere and ocean oscillations. In: *Arctic Oscillations*. No46 in Supplement to *EOS* Transactions, AGU, vol. 80 (November), p. F212, section A42C-01.
- Rigor, I., Colony, R., 1997. Sea-ice production and transport of pollutants in the Laptev Sea, 1979–1993. *Sci. Total Environ.* 202, 89–110.
- Rumyantsev, V.M., 1993. Preliminary results on investigation of matters of the discharges of radioactive wastes into Barents and Kara Seas. *Proc. of Intern. Meeting on Assessment of Actual and Potential Consequences of Dumping of Radioactive Waste into Arctic Seas*, Oslo, February 1993.
- Serreze, M.C., Barry, R.G., McLaren, A.S., 1989. Seasonal variations in sea ice motion and effects on sea ice concentration in the Canadian Basin. *J. Geophys. Res.* 94 (C8), 10955–10970.
- Thomas, D.R., Rothrock, D.A., 1993. The Arctic Ocean ice balance: a Kalman smoother estimate. *J. Geophys. Res.* 98 (C6), 10053–10067.
- Thorndike, A.S., Colony, R., 1982. Sea ice motion in response to geostrophic winds. *J. Geophys. Res.* 87 (C8), 5845–5852.
- Vinje, T., 1982. The drift pattern of sea ice in the Arctic with particular reference to the Atlantic approach. In: *Rey, Eds. L., Stonehouse, B. (Eds.), The Arctic Ocean*. Macmillan, Indianapolis, IN, pp. 83–96.
- Vinje, T., 2001a. Anomalies and trends of sea-ice extent and atmospheric circulation in the Nordic seas during the period 1864–1998. *J. Climate* 14 (3), 255–267.
- Vinje, T., 2001b. Fram Strait ice fluxes and atmospheric circulation: 1950–2000. *J. Climate* 14 (16), 3508–3517.
- Vinje, T., Finnekasa, O., 1986. The ice transport through Fram Strait, Rep., 186:1-39, Norsk Polarinst., Oslo, Norway.
- Vinje, T., Nordlund, N., Kvambekk, A., 1998. Monitoring ice thickness in Fram Strait. *J. Geophys. Res.* 103 (C5), 10437–10449.
- Weeks, W., 1994. Possible roles of sea ice in the transport of hazardous material. *Arct. Res. U. S.* 8, 34–52.
- Yablokov, A.V., Karasev, V.K., Rumyantsev, V.M., Kokeyev, M.Y., Petrov, O.L., Lytsov, V.N., Yemelyankov, A.F., Rubtsov, P.M., 1993. *Facts and Problems Related to Radioactive Waste Disposal in Seas Adjacent to the Territory of the Russian Federation*. Office of the President of the Russian Federation, Moscow. Also known as Yablokov Report.
- Zubov, N.N., 1943. *Arctic Ice*. Moscow, Izd. Glavsevmorputi, Translated by US Navy Oceanographic Office, Springfield.



Particle tracking method in the approach for prediction of oil slick transport in the sea: modelling oil pollution resulting from river input

K.A. Korotenko^{a,b,*}, R.M. Mamedov^c, A.E. Kontar^b, L.A. Korotenko^b

^aThayer School of Engineering, Dartmouth College, 8000 Cummings Hall, Hanover, NH 03755-8000, USA

^bP.P. Shirshov Institute of Oceanology, 36 Nakhimovskiy pr., Moscow 117851, Russia

^cInstitute Geography of Azerbaijan Academy of Sciences, 31 Javida, Baku 370143, Azerbaijan

Received 2 September 2002; received in revised form 10 July 2003; accepted 5 November 2003

Available online 14 March 2004

Abstract

A 3-D hybrid flow/transport model has been developed to predict the dispersal of oil pollution resulting from river discharges. The transport module of the model takes predetermined current and turbulent diffusivities and uses Lagrangian tracking to predict the motion of individual particles (droplets), the sum of which constitutes hypothetical oil spills. Currents and turbulent diffusivities used in the model have been generated by a numerical ocean circulation model (POM) implemented for the Caspian Sea. The basic processes affecting the fate of the oil spill are taken into account and parameterised in the transport model. The process of evaporation is modelled with a new technique based on the pseudo-component approach.

The model is used to simulate a continuous oil release from the Volga river into the coastal waters of the north part of the Caspian Sea. Oil slick movement and risk of contamination of the coastline by beaching oil spills are illustrated for different wind conditions.

© 2004 Elsevier B.V. All rights reserved.

Keywords: Caspian Sea; Oil spill; River discharge; Particle tracking technique

1. Introduction

The Caspian is the largest inland body of water on the planet, with a surface area of 384,400 km², volume of 78,700 km³, and a coastline nearly 7000 km long. It

measures 1200 km from north to south and 200–450 km from east to west. The Sea (Fig. 1) extends zonally from 46.6° to 54.8°E and meridionally from 36.6° to 47.0°N. Over 60% of the Sea is shallower than 100 m. There are two relatively deep basins (about 600 and 900 m, respectively) in the central and southern parts of the sea. The shelf zone is very wide, and steep slopes occur only in the two deep basins. The Caspian Sea is an enclosed sea with major freshwater input from the Volga River balanced by evaporation. The dynamics of the Caspian Sea is dominated by mesoscale signals

* Corresponding author. NOAA/AOML/PhOD, 4301 Rickenbacker Csw, Miami, FL 33149, USA. Tel.: +1-305-361-4505; fax: +1-305-361-4392.

E-mail address: Konstantin.Korotenko@noaa.gov (K.A. Korotenko).

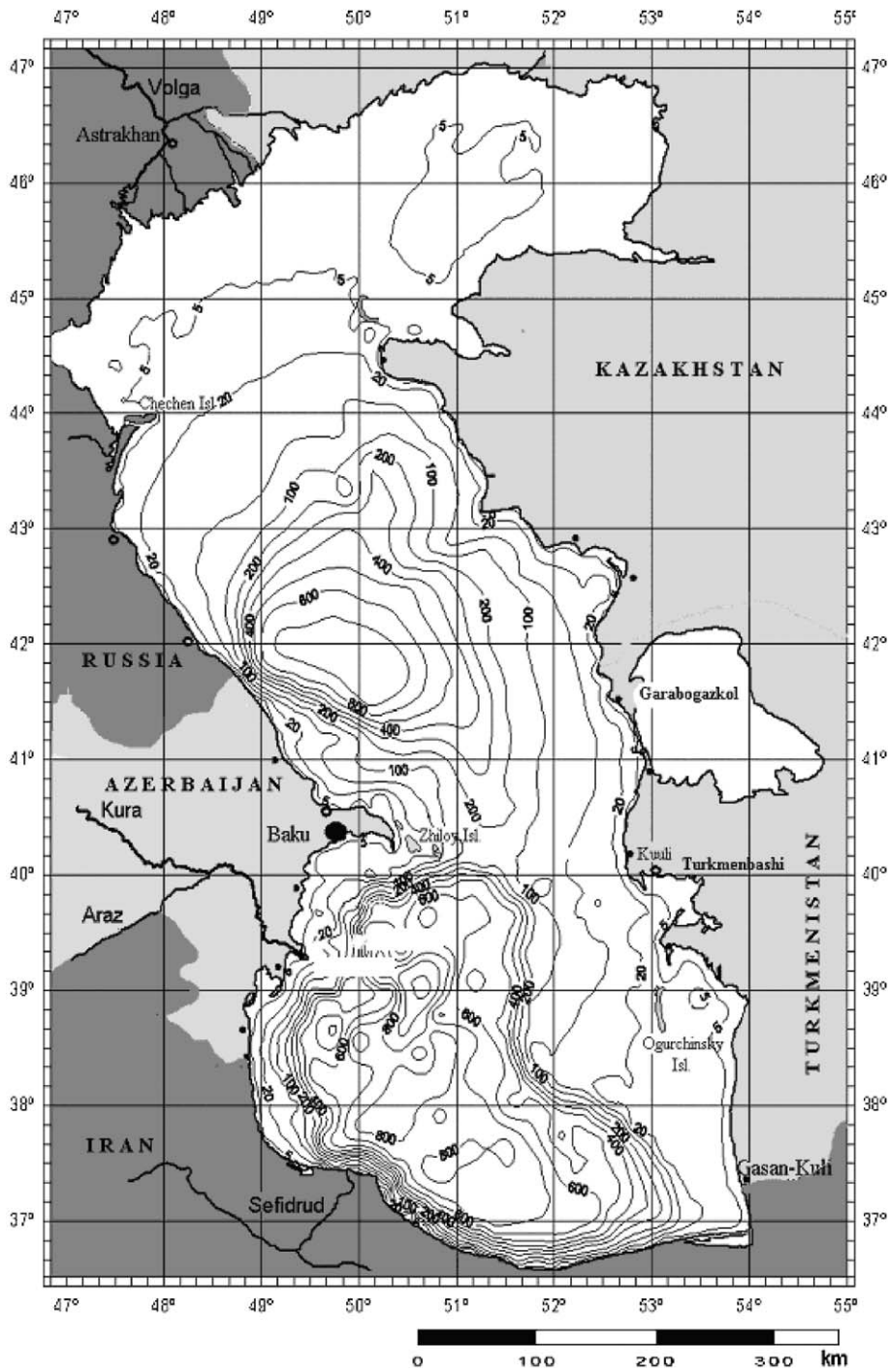


Fig. 1. The Caspian Sea bathymetry.

Table 1
Total oil pollution load to the Caspian Sea

Sources	Oil, tons/ year
Rivers	75,000
Municipalities	19,000
Industries	28,000
Atmosphere	350
Total	122,350

triggered by baroclinic processes and interactions with the very irregular bathymetry. There is however a wide variety of processes in the sea, e.g., interactions between shelf and deep basin circulation, deep basin ventilation, and ice dynamics.

In the Caspian Sea, salinity varies from zero in the shallow northern part (in vicinity of the Volga river discharge zone) to 14 ppt in the southeastern part. In general, salinity increases with longitude and depth. Mean temperature has large meridional and seasonal variations of up to 27 °C in summer to zero in winter. A relatively shallow seasonal thermocline occurs at

depths of 10–40 m, and is absent in winter. Salinity and temperature in the bottom layer of the two deep basins are almost constant and average about 13 ppt, 4 °C and 12 ppt, 6 °C, respectively, for the central and southern basins. Detailed analysis of physical properties and dynamics of the Caspian Sea are given in Korotenko et al. (2002).

The Caspian Sea is fed by numerous rivers, but the Volga River alone contributes about 82% of the annual input.

The Caspian is considered to have three sections: north, middle, and south. The extreme northern end is relatively shallow (~ 5 m average depth) when compared to the southern part (900 m average depth). Oil production, industry, and transportation have caused severe air, water, and soil pollution problems in the Caspian region. The Volga is a major (but not the only) conduits of pollutants to the Caspian Sea including oil pollution. The estimated amount of the input is given in Table 1. According to these data the total amount of oil discharged by Caspian rivers reaches about 75,000 tons/year and, among the rivers,

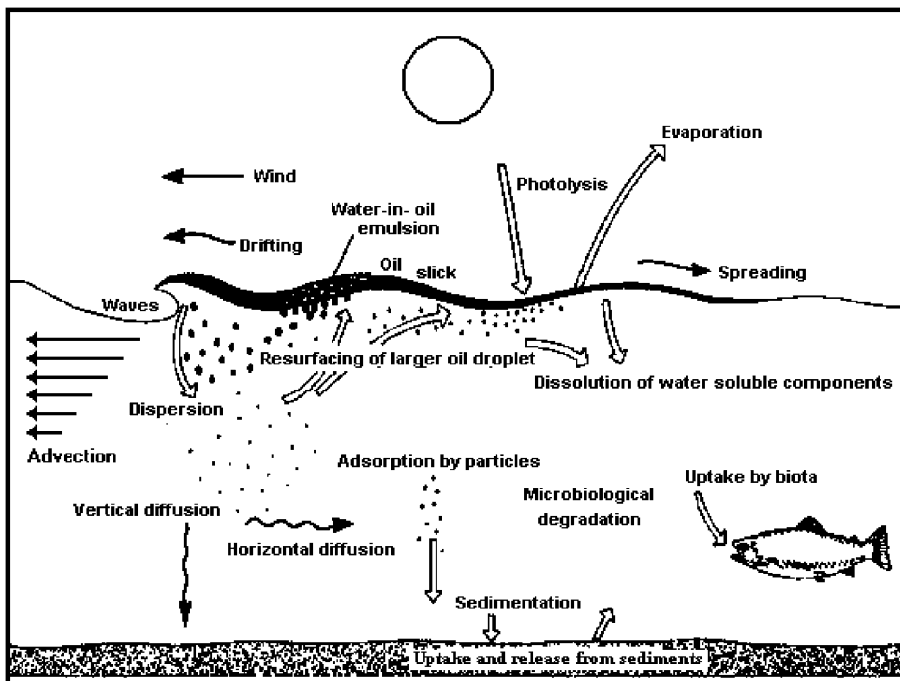


Fig. 2. Processes affecting the oil slick (modified from Daling et al., 1990).

the Volga input is the largest one with 95% of the total petroleum hydrocarbons input.

Once oil is discharged at the sea surface, it is transported by the flow and affected by many processes such as evaporation, emulsification, dissolution, photolysis, biodegradation, etc., that depend on the properties of the oil. Fig. 2 shows the most important such mechanisms affecting an oil slick in the marine environment. The accurate simulation of the fate of oil slicks also requires a good knowledge of the environmental conditions, e.g., winds, currents, waves, turbulence, salinity, temperature, and solar insolation. Surface winds and currents are the most important factors determining the direction and rate at which an oil slick moves. The physical, chemical, and biological reactions, which weather or modify oil as it drifts and spreads, take place over various time scales ranging from a few hours to months and even years. The main aspects of this dynamics have been summarised by Mackay and McAuliffe (1988), Spaulding (1988), and Korotenko et al. (2001, 2002, 2003).

Practical implementations of different approaches to oil spill modelling can be found in a large number of papers (e.g. Lehr et al., 1981; Belen et al., 1981; Proctor et al., 1994; Varlamov et al., 1998; Cekirge and Palmer, 2001; Korotenko et al., 2001, 2002, 2003).

This paper is structured as follows: In Section 2, the structure of the model proposed for modelling

oil spills and its implementation for the Caspian Sea are described. Results of simulations of oil slick resulting from the Volga river discharge for different wind conditions are analysed in Section 3. A short summary is given in Section 4.

2. Oil spill model

The presented model uses the random walk (also called Monte Carlo) technique to follow the motion of individual particles (oil droplets), the total amount of which constitutes the oil spill. Models based on the random walk concept are significantly more effective (Hunter, 1987) than the finite-difference models mainly because they describe exactly the advection, which is a very important transport process for oil slicks. The model consists of two main modules: transport and hydrodynamic. The modules are described below.

2.1. Transport model

The basic concept of this approach (Fig. 3) is similar to that of Proctor et al. (1994), except that oil is initially divided into fractions in order to describe the evaporation process with more accuracy.

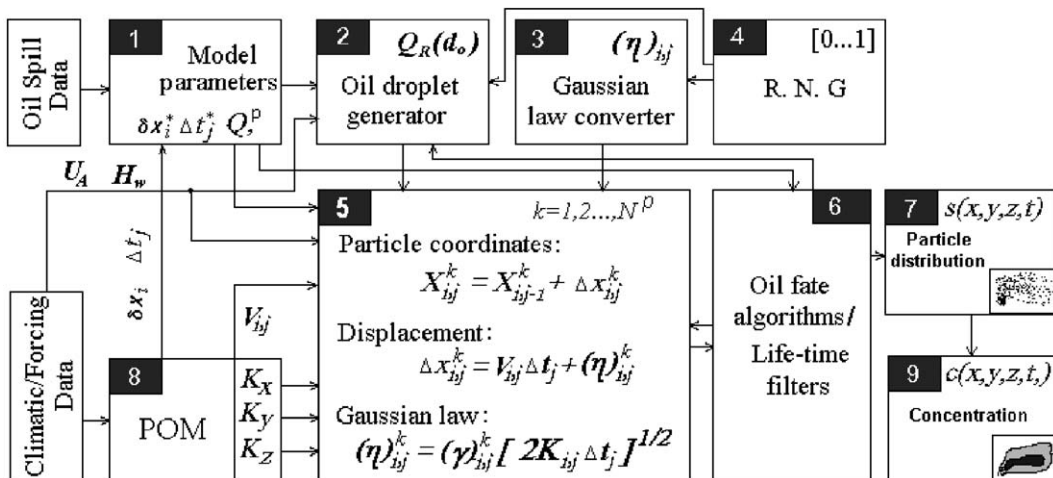


Fig. 3. Schematic of principal elements of the hybrid model.

The main part of the model is Block 5 where displacements of each particle are estimated by (Korotenko, 1994):

$$(\Delta x_i)_{j,k} = V_{i,j} \Delta t_j + (\eta_i)_{j,k}$$

$$(i = 1 - 3; j = 1, 2, \dots, N_t; k_f = 1, 2, \dots, N_f; f = 1, 2, \dots, 8) \quad (1)$$

The displacements $(\Delta x_i)_{j,k}$ are defined as the deterministic part of the motion due to the mean velocity field, $V_{i,j}$ and the random displacement, $(\eta_i)_{j,k}$ due to fluctuations of the velocity and denotes the displacement of the k th particle moving along the x_i axis at the j th instant of time, N_t is the number of time steps, Δt is the time step, N_f is the number of particles in each fraction, and the subscript f denotes a particle fraction.

The distribution of the number of particles in fractions (hydrocarbon groups) is initially assigned and distributed randomly depending on the type of oil. The total number of the particles launched in the model usually does not exceed 10^6 ; nevertheless, the behavior of the tracked particles proved to be representative of the entire spill, even though each droplet represents only a small part of the total volume of the oil. Within each fraction, each droplet is also randomly distributed to have its own half-life according to the empirical exponential laws (Fig. 4, right). In practice, those distributions are assigned randomly by means of a random number generator giving uniform numbers chosen uniformly between 0 and 1, and then they are transformed into an exponential distribution with a weight dependent on wind speed and oil temperature. The ‘long-living’ fractions such as C^2 , C^4 , C^6 , C^7 , and C^8 are randomly exponentially distributed within a

Description	Density, g/ml	Boiling Point, C	Molecular Weight
Paraffin $C_6 - C_{12}$	0.66-0.77	69-230	86-170
Paraffin $C_{13} - C_{25}$	0.77-0.78	230-405	184-352
Cycloparaffin $C_6 - C_{12}$	0.75-0.9	70-230	84-164
Cycloparaffin $C_{13} - C_{23}$	0.9-1.0	230-405	166-318
Aromatic (mono and di-cyclic) $C_6 - C_{11}$	0.88-1.1	80-240	78-143
Aromatic (poli-cyclic) $C_{12} - C_{18}$	1.1-1.2	240-400	128-234
Naphtheno-aromatic $C_9 - C_{25}$	0.97-1.2	180-400	166-300
Residual (including heterocycles)	1.0-1.1	400	300-900

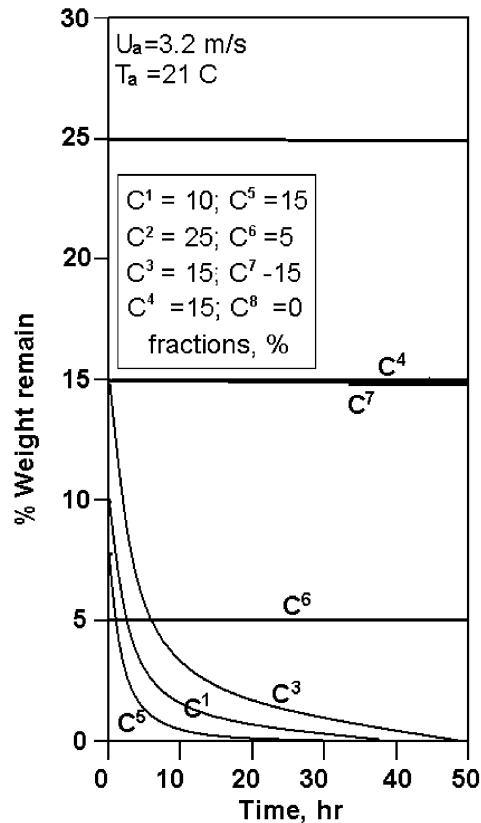


Fig. 4. Range of contents for hydrocarbon fractions (left) and the percent weight changes of individual fraction of light crude oil versus time (right) (modified from Yang and Wang, 1977).

range corresponding to the rather slow effect of total degradation. Their half-life for total degradation is chosen to be 250 h (Proctor et al., 1994).

In addition to the regular movements due to the mean current, oil droplets experience a random diffusion due to the velocity fluctuations, the distribution law of which is represented by the term, $(\eta_i)_{j,k}$, the latter being, in the general case, a function of time and space. The type of law for $(\eta_i)_{j,k}$ is determined by the statistical structure of deviations (fluctuations) of the velocity from its mean value at each time step Δt . Since these fluctuations are considered independent, the law for $(\eta_i)_{j,k}$ is thought to be Gaussian (Monin and Yaglom, 1965). In this case, the $(\eta_i)_{j,k}$ can be represented as $(\eta_i)_{j,k} = \gamma_{j,k}(2K_{i,j}\Delta t)^{1/2}$, where $\gamma_{j,k}$ is a random vector normally distributed with an averaged value of zero and unit standard deviation; $K_{j,k}$ represents the diffusion coefficient along the x_j axis at time $t_j = t_0 + j\Delta t$. The random vector, $\gamma_{j,k}$, is obtained with the use of the random number generator, Block 4, giving a homogeneous distribution of random numbers between 0 and 1, with consequent transformation to the Gaussian law in Block 3. The horizontal and vertical diffusion coefficients, $K_{x,j}$, $K_{y,j}$, and $K_{z,j}$, as well as the mean current velocity U_j^i are provided by the flow model, Block 8. In the presented version of the model, the horizontal diffusion coefficients, $K_{x,j}$ and $K_{y,j}$, were calculated in POM from Smagorinsky formula, while the vertical diffusivity, $K_{z,j}$, was obtained from the level 2.5 turbulence model (Mellor and Yamada, 1982).

In the ‘Oil Spill Data’ block, the location and configuration of source(s), its (their) regime of release and production rate, and type of oil and hydrocarbon groups are collected for subsequent initialization in Block 1, where initial parameters such as the size of the investigated area, spatial resolution and time steps are adjusted to those used in the flow model, Block 8.

In Block 2, the particles’ diameter, d_0 , is assigned randomly in the range $d_{\max} - d_{\min}$. The entrainment rate, $Q_R(d_0)$, is defined as a function of U_A and H_{rms} . The critical diameter, d_c (Aravamudan et al., 1982), is given by the expression $d_c = 9.52v^{2/3}/(g^{2/3}(1 - \rho_0/\rho)^{1/3})$. The buoyancy force depends on the density and size of the droplets and the vertical velocity, w (Proctor et al., 1994), which can be estimated as $w = (gd^2(1 - \rho_0/\rho))/18v$ for small droplets $d \leq d_c$, and as $w = ((8/3)gd(1 - \rho_0/\rho))^{1/2}$ for large drop-

lets $d > d_c$. Hence, the larger droplet sizes are more buoyant and tend to remain near the sea surface, while the smaller droplets are less buoyant and could be transported downwards due to turbulence. Each particle, droplet or slicklet k belonging to fraction f is characterized by its size, density, position $X_{i,j}^k$, age, and its own ‘half-life’, the latter being assigned a priori when the particle is launched.

The transport model includes the effects of evaporation, emulsification, and decomposition, the latter due to biochemical and physical degradation. Algorithms for these effects are incorporated in Block 6, and they are parameterized in terms of ‘half-life’ time filters, which compare current time and the ‘half-life’ time assigned for each particle. Only particles that occur within the subsurface ‘evaporation layer’ of thickness, z_{ev} (0.1 m), experience evaporative decay, while particles at all depths in the water column experience disintegration.

The model takes into account the beaching of oil: If the oil droplet reaches the coastline, it is marked as beached. In this case, the droplet is fixed at the point where it reached the beach; otherwise, the droplet is reflected back to sea and remains in the computational process.

Finally, data of coordinates $S_j = \{(X_1; X_2; X_3)_j\}$ are stored in Block 7, the latter being also used for identification of space cells where each particle is found at time t_j . The particle concentration $C(x,y,z,t)$ in a cell is defined in Block 9 as the number of particles found in the cell relative to the volume of the cell. In this block, the particles remaining in the water column, at the sea surface, beached, and decayed are counted separately and inventoried in an updated summary.

Operationally, the hybrid model is controlled primarily by ‘‘Oil Spill Model’’ Dialog with a map of the Caspian Sea shown in Fig. 5. The model is started with ‘‘Update and Run’’ button, which reads in bathymetry, predetermined current velocities, and model and source parameters. A source position is determined by the mouse pointer location; in doing so the Lat/Long coordinates and instantaneous depth will be displayed. The user may choose whether the spill is bulk or continuous, and specifies the period of spill in the later case. Once the model is running, the user may also specify the wind and wave conditions as well as choose which fraction (evaporated,

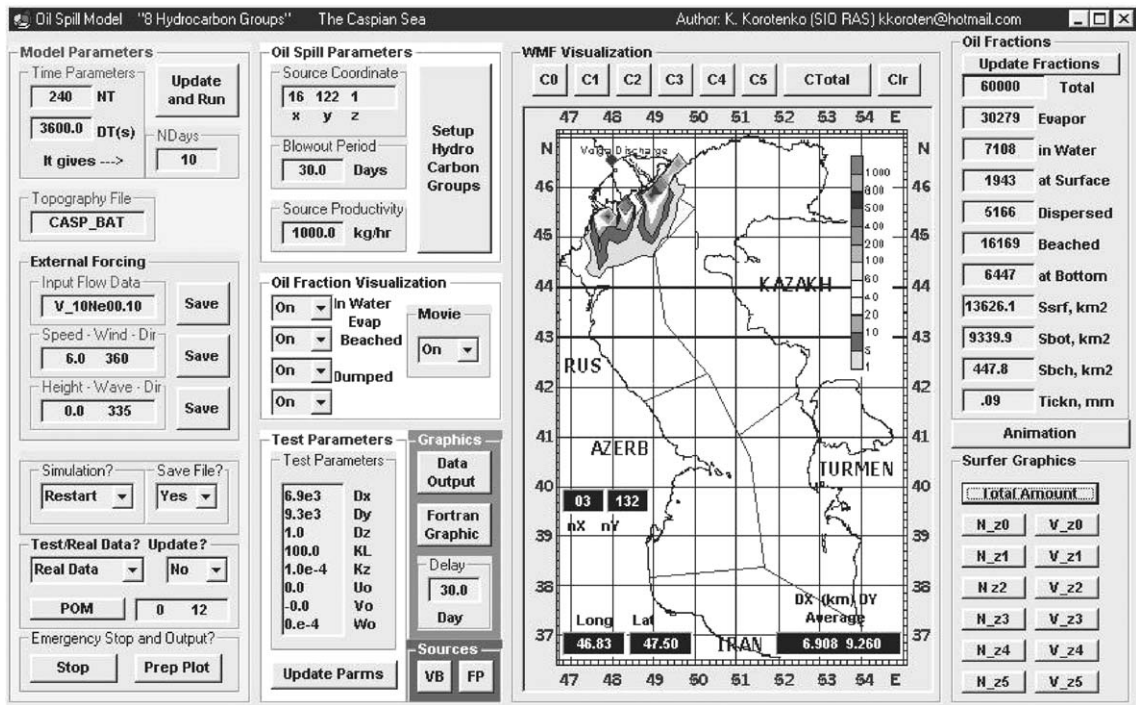


Fig. 5. Main Dialog of the oil spill model.

beached, deposited, etc.) must be displayed during the calculations. It should be noted that once “Update and Run” button is clicked, it runs a separate graphic window displays real-time motion of droplets. The concentration recalculated from particle density and oil fraction distributions during the spilling process are displayed at the map and in correspondent frames at the upper right corner of the main Dialog. A special Properties Dialog, which appears by clicking “Setup Hydrocarbon Groups” button, allows the user to input type and properties of oil.

2.2. Flow module

A high-resolution circulation model is required to describe the complex hydrodynamics and thermohydrodynamics of coastal waters and provide appropriate simulations of the detailed influence of evaporation, river discharge, and synoptic atmospheric forcing. For this purpose, the sigma-coordinate (terrain-following) primitive equation Princeton Ocean Model (POM) (Blumberg and Mellor, 1987)

has been implemented (Block 8) with horizontal and vertical resolutions of respectively, about 5 ft and 1 m (for upper layer of the sea). The model is first used to compute the climatological mean flow, V_i^c . This is done by forcing the model with monthly averaged wind stresses. In a second step, wind-driven currents, V_i^d , are computed using synoptic winds for the winter and summer seasons. In these runs, the surface stress is calculated using a wind speed dependent drag coefficient, C_A ($C_A = 1.1 \times 10^{-3}$ for $U_A \leq 6.5$ m/s and $C_A = 0.61 \times 10^{-3}$ for $U_A > 6.5$ m/s). The bottom stress is calculated with a drag coefficient chosen to be either dependent on grid size or constant, 0.0025, in case of a grid with low resolution (Blumberg and Mellor, 1987). Tidal currents in the Caspian Sea are negligible.

2.3. Implementation of the model for the Caspian Sea

The Princeton Ocean Model coarse grid area covers the entire Caspian Sea from $38^\circ 40'$ to $47^\circ N$ and from 47° to $54^\circ E$. The grid size is $1/12^\circ$ in both longitudinal and latitudinal directions. It

Table 2
Probability (%) of different wind directions in summer

Wind speed, m/s	Wind Direction							
	N	NE	E	SE	S	SW	W	NW
0	7.24	0.02	0	0	0	0	0	0
0–5.0	4.28	5.48	3.5	5.44	1.87	1.71	1.75	5.46
5.0–7.5	11.53	8.50	3.45	5.45	2.29	1.48	1.60	11.5
7.5–12.5	4.61	1.81	0.56	1.04	0.31	0.15	0.1	5.7
12.5–17.5	0.81	0.14	0	0.04	0.02	0	0	1.87
17.5–22.5	0.04	0	0	0	0	0	0	0.22

corresponds to the zonal resolution ranging from 6.09 km at 37°N to 7.50 km at 47°N, and a meridional resolution of 9.02 km. POM has 21 sigma levels and was initialized with seasonally averaged climatic temperature and salinity fields. These seasonal characteristics were used as the

initial background condition for the calculation of short-term variations due to synoptic winds. Spinning up of the model was performed under steady southward wind 6 m/s during 3 months. The probability of occurrence of various wind directions in summer (Table 2) was used for the simulation of drift currents and oil spreading from the Volga river discharge. Southeastward, southward, and southwestward winds are the most prevalent winds for summer. Examples of surface drift currents generated by steady southward wind of 6 m/s are presented in Fig. 6. The circulation is strongest in the extensive shallow shelf areas, taking the form of coastal jets. This effect was also noted numerically (Korotenko and Mamedov, 2001; Korotenko et al., 2001, 2002). The jet-like structure of the surface currents appears along both the western and eastern boundaries. Under non-stationary wind forcing,

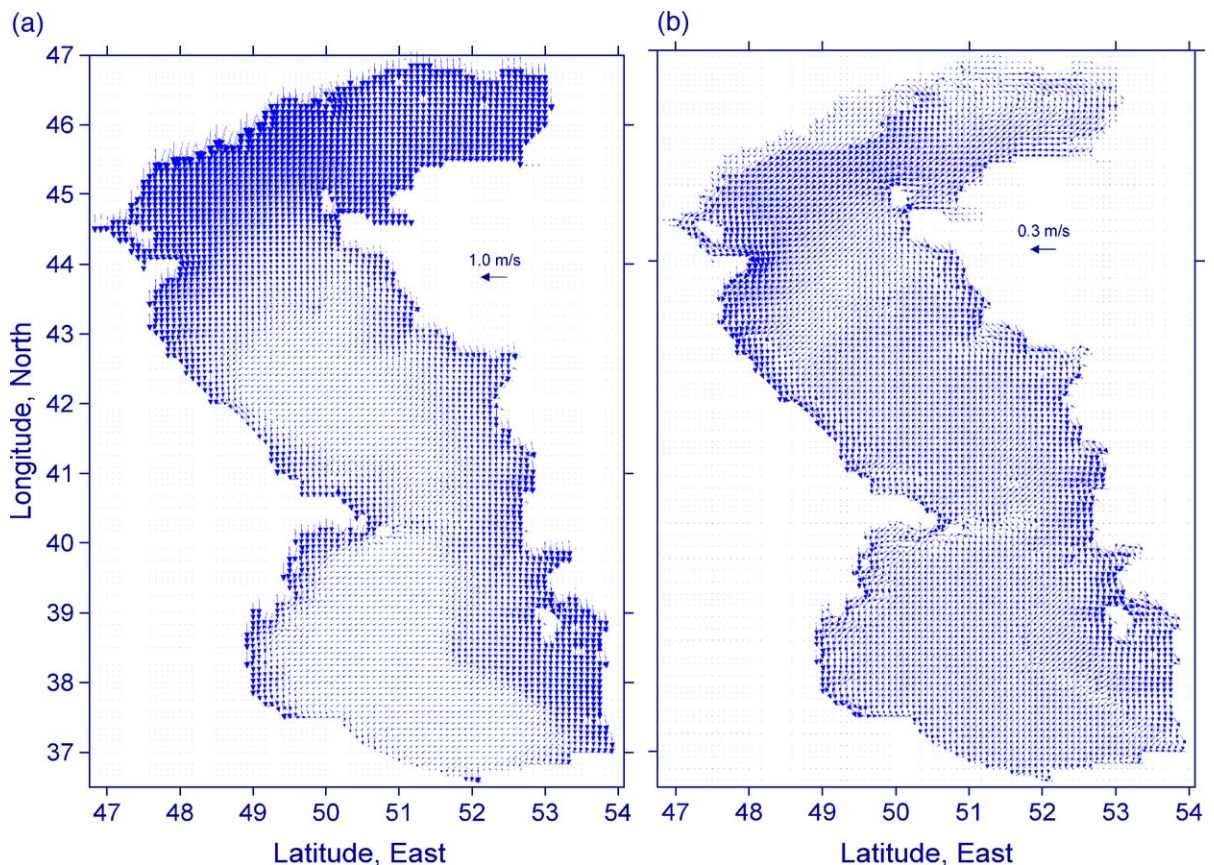


Fig. 6. Wind drift component of the currents under southward wind at the sea surface (a) and at 2 m depth (b).

strong changes in the upper layer circulation occur within a few days in numerical simulations, as has also been noted numerically by Badalov and Rzhaplinsky (1989).

In the model, the Volga river fresh water input is divided into five passages to simulate fresh water plume and current velocity more realistically. The passages are treated as individual sources of fresh water which are implemented in the model's continuity equations (see Kourafalou et al., 1996). The velocity field presented in Fig. 6 shows the strong influence of this river discharge in the north part of the Caspian Sea.

3. Simulation of oil slick from the Volga river discharge

Before simulating the transport of oil slicks, a number of initial parameters had to be specified. The oil (Gunashly type) was specified by density $\rho_{oil} = 872 \text{ kg/m}^3$, droplet diameters, $d_{min} = 60 \text{ }\mu\text{m}$ and $d_{max} = 600 \text{ }\mu\text{m}$, the evaporation times, and 'half-

life times' $T_{ev1} = 20 \text{ h}$, $T_{ev3} = 30 \text{ h}$, and $T_{ev5} = 10 \text{ h}$ for the fractions C^5 , C^1 , and C^3 , respectively. For the 'long-living' fraction, C^2 , C^4 , C^6 , C^7 , and C^8 , as mentioned above $T_{ev4} = 250 \text{ h}$. A percentage ratio between C-fractions, which a priori was set initially during a distribution of droplets between fractions for the light crude oil, was the following: C^1 , C^2 , and $C^8 = 15\%$; C^3 and $C^4 = 20\%$; $C^5 = 5\%$; $C^6 = 3\%$; and $C^7 = 7\%$. These ratios mean that about 40% of oil is predicted to evaporate within the few first days.

Since the transport model was designed in a z-level coordinate system, the simulated velocity and diffusivity data from POM were converted from sigma levels to z-levels, and linear interpolation between the two types of levels was implemented. The transport model had 400 vertical levels; the vertical resolution, Δz , was 0.1 m. The transport and flow models share the same horizontal resolution. Time steps for flow model were 6 and 180 s corresponding to the external and internal modes of POM, respectively, and 1800 and 180 s in simulations of droplet transport.

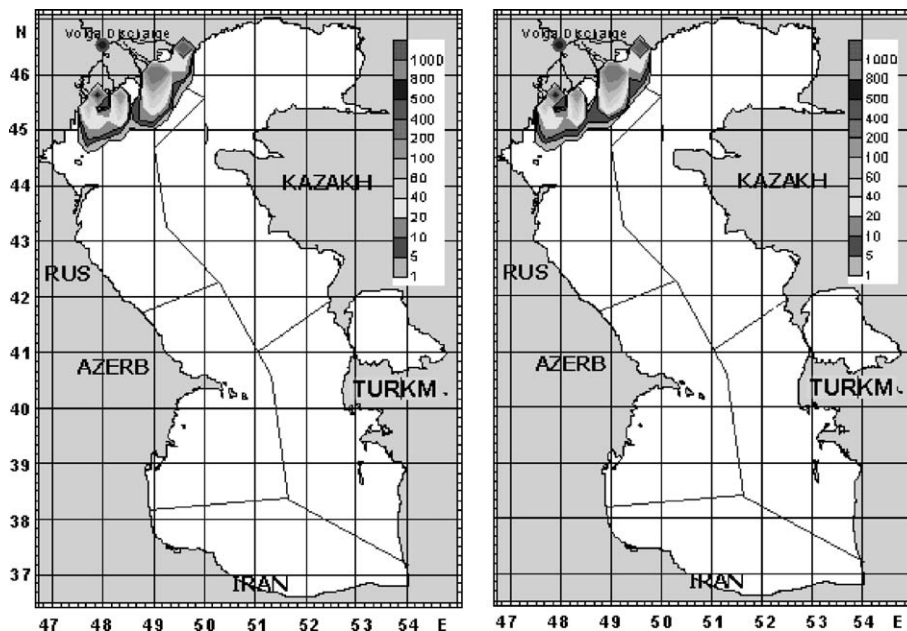


Fig. 7. Time series of the concentration of oil discharged by the Volga River for southward wind, 6.0 m/s: in 5 days (left), in 10 days (right) after release.

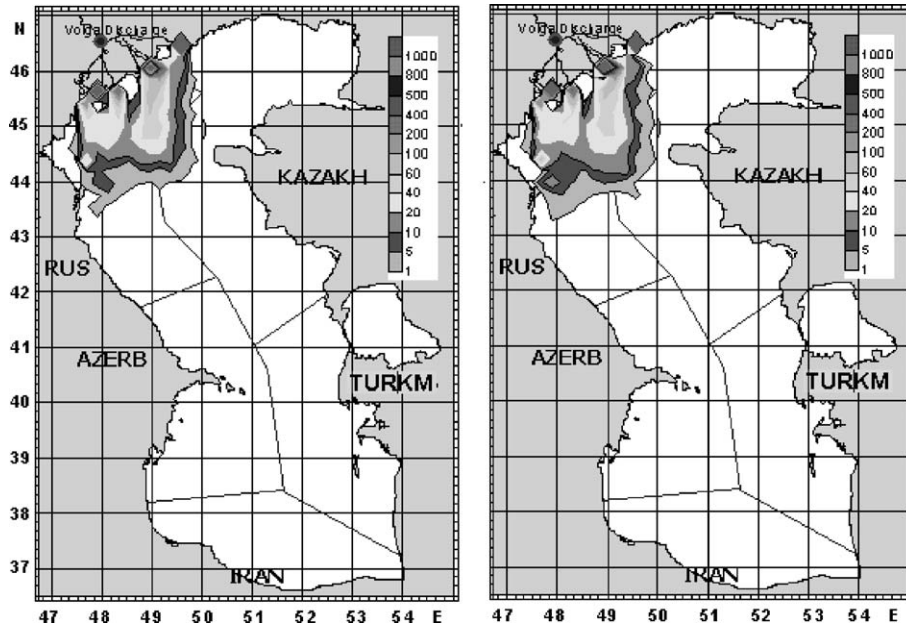


Fig. 8. The same as Fig. 7 but in 20 days (left), in 30 days (right) after release.

As was mentioned above, the total amount of oil discharged by Caspian rivers is equal approximately 75,000 tons/year (see Table 1). Among the all rivers

the contribution of hydrocarbons from the Volga is equal approximately to 95% of the total petroleum input. This gives the value of 8.13 tons/h, which was

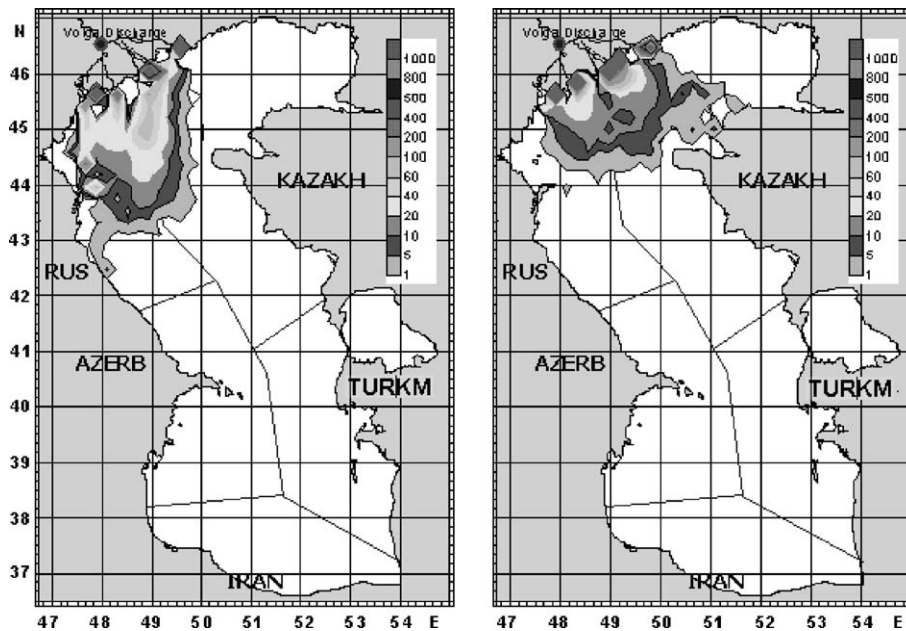


Fig. 9. Surface concentration of oil dispersed under different winds: southeastward (left) and eastward (right) winds of 6 m/s.

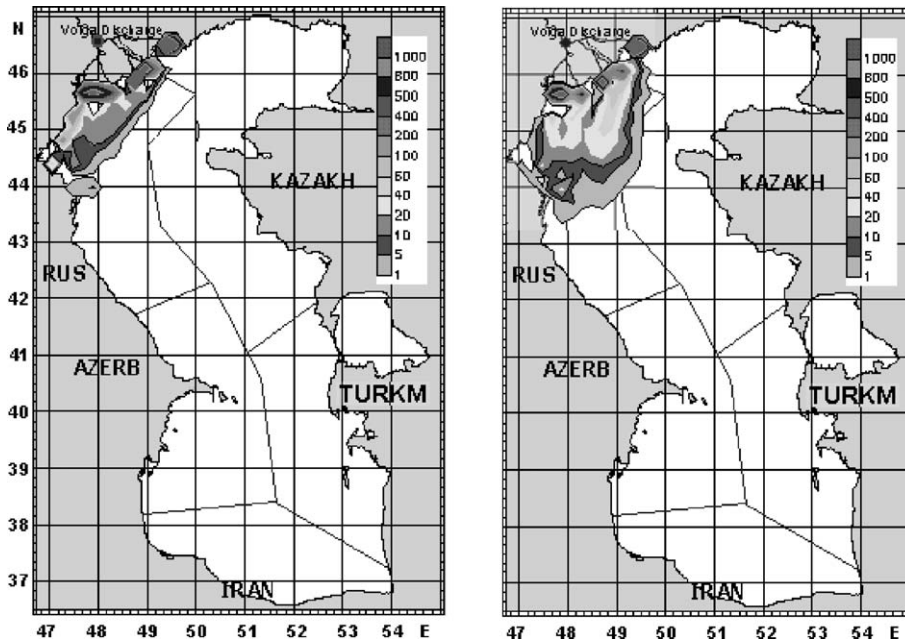


Fig. 10. Surface concentration of oil dispersed under different winds: southwestward (left) and southward (right) winds of 6 m/s.

used in numerical experiments, doing so this amount was distributed between the five passages in order to specify five-mouth river runoff. In each experiment, the calculations cover a 30-day period and carried out under different winds with the aim of assessing the probability of the cross-boundary transport, i.e., transport of oil pollution across borders of FSU¹ countries. Results are presented in Figs. 7–10. Figs. 7 and 8 depict the successive phases of the oil spill moving under climatic mean current and southward wind 6 m/s in the 30-day release scenario. Under this wind condition, oil mostly remains in the Russian zone and some part, about 25%, of the oil pollution penetrates into the Kazakhstan zone. As is seen in Fig. 9, southeastward and particularly eastward directions of wind are predicted to be the most unfavourable for the internal waters and coast of Kazakhstan. In the case of eastward winds, the minimal time taken for the oil slick to beach oil is predicted to be about 15 days. Southward and particularly southwestward directions of wind are the most unfavourable for the Russian coast.

Fig. 11 summarizes the computed oil fate as a time history of oil emitted, oil evaporated, oil dispersed below the surface, oil beached, and oil deposited at the bottom for the experiments with the southeastward wind of 6 m/s. Fig. 11 shows an intensive depositing and beaching of oil accompanied the slick moving along the shallow zone with a depth of about 5 m. As is also seen, evaporation leads to significant mass loss for the chosen type of crude oil, i.e., more than 40%.

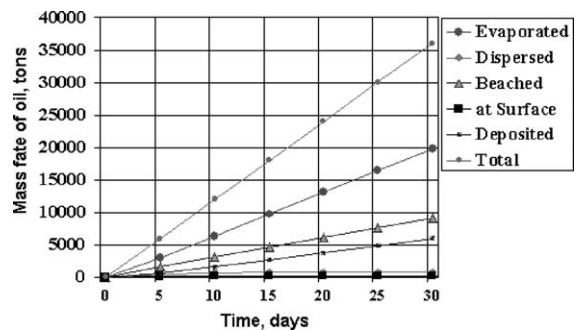


Fig. 11. Time series of oil mass components for the experiment under southwestward wind of 10 m/s.

¹ FSU is Former Soviet Union.

4. Summary

As with most of oil spill transport models, the model presented in this paper is divided into three major modules: input, trajectory and fate prediction algorithms, and output; the latter, in turn, is subdivided into the oil data output and environmental data output. The oil spill prediction procedure is split into two parts: (1) the computation of the current field by means of the Princeton Ocean Model (POM) and input of the mean currents together with winds to the oil spill transport model; and (2) the oil spill model which uses a random walk particle-tracking method, together with the mean current from Eq. (1), to predict the three-dimensional movements and fate of oil droplets. Among the processes affecting the fate of oil, advection, turbulent diffusion, evaporation, and decay are included; the decay is modelled as the combined effect of all the biochemical and physical mechanisms that decompose oil. The combination of incident-specific environmental data and spilled oil characteristics allows conducting diagnostic and prognostic simulations of behaviour of the oil slick in the marine environment.

The transport model has been implemented for the Caspian Sea to predict oil slick movement and the area covered by the oil; also, risks coastline contamination by the beaching of offshore oil spills were illustrated. Numerical experiments with 30-day scenarios of the possible oil input resulting from Volga river discharge show the potential threat caused by beaching and cross-boundary transport of the oil pollution in the northern part of the Caspian Sea.

References

- Aravamudan, K., Ray, P., Ostund, J., Newman, E., Tucker, W., 1982. Break up of oil on rough seas—simplified models and step-by-step calculation. Report No CG-D28-82, U.S. Coast Guard, NTIS, No. ADA118, 372.
- Badalov, A.B., Rzheplinsky, D.G., 1989. Modeling of the Caspian Sea upper layer dynamics under the forcing by synoptic atmospheric processes. In: Sarkisyan, A.S. (Ed.), *Modeling of Hydrophysical Processes and Fields in Closed Basins and Seas*. Nauka, Moscow, pp. 31–51 (in Russian).
- Belen, M.S., Lehr, W.J., Cekirge, H.M., 1981. Spreading, dispersion, and evaporation of oil slicks in the Arabian Gulf. Proc. 1981 Oil Spill Conference (Prevention, Behavior, Control, Clean-up). API, Washington, D.C., pp. 161–164.
- Blumberg, A.F., Mellor, G.L., 1987. A description of a three-dimensional coastal ocean circulation model. Heaps, N. (Ed.), *Three-Dimensional Coastal Ocean Models*, vol. 4. AGU, Washington, pp. 1–16.
- Cekirge, H.M., Palmer, S.L., 2001. Mathematical modeling of oil spilled into marine environments. In: Brebbia, C.A. (Ed.), *Oil Spill Modelling and Processes*. WIT Press, Southampton, pp. 124–131.
- Daling, S., Brandvik, J., Mackay, D., Johansen, Ø., 1990. Characterization of crude oils for environmental purposes. *Oil and Chemical Pollution* 7, 199–224.
- Hunter, J.R., 1987. Application of Lagrangian particle-tracking technique to modelling of dispersion in the sea. In: Noye, J. (Ed.), *Numerical Modelling: Applications for Marine Systems*. North Holland, Amsterdam, pp. 257–269.
- Korotenko, K.A., 1994. The random walk concept in modelling matter transport and dispersion in the Sea. *J. Mosc. Phys. Soc.*, vol. 4 (4). Allerton Press, New York, pp. 335–338.
- Korotenko, K.A., Mamedov, R.M., 2001. Modeling of oil slick transport processes in coastal zone of the Caspian Sea. *Oceanology* 41 (1), 37–48.
- Korotenko, K.A., Mamedov, R.M., Mooers, C.N.K., 2001. Prediction of the dispersal of oil transport in the Caspian Sea resulting from a continuous release. *Spill Science and Technology Bulletin* 6 (5/6), 323–339.
- Korotenko, K.A., Mamedov, R.M., Mooers, C.N.K., 2002. Prediction of the transport and dispersal of oil transport in the south Caspian Sea resulting from Blowouts. *Journal of Environmental Fluid Mechanics* 1 (4), 383–414.
- Korotenko, K.A., Bowman, M.J., Dietrich, D.E., 2003. Modeling of the circulation and transport of oil spills in the Black Sea. *Oceanology* 43 (4), 367–378.
- Kourafalou, V.H., Oey, L.-Y., Wang, D.W., Lee, T.N., 1996. The fate of river discharge on the continental shelf: 1. Modeling the river plume and inner shelf coastal current. *Journal of Physical Research* 101 (C2), 3415–3434.
- Lehr, W.J., Belen, M.S., Cekirge, H.M., 1981. Simulated oil spills at two offshore fields in the Arabian Gulf. *Marine Pollution Bulletin* 12 (11), 371–374.
- Mackay, D., McAuliffe, C., 1988. Fate of hydrocarbons discharged at sea. *Oil and Chemical Pollution* 5, 1–20.
- Mellor, G.L., Yamada, T., 1982. Development of a turbulence closure model for geophysical fluid problems. *Reviews of Geophysics and Space Physics* 20, 851–875.
- Monin, A.S., Yaglom, A.M., 1965. *Statistical Hydromechanics: Part I*. Nauka, Moscow, 640 pp.
- Proctor, R., Flather, R.A., Elliot, A.J., 1994. Modeling tides and surface drift in the Arabian Gulf—application to the Gulf Spill. *Continental Shelf Research* 14 (5), 531–545.
- Spaulding, M.L., 1988. A state-of-art review of oil spill trajectory and fate modeling. *Oil and Chemical Pollution* 4, 39–55.
- Varlamov, S.M., Yoon, J.-H., Hirose, N., Kawamura, H., 1998. . In: Garsia-Martinez, R., Brebbia, C.A. (Eds.), *Oil and Hydrocarbon Spills. Modelling Analysis and Computing*. Computation Mechanics Publications, Southampton, pp. 359–369.
- Yang, W.C., Wang, H., 1977. Modeling of oil evaporation in aqueous environment. *Water Research* 11, 879–887.



ELSEVIER

Available online at www.sciencedirect.com

SCIENCE @ DIRECT®

Journal of Marine Systems 48 (2004) 171–189

JOURNAL OF
MARINE
SYSTEMS

www.elsevier.com/locate/jmarsys

Interpretation of tracer experiments with fine-grained dredging material at the Belgian Continental Shelf by the use of numerical models

Dries Van den Eynde*

Management Unit of the North Sea Mathematical Models, Gulledele 100, B-1200 Brussels, Belgium

Received 24 September 2002; received in revised form 28 February 2003; accepted 28 March 2003

Available online 2 March 2004

Abstract

Radioactive tracer experiments were used by HAECON NV to give insight into the transport of the dredged material in Belgian coastal waters. The experiments showed that material dumped less than 25 km from the coast recirculated rapidly to the coast, while material dumped further from the coast disappeared from the Belgian Continental Shelf. The degree of recirculation was however not well determined, due to large uncertainties in the experiments. A vertically integrated sediment transport model is therefore used to simulate the dispersion of dredged material in the Belgian coastal waters. The model is a semi-Lagrangian model, based on the Second Moment Method. The bottom stress is calculated under the influence of prevailing currents and waves. Although many uncertainties still remain in the modelling of sediment transport, this simple sediment transport model gives satisfying results in simulating the tracer experiments. By a careful interpretation of the experimental and model results, new insight is obtained about the existence of the turbidity maximum in the Belgian coastal waters.

© 2004 Elsevier B.V. All rights reserved.

Keywords: Radioactive tracers; Sediment transport; Mathematical models; Cohesive sediments; Dredging; Turbidity; North Sea; Southern Bight; Belgian Continental Shelf

1. Introduction

The silting up of the Belgian sea harbours (Zeebrugge, Oostende, Nieuwpoort, Blankenberge) and of the fair channels towards these sea harbours and towards the Westerschelde, is significant. Around 10 million tons of dry material is dredged each year to maintain and to deepen the fair channels and the

harbours. Most of this material is dumped back into sea (Malherbe, 1991). The selection of dumping sites with a high efficiency, i.e. the ratio between the mass of the material that stays at the dumping site and the mass of the material which was dumped there, is essential. First of all, there is an economical interest: one has to avoid as much as possible that the dumped material returns to the place where it was dredged originally. Further, it is ecologically important that the chemical and biological effects, which are related to the dumping activities, stay as localised as possible.

* Tel.: +32-2-773-2130; fax: +32-2-770-6972.

E-mail address: D.VandenEynde@mumm.ac.be
(D. Van den Eynde).

Monitoring of the volumetric and granulometric changes of the dumping sites showed that most of the fine-grained sediments are washed out, while only the sand remains. The efficiency of the dumping sites was estimated at between 25% and 0% (Ministerie van Volksgezondheid en Leefmilieu-BMM and Administratie Infrastructuur en Zeevezen – AWK, 1993).

Commissioned by the Flemish government, Afdeling Waterwegen en Zeevezen, a series of tracer experiments with long-life radioisotopes were carried out by HAECON NV, to study the dispersion of the dumped material (HAECON NV, 1993a,b, 1995). These experiments illustrated the complexity of the problem and gave some first impressions on the behaviour of the mud at the Belgian coast. The experiments suggested that the mud offshore of the Belgian coast is trapped in a so-called “turbidity maximum”, from which it cannot escape. This turbidity maximum area is well known, but the reason

for its existence in this very dynamic environment is still poorly understood.

Since the results of the tracer experiments are not straightforward to interpret, it is necessary to adopt a more integrated approach and to combine the measurements of the sediment transport with results obtained using mathematical models. Therefore, numerical models were applied in parallel to study the dispersion of the dredged material.

In the present paper, some results of these numerical models are presented. In a first section, the hydrodynamics and the sedimentology of the Belgian Continental Shelf (BCS) are presented. The numerical models are briefly introduced in the next section. In the main section of the paper, the simulation of the tracer experiments with the numerical models is discussed. The original results of the tracer experiments are presented first. Next, the model results are discussed. It will be shown that by a careful interpretation

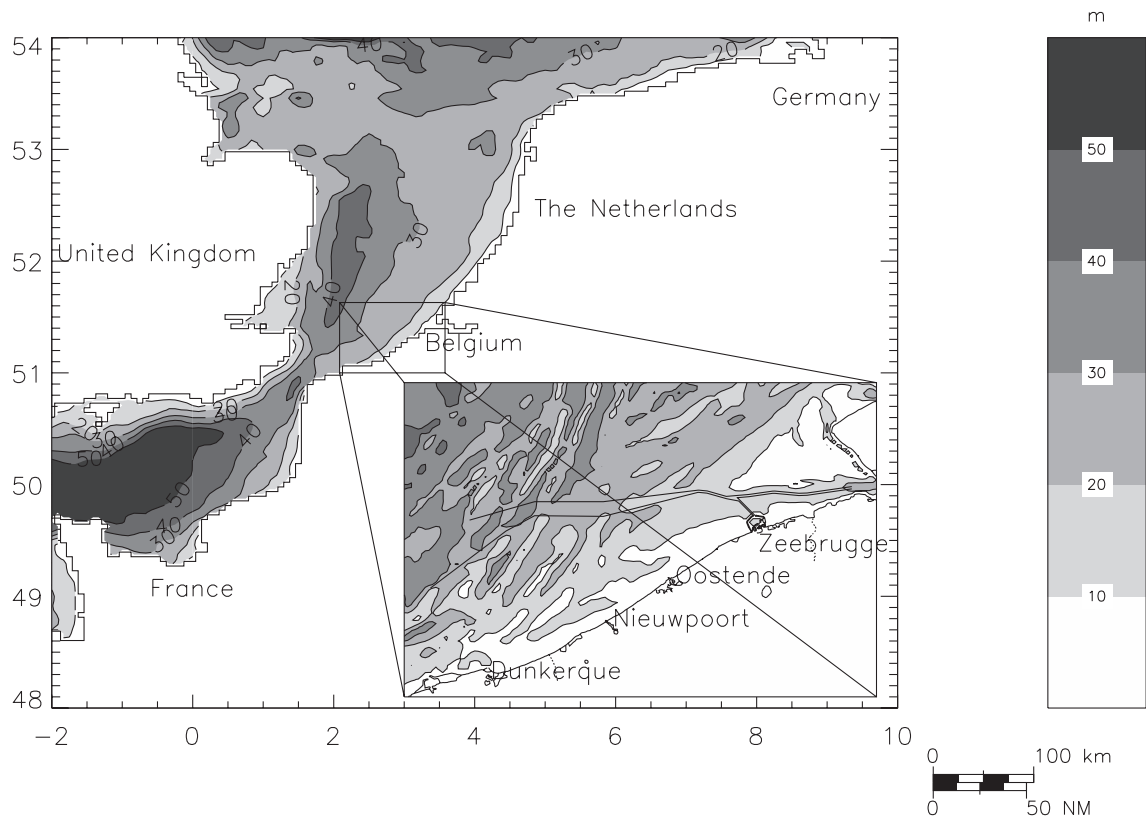


Fig. 1. Bathymetry of the Southern Bight of the North Sea and of the Belgian Continental Shelf.

of both experiments and model results valuable information can be gathered on the behaviour of the dumped matter. Some conclusions are formulated in the last section.

2. Hydrodynamics and sedimentology of the BCS

The bathymetry of the BCS is shallow and irregular. The water depth varies between 3 and about 40 m, while the fair channels are dredged to about 15 m below mean sea level. The area of interest and the bathymetry of the modelled area are presented in Fig. 1.

The hydrodynamics of the Belgian coastal waters is mainly determined by the tides, by the prevailing wind and by wave activity. The tides are semi-diurnal and slightly asymmetrical. The mean tidal range at Zeebrugge is 4.3 m at spring tide and 2.8 m at neap tide. The tidal current ellipses are elongated in the coastal zone and become more elliptical further out of the

coast (Fig. 2). The current velocities can be more than 1 m/s at spring tide. The water column in the area is well mixed during the entire year (De Ruijter et al., 1987). There is no stratification due to salinity or temperature gradients. The outflow (inflow) of the Westerschelde has a mean of 50,000 m³/s during ebb (flood). The freshwater outflow is low and is governed by rainfall. It fluctuates between 20 m³/s during summer and 400 m³/s during winter with a long-term (1949–1997) annual mean of 107 m³/s. The winds and consequently also the waves are mainly from the southwest or from the northeast. The winds are for almost 90% of the time below 5 Bft, while the significant wave height at Westhinder is for 87% of the time below 2.0 m. The residual transport of the water masses is mainly to the northeast.

The surface sediments on the BCS mainly consist of medium size sand to fine sand (Ceuleneer and Lauwaert, 1987). Further from the coast, at water depths greater than 12 m, medium size sand is found

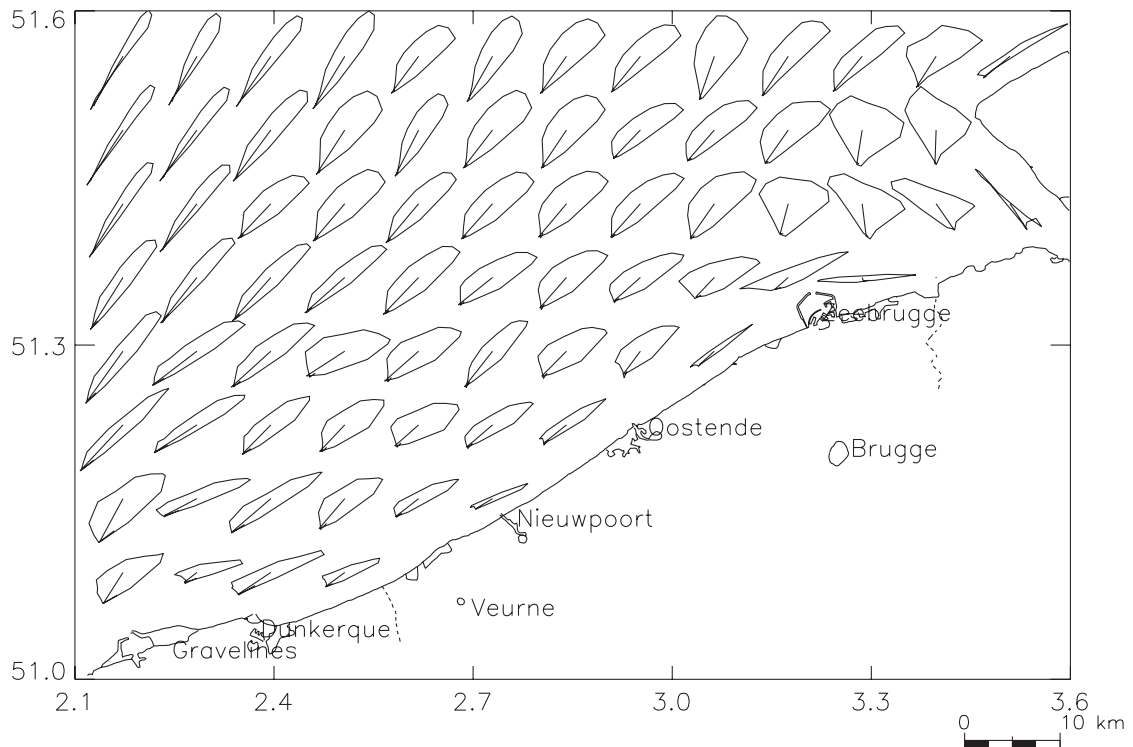


Fig. 2. Current ellipses on the Belgian Continental Shelf, calculated with the two-dimensional hydrodynamic model MU-BCZ, for tides only and for mean tide.

with a median grain size up to more than 400 μm . Nearer to the coast and east from Oostende, more fine sand is found with a median grain size lower than 200 μm . A map indicating the median grain size in the area of interest is presented in Fig. 3. The map was prepared by distance-weighted averaging of more than 2200 grain-size distributions. In the eastern part, near the coast, large mud fields are found (Fig. 4), whereby mud is defined as cohesive material with a grain size smaller than 63 μm . These mud fields are partly correlated with the high-turbidity zone between Oostende and Zeebrugge and in the mouth of the Westerschelde.

Since the area where the dredging is carried out (the fair channels and the sea harbours, mainly Zeebrugge) is also the area where the mud fields occur, a very significant part of the dredged material consists of mud. Measurements with a Hopper Well Densimeter have shown that the amount of mud in the dredging vessels can be very high. More than 90% of the material dredged in the harbour of Zeebrugge consists of mud (Tijdelijke Vereniging Noordzee en Kust, 1998).

3. Description of the numerical models

3.1. Introduction

Since the Belgian coastal waters are well mixed during the entire year (De Ruijter et al., 1987), a two-dimensional vertical integrated model was used for the current application.

In a first section, a short description is given of the hydrodynamic model, which is used for the calculation of the water levels and the currents in the area of interest. The wave model is discussed in Section 3.3, while the sediment transport model is briefly presented in Section 3.4.

3.2. The hydrodynamic model

The two-dimensional hydrodynamic model MUBCZ calculates the depth-integrated current and the elevation of the free surface with respect to mean sea level under the influence of the tides and meteorological effects. The model solves the classical shal-

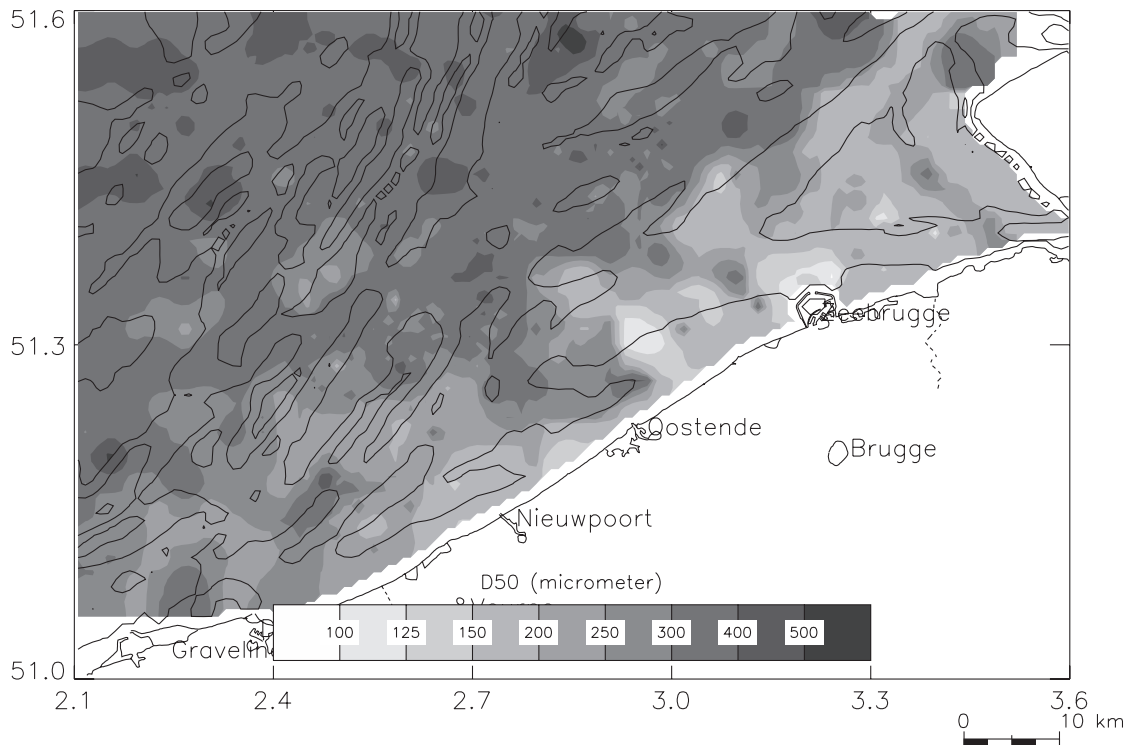


Fig. 3. Map of median grain size of sand on the BCS.

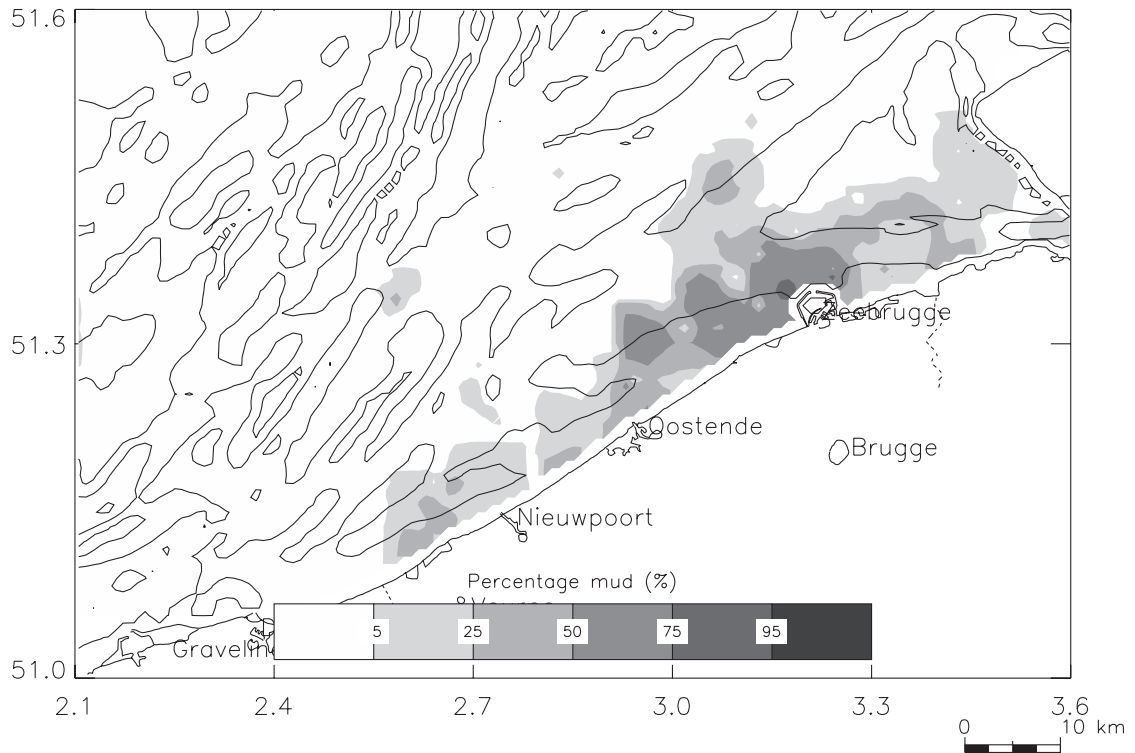


Fig. 4. Map of percentage of mud at the bottom on the BCS.

low-water equations and an equation for the conservation of mass in a system of Cartesian co-ordinates. The bottom and surface stresses are computed using conventional quadratic friction laws. The wind friction coefficient is calculated following Smith and Banke (1975). The equations are solved using an explicit finite difference method on a staggered Arakawa-C grid. More information on the model equations and on the numerical scheme can be found in Adam (1979).

The hydrodynamic model is implemented on a geographical grid, covering the Belgian coastal area and the Flemish Banks, from $2^{\circ}5' E$ to $3^{\circ}35' E$ and from $51^{\circ}N$ to $51^{\circ}37' 55''N$. The model grid has 135×91 elevation points and has a resolution of $25 \times 40''$ (approximately 772×772 m). Since most sandbanks are some kilometres long and have a width of more than a kilometre, this resolution should be sufficient to model the dispersion of mud on the BCS, although some finer structures could be missed. A presentation of the model bathymetry is given in

Fig. 1. At the open sea boundaries, the MU-BCZ model is forced by the water elevations calculated by a larger hydrodynamic model, the MU-STORM model, which calculates the hydrodynamic environment in the North Sea and the Channel. This model is basically the same model as the MU-BCZ model, but is implemented on three coupled grids: a coarse grid with a resolution of $20 \times 20'$ (approximately 22×37 km) for the central North Sea, a coarse grid with the same resolution for the eastern Channel and a fine grid ($4' \times 6' 40''$ or 7.7×7.4 km) for the Southern Bight of the North Sea. Four semi-diurnal tidal components (M_2 , S_2 , N_2 , K_2) and four diurnal tidal components (O_1 , K_1 , P_1 , Q_1) are used to force the tidal elevation on the open boundaries. At the outflow of the Westerschelde, the MU-BCZ model is coupled with a one-dimensional model for the estuary and its main tributaries (Mouchet and Ronday, 1992). Realistic wind and atmospheric pressure fields, provided by the United Kingdom Meteorological Office, Bracknell, were used to force the model.

The hydrodynamic model has been validated (Van den Eynde, 1997) using OSCR current measurements, which were collected by Proudman Oceanographic Laboratory at the Middelkerke Bank (CSTAB Group, 1996). The surface currents, measured by the OSCR HF radar, were compared with the modelled surface currents. These were calculated from the depth-averaged currents of the 2D hydrodynamic model, by applying a logarithmic profile over the water depth. The Root-Mean-Square-Errors (RMSE) on the major axis and on the minor axis of the M_2 tidal ellipses were 0.057 and 0.034 m/s, respectively. The corresponding Scatter Indices (SI), which are defined as the RMSE divided by the mean of the observations, were 9% and 20%. The RMSE on the residuals (Z_0 -component) was 0.042 m/s. In addition, tidal elevation and current measurements, carried out by the Management Unit of the North Sea Mathematical Models over a period of 8 years and in different stations on the BCS, were used to validate the model results. This gave a RMSE on the M_2 tidal elevation of 0.09 m and

a RMSE on the major axis of the M_2 tidal ellipses of 0.13 m/s.

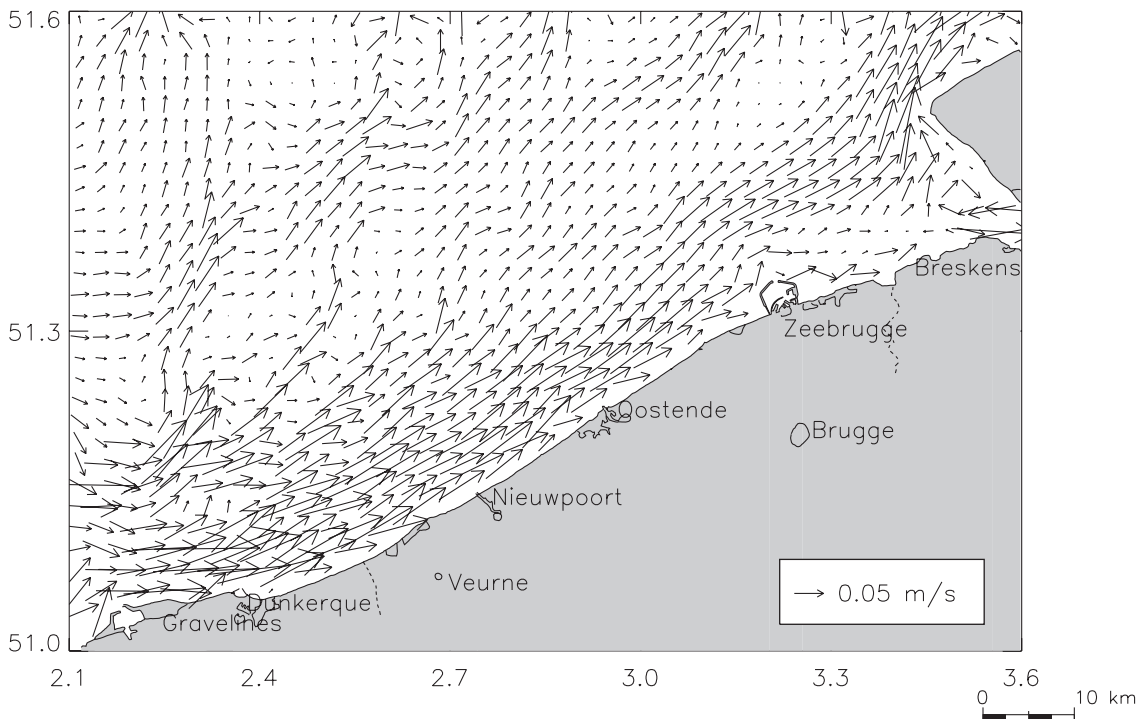
The Eulerian residual transport velocity \vec{U}_{res} [m/s] was calculated for the year 1999 (see Fig. 5) using the following expression:

$$\vec{U}_{\text{res}} = \frac{\sum_{i=1}^n h_i \vec{u}_{ci}}{\sum_{i=1}^n h_i} \quad (1)$$

where \vec{u}_{ci} is the velocity vector [m/s] at time i , h_i the total water depth [m] at time i and n the number of current vectors, used to calculate the residual water transport.

3.3. The wave model

For the calculation of the wave environment in the Belgian coastal area, the MU-WAVE model (Van den Eynde, 1992) is used. The core of the model is



Wed Feb 5 16:38:07 CET 2003

Fig. 5. Eulerian residual transport velocities for the year 1999 (tide and wind forcing) as calculated with the MU-BCZ model.

formed by the HYPAS wave model (Günther and Rosenthal, 1985), a second-generation wave model. It is a hybrid model, which combines the independent calculation of swell energy for each frequency and direction through a ray technique, with a parametrical wind sea model, using the JONSWAP parameters and the mean wind sea direction as prognostic variables.

For the present application, the model is implemented on two nested stereographical grids. The North Sea grid has a resolution of 50×50 km, while for the Southern Bight of the North Sea a grid with a higher resolution of 5×5 km is used. The calculated wave parameters are interpolated to the MU-BCZ model grid.

The MU-WAVE model has been tested extensively and is used in operational mode for the prediction of the waves on the BCS. Results of the first validation were presented in Van den Eynde (1992). The RMSE of the significant wave height on the BCS was 0.35 m, which gives a SI of 31.8%. During later validations of the MU-WAVE model, the results were compared with ERS-1 data, with buoy data and with results of the third-generation wave model WAM (Ovidio et al., 1994). For the Southern North Sea, a SI of 27% was found for the significant wave height results. Taking into account the uncertainty in the wind fields, these results are very satisfactory.

3.4. Sediment transport model

The sediment transport model MU-STM is a two-dimensional model, which solves the advection–diffusion equation, describing the transport of the material in suspension through the model grid:

$$\begin{aligned} & \frac{\partial(hC)}{\partial t} + \frac{\partial(huC)}{\partial x} + \frac{\partial(hvC)}{\partial y} \\ & = \frac{\partial}{\partial x} \left(hK_1 \frac{\partial C}{\partial x} \right) + \frac{\partial}{\partial y} \left(hK_2 \frac{\partial C}{\partial y} \right) + E - D \end{aligned} \quad (2)$$

where C is the depth-averaged suspended particulate matter (SPM) concentration [kg/m^3], h is the water depth [m], u and v are the depth-averaged velocity components [m/s], K_1 and K_2 are the diffusion coefficients [m^2/s], E and D the erosion and deposition rates [$\text{kg}/\text{m}^2/\text{s}$]. The model is a semi-Lagrangian

model and uses the Second Moment Method (Egan and Mahoney, 1972; Pedersen and Prahm, 1974; de Kok, 1994) for the advection of the material in suspension. In this method, all material in each grid cell is represented by one “rectangular mass”, with sides parallel to the model grid, characterised by its zeroth moment (the total mass), its first mass moments (the mass centre) and its second mass moments (the size of the rectangle). The great advantage of this semi-Lagrangian method is that it introduces less numerical diffusion than classical Eulerian methods. Fronts and long thin distributions therefore can be better represented using this method. The method has already been used with success to model the dispersion of dumped material in the Dutch coastal zone (de Kok, 1994). The horizontal diffusion in the model is calculated following a Fickian law (Johnson et al., 1988). The model can account for different sediment classes and calculates for each of them the advection and diffusion of the material in suspension under the influence of the tidal currents and of the currents generated by the waves (Stokes drift).

Since the dispersion of cohesive sediments is a complex phenomenon, for which not all essential relations and processes are yet well understood or known (e.g. O’Connor, 1984; ECOPS Coastal Zone Steering Group, 1993), the model uses simple empirical relations to calculate the bottom stress and the erosion and sedimentation of the material. The bottom stress is calculated under the combined effect of currents and waves with an adapted formulation of the Bijker’s formulae of 1966 (Koutitas, 1988):

$$\tau_b = \tau_c \left[1 + 0.5 \left(\frac{c}{\sqrt{2}g} \sqrt{f_w} \frac{u_b}{u_c} \right)^2 \right] \quad (3)$$

where τ_c is the bottom stress due to currents [Pa], g the acceleration due to gravity [m/s^2], u_b the orbital wave velocity [m/s], u_c the depth-averaged current velocity [m/s], f_w the wave friction factor and c , originally, an empirical constant. The following relation has been used in order to calculate c (Van den Eynde and Ozer, 1993):

$$c = 77.5 + 14.18 \min \left(\frac{u_c}{u_b}, 0.67 \right) \quad (4)$$

The rate of erosion E is modelled according to Partheniades (1962), which uses a linear relation between the excess shear stress and the rate of erosion:

$$E = M(\tau_b - \tau_{ce})/\tau_{ce} \quad \tau_b > \tau_{ce} \quad (5)$$

where M is the erosion constant [$\text{kg}/\text{m}^2/\text{s}$] and τ_{ce} the critical shear stress for erosion [Pa]. In the formula, the rate of erosion is independent of the sediment concentration in the eroding current. The sand–mud interactions, including a consolidation model, are omitted because they only complicate the erosion formula. At the present time, it is not clear that using a more complex parameterisation for the erosion will improve the model results.

The equation of Krone (1962) is used for calculating deposition. In this formula, the probability that mud particles will attach to the bottom varies linearly between 0 and 1 if the bottom stress reduces from a

critical value to zero. The deposition rate D then is written as:

$$D = w_s C(\tau_{cd} - \tau_b)/\tau_{cd} \quad \tau_b < \tau_{cd} \quad (6)$$

with w_s the fall velocity [m/s] and τ_{cd} the critical shear stress for deposition [Pa]. This equation essentially represents the rate of deposition in the case of low suspended sediment concentration. More complicated laws for deposition exist, but their use in tidal conditions does not significantly improve the results when compared to the Krone formula (Teisson, 1994).

4. Simulation of the tracer experiments

4.1. General information on the tracer experiments

Six radioactive tracer experiments were executed by HAECON NV (1993a,b, 1995) to investigate the

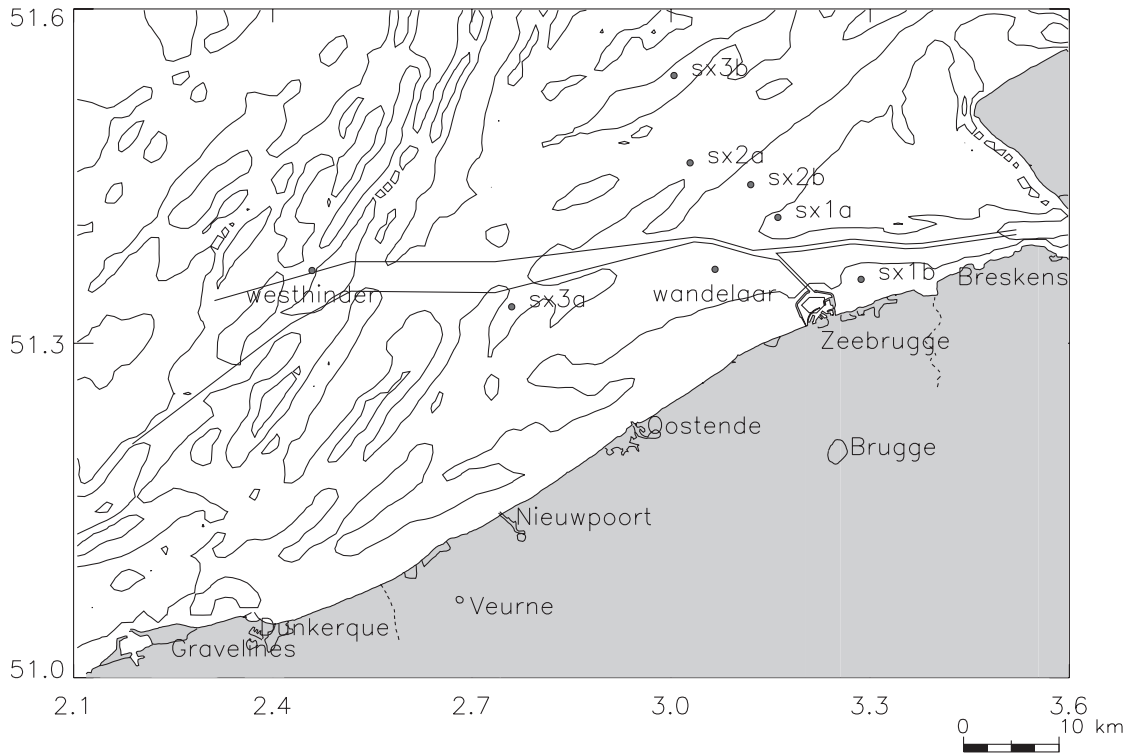


Fig. 6. Location of the stations Westhinder and Wandelaar and of the initial positions of the radioactive tracers dumped by HAECON NV (1993a,b, 1995).

Table 1
Place and time of tracer experiments carried out by HAECON NV (1993a,b, 1995)

Exp.	Place	Longitude λ	Latitude φ	Time (GMT)
sx1a	B/2	3°08' 30"	51°26' 00"	22/04/92 16h12
sx1b	B/6	3°16' 00"	51°22' 30"	22/04/92 17h24
sx2a	Noordflank Akkaert	3°00' 35"	51°29' 05"	18/01/93 15h00
sx2b	Ebschaar B/1 and B/2	3°06' 03"	51°27' 51"	18/01/93 16h18
sx3a	Negenvaam	2°44' 30"	51°20' 57"	29/09/93 10h12
sx3b	Noordflank Thornton	2°59' 08"	51°34' 01"	29/09/93 13h36

recirculation of the dumped material in the Belgian coastal zone. The place of the experiments and the time of the dumping of the radioactive tracer are given in Table 1. The positions of the six sites are indicated in Fig. 6. Note that five sites are within a range of

about 20 km off the coast, while one site (*sx3b*) is about 30 km from the coast.

For each experiment, about 4 kg of mud was injected with Hafnium (Hf) or Terbium (Tb) and was dumped at the selected sites. After the dumping of the radioactive mud, bottom samples were taken at different stations over a period of several months to trace the dispersion of the dumped material. The results of the analysed bottom samples were used to prepare time series of radioactivity in different sample stations, to draw maps of radioactivity and to calculate activity balances, which give an indication of the percentage of the material that is found again.

The main findings of these experiments can be summarised as follows. The material dumped at the five stations within about 20 km of the coast recirculated rapidly to the coast. In some cases, radioactive material was found in the harbours after only 2 or 3 days. The mud dispersed over the entire Belgian coast

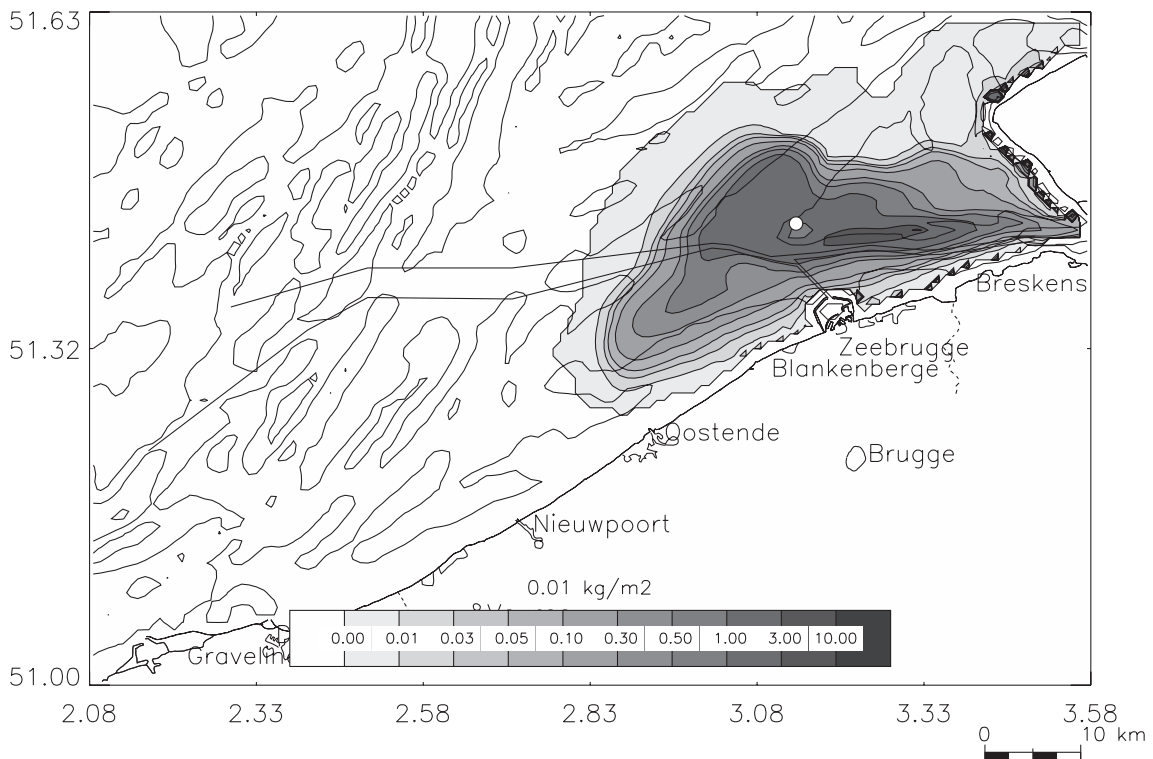


Fig. 7. Tide-averaged distribution of mud per m^2 for the *sx1a* experiment, 13 days after the dumping, as calculated with MU-STM. The original dumping site is indicated by the white circle.

and migrated into the Westerschelde. During storm periods, the material could disappear for a period, but after time, it was found back at the coast. The radioactive mud dumped at site *sx3b* however did not flow to the coast. During the entire sampling period, almost no tracer was detected on the BCS. Malherbe (1991) concluded that the experiments demonstrate the existence of the turbidity maximum area, near the coast. Furthermore, it was suggested that the mud in the Belgian coastal waters was trapped in a “closed system”, from which the mud can almost not escape.

4.2. Model simulations

To better understand and interpret the tracer experiments, the numerical models were used, simulating the dispersion of mud during the same period of the experiments. Since the sediment transport model is unable to model the radioactivity directly or to model the mixing of the radioactive material with the other sediments, only a qualitative comparison between the

model simulations and the tracer experiment results will be possible. On the other hand, one has to realise that the tracer experiments themselves only give qualitative results, since the calculation of the activity balances is subject to large uncertainties and indicates that only a small amount of radioactive material is traced back.

Since most of the dumped material is mud, since mainly the mud is washed away from the dumping sites and since only mud is used in the tracer experiments, the simulations are performed for mud only. For each of the tracer experiments, the dumping of 5500 tons of mud is simulated. The material is dumped on an area of 250×250 m. Ninety percent of the dumped material is put at the bottom, while 10% is supposed to stay in suspension (Johnson et al., 1988). It is assumed that no other sediments are present at the bottom and that no mud enters the model grid through the boundaries.

The results of the simulations are largely influenced by the choice of the parameters which are used

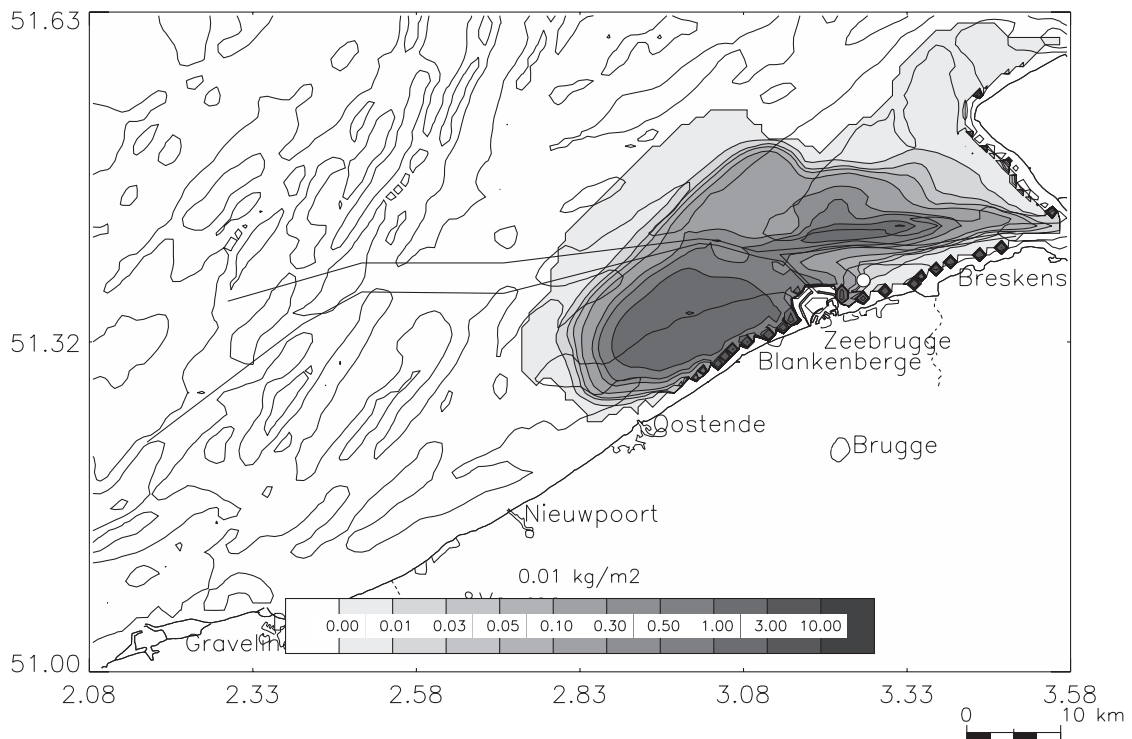


Fig. 8. Tide-averaged distribution of mud per m^2 for the *sx1b* experiment, 13 days after the dumping, as calculated with MU-STM. The original dumping site is indicated by the white circle.

to calculate the erosion and deposition of the sediments. Unfortunately, these parameters can vary over several orders of magnitude, depending on many different factors (e.g. Berlamont et al., 1993). Consequently, also the values used in the sediment transport models, cited in literature, differ over a large range.

The parameters used in these simulations were selected after a literature study and some sensitivity tests, whose description falls out of the scope of this paper. From these tests, it appeared that the results of the model are highly sensitive to the chosen parameter values. It is therefore clear that the model parameters were chosen in such a way to model well the behaviour of the mud.

The critical stresses for erosion and for deposition are both set to 0.5 Pa, while the erosion constant is taken as 0.12 g/m² s. For the fall velocity, the rather high value of 0.01 m/s is used. This value is used to account for the rapid decrease of suspended matter observed, e.g. in measurements with a digital multi-

spectral airplane scanner (Fransaer, 1994). In addition, calibration of the sediment transport parameters, using measurements executed by Rijkswaterstaat (1993) offshore of Zeebrugge, showed high fall velocities. The constant horizontal diffusion coefficient was set to 10 m²/s.

In all figures representing model results, the amount of the material per m² is presented. This amount includes the material at the bottom and the material in the water column. In (Figs. 7, 8, 11–13), tide-averaged values are shown.

4.3. Results

4.3.1. Tracer experiments *sx1a* and *sx1b*

After the dumping of the radioactive material on the sites *sx1a* (at dumping site B/2) and *sx1b* (at dumping site B/6) on April 22nd 1992, the meteorological conditions were relatively calm. During the first 3 weeks after the dumping, the wind speed was

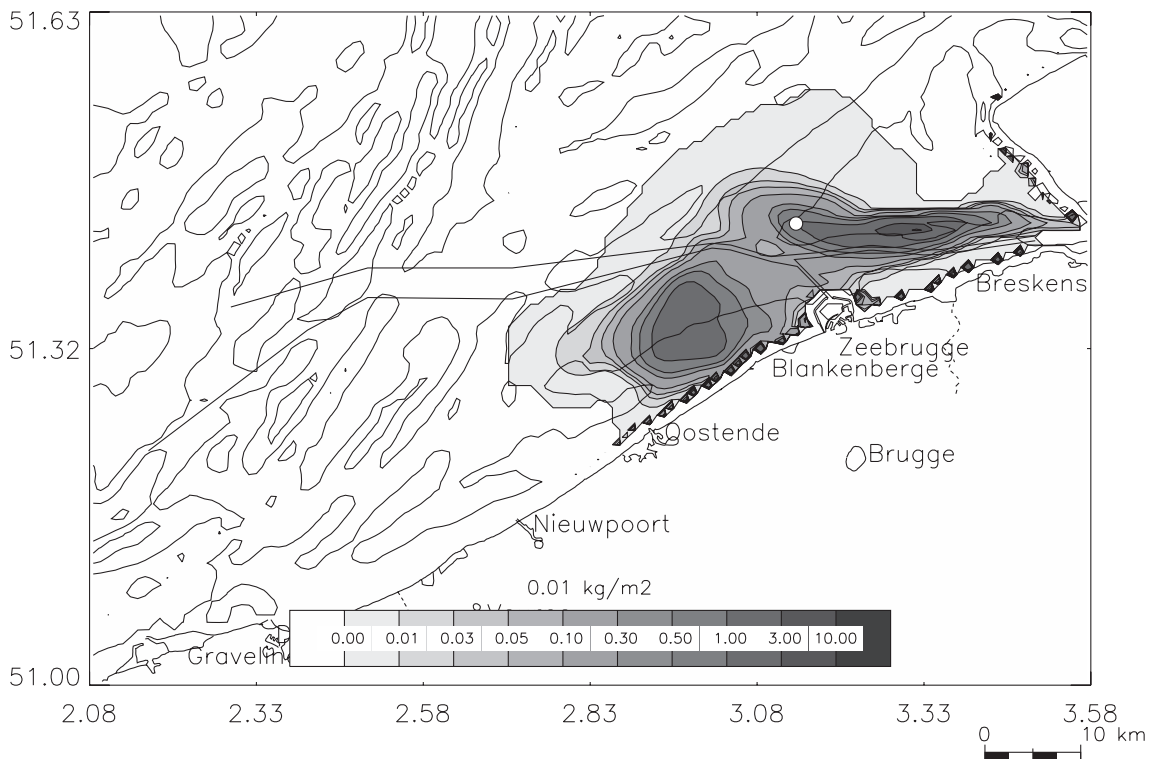


Fig. 9. Distribution of mud per m² for the *sx1a* experiment at 21/05/1992 16h12, 29 days after the dumping, as calculated with MU-STM. The original dumping site is indicated by the white circle.

Table 2

Amount of the material still on the model grid after 14 days of simulation with the sediment transport model MU-STM

Exp.	Place	Amount on the grid (%)
sx1a	B/2	70.3
sx1b	B/6	93.0
sx2a	Noordflank Akkaert	61.0
sx2b	Ebschaar B/1 and B/2	14.5
sx3a	Negenvaam	95.6
sx3b	Noordflank Thornton	0.1

limited to maximum 12.5 m/s and the wind was blowing in northeastern to southeastern direction. The wave heights at dumping site B/1 were less than 1.5 m. The two following months the wind speeds dropped to less than 10 m/s, while the wind was mainly in western to southwestern direction.

Six days after the start, a first measuring campaign was carried out. Five stations were sampled, all of them near the coast or in the harbours. Both for the

material dumped at B/2 (*sx1a*) and for the material dumped at B/6 (*sx1b*), radioactivity was detected in all samples from the harbour of Oostende to the harbour of Breskens indicating a fast transport to the coast. In the model results, the material dumped at the B/2 dumping site (*sx1a*) has not reached the coast after 1 week of simulation. Thirteen days after the dumping, the model results show that mud can be found near the coast between Oostende and Breskens (Fig. 7). The material dumped at B/6 stays near the coast and is dispersed over the area from Oostende to the Westerschelde as well (Fig. 8). Both measurements and model results therefore indicate that the mud recirculates to the coast and is dispersed over an area from Oostende to the Westerschelde, although the recirculation and the spreading over the entire Belgian coastal waters seems faster in the experiments.

The second measuring campaign was carried out 20 to 22 days after the start of the experiment. While in the model results the material is dispersed over a

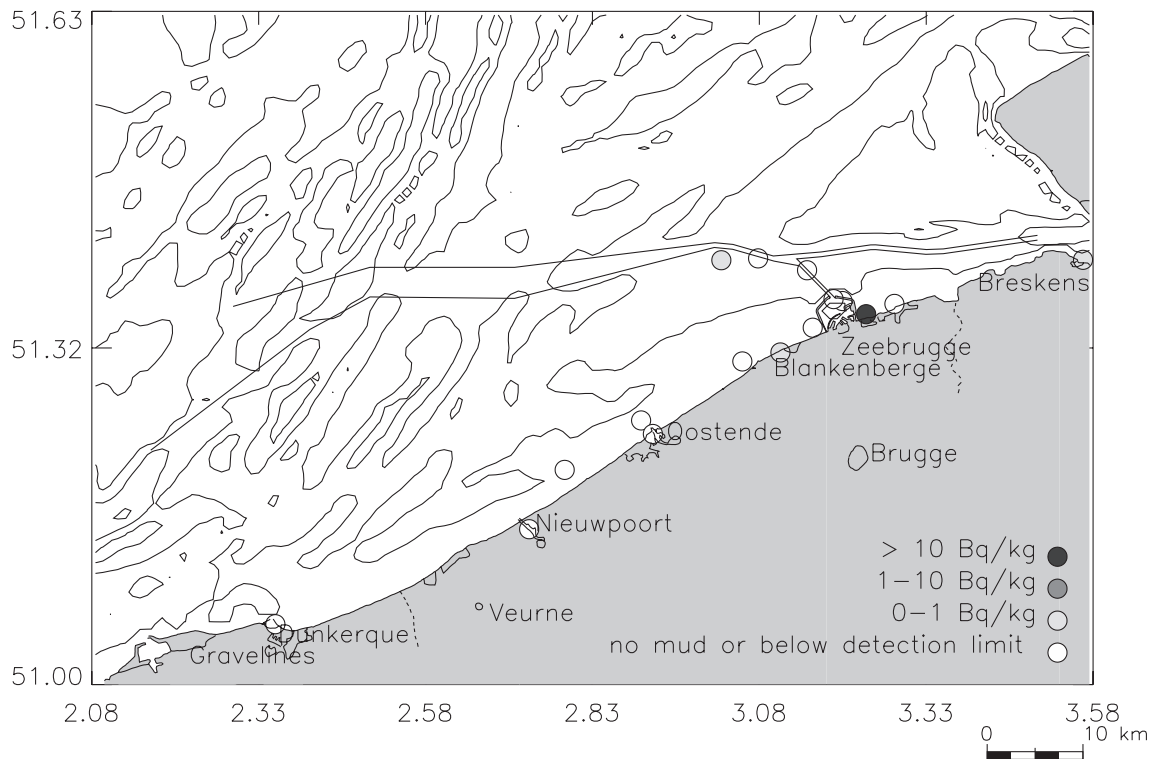


Fig. 10. Measured radioactivity for experiment *sx2a* in the bottom samples, 10 days after the dumping. Experiment executed by HAECON NV (1993b).

large area, some samples taken in open sea seem to indicate that the mud stays nearer to the coast.

During the following months, radioactive mud was found regularly in some bottom samples. The model simulations show that a significant fraction of the mud patch stays at the BCS. After 69 days, some 40% of the material, dumped at B/2 dumping site (*sx1a*) stayed on the model grid, while some 60% of the material dumped at B/6 (*sx1b*) is found on the BCS. This mud is mobile and will be displaced under the influence of the prevailing meteorological conditions. During a period with southerly winds the patch will be transported to the north, to the Netherlands, while during periods with northerly winds, the fine-grained sediments will be displaced to the south. When the meteorological conditions remain quiet for a sufficiently long period, the material returns back to the coast and a tendency for the formation of a turbidity maximum located between Oostende and Zeebrugge and in the mouth of the Westerschelde is clear (e.g. Fig. 9).

4.3.2. Tracer experiments *sx2a* and *sx2b*

The second series of tracer experiments started on January 18th 1993. The first week after the dumping of the radioactive material at sites *sx2a* (at the Noordflank Akkaert) and *sx2b* (at the Ebschaar B/1 and B/2), the weather conditions were rough. Wind speeds up to almost 20 m/s and wave heights up to 2.5 m were observed offshore of Zeebrugge on January 24th and 25th. Both wind and waves were directed to the north to northeast.

In the first 14 days after the start of the experiment, only a very limited number of bottom samples was taken, due to the rough weather conditions. In the few bottom samples, taken during the first week, some radioactivity could be detected in the sea harbours. After the storm, much less radioactive matter is found in the bottom samples. Certainly for the dumping at the 'Ebschaar B/1 and B/2' (*sx2b*), the material seems to have disappeared from the BCS. The calculated tracer activity balances show that only a very limited

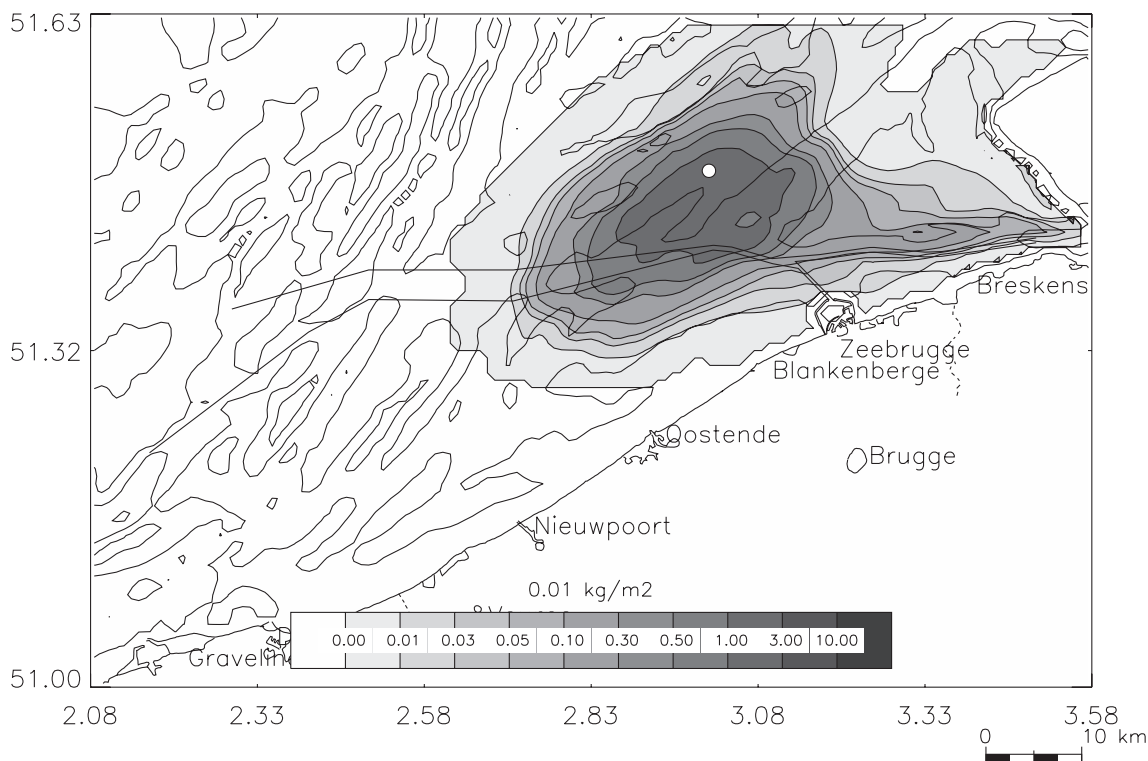


Fig. 11. Tide-averaged distribution of mud per m^2 for the *sx2a* experiment, 10 days after the dumping, as calculated with MU-STM. The original dumping site is indicated by the white circle.

amount of radioactive material is found again after the storm. During different later campaigns material has been detected in the open sea and in the Oosterschelde. Remark that, although the site *sx2a* is further located from the coast than the site *sx2b*, more material is detected in the bottom samples that originated from the former station.

The model results indicate that the dumped material is transported mainly in the direction of the wind and wave fields. A considerable amount of the mud (especially for the material dumped at site *sx2b*) leaves the model area towards the Netherlands and the Oosterschelde. A certain fraction enters the Westerschelde. As shown in Van den Eynde (1996), the residual currents and transports are strongly influenced by the meteorological conditions. Therefore, it is reasonable to assume that the mud will be transported mainly in the direction of the strong wind fields and that only a small fraction of the mud will be transported, due to strong diffusion, towards the

coast. This agrees with the fact that material is only detected again at a much later date, that only a very limited amount of material is found after the storm and that material is found in open sea and in the Oosterschelde. Remark that, as in the measurements, the material dumped at the *sx2b* site, disappears faster from the BCS than the material dumped at the *sx2a* site. While still 61% of the material dumped at *sx2a* is still on the model grid after 14 days of simulation, only 15% of the *sx2b* mud was left behind (see Table 2).

In Figs. 10 and 11, the measurements and the model results are presented 10 days after the dumping of the radioactive material at site *sx2a*. In the tracer experiments, no material is detected in the bottom samples, except east of Zeebrugge and in Blankenberghe, in Breskens and in the station Wandelaar (Fig. 6) in open sea. In the model results, the material is dispersed over a larger area, but the core of the material in suspension is located near station Wandelaar.

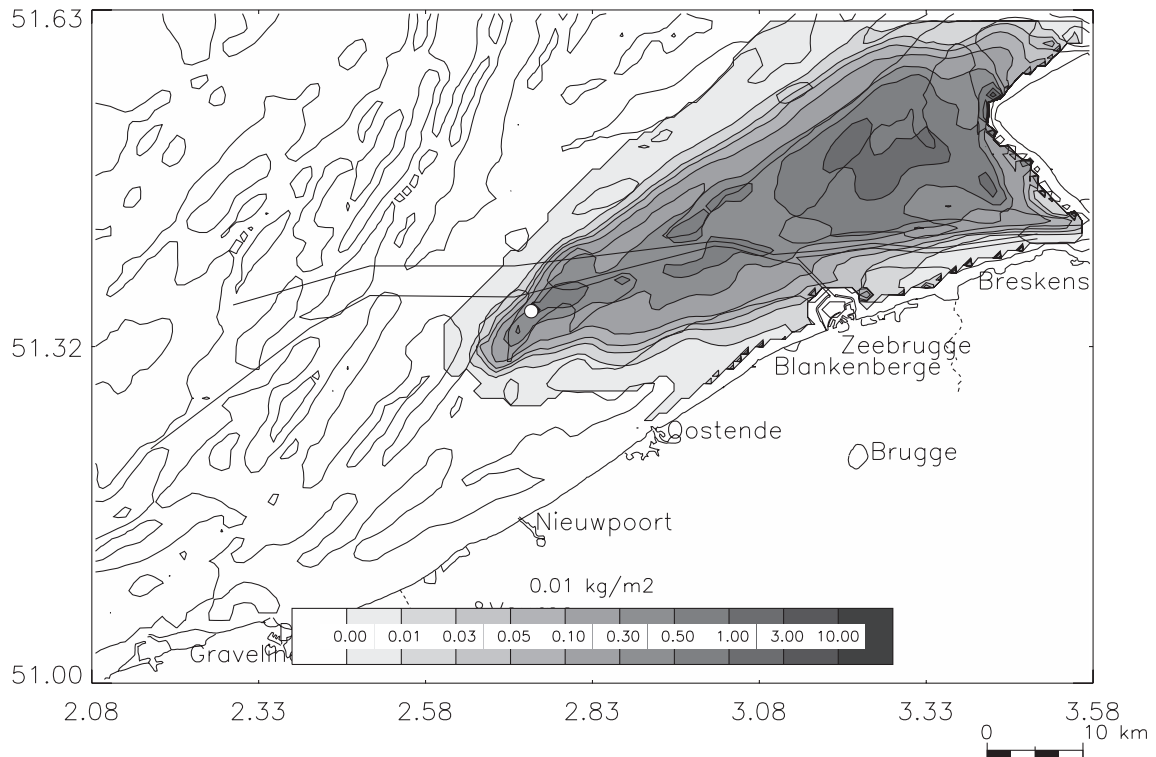


Fig. 12. Tide-averaged distribution of mud per m^2 for the *sx3a* experiment, 13 days after the dumping, as calculated with MU-STM. The original dumping site is indicated by the white circle.

4.3.3. Tracer experiments *sx3a* and *sx3b*

On September 29th 1993, two more tracer experiments were started, with dumpings of radioactive tracer at the Negenvaam (*sx3a*) and at the Noordflank Thornton (*sx3b*), some 30 km from the coast. From the start of the experiment at the end of September 1993 to the beginning of November 1993, calm weather conditions prevailed. After a storm around November 15th, with the wind blowing to the southeast, the weather conditions improved again. After November 28th, the wind turned, blowing to the north to north-east, and increased in speed, with peaks of more than 20 m/s on December 9th and December 18th.

In contrast with the results of the previous tracer experiments, the radioactive material dumped at the two sites behaved very differently in this case. The material dumped at the Negenvaam (*sx3a*) recirculates to the coast rapidly. Radioactive material is detected in coastal stations already 3 days after the dumping. During the following months, tracer can still be found

in coastal stations, until measuring campaign 10, which was carried out in the beginning of December. After this campaign, only a limited amount of material was detected anymore, until the end of the measuring campaigns in April 1994. The material dumped at the Noordflank Thornton (*sx3b*) however has never been detected in the area. Only in the Westerschelde, some very low values of radioactivity were sometimes found.

These main characteristics are well reproduced in the model. This is illustrated in Figs. 12 and 13 where for both simulations, the tidally averaged amount of mud per m^2 is presented 14 days after the dumping. While for the material dumped at the Negenvaam (*sx3a*) still almost 96% of the dumped material is located on the model grid, more than 99% of the material dumped at Noordflank Thornton (*sx3b*) disappeared (Table 2).

Also in this simulation, it is shown that the remaining mud is very mobile and will be displaced under the influence of the prevailing meteorological

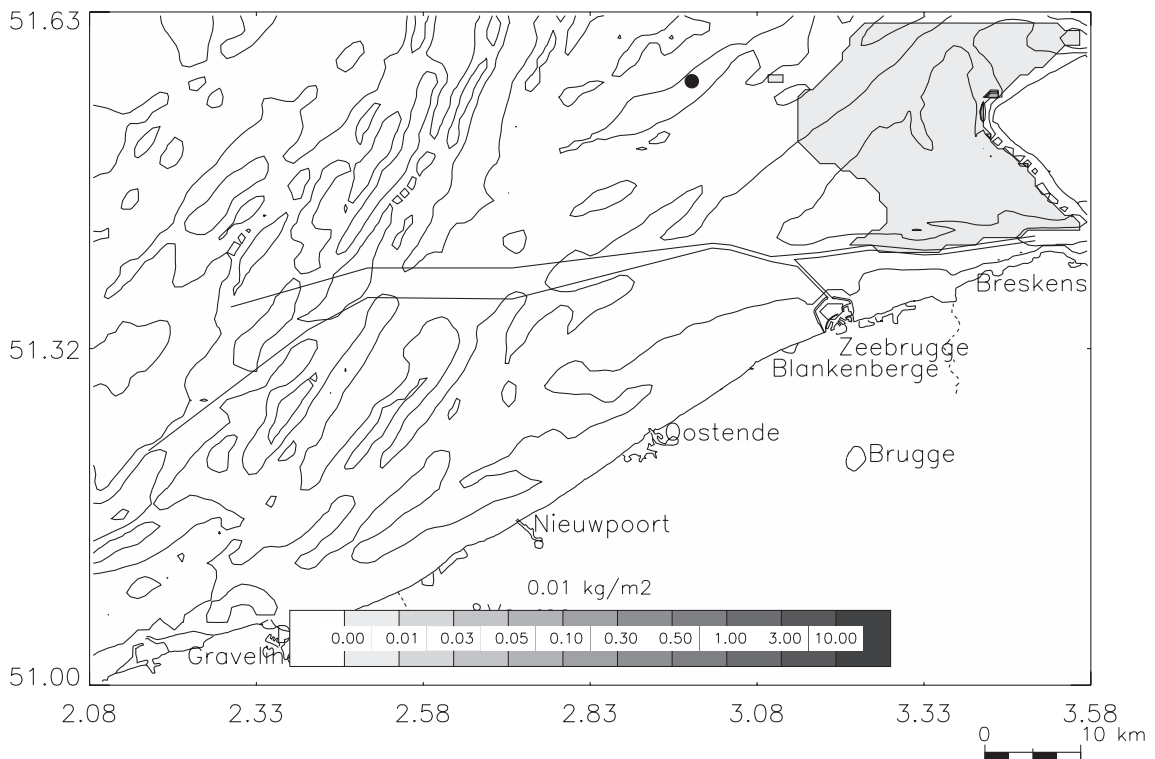


Fig. 13. Tide-averaged distribution of mud per m^2 for the *sx3b* experiment, 13 days after the dumping, as calculated with MU-STM. The original dumping site is indicated by the black circle.

conditions. Until the end of November 1993, 65% of the material dumped at the Negenvaam (*sx3a*) stays on the model grid. The storms with strong winds blowing to the north in the course of December, forces all material to the North, where it disappears from the model grid. This explains why no tracer is detected anymore after this period.

4.4. The turbidity maximum area

The simulations show that mud at the BCS is mobile and that it will be displaced under the influence of the prevailing meteorological conditions. However, when the meteorological conditions remain calm for a sufficiently long period, the material seems to return to the coast and tends to form a turbidity maximum located between Oostende and Zeebrugge and in the mouth of the Westerschelde (e.g. Fig. 9). The presence of such a turbidity maximum in the area is well known and is also observed in satellite images (e.g. Fig. 14 from Ruddick et al., 1998).

The main reason for the existence of a turbidity maximum in this highly energetic hydrodynamic

environment is still under debate. Different explanations have been proposed. Bastin (1973) attributed the high turbidity zone to convergent tidal currents, while Gullentops et al. (1976) suggested that the residual circulation system consists of a gyre, as an effect of the lateral pumping of the estuary of the Westerschelde. Nihoul and Runfola (1981) were able to simulate this gyre using hydrodynamic models. In the results, obtained with the hydrodynamic model presented in this paper, such a large gyre is not found in the calculated residual transports.

Other researchers stress the importance of the suspended matter supply through the Strait of Dover and from cliff and sea bed erosion along the east coast of the UK (e.g. Eisma, 1981). Recent research indicate that the flux of suspended particulate matter from the south to the BCS seems to be two or three times larger than was initially thought (Velegrakis et al., 1997). In addition, the seafloor erosion on the Flemish Banks (Gossé, 1977; Eisma, 1981; Van Alphen, 1990) and the erosion of tertiary clay layers (Gullentops et al., 1976; Malherbe, 1991) are mentioned as a source of suspended particulate matter on the BCS and as the

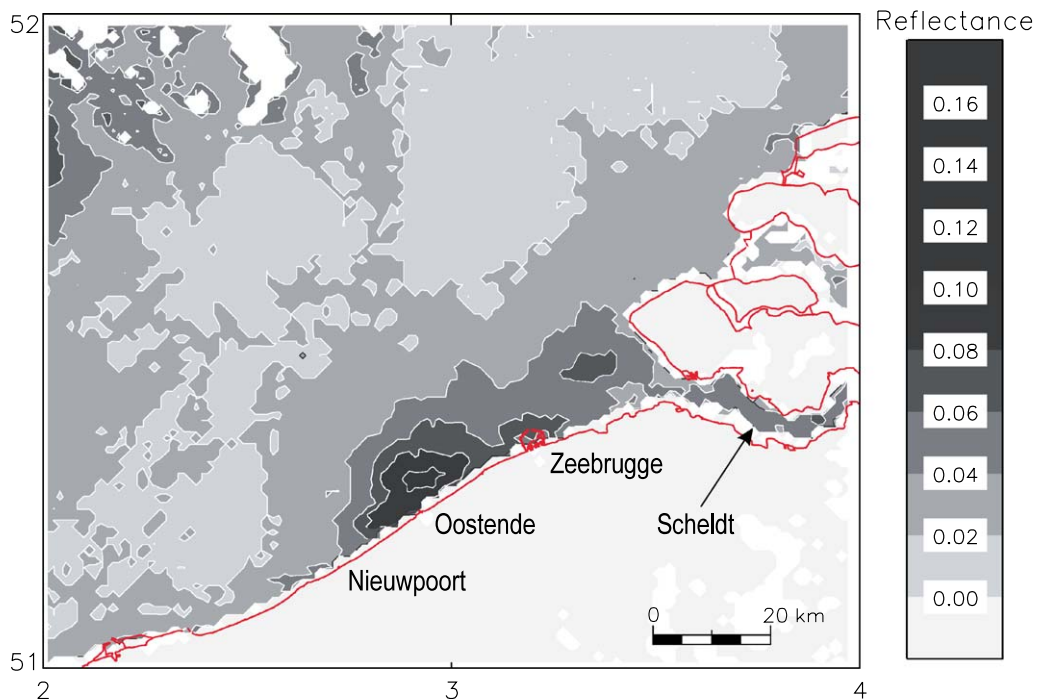


Fig. 14. Sub-surface irradiance reflectance for AVHRR channel 1 from NOAA-14 taken on 11/7/1997 at 13h24 (from Ruddick et al., 1998).

main explanation of the existence of the turbidity maximum area. More recently, Fettweis and Van den Eynde (2003) suggest by the analysis of model results that the processes responsible for the high turbidity zone formation are the decreasing magnitude of residual transport, the shallowness of the area and the inflow of suspended matter from the south.

Although the present paper does not focus on the explanation of the existence of the turbidity maximum, it is however encouraging to see that by the use of a simple two-dimensional sediment transport model, a turbidity maximum in Belgian coastal waters between Oostende and Zeebrugge and in the mouth of the Westerschelde can be reproduced.

5. Conclusions

In the paper, a vertically integrated sediment transport model, developed to simulate the dispersion of dredged material at the Belgian coast, is presented. The model is used to calculate the dispersion of fine-grained material for the same period during which experiments with radioactive tracers were carried out.

The main features of the behaviour of the mud are well reproduced by the model. In five experiments, the material recirculates and spreads out over the entire BCS rapidly, both in the measurements and in the model results. However, the recirculation in the model is not as fast as in the measurements.

On the other hand, one must realise that the recirculation as observed in the tracer experiments is very fast. The transport from the dumping site *sx2b* to the harbour of Nieuwpoort in 2 days implies a movement of the mud in the direction of the harbour of Nieuwpoort at a continuous velocity of almost 0.25 m/s, and this with wind speeds of 10 m/s or more in opposite direction. The exact reason for this very rapid return to the coast is not yet well identified or understood. It is therefore not unexpected that this very fast recirculation cannot be reproduced in the model results.

In the last experiment, where the material was dumped at the Noordflank Thornton, no transport of material to the Belgian coast was observed, neither in the measurements, neither in the model results. These numerical results are thus confirmed by observations.

The model results indicate that the material is spread out over a wide area and that the mud is

displaced under the influence of the prevailing meteorological conditions. In calmer weather conditions, the mud forms a turbidity maximum located between Oostende and Zeebrugge and in the mouth of the Westerschelde. The presence of such a turbidity maximum in the area is well known and can also be observed in satellite images.

As shown in the model results for the experiments *sx2a* and *sx2b*, the mud can eventually be transported to the northeast and escape from the BCS to the Netherlands. This seems to be confirmed by the experimental data. In contradiction to the idea that the suspended matter in Belgian coastal waters is trapped in a 'closed system', from which material can hardly escape (Malherbe, 1991), the model results and a re-evaluation of the tracer experiments indicate that the material can escape from the turbidity maximum. The material in the turbidity maximum then should be replaced by inflow of new material from the south. This agrees with the recent insight that the sediment flux from the south is larger than was estimated.

The fact that the turbidity maximum does not seem to be a 'closed system' may have important implications for the management of the dumping sites. In a closed system, the extraction of material from the system by dumping the material far enough from the coast, from where it will not return to the coast, e.g. at the Noordflank Thornton, will reduce the total amount of material in the system and therefore, on a longer term, the amount of dredging works needed in the future. If the system is not a closed system however, the exact place of the dumping site could not be a crucial factor in the mud balance on the BCS, since the material would escape from the system and would be replaced by new material anyway. Therefore, it is important to investigate and to estimate the natural transport and fluxes of suspended matter on the BCS. More research has to be executed to give a more definitive answer to these questions.

Although the model presented here is a simple, two-dimensional sediment transport model, which uses a number of parameters in the calculation of the erosion and the sedimentation of the material, the results of the model are satisfying and encouraging. The main characteristics of the tracer behaviour are well modelled, while in the longer simulations, the turbidity maximum is well reproduced.

Acknowledgements

José Ozer, Jaak Monbaliu and Michael Fettweis are thanked for useful discussions of the model results and for their constructive criticism on this paper. Kevin Ruddick is thanked for providing the AVHRR satellite image. Guido Dumon is acknowledged for providing the measurement data. The CAMME team is acknowledged for computing support. This study was supported by the Flemish government under the “VESTRAM” contract.

References

- Adam, Y., 1979. Belgian real-time system for the forecasting of currents and elevations in the North Sea. In: Nihoul, J.C.J. (Ed.), *Marine Forecasting*. Elsevier Oceanography Series, vol. 25. Elsevier, Amsterdam, pp. 411–425.
- Bastin, A., 1973. Natural radioactive tracers and their use in Belgium. *Tracer Techniques in Sediment Transport*. Technical Report 145, IAEA, Vienna.
- Berlamont, J., Ockenden, M., Toorman, E., Winterwerp, J., 1993. The characterisation of cohesive sediment properties. *Coastal Engineering* 21, 105–128.
- Ceuleneer, G., Lauwaert, B., 1987. The superficial sediments in the zone of the Flemish Banks (in French). MUMM Report, 34 pp. + 8 maps.
- CSTAB Group, 1996. Circulation and sediment transport around banks: project CSTAB. Project MAS2-CT92-0024. CSTAB Handbook and Final Report. B.A. O'Connor (Ed.), Report CE/05/96. Department of Civil Engineering, The University of Liverpool.
- de Kok, J.M., 1994. Numerical modeling of transport of processes in coastal waters, PhD Thesis, University of Utrecht. 158 pp.
- De Ruijter, W., Huber, K., Backhaus, J., 1987. North Sea circulation. 2nd International Conference on the Protection of the North Sea. Report of the Oceanography Subgroup. Scientific and Technical Working Group, pp. 19–36. Chap. 4.
- ECOPS Coastal Zone Steering Group, 1993. Outcome of the ECOPS-Euroconference on Prediction of Changes in Coastal Seas, Grand challenges for European co-operation in coastal marine science. Euroconference, held in Port d'Albret, France, 19–24 June. RIKZ, Den Haag, Nederland 52 pp.
- Egan, B.A., Mahoney, J.R., 1972. Numerical modeling of advection and diffusion of urban area source pollutants. *Journal of Applied Meteorology* 11, 312–322.
- Eisma, D., 1981. Supply and deposition of suspended matter in the North Sea. Special Publication of the International Association of Sedimentologists 5, 415–428.
- Fettweis, M., Van den Eynde, D., 2003. The mud deposits and the high turbidity in the Belgian–Dutch coastal zone, southern Bight of the North Sea. *Continental Shelf Research* 23, 669–691.
- Franssaer, D., 1994. Variation of the concentration of material in suspension as a function of tide at the Flemish coast (in Dutch). In: *Proceedings Conference on Influence of dumping of dredging material on the environment in the Southern North Sea*, March 2nd, 1994, Oostende. Administratie Waterwegen en Zeewezen and Beheersing Mathematisch Model Noordzee, 18 pp., Brussel.
- Gossé, J.G., 1977. A preliminary investigation into the possibility of erosion in the area of the Flemish Banks, Report FA 7702, Rijkswaterstaat, Dienst Getijdewateren. 30 pp.
- Gullentops, F., Moens, M., Ringelé, A., Sengier, R., 1976. Geologische kenmerken van de suspensie en de sedimenten. In: Nihoul, J.C.J., Gullentops, F. (Eds.), *Project Zee–Projet Mer, Sedimentologie*, vol. 4. Science Policy Office, Brussel, pp. 1–137.
- Günther, H., Rosenthal, W., 1985. The Hybrid Parametrical (HYPA) wave model. *Ocean Wave Modelling*, the SWAMP Group. Plenum, New York, pp. 211–214.
- HAECON NV, 1993a. Recirculation experiment Sx1 at the dumpings sites ZB-Oost en S2. Synthesis of the measuring results (in Dutch). Report MSB0721/93/00232. 43 pp.
- HAECON NV, 1993b. Recirculation experiment Sx2 at the north side of the Akkaert Bank and at the ebb gully between S1 and S2. Synthesis of the measuring results (in Dutch). Report MSB0721/93/00287. 42 pp.
- HAECON NV, 1995. Recirculation experiment Sx3 at the North side of the Thornton Bank and at the Negenvaam. Synthesis of the measuring results (in Dutch), Report MSB0721/95/00418. 43 pp.
- Johnson, B., Trawle, M.J., Adamec, S., 1988. Dredged material disposal modelling in Puget Sound. *Journal of Waterway, Port, Coastal and Ocean Engineering* 114, 700–713.
- Koutitas, C.G., 1988. *Mathematical Models in Coastal Engineering*. Pentech Press, London, UK 156 pp.
- Krone, R.B., 1962. Flume studies of the transport of sediment in estuarial shoaling processes. Final Report, Hydraulic Engineering Laboratory And Sanitary Engineering Research Laboratory, University of California, Berkeley.
- Malherbe, B., 1991. A case study of dumping in open seas. *Terra et Aqua* 45, 5–32.
- Ministerie van Volksgezondheid en Leefmilieu-BMM and Administratie Infrastructuur en Zeewezen – AWK, 1993. Ecological impact of dumpings of dredging material at the Belgian coast (in Dutch). Final Report, Brussels. 101 pp.
- Mouchet, A., Runday, F., 1992. Model of the transport of pollutants in the Scheldt estuary. Part I: Hydrodynamical model (ESHYDR package). Study for the Management Unit of the North Sea Mathematical Models, Ref. BH/90/37, Technical Report, University of Liège, Mécanique des fluides géophysiques. 64 pp.
- Nihoul, J.C.J., Runfola, Y., 1981. The residual circulation in the North Sea. In: Nihoul, J.C.J. (Ed.), *Ecodynamica-Elsevier Oceanography Series*, vol. 32. Elsevier, Amsterdam, pp. 219–271.
- O'Connor, B.A., 1984. Coastal sediment modelling. In: Dyke, P.P.G., Moscardini, A.O., Robson, E.H. (Eds.), *Offshore and Coastal Modelling. Lecture Notes on Coastal and Estuarine Studies*, vol. 12. Springer Verlag, New York, pp. 109–136. Ch. 6.

- Ovidio, F., Bidlot, J.R., Van den Eynde, D., Luo, W., Monbaliu, J., 1994. Validation of the second generation wave forecasting model MU-WAVE: comparison with ERS-1, buoy data and WAM forecasts. Proceedings of the First ERS-1 Pilot Project Workshop, Toledo, Spain, 22–24 June 1994. ESA Publications Division, ESTEC, Noordwijk, The Netherlands, pp. 21–28.
- Partheniades, E., 1962. A study of erosion and deposition of cohesive soils in salt water. PhD Thesis, University of California, Berkeley.
- Pedersen, L.B., Prahm, L.P., 1974. A method for numerical solution of the advection equation. *Tellus*, 594–602.
- Rijkswaterstaat, 1993. Measurements of currents and sediment transport at the section Zeebrugge-Westkapelle, Section A (in Dutch). Rijkswaterstaat, Verwerking Hydrografie, Report ZLMD-92.N.109, 16.05 M 92.01, 7 pp., 20 app.
- Ruddick, K., Ovidio, F., Van den Eynde, D., Vasilkov, A., 1998. The redistribution and dynamics of suspended particulate matter in Belgian coastal waters derived from AVHRR imagery. Proceeding of the 9th Conference on Satellite Meteorology and Oceanography, 25–29 May 1998, Paris, vol. II. American Meteorological Society, Boston, Massachusetts, United States of America, pp. 626–629.
- Smith, S.D., Banke, E.G., 1975. Variation of the sea surface drag coefficient with wind speed. *Quarterly Journal of the Royal Meteorological Society* 101, 665–673.
- Teisson, C.M., 1994. A review of cohesive sediment transport models. 4th Nearshore and Estuarine Cohesive Sediment Transport Conference (INTERCOH '94).
- Tijdelijke Vereniging Noordzee en Kust, 1998. Rapport over stortplaats B and W S1. Rapport TVNK/ZB/MDR/98018/PHE. 24 pp.
- Van Alphen, J.S.L.J., 1990. A mud balance for Belgian–Dutch coastal waters between 1969 and 1986. *Netherlands Journal of Sea Research* 25, 19–30.
- Van den Eynde, D., 1992. MU-WAVE: an operational wave forecasting system for the Belgian coast. Proceeding of the 3rd International Workshop on Wave Hindcasting and Forecasting, May 19–22, 1992, Montréal, Canada. Environment Canada, Atmospheric Environment Service, Downsview, Ontario, Canada, pp. 313–324.
- Van den Eynde, D., 1996. Activity Report No. 2, Project Sediment Transport Model-Phase II (in Dutch), Report BMM/STM2/AR02, Management Unit of the North Sea Mathematical Model, Brussels. 113 pp.
- Van den Eynde, D., 1997. Activity Report No. 3, Project Sediment Transport Model-Phase II (in Dutch), Report STM2/1/DVDE/199708/NL/AR/3, Management Unit of the North Sea Mathematical Model, Brussels. 76 pp.
- Van den Eynde, D., Ozer, J., 1993. Sediment Trend Analysis: calculation of the sediment transport by the use of a mathematical model (in Dutch). Report BMM/STA/TR01, study executed in charge of HAECON 1993, Management Unit of the North Sea Mathematical Models, Brussels. 49 pp.
- Velegrakis, A.F., Bishop, C., Lafite, R., Oikonomou, E.K., Lecourtier, M., Collins, M.B., 1997. Sub-Task S3: Investigation of meso- and macro-scale sediment transport, Hydrodynamics Biogeochemical Processes and Fluxes in the Channel. Fluxmanche II Final Report, MAST II MAS2CT940089, 1997, pp. 128–143.